

Alma Mater Studiorum – Università di Bologna
DOTTORATO DI RICERCA IN ASTRONOMIA
Ciclo XXI
Settore scientifico disciplinare di afferenza: FIS/05

X-Ray studies of the physics of matter around super-massive
black-holes in nearby Seyfert galaxies

Tesi di:
Mauro Dadina

Relatore:
Chiar.mo Prof. Giorgio Palumbo

Coordinatore Dottorato:
Chiar.mo Prof. Lauro Moscardini

Esame finale 2009

Scuola di dottorato in Scienze Matematiche, Fisiche, Chimiche ed Astronomiche
Dottorato di ricerca in Astronomia – XXI ciclo
PhD Thesis in Astronomia
Bologna, Marzo 2009

*A tutte le persone belle
che ho avuto la fortuna di incontrare:
a quelle che sono sempre state qui,
a quelle che sono arrivate
e a quelle che ora non ci sono.*

*This thesis has been carried out
at INAF/IASF-Bo as part of
the institute's research activities*

Contents

1	<i>The scientific framework</i>	1
1.1	<i>The AGN</i>	2
1.2	<i>The unified models</i>	4
1.3	<i>The Seyfert galaxies in X-rays</i>	7
1.3.1	<i>The X-rays emission mechanism</i>	9
1.3.2	<i>The neutral absorption in type II Seyfert galaxies</i>	10
1.3.3	<i>The reflection component</i>	11
1.4	<i>Open questions</i>	14
1.4.1	<i>Testing the UM</i>	14
1.4.2	<i>The emission mechanism</i>	15
1.4.3	<i>Testing the matter flow around SMBH</i>	16
2	<i>The data</i>	19
2.1	<i>The BeppoSAX sample</i>	20
2.1.1	<i>Data reduction and analysis</i>	22
2.2	<i>The X-CfA sample</i>	23
2.2.1	<i>The X-ray data</i>	25
2.3	<i>The XMM-Nweton sample</i>	26
2.3.1	<i>Spatial and Timing Analysis</i>	27
2.3.2	<i>Spectral Analysis</i>	28
3	<i>Testing the UM using the X-ray continuum</i>	31
3.1	<i>The methods of analysis of the BeppoSAX data</i>	31
3.2	<i>The X-ray continuum parameters to test the UM</i>	34
3.3	<i>The average absorption properties</i>	38

3.4	<i>Identification of highly absorbed sources in the XMM–Newton sample</i>	40
3.5	<i>The origin of the narrow component of the FeKα line</i>	45
3.6	<i>Summary of the results obtained testing the UM</i>	53
4	<i>The X-ray emission mechanism</i>	55
4.1	<i>The emission mechanism</i>	55
4.2	<i>The multiwavelength characteristics of the X–CfA sample</i>	58
4.3	<i>Picking-up Compton-thick and Starburst dominated objects</i>	59
4.4	<i>The X-rays and the Optical emission line characteristics</i>	62
4.4.1	<i>X-ray vs. Hα luminosity</i>	63
4.4.2	<i>X-ray vs. [OIII]$_{\lambda 5007}$ luminosity</i>	67
4.5	<i>M$_{BH}$ and Eddington ratios for the X–CfA sample</i>	71
4.6	<i>Summary of the results obtained on the emission mechanism</i>	75
5	<i>Key study objects: i) Mrk 509</i>	79
5.1	<i>The case of Mrk 509</i>	80
5.2	<i>Observations and data reduction</i>	81
5.3	<i>Fe K band emission of Mrk 509: the XMM–Newton data</i>	82
5.3.1	<i>The 6.4 keV emission line</i>	85
5.3.2	<i>The ionized Fe K emission line</i>	85
5.3.3	<i>Ionized absorption?</i>	87
5.3.4	<i>Time resolved spectral variability and total rms spectrum</i>	87
5.4	<i>The view of the Fe K band emission</i>	91
5.4.1	<i>The Suzaku pin data to constrain the reflection fraction</i>	94
5.5	<i>A physically self-consistent fit: possible origin of the spectral features</i>	95
5.6	<i>Discussion</i>	96
5.6.1	<i>Neutral/lowly ionized Fe emission line</i>	97
5.6.2	<i>Ionized Fe emission lines</i>	97
5.6.3	<i>Ionized Fe absorption lines</i>	98
5.7	<i>Conclusions</i>	99
6	<i>Key study objects: ii) NGC 3783</i>	101
6.1	<i>XMM–Newton observations</i>	101
6.2	<i>Data analysis</i>	102

6.2.1	<i>Spectral features of interest and selection of the energy resolution</i>	102
6.2.2	<i>Selection of the time resolution</i>	103
6.3	<i>Excess emission maps</i>	104
6.3.1	<i>Continuum subtraction</i>	106
6.3.2	<i>Image smoothing</i>	106
6.4	<i>Results</i>	107
6.4.1	<i>Light curves of the individual spectral features</i>	107
6.4.2	<i>Correlation with the continuum light curve</i>	109
6.4.3	<i>High/Low flux state line profiles</i>	109
6.5	<i>The deduced scenario for NGC 3783</i>	110
7	<i>Key study objects: iii) IRAS 13197-1627</i>	115
7.1	<i>The XMM–Newton observation and first–look analysis</i>	116
7.2	<i>The 2–12 keV spectrum of IRAS 13197–1627</i>	118
7.2.1	<i>X–ray reflection from the accretion disc and F_{exxv} resonant absorption</i>	123
7.2.2	<i>A partial covering alternative</i>	127
7.3	<i>The previous ASCA and BeppoSAX observations</i>	127
7.3.1	<i>Confirming the reflection–dominated spectrum with BeppoSAX</i>	129
7.3.2	<i>Long–term spectral variability</i>	129
7.4	<i>Origin of the reflection–dominated spectrum</i>	132
8	<i>Overview on the obtained results</i>	135
8.1	<i>The UM</i>	136
8.2	<i>The emission mechanism</i>	137
8.3	<i>Matter flows close to SMBHs</i>	138
A	<i>The BeppoSAX data</i>	141
A.1	<i>Atlas of the 2–100 keV spectra</i>	163
B	<i>The X–CfA sample data</i>	191

<i>C The XMM–Newton sample data</i>	199
<i>C.1 Atlas of X-ray spectra</i>	204
<i>Bibliography</i>	209

List of Figures

1.1	<i>Schematic view of the UM. The scheme accounts for the different kinds of RL and RQ AGN. The physical components that are thought to be present in the circumnuclear region around the SMBH are represented (M. Polletta adapted from Urry & Padovani 1995)</i>	5
1.2	<i>Schematic representation of the continuum emission measured in Seyfert galaxies (Courtesy of J. Manners)</i>	7
1.3	<i>Schematic representation of the X-ray spectrum observed in type I Seyfert galaxies (Courtesy of M. Cappi)</i>	8
1.4	<i>Leftpanel : the X-ray reflection component emerging from a neutral slab (solid line). The dashed line shows the incident continuum. Most of the radiation below 20 keV is absorbed by metals in the reflecting slab and re-radiated at lower energies (i.e. thermalized). Rightpanel : the reflection spectra predicted assuming different ionization states for the reprocessing slab. The ionization states are described by the ionization parameter ξ (see text). When the reflector is ionized, strong emission lines are produced at $E \leq 2$ keV. (Figures from Fabian et al. 2000)</i>	11

1.5	<i>The shape of reflection lines from the accretion disk is sculpted by the interplay of Doppler and transverse Doppler shifts, relativistic beaming and gravitational redshift. These effects are taken into account step-by-step moving from the upper to the lower panel of this figure. In the first three panel, only the contribution coming from two narrow annuli of the accretion disk are considered. In the lower panel it is plotted the summed profile considering the emission from the entire accretion disk (Figures from Fabian et al. 2000)</i>	13
3.1	<i>Photon index Γ (first row), R (second row) and E_c (third row) in units of cm^{-2} distributions for the whole dataset (left column), for type I objects (center column), and for type II objects (right column).</i>	35
3.2	<i>Distribution of the observed photon index for the XMM–Newton sample. The upper panel refers to the entire sample, the middle panel to the type I objects and the lower panel to the type II Seyferts.</i>	37
3.3	<i>N_H (in units of cm^{-2}) distributions for the whole dataset (left column), for type I objects (center column), and for type II objects (right column).</i>	38
3.4	<i>Distribution of the observed absorbing columns for the XMM–Newton sample. The upper panel refers to the entire sample, the middle panel to the type I objects and the lower panel to the type II Seyferts.</i>	39
3.5	<i>Diagram of the absorbing column density N_H versus the ratio between the observed 2–10 keV flux and the reddening-corrected [O III] flux taken from Panessa (2004). Filled polygons are type 1 Seyferts and open polygons are type 2 Seyferts. The shaded region (lower-left to upper-right diagonals) indicates the expected correlation under the assumption that $L_{2-10\text{keV}}$ is absorbed by the N_H reported on the ordinate, starting from the average $F_{\text{HX}}/F_{[\text{O III}]}$ ratio observed in type I Seyfert galaxies and by assuming a 1% reflected component. Also, the shaded region (upper-left to lower-right diagonals) obtained by Maiolino et al. (1998) is shown.</i>	42

3.6	<i>Distribution of the photon index before (left panel, see Figure 3.2) and after (right) correction for Compton-thick candidates for which a value of $\Gamma=1.62$ is assumed (see text for details).</i>	44
3.7	<i>Distribution of the absorption column densities before (left, see Figure 3.4) and after (right) correction for Compton-thick candidates. Upper and lower limits are indicated with arrows.</i>	45
3.8	<i>Distribution of the $FeK\alpha$ emission line energy centroid (first row) and of its EW (second row). Distributions for the whole sample of observations (left panel), for the type I objects (center panel) and for type II objects (right panel).</i>	46
3.9	<i>Upper panel: $\text{Log}(EW_{FeK\alpha})$ vs. $\text{Log}(N_H)$. As expected, the sources are divided in two families: the ones that follow the expectations if the $FeK\alpha$ line is produced in the absorption matter and the candidate Compton-thick ones that display low absorption and large EW. The solid line indicates the prediction by Makishima (1986). Left panel: $\text{Log}(F_{2-10keV}/F_{20-100keV})$ vs. $\text{Log}(N_H)$. The two quantities are correlated as expected since the 2-10 keV band is strongly affected by the absorption while the 20-100 band is almost free from absorption. The solid line is the best fit obtained with linear regression methods Right Panel: $\text{Log}(EW_{FeK\alpha})$ vs. $\text{Log}(F_{2-10keV}/F_{20-100keV})$. The two quantities are strongly correlated ($P_{null} \leq 0.01$). The ratio between X-ray fluxes is a model independent indicator of the absorption affecting the low energy band. Thus, this correlation strongly indicates that the narrow component of $FeK\alpha$ line in emission is indeed produced by the same matter responsible for the absorption. The solid line is the linear regression obtained using Bukley-James method (Isobe et al. 1986).</i>	49

- 3.10 Panel (a): $\text{Log}(EW_{\text{FeK}\alpha})$ vs. $L_{2-10,\text{observed}}$. Panel (b): $\text{Log}(EW_{\text{FeK}\alpha})$ vs. $F_{2-10,\text{observed}}$. Panel (c): $\text{Log}(EW_{\text{FeK}\alpha})$ vs. $L_{20-100,\text{observed}}$. Panel (d): The same as panel (c) but only for Seyfert 1 objects. Panel (e): $\text{Log}(EW_{\text{FeK}\alpha})$ vs. $F_{20-100,\text{observed}}$. Solid lines in panel (a), (b), and (c) are the linear regressions obtained for the whole sample of observations. The dashed line in panels (c) and (e) is the linear regression obtained considering only type I objects. As visible in panel (b) the less scattered relation is obtained considering the 2-10 keV observed flux. The relation is linear, as expected if the correlation is due to selection effects, i.e. considering that in faint objects only large EW were detectable by the MECS instruments on-board BeppoSAX. 51
- 4.1 Distribution of the 2–10 keV luminosities before (left) and after (right) correction for Compton-thick candidates (after Table 3.3). Upper limits have been indicated with arrows. 56
- 4.2 Left panel: Photon index Γ plotted versus the measured N_{H} (in units of cm^2). No significant trend relating these two quantities is found; center panel: R vs. E_{c} (in units keV), no correlation is found between these quantities; right panel R vs. Γ . The two quantities are correlated with a high significance level ($P_{\text{null}} \leq 1\%$). The line is the linear regression best fit. 57
- 4.3 $F_{\text{X}}/F_{[\text{OIII}]}$ vs. $F_{[\text{OIII}]} / F_{\text{IR}}$ diagram. Compton thin, Compton thick and starburst regions have been separated by dashed lines. Type 1 objects are plotted as filled polygons, type 2 as empty polygons, 'mixed Seyfert' objects as crosses and Compton thick candidates as stars. 60

4.4	<i>Left panel: Log of 2-10 keV luminosity versus log of H_{α} luminosity (narrow+broad components) corrected for the Galactic and NLR extinction. The dotted line shows the best fit linear regression obtained by fitting type I Seyferts and low-z quasars from Ward et al. (1988). Right panel: the same plot using the 'Compton thick' corrected luminosity. The solid line shows best fit linear regression line obtained by fitting the total sample of Seyfert galaxies and the low-z quasars. Filled polygons are type I Seyfert, open polygons are type II Seyfert, 'mixed Seyfert' objects are indicated as crosses, Compton thick candidates are stars and low-z quasars are 'rounded-stars'.</i>	64
4.5	<i>Correlation between 2-10 keV versus H_{α} fluxes. H_{α} narrow+broad components are corrected for the Galactic and NLR extinction. Symbols as in Fig. 4.4</i>	66
4.6	<i>Left panel: Log of 2-10 keV luminosity versus log of $[OIII]_{\lambda 5007}$ luminosity corrected for the Galactic and NLR extinction. The solid line shows the best fit linear regression line obtained by fitting type I Seyfert, a sample of bright type I Seyferts (QSO, Mulchaey et al. 1994) and a sample of PG quasar (PG, Alonso-Herrero et al. 1997). Right panel: the same plot using 'Compton thick' corrected luminosity. The solid line shows our best fit linear regression line for the total sample of Seyfert galaxies, the PG quasars and bright type I Seyfert. Symbols are as in Fig. 4.4</i>	69
4.7	<i>Correlation between log of 2-10 keV versus log of $[OIII]_{\lambda 5007}$ fluxes, the latter corrected for the Galactic and NLR extinction.</i>	70
4.8	<i>Left panel: Distribution of the log of black hole masses in unit of solar masses . Right panel: Distribution of the log of L_{Bol}/L_{Edd} ratio, assuming that $L_{Bol}/L_X \sim 30$. In both panels the shaded areas represent the distribution of type I Seyferts only.</i>	73
4.9	<i>Log of 2-10 keV luminosity versus log of black hole mass (symbols as in fig 4.6). Compton thick candidates are plotted as stars. The solid lines show the $L_{2-10keV}$ as a function of the black hole mass for Eddington ratios of 1.0 and 0.01.</i>	74

- 5.1 *3.5–10 keV EPIC–pn light curves of the XMM-Newton observations. The abscissa shows the observation time in seconds. The time between the different observations is arbitrary. The black, red, green, blue and light blue show the light curves during the 2000–10–25, 2001–04–20, 2005–10–16, 2005–10–20 and 2006–04–25 observations, respectively. 82*
- 5.2 *(Upper panel) Observed–frame 3.5–10 keV summed XMM-Newton EPIC–pn spectrum fitted in the 3.5–5 and 8–10 keV band with a power law. (Panel a) Data/model ratio. This ratio shows a clear evidence for a neutral Fe K emission line and further emission from ionized Fe, as well as other complexities around 7 keV. (Panel b) Data/model ratio when two resolved emission lines (for the Fe K α and K β) are included in the spectral fitting. Strong residuals are still present, indicative of ionized Fe K emission, while no residual emission redward of the neutral Fe K line appears. (Panel c) Data/model ratio when a narrow emission line is included in the model to reproduce the ionized emission. (Panel d) Same as panel c, but with a single broad emission line instead of a narrow line. In both cases (panel c and d), an absorption feature is present around 7 keV. (Panel e) Data/model ratio when an absorption component (modeled using xstar) and a relativistic ionized line are added to the power law and the emission from neutral Fe K. 84*
- 5.3 *(Left panel) Contour plot of the sigma vs. intensity of the neutral Fe K line. (Right panel) Contour plot of the energy vs. intensity of the narrow line used to fit the ionized Fe K emission. The narrow line energy is not consistent with emission from Fe XXV (neither with the forbidden at 6.64 keV, nor with the resonant at 6.7 keV), Fe XXVI or Fe K β , whose energy is indicated by the vertical dotted lines (from left to right). 85*

5.4	<i>Superposition of the pn (green), MOS1 (black) and MOS2 (red) summed spectra of all the XMM-Newton observations. The data are fitted, in the 3.5–5 and 8–10 keV bands with a power law, absorbed by Galactic material. The same structures are present in the three spectra. In particular, a narrow drop of emission is present in all the instruments at the same energy (see vertical dotted line). (Inset panel) Confidence contour plot of the intensity vs. energy of the narrow unresolved ionized absorption when using the pn data alone (dashed contours) and including the MOS data as well (solid contours). The lines indicate the 68.3 (black), 90 (red), 99 (green) and 99.9 (blue) per cent confidence levels.</i>	88
5.5	<i>Lower panel: Total rms variability spectrum of the XMM-Newton observations. The data (blue crosses) show the spectrum of the variable component. The best-fit model is a power law with spectral index $\Gamma=2.18$ (red line) plus a Gaussian emission line (improving the fit by $\Delta\chi^2$ of 8.9 for the addition of 2 parameters). The dashed line highlights the centroid energy of the neutral Fe $K\alpha$ line, while the dotted line is placed at the maximum of the variability excess, modeled with the Gaussian emission line. The excess variability energy corresponds to a drop of emission of the real spectrum. . .</i>	90
5.6	<i>XMM-Newton (black) and XIS0+XIS3 (red) summed mean spectra. The data are fitted, in the 3.5–5 and 7.5–10 keV bands, with a simple power law, absorbed by Galactic material, and the ratio of the data to the best fit model is shown. The arrows mark absorption features in the spectrum.</i>	92
6.1	<i>The X-ray light curves of NGC 3783 in the 0.3–10 keV band. Left panel: light curve of the 2000 observation. Right panel: light curves of the 2001a and 2001b observations.</i>	102
6.2	<i>The 4–9 keV residuals against a simple power-law plus cold absorption continuum model for the spectrum of NGC 3783 during the 2001b observation. The data are obtained from EPIC pn. . . .</i>	104

- 6.3 *The excess emission maps of the 4–9 keV band in the time-energy plane at 2.5 ks time resolution. The images have been smoothed. Since the 6.4 keV line core is very strong and stable, the color map is adjusted to saturate the line core and allow lower surface brightness features to be visible. Left panel: excess emission map from the 2000 observation. Right panel: excess emission map from the 2001a and 2001b observations. 105*
- 6.4 *The light curves of the total 0.3–10 keV continuum flux and of the four spectral features (Tab. 2) extracted from the excess maps of the 2001a and 2001b observations (Fig. 6.3, Right panel), with errors computed from simulations. The time resolution is 2.5 ks. 108*
- 6.5 *Upper panel: The 0.3–10 keV light curve of NGC 3783 during 2001b observation at 2.5 ks time resolution. Middle panel: The 0.3–10 keV light curve of NGC 3783 during the 2001b observation after subtraction of a 4th degree polynomial (long-term variations) at 2.5 ks time resolution. Lower panel: The 5.3–6.1 keV ('red+wing energy band) light curve extracted from the excess emission map of the 2001b observation (Fig. 6.3, Right panel) at 2.5 ks time resolution. 110*
- 6.6 *The cross correlation function calculated between the de-trended 0.3–10 keV continuum light curve and the 5.3–6.1 keV feature (red+wing) light curve. 111*
- 6.7 *The Fe K line profile during the High flux (open squares) and the Low flux (solid circles) phases of the 5.3–6.1 keV feature. The ratios are computed against the best-fitting continuum model. The energies are in the observer frame. 111*
- 7.1 *Soft (S: 0.3–3 keV) and a hard (H: 3–12 keV) EPIC-pn source light curve together with the resulting hardness ratio (bottom panel). As revealed by fitting a constant to the data, the hard band is more variable than the soft one ($\chi_r^2 = 1.65$ vs. $\chi_r^2 = 0.85$ for 67 dof). However, the hardness ratio is still consistent with a constant value throughout the observation. 117*

- 7.2 *The broadband (0.3–12 keV) EPIC–pn spectrum of IRAS 13197–1627. The spectrum exhibits strong curvature in the hard band which is a clear sign of absorption by a substantial column of gas in the line of sight. Fe emission is detected at 6.4 keV in the rest–frame (vertical dotted line) together with a deep absorption edge at 7 keV. A soft excess is present below ~ 3 keV and is characterised by a bump around 0.9 keV. Data have been rebinned for visual clarity.* 118
- 7.3 *The 2–12 keV pn spectrum is shown together with a simple model (solid line) comprising a power law absorbed by a column density of $\sim 6.2 \times 10^{23} \text{ cm}^{-2}$ of neutral matter at the redshift of the source and a resolved ($\sigma \sim 90 \text{ eV}$) Gaussian emission line at 6.4 keV. Only the pn data are shown but all spectral analysis is performed simultaneously with the MOS data as well. Notice several residuals: absorption structures are seen around 6.8 keV and 7.1 keV. Moreover the model systematically underestimates the data in the 5–6 keV band and above 10 keV. In the Figure, data have been rebinned for visual clarity.* 119
- 7.4 **Top:** *A Gaussian line is added to the baseline model and its energy and normalisation are varied. The contours represent an improvement of $\Delta\chi^2 = -1, -2.3, -4.61, -9.21$ in fitting the joint pn–MOS data. The $\Delta\chi^2 = -1$ contour (outermost) is shown as a reference of the best–fitting continuum model. **Bottom:** *In this case the Fe K α line of the baseline model is forced to be unresolved. The shape of the residuals strongly suggests the presence of X–ray reflection from the disc (broad Fe emission line and broad Fe absorption edge).* 121*
- 7.5 *Same as in Figure 7.4, but now for the best–fitting model comprising Compton–thin absorption and reflection from the accretion disc, both with slightly super–solar Fe abundance (see text for details). The only remaining residual is a narrow absorption line at 6.8 keV. The rest–frame energies of the closest transitions (Fe xxv and Fe xxvi resonant absorption) are shown as vertical lines. . . .* 122
- 7.6 *In the top panel I show the result of our best–fitting model in the 2–12 keV band (see Table 1). Only the pn data are shown for clarity. In the bottom panel, I show the model components.* 126

-
- 7.7 *In the top panel I show the baseline XMM–Newton model applied to the BeppoSAX data (MECS and PDS detectors). The fit is acceptable but large residuals are seen around 20–30 keV where reflection is expected to dominate. In the bottom panel, I add the disc reflection component, i.e. I apply the XMM–Newton best–fitting model to the BeppoSAX data. 128*
- 7.8 *The 2–10 keV reflection flux is plotted against the 2–10 keV continuum flux from the three available observations. This demonstrates that the reflection component responds to the continuum long–term variability within the errors. As a reference the best–fitting linear relationship is shown. 131*

List of Tables

3.1	<i>General characteristics of the data analyzed here. The number of detections and censored data are reported for the interesting parameters for the whole sample of objects (columns 2 and 3), for the Seyfert 1 galaxies (columns 4 and 5), and for the Seyfert 2 objects (column 6 and 7). The 90% confidence interval limits were used for censored data and the detected values were defined if determined with a 99% confidence level</i>	33
3.2	<i>Mean spectral properties obtained with the BeppoSAX sample. Col. I: Spectral parameter; Col. II: Seyfert 1 mean value; Col.III: Seyfert 2 mean value; Col. IV: Probability that Seyfert 1 and Seyfert 2 are drawn from the same parent populations.</i>	36
3.3	<i>Compton-thick/thin Seyfert 2 candidates</i>	43
3.4	<i>Mean properties of the FeKα emission line. Col. I: spectral parameter; Col. II mean value for the whole sample; Col. III: mean value for Seyfert 1; Col. IV: mean value for Seyfert 2. Col. V: Probability that the parameters of type I and type II objects are drawn from the same parent population.</i>	47
4.1	<i>Correlation statistics in luminosities</i>	68

- 5.1 *Top panel: Best-fit values of the summed spectra (XIS0+XIS3) of all observations fitted in the 3.5–10 keV band. Both model A and B include a power law and two Gaussian lines $K\alpha+\beta$ to fit the 6.4 keV excess. In addition to this baseline model, either another Gaussian component (Model A) or a DISKLINE profile (Model B) have been added to reproduce the ionized line, respectively. In Table the best-fit power law spectral index (Γ) and normalization as well as the Fe $K\alpha$ energy, width and normalization are reported for model A and B. The energy, width and normalization are reported when a Gaussian profile for the ionized Fe K line is considered (Model A), while the best fit energy, inner radius and normalization are presented when a DISKLINE profile is fitted (Model B). Standard disc reflectivity index, outer disc radius and disc inclination of $\alpha = 3$, $r_{out} = 400 r_g$ and 30° have been assumed for the relativistic profile. Bottom panel: Best fit results of the summed XMM-Newton EPIC-pn and EPIC-MOS data of Mrk 509 (fitted in the 3.5–10 keV band). The model ($wabs*zxipcf*(pow+zgaus+zgaus+pextrav+kdblur*(reflion))$) consists of: i) a power law; ii) two Gaussian emission lines for the Fe $K\alpha$ and $K\beta$ emission (this latter has energy is fixed to the expected value, 7.06 keV, intensity and width tied to the $K\alpha$ values); iii) a neutral reflection continuum component (pextrav in Xspec) with $R=1$ (value broadly consistent with the pin constraints and the values previously observed; De Rosa et al. 2004), Solar abundance and high energy cut off of the illuminating power law at 100 keV; iv) a ionized disc reflection spectrum (reflion model; Ross & Fabian 2005) with the disc inner and outer radii and the emissivity of 6, $400 r_g$ and -3 , respectively. The best fit disc inclination and ionization and the normalization of the disc reflection component are shown; v) an ionized absorption component (zxipcf) totally covering the nuclear source. The best fit column density, ionization parameter and outflow velocity are reported. a) In units of 10^{-2} photons $keV^{-1} cm^{-2} s^{-1}$ at 1 keV; b) In units of 10^{-5} photons $cm^{-2} s^{-1}$; c) In units of eV; d) In units of 10^{22} atoms cm^{-2} 93*

6.1	<i>Date, duration, useful exposure and mean EPIC pn 0.3–10 keV count rate for each XMM-Newton observation of NGC 3783. . . .</i>	103
6.2	<i>Spectral features of interest in the 4–9 keV band with the selected band-passes and mean intensity.</i>	105
7.1	<i>The best-fitting parameters from joint fits to the 2–12 keV (pn) and 2–9.5 keV (MOS) spectrum of IRAS 13197–1627 ($\chi^2 = 442$ for 438 dof).</i>	124
7.2	<i>The best-fitting model to the XMM-Newton data is applied to the previous ASCA (2–10 keV) and BeppoSAX (2–80 keV) observations. I report the most relevant best-fitting parameters and the resulting statistics (χ^2/dof). For the BeppoSAX (XMM-Newton) observation, the baseline model also comprises a ~ 7.5 keV (~ 6.8 keV) absorption line.</i>	130
A.1	<i>List of the sources analyzed in this thesis. Col. I: Object Name; Col. II and III: Right ascension and declination (Equinox 2000); Col. IV: Redshift; Col. V: Seyfert type; Col. VI: Radio class. . . .</i>	141
A.2	<i>Observations Log. Col. I: Object name; Col. II: Observation date; Col. III: MECS exposure in ks; Col. IV: PDS exposure in ks; Col. V: MECS detection significance in the 2-10 keV band express in terms of standard deviation; Col. VI: PDS detection significance in the 20-100 keV band express in terms of standard deviations. In parentheses, values concerning the 20-50 keV band for those sources that are not detected in the 15-100 keV band.</i>	144
A.3	<i>Best-fit spectral parameter. Col. I: Observation name; Col. II: Total absorber Col. density; Col. III: Photon index; Col. IV: Energy centroid of the emission FeKα line; Col. V: EW of the emission line; Col. VI: Reflection parameter R; Col. VII: High-energy cut-off; Col. VIII: 2-10 keV flux; Col. IX: 2-10 keV observed luminosity; Col. X: 20-100 keV flux. Upper limits (3σ confidence level) have been calculated following the method presented in Sect. 3.3; Col. XI: 20-100 keV observed luminosity.</i>	150

B.1 The X-CfA galaxy sample Col. (1): Galaxy name; Col. (2): optical classification, '*'= objects with a changed classification with respect to the original given by HFS97. The quality rating is given by ":" and "::" for uncertain and highly uncertain classification, respectively, as reported in HFS97.; Col. (3): Hubble type; Col. (4) total apparent B magnitude of the galaxy; Col. (5): galaxy distances; Col. (6): Col. (7)-(8) optical position in epoch J2000. . 191

B.2 Multi-wavelength luminosities and M_{BH} of the total X-ray sample: Col. (1): galaxy name; Col. (2): optical classification; Col. (3): Satellite used: 'C'=Chandra, 'X'=XMM-Newton, 'A'=ASCA; Col. (4): logarithm of the 2-10 keV flux in units of $\text{erg cm}^{-2} \text{s}^{-1}$, not corrected for Compton thick candidates. Col. (5): logarithm of the 2-10 keV luminosity, corrected for Compton thick candidates. Col. (6): X-RAY REFERENCES: (1) Cappi et al. 2006; (2) This work; (3) Pappa et al. 2001; (4) Guainazzi et al. 2005b; (5) Terashima et al. 2002; (6) Eracleous et al. (2002); Col. (7): Final classification: '√'=Compton thick candidates, '×'=Compton thin candidate and '?'=doubtful objects.; Col. (8): logarithm of the $[OIII]_{\lambda 5007}$ luminosity corrected for Galactic absorption and NLR extinction; Col. (9): logarithm of the $H\alpha$ (broad+narrow component) luminosity corrected for Galactic absorption and NLR extinction; Col. (10): logarithm of the M_{BH} value in units of M_{\odot} ; Col. (11): M_{BH} measurement methods; M: maser kinematics; G: gas kinematics; S: stellar kinematics; R: reverberation mapping; I_{σ} : inferred from the mass-velocity dispersion correlation; Col. (12): M_{BH} REFERENCES. 194

C.1	<i>The XMM–Newton sample: Col. (1): galaxy name. Col. (2): other name. Col. (3): optical classification as given by HFS97: “S” represents Seyfert, “L” represents LINER, and “T” represents objects with LINER plus H II-region spectra. “2” implies that no broad Hα is detected; “1.9” implies that broad Hα is present, but not broad Hβ; “1.5” implies that both broad Hα and broad Hβ are detected, with substantial contributions from both the BLR and NLR (Osterbrock 1981). Objects with a changed classification with respect to the original given by HFS97 (see also Ho et al. 1997b and HU01) are denoted by “*” after their name. Col. (4): Hubble type as listed in HFS97. Col. (5): distance from Tully (1988), except when marked with (a) Paturel et al. (2002), (b) Cecil et al. (2002), (c) Tonry et al. (2001), and (d) Thim et al. (2004). Col. (6): total apparent B_T magnitude of the galaxy. Col. (7)–(8): nuclear optical position in epoch J2000 as given by HU01.</i>	199
C.2	<i>Col. (1): galaxy name. Col (2): Galactic absorption along the line of sight, in units of 10^{20} cm^{-2}. Col. (3): measured absorption column density, in units of 10^{22} cm^{-2}. Col. (4): power-law photon index. Col. (5): photon index of the soft power-law component. Col. (6): temperature of the thermal component (kT) in units of keV. Col. (7): equivalent width of the Fe K line, in units of keV. Col. (8): reduced chi-squared and number of degrees of freedom. Col. (9)–(10): observed fluxes in the soft (0.5–2 keV) and hard (2–10 keV) X-ray bands, in units of $10^{-13} \text{ erg cm}^{-2} \text{ s}^{-1}$. Col. (11)–(12): Log of the absorption-corrected luminosities in the soft (0.5–2 keV) and hard (2–10 keV) X-ray bands (computed using distances from Table C.1)</i>	202

Abstract

Seyfert galaxies are the closest active galactic nuclei. As such, we can use them to test the physical properties of the entire class of objects. To investigate their general properties, I took advantage of different methods of data analysis. In particular I used three different samples of objects, that, despite frequent overlaps, have been chosen to best tackle different topics: the heterogeneous *BeppoSAX* sample was thought to be optimized to test the average hard X-ray ($E \geq 10$ keV) properties of nearby Seyfert galaxies; the *X-CfA* was thought to be optimized to compare the properties of low-luminosity sources to the ones of higher luminosity and, thus, it was also used to test the emission mechanism models; finally, the *XMM-Newton* sample was extracted from the *X-CfA* sample so as to ensure a truly unbiased and well defined sample of objects to define the average properties of Seyfert galaxies.

Taking advantage of the broad-band coverage of the *BeppoSAX* MECS and PDS instruments (between ~ 2 -100 keV), I infer the average X-ray spectral properties of nearby Seyfert galaxies and in particular the photon index ($\langle \Gamma \rangle \sim 1.8$), the high-energy cut-off ($\langle E_c \rangle \sim 290$ keV), and the relative amount of cold reflection ($\langle R \rangle \sim 1.0$). Moreover the unified scheme for active galactic nuclei was positively tested. The distribution of isotropic indicators used here (photon index, relative amount of reflection, high-energy cut-off and narrow $\text{FeK}\alpha$ energy centroid) are similar in type I and type II objects while the absorbing column and the iron line equivalent width significantly differ between the two classes of sources with type II objects displaying larger absorbing columns. Taking advantage of the *XMM-Newton* and *X-CfA* samples I also deduced from measurements that 30 to 50% of type II Seyfert galaxies are Compton thick.

Confirming previous results, the narrow $\text{FeK}\alpha$ line is consistent, in Seyfert 2

galaxies, with being produced in the same matter responsible for the observed obscuration. These results support the basic picture of the unified model. Moreover, the presence of a X-ray Baldwin effect in type I sources has been measured using for the first time the 20-100 keV luminosity ($EW \propto L(20-100)^{-0.22 \pm 0.05}$). This finding suggests that the torus covering factor may be a function of source luminosity, thereby suggesting a refinement of the baseline version of the unified model itself.

Using the *BeppoSAX* sample, it has been also recorded a possible correlation between the photon index and the amount of cold reflection in both type I and II sources. At a first glance this confirms the thermal Comptonization as the most likely origin of the high energy emission for the active galactic nuclei. This relation, in fact, naturally emerges supposing that the accretion disk penetrates, depending to the accretion rate, the central corona at different depths (Merloni et al. 2006): the higher accreting systems hosting disks down to the last stable orbit while the lower accreting systems hosting truncated disks. On the contrary, the study of the well defined *X-CfA* sample of Seyfert galaxies has proved that the intrinsic X-ray luminosity of nearby Seyfert galaxies can span values between 10^{38-43} erg s⁻¹, i.e. covering a huge range of accretion rates. The less efficient systems have been supposed to host ADAF systems without accretion disk. However, the study of the *X-CfA* sample has also proved the existence of correlations between optical emission lines and X-ray luminosity in the entire range of L_X covered by the sample. These relations are similar to the ones obtained if high-L objects are considered. Thus the emission mechanism must be similar in luminous and weak systems.

A possible scenario to reconcile these somehow opposite indications is assuming that the ADAF and the *two phase* mechanism co-exist with different relative importance moving from low-to-high accretion systems (as suggested by the Γ vs. R relation). The present data require that no abrupt transition between the two regimes is present.

As mentioned above, the possible presence of an accretion disk has been tested using samples of nearby Seyfert galaxies. Here, to deeply investigate the flow patterns close to super-massive black-holes, three case study objects for which enough counts statistics is available have been analysed using deep X-ray observations taken with *XMM-Newton*. The obtained results have shown that the accretion flow can significantly differ between the objects when it is analyzed with the appropriate detail. For instance the accretion disk is well established down to the

last stable orbit in a Kerr system for IRAS 13197-1627 where strong light bending effect have been measured. The accretion disk seems to be formed spiraling in the inner $\sim 10-30 r_g$ in NGC 3783 where time dependent and recursive modulation have been measured both in the continuum emission and in the broad emission line component. Finally, the accretion disk seems to be only *weakly detectable* in rk 509, with its weak broad emission line component.

Finally, blueshifted resonant absorption lines have been detected in all three objects. This seems to demonstrate that, around super-massive black-holes, there is matter which is not confined in the accretion disk and moves along the line of sight with velocities as large as $v \sim 0.01-0.4c$ (where c is the speed of light). Whether this matter forms winds or blobs is still matter of debate together with the assessment of the real statistical significance of the measured absorption lines. Nonetheless, if confirmed, these phenomena are of outstanding interest because they offer new potential probes for the dynamics of the innermost regions of accretion flows, to tackle the formation of ejecta/jets and to place constraints on the rate of kinetic energy injected by AGNs into the ISM and IGM. Future high energy missions (such as the planned Simbol-X and IXO) will likely allow an exciting step forward in our understanding of the flow dynamics around black holes and the formation of the highest velocity outflows.

Chapter 1

The scientific framework

It is universally assumed, that the vast majority of massive galaxies host super-massive black-holes (SMBH) at their center (Kormendy & Richstone 1995, Magorrian et al. 1998). This was assumed as a paradigm for active galactic nuclei (AGN) only ~ 10 years ago. Now, deep infra-red observations have proved that this is indeed the real nature of the massive dark object that lies, for example, in the nucleus of the Galaxy (Eckart & Genzel 1996).

AGN are the compact objects that display the largest stable release of energy in the Universe ($L_{bol} \sim 10^{38-47}$ erg s $^{-1}$). As such, they are of intrinsic interest and, giving their luminosity, they could represent powerful markers to trace the distant Universe.

In recent years it has been discovered that the SMBH and the bulge/spheroidal component of the host galaxies have most probably evolved together. This is proved by the existence of the tight relations between the mass of the SMBH and the mass of the bulge and the dynamics of the stellar population that form the bulge (Magorrian et al. 1998; Merritt & Ferrarese 2001a, 2001b; Marconi & Hunt 2003; Marconi et al. 2004).

Finally, it has been definitively proved that the cosmic X-ray background (CXB) is synthesized by a mix of absorbed and unabsorbed AGN that must rapidly evolve with cosmic time, the evolution depending on the mass of the SMBH itself (Comastri et al. 1995, Gilli et al. 2001, 2007) and thus on the mass of the spheroid of the host galaxies.

These evidences clearly indicate that the understanding of the physics of AGN,

of their structure and evolution are among of the most important goals of modern astrophysics.

In this thesis, I will focus on some specific topics regarding nearby radio-quiet (RQ) AGN. These AGN are privileged targets since the absence of relativistic enhanced emission due to the jets of radio-loud (RL) objects offers an undisturbed vision of the nuclear regions. In particular, I will focus only on the nearby AGN, the Seyfert galaxies, and the problematic involving their inner few parsecs. The main scope of this work, in fact, was to investigate the physics of the AGN core from the edges of the putative *dusty torus* towards inner limits of the *accretion disk* (see next section). In doing so, I will present some open problems that I tried to tackle and the results I obtained.

The main astrophysical problematic I will face may be divided in two major families: a) the validity of the Unified Models for AGN (UM, Antonucci 1993) and b) the physics of the accreting matter close to the last stable orbits.

While the first topic was investigated using samples of nearby objects, the second topic was studied both using the same samples as for point a) but also focusing the attention of few objects that can be regarded as three case studies.

1.1 The AGN

Early after their discovery, it was supposed that the energy emission of AGN could hardly be reconciled with stellar activity given the fast variability patterns measured in the electromagnetic emission of AGN. This put very small and tight constraints on the dimensions of the regions from which the AGN emission was produced. Moreover, while the energy output of a typical galaxy is usually concentrated within no more than a decade in the frequency domain (being the sum of almost co-eval star populations), the AGN spectra are clearly described by a power-law emission from radio (I.R.) to X- (γ -) rays with similar energy release in decades of frequencies. In particular, one of the fingerprints of AGN emission is that the X-rays are at least 1000 times more intense in AGN with respect to normal galaxies. This fact alone explains why the high-energy bands are fundamental tools in understanding the AGN physics.

High luminosity, variability and spectral shape, clearly indicated that the mechanism acting at the center of the AGN should be highly efficient and restricted

to operate in regions with dimensions of few/some light-sec. Simple order-of-magnitude estimates clearly indicated, since the 70ies, that extraction of gravitational energy due to accreting matter onto a SMBH was the most likely explanation to the observed emission. The basic considerations were that:

1. the typical dimensions (Swartschild radius, $r_s = \frac{GM}{r}$) of systems centered around SMBH are of the order of a few to a few thousands of light-second moving from 10^6 to $10^9 M_\odot$ objects, i.e. these dimensions are in accordance with the variability measured in AGN;
2. the gravitational potential energy induced by a SMBH is a huge reservoir of energy;
3. the gravitational energy can be transformed in electromagnetic radiation with an efficiency ($\eta \sim 0.42$ for Kerr BH) that is almost 60 times higher than the efficiency of $p^+ - p^+$ cycle.

These were the theoretical and observational evidences at the basis of the so called *SMBH paradigm*.

During the now five decades of active studies on the AGN, these cosmic sources have been classified in a large variety of sub-classes. These sub-classes often directly reflected the methods of discovery/detections of the AGN activity in the studied objects (this is, for instance, the case of narrow emission line galaxies, NELG, detected first in X-ray and than optically classified as narrow line objects, i.e. Seyfert 2 galaxies). This led to the creation of the Seyfert, LINER, NELG, OVV, BLLac, Quasar, BLRG, NLRG... and so on classes. This tendency have been, at least partially inverted in the last decade during which the AGN zoo has been significantly reduced to a few major families.

From an observational point of view, within the AGN family clearly exist a major separation between objects that display strong radio emission (radio loud objects, RL) and the ones that display a drop of power at frequency lower than the IR (RQ objects).

Another major difference between AGN classes rises from the spectral characteristics in the IR-optical-UV domain. In this energy range, in fact, all the sources display narrow ($\text{FWHM} \leq 1000 \text{ km s}^{-1}$) emission lines of both permitted and forbidden transitions. Only a fraction of AGN shows, with the narrow lines, also

broad ($\text{FWHM} \geq 2000 \text{ km s}^{-1}$) lines due to permitted transitions only. The latter objects have been classified as type I AGN and the former as type II.

As above mentioned, the Seyfert galaxies are the closest AGN to our Galaxy and are found at $z \leq 0.2/0.3$. As such their observation, especially in X-rays, often provide good quality spectra making of the Seyfert galaxies a privileged class of objects to test the physics of the inner regions of the AGN. They are defined as RQ AGN with $L_{\text{bol}} \leq 2 \times 10^{42} \text{ erg s}^{-1}$. Seyfert nuclei are typically associated to spiral galaxies with absolute magnitude upto $M_v \sim -21, -22$.

1.2 The unified models

In the middle of 80ies it was proposed by Antonucci & Miller 1985 (see Antonucci 1993 for a review on this topic) the so-called unified model (UM) of AGN. The basic idea of such scenario is that all the differences between the classes of AGN are due to two simple facts: a) the geometry of the observer-object system and b) the presence of a relativistic jet of matter coming from the core regions of the accretion systems.

The UM (see Figure 1.1) assumes that if a few basics conditions are fulfilled than, at least at the zero-th order, almost all classes of AGN can be reconciled in a single picture. These conditions may be summarized as follow:

- a SMBH, is located at the center of the AGN and it's responsible of the emission of a huge quantity of energy;
- the source is surrounded by a geometrically thin accretion disk;
- the accretion disk is surrounded by a geometrically and optically thick dusty torus;
- above the accretion disk and within the dusty torus are located the clouds responsible for the production of the broad permitted emission line detected in the IR-optical-UV spectra of type I AGN (BLR);
- at larger distances from the nucleus and well outside the dusty torus, are located the clouds responsible for the emission of the narrow lines observed in both type I and II objects;

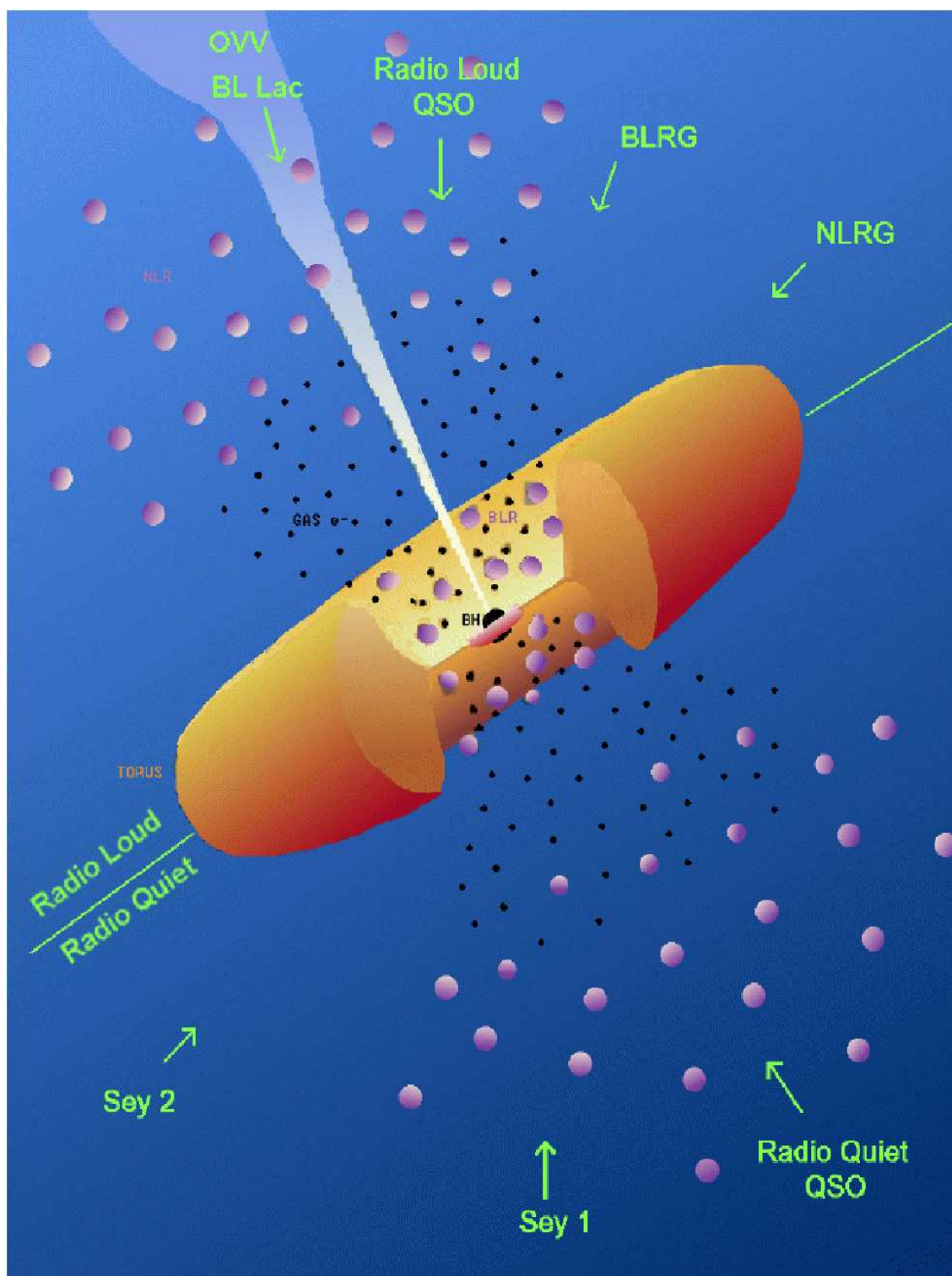


Figure 1.1: Schematic view of the UM. The scheme accounts for the different kinds of RL and RQ AGN. The physical components that are thought to be present in the circumnuclear region around the SMBH are represented (M. Polletta adapted from Urry & Padovani 1995)

- in some (~10%) of the AGN, the presence of jet that carry outward the matter at relativistic speeds is responsible of the emission in the radio frequencies.

It is clear that the UM was and is a simple geometrical model/scenario that, apart for the existence of a compact accretor as primary responsible of the energy release, does not assume, for example, any model for the formation of the jets or the production of the X-rays. As such, the testing of the UM is, in principle, only the validation of a geometrical scheme. Nonetheless, being born to explain the observational evidences, it justifies in an elegant way a number of experimental proofs and it was also able to predict many observational evidences obtained only after the formulation of the model itself. Moreover, the UM has been assumed as a basic model for a variety of physical scenarios such as the synthesis of the cosmic X-ray background. Thus, the testing of the UM is of fundamental importance also for this and other research fields. By the way, in the following of this section, for purposes of simplicity, I will briefly describe the general properties of the Seyfert galaxies using the UM scenario as the reference one.

At a first order approximation, the broad band nuclear spectrum of Seyfert galaxies can be described by a simple power-law:

$$F_{\nu} \propto \nu^{\alpha} \quad (1.1)$$

where F_{ν} is the energy irradiated per time unit, ν is the frequency and α is the spectral index ($\alpha \sim 1$ from IR to optical). On this major pattern, other important spectral features are overlaid (see Figure 1.2).

The most prominent ones are the emission bump peaking in the B band and called big blue bump (BBB). It is visible only in type I source thus its origin must be located within the *dusty torus*. Its shape resembles the black-body one and thus the BBB is most probably due to the superimposition of multitemperature black-body emission due to the different region of the accretion disk itself. This interpretation have, nonetheless, to face some controversial observational results. It is expected that the observed variability should have different characteristic times moving from optical to UV since in the different bands the accretion disk should contribute with the matter at different radii. This is not what has been observed in some cases (Ulrich et al. 1997) where the variations were observed to occur simultaneously at all wavelength.

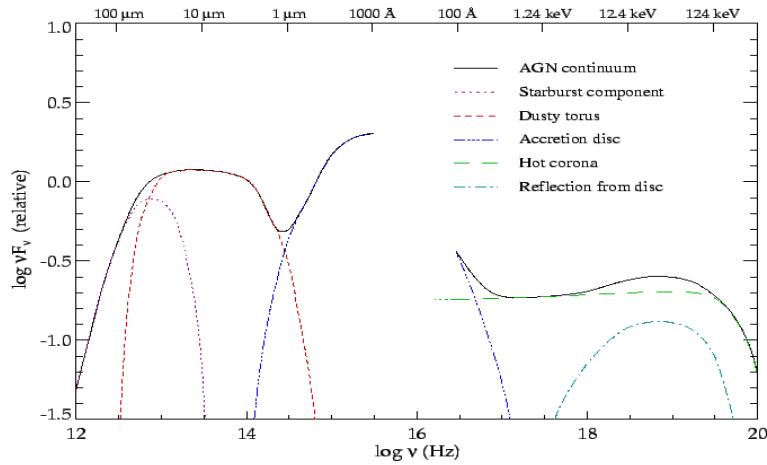


Figure 1.2: Schematic representation of the continuum emission measured in Seyfert galaxies (Courtesy of J. Manners)

Also the IR emission is thought to be of thermal origin and due to the reprocessing of the primary radiation from dust. Indeed, the presence of a local minimum at $\sim 1\mu\text{m}$ hints at a thermal emission mechanism. This is, in fact, likely due to reprocessing from dust closest to the nuclear source (~ 0.1 pc) having temperature of the order of 2000 K: at higher temperatures the grains sublimate.

1.3 The Seyfert galaxies in X-rays

The high energy emission from AGN comes from the innermost regions of the accreting systems centered around SMBH. For this reason, X-rays are expected to be tracers of the physical conditions experienced by matter before disappearing into SMBH. Moreover, thanks to their high penetrating power, energetic photons, escaping from the nuclear zones, test the matter located between their source and the observer. Thus, they offer powerful diagnostics to understand the geometry and the physical conditions of the matter surrounding the SMBH.

Figure 1.3 shows the typical X-ray spectrum of a Seyfert 1 galaxy and a sketch of the regions close to the SMBH that are thought to be responsible for the observed spectral features. In the framework of the standard model, these components can be briefly listed and identified as follows:

- the X-ray spectrum is dominated by a power-law (red dashed line in Figure

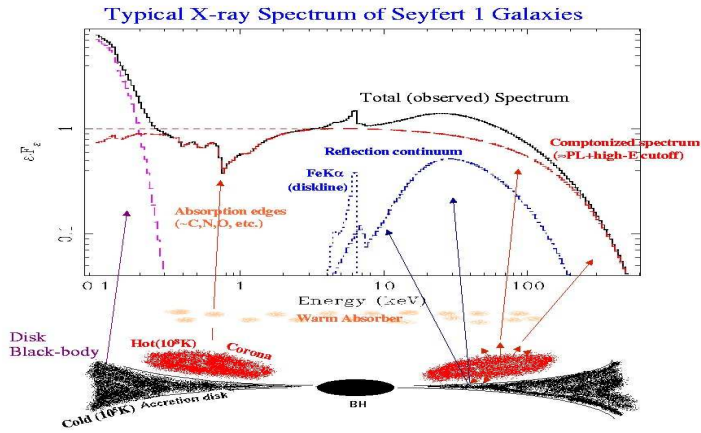


Figure 1.3: Schematic representation of the X-ray spectrum observed in type I Seyfert galaxies (Courtesy of M. Cappi)

1.3). At $E \geq 50$ eV, the power-law emission decline after an exponential cut-off;

- a reflection component is also measured above ~ 6 keV and peaking at $E \sim 30$ -40 keV. It also includes also the strongest emission line measured in X-ray, i.e. the broad $\text{FeK}\alpha$ emission line at 6.4 keV. This component comes from the accretion disk and/or the inner walls of the dusty torus (Ghisellini, Haardt & Matt 1994)
- in a significant fraction of type I AGN, the nuclear radiation passes through a partially ionized plasma (the so-called *warm absorber*). This plasma imprints on the primary continuum the main narrow absorption features in soft X-ray band;
- in most type I sources an excess above the power-law is observed at low energies ($E \leq 2$ -3 keV). This component is named *soft excess*. It's origin is unknown and still highly debated. It is supposed to be peaked at $E \sim 0.1$ -0.2 keV (Gierliński & Done 2006) independently from the mass of the SMBH. This hardly disfavors a thermal origin of such component since, in that case, the emission peak should scale with the mass of the SMBH ($T \propto M_{BH}^{1/4}$). A probable atomic origin has been proposed both in terms of absorption due to atomic transitions or emission of forests of lines due to Iron and other

elements (Gierliński & Done 2006, Crummy et al. 2006).

As previously said, the UM predicts that the type II objects are intrinsically identical to type I but with observational differences introduced by absorbing matter that intercept the line of sight. Thus the type II Seyfert are expected to display all those spectral features that are not hidden by the absorption matter. They are also expected to show in the X-ray spectra, a low-energy cut-off due to the cold absorption induced by the *dusty torus*. This is indeed observed (see §1.3.2).

1.3.1 The X-rays emission mechanism

The baseline model for the production of X-rays in Seyfert galaxies is known as *two-phase* model (Haardt & Maraschi, 1991, 1993). It assumes that close the SMBH the optically thick, geometrically thin accretion disk (cold phase, $T \sim 10^{5-6}$ K) is sandwiched by a optically thin and geometrically thick corona (hot phase). It is assumed that the largest part of the gravitational energy is released in the corona, probably for the reconnection of magnetic fields (Burm, 1986) as it happens in the sun. Whatever the mechanism, it is assumed that the corona reaches temperatures of the order of $T \sim 10^9$ (i.e. $kT \sim 100$ keV). At this temperature the the electron population in the corona becomes mildly relativistic ($\beta \sim 0.7$ and the corresponding Lorentz factor becomes $\gamma \sim 1.4$). The interactions between the photons and the matter in the two phases leads to a complex process that can be simplified in the following cycle:

1. the X-ray emission from the corona is emitted in part towards the observer and in part towards the accretion disk;
2. the accretion disk thermalize the X-ray photons coming from the corona and re-emit the energy budget received by the corona in the UV/soft X-ray regime. These photons must cross the corona;
3. here, UV photons are Comptonized to X-ray energies by the e^- in the Corona that emits part of the photons towards the disk and part towards the observer sustaining the cycle (return to point 1).

In the *two-phase* model, the power-law shape typical of the X-ray spectrum (Turner & Pounds 1989, Nandra & Pounds 1994) of the Seyfert galaxy is indeed

due to the sum of the different *Maxwellian*-like distribution of the X-ray photons produced in different order of scattering. It is worth considering here that in this scenario the inverse Compton is the main cooling mechanism acting in the Corona and that the final spectral shape depends also on the cooling rate (Merloni et al. 2006). Finally, it is worth noting that in this picture it is predicted the presence, in the X-ray spectra of Seyfert galaxies, of an high-energy cut-off (E_c) corresponding to the temperature of the e^- of the Corona.

1.3.2 The neutral absorption in type II Seyfert galaxies

The most striking broad feature observed in the X-ray spectra of Seyfert galaxies is the cut-off in the soft X-ray band due to absorption by material associated to dusty torus. This material suppresses the primary emission via photoelectric absorption. The observed absorption (hydrogen equivalent) column density (N_H) in type I objects are often consistent with what expected to take into account the absorption due to the matter located in the Galaxy along the line of sight. In type II sources, the measured N_H spans from few 10^{22} cm^{-2} up to $N_H \geq 10^{25} \text{ cm}^{-2}$. When the absorbing column exceeds $\text{few} \times 10^{24} \text{ cm}^{-2}$, the primary emission is completely blocked and only a reflected component is accessible to the observers. In this case, the source is named Compton-thick (CT).

Even though somewhat at odds with the UM, some examples of type I (type II) sources suffering (non suffering) of absorption in X-rays have been found (Maccacaro et al. 1982, Fiore et al. 2001a, Panessa & Bassani 2002, Bianchi et al. 2008a, Brightman & Nandra 2008). Some possible explanation of this occurrence can be listed as follow: i) the dust-to-gas ratio of the X-ray absorbing material could be lower than it is in the Galaxy (Maiolino et al 2001a); ii) the dust grain size of this material could be larger than Galactic ones (Maiolino et al 2001b); iii) the line of sight does not intercept the torus but pass through disk winds located within dust sublimation radius (Weingartner & Murray 2002).

Nonetheless, it must be stressed that some *bona fide* type II Seyferts do not display any significant hints of absorptions have been observed (Bassani et al. 1999; Panessa & Bassani 2002; Bianchi et al. 2008a; Brightman & Nandra 2008). These sources, thus, are that targets that Antonucci (1993) defined as the *true* Seyfert 2, i.e. the ones that could pose serious problems to the UM theory. If confirmed,

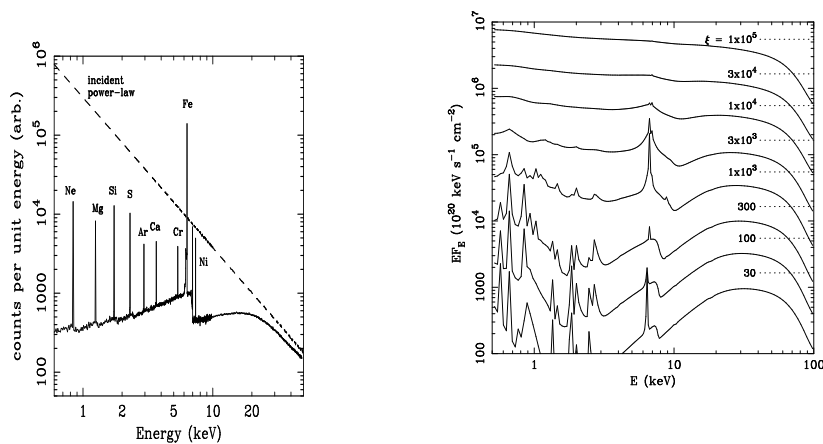


Figure 1.4: *Left panel* : the X-ray reflection component emerging from a neutral slab (solid line). The dashed line shows the incident continuum. Most of the radiation below 20 keV is absorbed by metals in the reflecting slab and re-radiated at lower energies (i.e. thermalized). *Right panel* : the reflection spectra predicted assuming different ionization states for the reprocessing slab. The ionization states are described by the ionization parameter ξ (see text). When the reflector is ionized, strong emission lines are produced at $E \leq 2$ keV. (Figures from Fabian et al. 2000)

they are most probably few (Panessa & Bassani 2002). Thus it is possible to assess that the UM is, in general, a valid interpretation scheme.

1.3.3 The reflection component

As previously said (§1.3.1) the optically thick material of the disk is irradiated by the primary emission produced in the hot corona. The hard X-ray photons thus should penetrate the surface slab of material and penetrate within the disk. Here these photons are expected to be subjects to many interactions like Compton scattering by free or bound electrons, photoelectric absorption and either fluorescent line emission or Auger de-excitation. Each photon undergoes either destruction through Auger de-excitation, or is scattered out of the slab, or reprocessed into fluorescent line photons which escapes from the slab.

The left panel of Figure 1.4 shows the expected X-ray reflection continuum from an illuminated slab. The dashed line shows the incident spectrum while the solid line shows the reflected component (Reynolds 1997; Fabian et al. 2000).

When the disc ionization is low, as shown in the left panel of Figure 1.4, low energy photons ($E \leq 10\text{-}20$ keV) are mainly photoelectrically absorbed by the ions in the slab. The higher energy photons, on the contrary, are mostly back scattered via Compton down scattering. Thus, the net effect is that the reflection spectrum shows an hump between 30-40 keV. This spectral feature has been observed in the X-ray spectra of Seyfert galaxies with the *Ginga* satellite (Pounds et al. 1990; Nandra & Pounds 1994), then with *BeppoSAX* (Perola et al. 2002), and now with *Suzaku* (Reeves et al. 2006).

The high luminosity of the corona can photoionize the surface layers of the accretion disk (Ross & Fabian 1993; 2005). The right panel of Figure 1.4 shows the expected reflection continuum and the associated emission lines for different values of the ionization parameters ξ defined as $\xi = 4\pi \frac{L}{r^2 n}$, where L is the X-ray luminosity received by the ionized matter, n is the number density of the ionized matter and r is its distance from the source of ionizing photons. The emerging emission lines in the ionized reflection case are mainly due to Oxygen, Carbon, Nitrogen, Neon and the Iron L-shell transitions. These lines appear when the ionization state is moderate ($\xi \leq 5000$ erg cm s⁻¹). On the other hand, for higher ionization states, all the elements (including Iron) are completely ionized and the reflection spectrum mimics the incident power-law and the slab behave like an almost perfect mirror.

In addition to the continuum, the reflection component contains also a series of emission lines (see left panel of Figure 1.4). The strongest emission line is the FeK α because of the highest fluorescent yield and abundance. This emission line is emitted for fluorescence at an energy ranging between 6.4 to 7.1 keV depending on the ionization state of the matter.

Even if thought to arise as an intrinsically narrow emission line, this feature is supposed to originate close to the SMBH where the relativistic effects induced by the strong gravitational field and the high velocity reached by the accreting matter are supposed to be able to act on the emission line (see Figure 1.5).

These effects were first measured with ASCA satellite (Tanaka et al. 1995) in the X-ray spectrum of the Seyfert 1 MCG-6-30-15 and were later confirmed by the detections of similar features in the spectrum of several Seyfert galaxies (Nandra et al. 1997).

The new generation high sensitivity X-ray telescopes have shown clear evidence of an almost ubiquitous narrow component of the Fe narrow line (Nandra

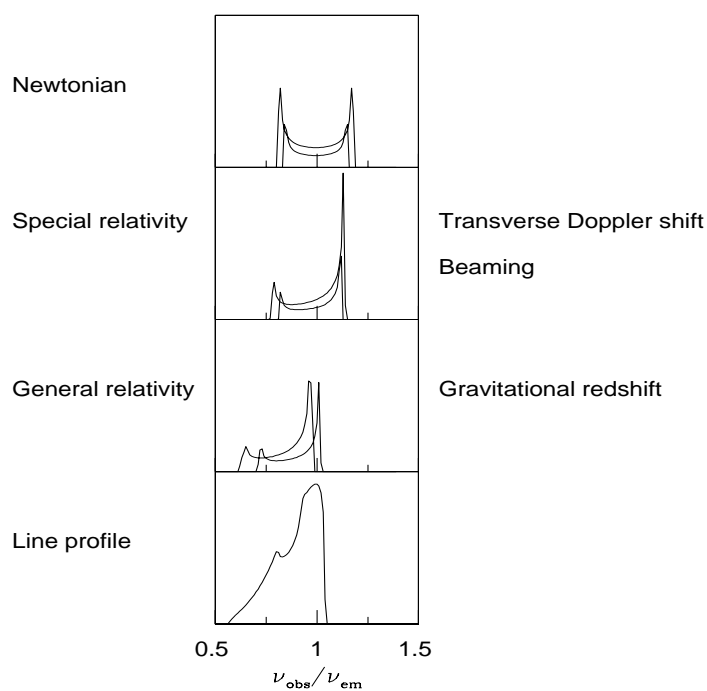


Figure 1.5: The shape of reflection lines from the accretion disk is sculpted by the interplay of Doppler and transverse Doppler shifts, relativistic beaming and gravitational redshift. These effects are taken into account step-by-step moving from the upper to the lower panel of this figure. In the first three panel, only the contribution coming from two narrow annuli of the accretion disk are considered. In the lower panel it is plotted the summed profile considering the emission from the entire accretion disk (Figures from Fabian et al. 2000)

2006) produced by matter far from the SMBH. They also confirmed the presence of such broad line (Longinotti et al. 2008) but cast doubts about their interpretations since at least part of the so-called *red wing* can be explained in term of ionized and/or partial covering models (Pounds et al. 2003; Pounds et al. 2004; Turner et al. 2005).

1.4 Open questions

In the previous sections I introduced some fundamental pieces of evidence and theoretical scenarios that compose the average picture of the Seyfert galaxies. In this section I will briefly described some open problems that I tried to tackle during the work done for this thesis. I will also introduce the applied methods.

1.4.1 Testing the UM

In recent years, the number of cases in which the zeroth-order UM predictions seem not to be completely adequate to explain all observational evidences is increasing, both in the local and in the distant universe. Type I AGN with significant absorption have been found (Mateos et al. 2005, Fiore et al. 2001a, etc.) as well as type II AGN without X-ray absorption (Caccianiga et al. 2004, Corral et al. 2005, Barcons, Carrera & Ceballos 2003, Panessa & Bassani 2002, Pappa et al. 2001, Bianchi et al. 2008a). As above mentioned (see §1.3) X-rays are one of the most direct evidences of nuclear activity and are, therefore, fundamental to study the accretion processes.

Here I will take advantage of the broad-band of *BeppoSAX* that offered, for the first time, the opportunity to measure with a remarkable sensitivity the spectral shape of AGN in the 0.1-200 keV range simultaneously. This potential had been exploited to study in detail a number of sample selected in different manners (see for example Maiolino et al. 1998; Malizia et al. 2003; Perola et al. 2002). These studies were fundamental in making important steps forward in the comprehension of the emitting mechanism at work in the production of X-rays (Perola et al. 2002) and to partially reveal the geometry of the cold matter surrounding the central SMBH (Maiolino et al. 1998; Bassani et al. 1999; Risaliti et al. 1999). Here the broad band X-ray data from *BeppoSAX* will be statistically inspected to

infer the average characteristics of the nearby Seyfert galaxies contained a sample of ~ 100 sources (see §2). Their the 2-100 keV band spectra will be used to perform simple tests on the UM for the AGN. The broad-band of BeppoSAX, in fact, allows for the very first time to test the UM using as indicators as the relative amount of reflection and the E_c . The problem of *BeppoSAX* sample resides in the fact that it is an heterogeneous sample of objects. As such, it cannot be used to infer the average properties of the Seyfert family. To do that, I will take advantage of two other samples named *XMM-Newton* and *X-CfA* samples (see §2.2 and 2.3 respectively) that are expected to be complete and unbiased.

1.4.2 The emission mechanism

It is not clear whether at very low luminosities the predictions of UM are still valid (Panessa & Bassani 2002, Ho et al. 2001, Merloni et al. 2003). The key for the comprehension of the whole AGN phenomenon seems to reside in a combination of the UM hypothesis and the fundamental parameters of AGN, such as black hole mass, Eddington ratio, and perhaps the black hole spin. After the discovery that SMBHs reside at the center of most, if not all, galaxies in the nearby universe (Kormendy & Richstone 1995, Magorrian et al. 1998) and that a large fraction of them are active (at least 40%, Ho, Filippenko & Sargent 1997b), it is of fundamental importance to understand the accretion physics in AGN and what triggers the different levels of activity.

One of the distinctive characteristic of nearby nuclei is their intrinsic faintness, i.e. $L_{Bol} < 10^{44}$ erg/s (Ho 2003), as well as their low level of activity; in terms of Eddington luminosity most of them have $L/L_{Edd} < 10^{-2}$ compared to $L/L_{Edd} \sim 1$ of luminous AGN.

Whether low luminosity AGN (LLAGN) are a scaled-down luminosity version of classical AGN or objects powered by different physical mechanism is a debated issue. It is not clear in fact, whether LLAGN are powered by radiatively inefficient accretion flows, such as advection dominated accretion flows (ADAF) and their variants (Narayan & Yi 1994, Abramowicz 1997) instead of the standard geometrically thin optically thick accretion disk typically proposed as the accretion mechanism acting in the central regions of luminous AGN (Shakura & Sunyaev 1973). LLAGN could also represent scaled up versions of black hole binaries in

the steady-jet, hard X-ray state, as pointed out by the scaling relations reported in Merloni et al. (2003) and Falcke et al. (2004).

On one hand, ADAF models are able to predict some of the spectral properties observed in many LLAGN, such as the lack of the 'big blue bump' (Ho 1999). On the other hand, some LLAGN show properties which are common to luminous AGN, such as the observed correlations between optical emission lines and ionizing continuum (Ho & Peng 2001) or X-ray emission (Ward et al. 1988, Terashima et al. 2000, Ho et al. 2001).

Here I will take advantage of the information collected for the *BeppoSAX* and *X-CfA* sample to investigate the nature of the emission mechanism acting at the center of the close Seyfert galaxies. In particular, the *X-CfA* will allow to reach very low luminosity in X-rays so as to test the emission mechanism also in very low efficient systems.

1.4.3 Testing the matter flow around SMBH

As exposed in §1.3.3, we can obtain information on the physical characteristics of the accretion disk close to the SMBH via the spectral studies of the reflection components (reflection hump and broad $\text{FeK}\alpha$ emission line). As such, the outputs from the *BeppoSAX* sample on R can be a first answer in the determination of the mean geometrical properties of the accretion disk in the nearby Seyfert galaxies.

It must be noted, however, that the study of the accretion disk have become particularly effective in the last 10 years thanks to the high sensitivity X-ray satellites like *XMM-Newton* in the band of the $\text{FeK}\alpha$ emission line. Although it was demonstrated that the presence of broad (neutral or ionized) components of Fe K lines can only be tested via relatively long exposures of the brightest sources (e.g., Guainazzi et al. 2006; Nandra et al. 2007) since in other cases it is almost impossible to break the degeneracy between the continuum, broad absorption feature and broad emission line spectral parameters.

Here I'll present such kind of studies for two bright Seyfert galaxies, the type I object Mrk 509 and the type II object IRAS 13197-1627. These are two of the brightest objects in their classes (see §5.1 and 5.2 respectively). The average spectral properties of these sources will be studied in order to probe the accretion flow in the disk.

On the other hand, it must be recalled here, that the observational evidence for broad lines and their interpretation in terms of relativistic effects may be questioned when an important absorbing ionized component is present. Spectral variability studies help in disentangling the different, often degenerate, spectral components (Ponti et al. 2004; Iwasawa et al. 2004; Ponti et al. 2006; Petrucci et al. 2007; De Marco et al., in prep.). Thus detailed modelling of time-averaged spectra have been used to obtain important estimates of the disc ionization state, its covering factor and, at least for the brightest and best cases, its emissivity law, inner radius and BH spin (Brenneman & Reynolds 2006; Miniutti et al. 2007; Guainazzi et al. 2006; Nandra et al. 2007). It is also well established that time-resolved spectral analysis is a fundamental tool if we want to understand not only the geometry and kinematics of the inner accretion flow but also its dynamics. Early attempts (i.e. Iwasawa et al. 1996; Vaughan & Edelson 2001; Ponti et al. 2004; Miniutti et al. 2004) have clearly shown that the redshifted component of the Fe $K\alpha$ line is indeed variable and that complex geometrical and relativistic effects should be taken into account (Miniutti et al. 2004).

More recently, results of iron line variability have been reported (Iwasawa, Miniutti & Fabian 2004; Turner et al. 2006; Miller et al. 2006). These are consistent with theoretical studies on the dynamical behaviour of the iron emission arising from localized hot spots on the surface of an accretion disc (e.g. Dovčiak et al. 2004). Iwasawa, Miniutti & Fabian (2004), for example, measured a ~ 25 ks modulation in the redshifted Fe $K\alpha$ line flux in NGC 3516, which suggests that the emitting region is very close to the central black hole. However, these are likely to be transient phenomena, since such spots are not expected to survive more than a few orbital revolutions. For this reason, it is inherently difficult to establish the observational robustness of these type of models, if not by accumulating further observational data.

Here the *XMM-Newton* data of the Seyfert 1 galaxy NGC 3783 are presented and the target is used as a case studies to investigate the time properties of the reflection components arising from accretion disk.

Finally, it is worth noting that in the last years narrow emission and absorption lines due to highly ionized matter in outflow and in inflow (see Cappi 2006 and reference therein for a review on this topic) were observed (but see the discussion by REF on the intrinsic significance of these detections) in the X-ray spectra of

many Seyfert galaxies.

Such features were interpreted as evidences of blobs/clouds motions (Dadina et al. 2005) and/or as probes of winds (Pounds et al. 2001, 2003). In any case, these features must be considered tracers of motion with radial velocities that do not follow the accretion disk motion pattern. Thus they may be of fundamental importance to define the flow pattern close to SMBH.

The three sources assumed here as case studies, displayed evidences of narrow absorption lines, both red- and blue-shifted, in past X-ray observations. As such they have been used also to test these motion patterns.

Chapter 2

The data

The best way to test astrophysical scenarios and physical hypothesis is to collect high quality and broad band data on large, well defined, complete and bias-free samples of objects. These conditions are rarely, if never, achieved. Here, I had to face this limitation.

For this reason, I decided to use three different samples of objects and to tackle the problematics introduced in the previous chapter. The samples have different contents even if there are sometimes large overlapping between them. The main fact here is, however, that each sample is tuned to tackle few and focused targets on the astronomical and astrophysical problem faced at a time.

Each sample will be accurately described in dedicated sections. The three samples are named the *BeppoSAX* sample, the *XMM-Newton* sample and the *X-CfA* sample and, at the zero-th order, they are thought to be optimized to test the physics of the X-ray emission processes, the geometrical set-up of the AGN core and the accretion/emission efficiency of the system respectively.

The *BeppoSAX* sample is heterogeneous and therefore inadequate to determine class properties. Nonetheless, it allows deeply studies of the broad-band X-ray properties of the nearby Seyfert thus making possible a detailed description of their X-ray emission. As such, it can be used to test the predictions of the UM by comparing the isotropic and anisotropic quantities. The *BeppoSAX* sample also allows to test the emission mechanism acting at the centre of the Seyfert galaxies.

On the other hand, the *X-CfA* sample is well defined, flux limited and, *bona-fide*, un-biased. It contains nearly fifty sources and thus allows to describe the

average properties of the Seyfert populations. Nonetheless, the X-ray data are not always of good quality and often only bare detections of the nuclei are available. Thus this sample has been used primarily to test the efficiency with which the Seyfert galaxies convert the gravitational energy in electromagnetic waves.

Finally, the *XMM-Newton* sample is formed by the 27 objects closer than 22 Mpc to the Galaxy included in the *X-CfA* Mpc. As such, the sample is surely complete and un-biased. For all the sources in the sample, good quality *XMM-Newton* data are available. They have been used to determine the average spectral properties of Seyfert galaxies in the local Universe allowing, for example, the testing of UM.

Obviously, this scheme has not to be considered as formed by watertight compartments and all the information is obtained, as usual, when evidences from the different samples are merged together. This is, for example, the case of the study of the dusty torus and of the emission efficiency.

Finally, the tables containing the information about the samples presented here are quite large. Thus, I decided to put all the information about the data in appendices and namely Appendix A for the *BeppoSAX* sample, Appendix B for the *X-CfA* sample and Appendix C for the *XMM-Newton* sample. Appendix A and C also contain two spectral atlas.

2.1 The BeppoSAX sample

In its six years of operation in orbit, the Italian-Dutch X-ray satellite *BeppoSAX* (Boella et al. 1997) observed many Seyfert galaxies of all types in pointing scheduled as “core program” and “guest observer” sources. These pointings had very different observing exposures, as requested by the proponent scientist, who had a project in mind. These data in general (but not always) have been analyzed and published by the data owner.

The most important fact is that *BeppoSAX* formed what can be still considered the largest reservoir of good quality and simultaneous soft- and hard X-ray data. For this reason, all public data in the *BeppoSAX* data bank have been uniformly analyzed making use of the best software and response matrices available.

The *BeppoSAX* sample is material to address many open issues, the most outstanding being a) the unification model paradigm (see §3) and b) some insights on

the emission mechanism acting in the Seyfert galaxies (see §4).

With this aim in mind all *BeppoSAX* observation of Seyfert galaxies have been extracted from the data bank and inspected according to the following criteria. As a first step, the public archive of *BeppoSAX* observations has been cross correlated with the Véron-Céty-Véron (2006) AGN catalog. Source were extracted when:

- a) classified as Seyfert galaxies (type I to II)
- b) $z \leq 0.1$

Such criteria allowed radio loud objects, e.g. some 3C sources, to be included in the list. However, much attention has been paid to excluding BL Lac type objects in order to avoid the inclusion of X-ray emitting objects heavily dominated by non thermal/relativistic effects. After completion of the above-mentioned selection, the *BeppoSAX* archive has been searched for Seyfert galaxies not included in the list obtained as described above. Thus, each pointing in the AGN section of the *BeppoSAX* data bank of NFI targets has been checked. Every source that, according to the classification reported in NED, resulted in hosting a Seyfert-like nucleus has also been included in the present sample. The result of the application of these criteria to the whole *BeppoSAX* data archive is the catalog presented in Table A.1.

BeppoSAX has observed 113 Seyfert galaxies (44 type I, including types 1.0, 1.2, and 1.5, and 69 type II including types 1.8, 1.9, and 2.0) with $z \leq 0.1$ in 175 pointings, as some sources were observed several times (see Table A.2 in appendix A). Since the main purpose of this work is to perform the spectral analysis of the X-ray emission, all sources with low detection in the MECS ($\leq 10\sigma$ between 2-10 keV, Table A.2 in appendix A), were excluded by the analysis procedure. Twelve pointings did not match this criterium. Therefore the number of useful observations amounts to 164, and the X-ray spectra for 8 (7 type II and 1 type I) out of the 113 Seyfert are not reported. To conclude, 84 out of 163 X-ray spectra reported here are referred to 43 type I Seyfert galaxies, while 79 X-ray spectra are referred to 62 type II Seyfert galaxies (see Table A.3 in appendix A).

An additional criterium has been to exclude LECS data (energy range ~ 0.1 -4 keV, Parmar et al. 1997) and to consider only MECS+PDS data (energy range ~ 2 -100 keV, Boella et al. 1997; Frontera et al. 1997). This choice has been made to simplify data analysis, which was fully automatic. In fact, in the soft (~ 0.1 -2 keV) band, particularly for type I objects, spectral features connected to the warm

absorber are present in the spectra and difficult to account for in “standard” models. A detection in the PDS is registered whenever a 3σ or higher significance signal is present between ~ 20 -100 or 20-50 keV.

2.1.1 Data reduction and analysis

ASI Science Data Center pre-processed data have been used and were reduced following the handbook prepared by Fiore, Guainazzi & Grandi (1999). MECS data have been filtered for the extraction regions using FTOOLS and, in particular, the software package XSELECT. MECS data are filtered over a circular, 30' radius region centered on the source. Data have been binned to have at least 20 counts for energy bin. This assures a safe application of χ^2 statistics. PDS data are binned in 18 channels through a logarithmic sampling of the instrument response between 20-200 keV. Spectral analysis has been performed using the most recent calibration matrices. MECS background has been extracted from empty fields.

To perform automatic analysis of the data it has been necessary to build a consistent set of template models. The basics of such models are those components that describe a classical continuum of Seyfert galaxies. This continuum has been constructed using models of increasing complexity such a:

- i) power law;
- ii) power law + FeK α emission line;
- iii) power law + FeK α emission line + cold reflection component.

In all cases an absorption component, in addition to the Galactic one (from Dikey & Lockman 1990), has been added, while to model the cold Compton reflection component, the PEXRAV model (Magdziarz & Zdziarski 1995) in XSPEC was used.

Some Seyferts were not fit by any of the above models to any acceptable degrees. This was due to low energy data (~ 1.7 -3 keV), which often exhibit excess residuals. An additional blackbody emission component at low energy has therefore been introduced for type I objects. Type II Seyfert galaxies with low energy excess were instead fitted adding an additional power-law. The spectral index of this soft component has been set either to be equal to the hard one or to be free. Moreover, other spectral components have been added, when necessary, to account for: a) the possible presence of a broad Gaussian emission line (as in IC 4329a); b)

the presence of a relativistically widened FeK α line (as in MCG-6-30-15); c) the presence of more than one emission line (as in NGC 1068); d) spectra due entirely to reflection (as in NGC 7674); e) the presence of partial and/or warm absorbers (as in NGC 3516). When warm absorbers were required, they were wfit with the ABSORI model.

The models outlined above have been used to fit the data. The criterion used has been the one of increasing complexity of the model applied in subsequent steps. As a first order approximation a best fit has been recognized for those models for which the added element of complexity corresponds to at least a 90% increase of statistical significance of the last added component. Final acceptance of a best fit has been based on inspection of the physical significance of the derived parameters by the automated fit procedure. The final results are summarized in Table A.3 and to obtain the luminosities reported in there, $H_o=75 \text{ km s}^{-1} \text{ Mpc}^{-1}$ and $q_0=0.5$ were used.

2.2 The X-CfA sample

This sample of Seyfert galaxies has been derived from the Palomar optical spectroscopic survey of nearby galaxies (Ho, Filippenko, & Sargent 1985). From this survey, high-quality optical spectra of 486 bright ($B_T \leq 12.5$ mag), northern ($\delta > 0^\circ$) galaxies have been taken and a comprehensive, homogeneous catalog of spectral classifications of all galaxies have been obtained (, Ho, Filippenko & sargent 1997a, hereafter HFS97). The Palomar survey is complete to $B_T = 12.0$ mag and 80% complete to $B_T = 12.5$ mag (Sandage, Tammann, & Yahil 1979). This sample offers the advantage to have an accurate optical classification and the opportunity of detecting weak nuclei since the AGNs included covers a large range of luminosities ($L_{bol} \sim 10^{41-44} \text{ erg s}^{-1}$).

The spectroscopic classification system of the Palomar survey can be briefly summarized (see HFS97 for a more accurate description) as follow: the relative strength of the low-ionization optical forbidden lines ([OI] $\lambda\lambda 6300, 6364$, [NII] $\lambda\lambda 6548, 6583$, [SII] $\lambda\lambda 6716, 6731$) compared to the hydrogen Balmer lines determines the classification of emission-line nuclei into two classes: H II nuclei (powered by stars) and AGN (powered by black-hole accretion). The separation between LINERs and Seyferts is instead given by the ratio $[\text{OIII}]_{\lambda 5007}/\text{H}\beta$ which corresponds

to the ionization state of the narrow-line gas in AGN, i.e. $[\text{OIII}]_{\lambda 5007}/\text{H}\beta < 3$ for LINERs and $[\text{OIII}]_{\lambda 5007}/\text{H}\beta \geq 3$ for Seyferts. Emission line nuclei having [OI] strengths intermediate between those of H II nuclei and LINERs are classified as "transition objects". As such, symbols used in table B.1 are: L = LINER, T = "transition object" (LINER + HII nucleus), and S = Seyfert. The classification in "type 1" or "type 2" depends on the presence or absence of broad permitted lines. The measurement of the relative strength of the broad component of the hydrogen Balmer lines lead to subdivisions in the classification (type 1.0, 1.2, 1.5, 1.8 and 1.9; see Osterbrock 1981).

All the Seyfert galaxies presented in the original sample have been extracted to form the present sample that is formed of 60 Seyfert galaxies. The sample includes 39 type 2 (type 2 and 1.9) and 13 type 1 AGN (type 1.0, 1.2, 1.5). Eight objects, which are placed near the boundary between Seyfert and LINER, HII or transition classification, with a double classification (e.g., S2/T2, L2/S2, H/S2, etc.), have been included in the final sample. Hereafter I refer to these objects as 'mixed Seyferts'.

Seyfert galaxies classified as type 2 and 1.9 have been grouped into a more general 'type 2' classification, while type 1.0, 1.2 and 1.5 have been grouped in the 'type 1' class. Type 2 and type 1.9 sources are normally both absorbed objects, while the type 1 group is referred to objects which are normally not affected by heavy absorption.

Two sources of the sample, NGC 4395 and NGC 4579, which have been classified by HFS97 as S1.8 and S1.9/L1.9 respectively, have been reclassified as type 1.5. A broad component is present in a number of optical (Filippenko & Sargent 1989) and ultraviolet (Filippenko, Ho & Sargent 1993) emission lines of NGC 4395. Extremely broad permitted lines have been detected in NGC 4579. *HST* observations have revealed an $\text{H}\alpha$ component with FWZI of ~ 18000 km/s (Barth et al. 1996 and Barth et al. 2001).

In objects like NGC 3608, NGC 3941, NGC 4472 and NGC 6482, the difficulty in the starlight subtraction process has lead to uncertainties in the classification (HFS97a). Finally, the classification of NGC 185 is also uncertain, i.e., it is a dwarf spheroidal galaxy whose Seyfert-like line ratios maybe produced by stellar processes (Ho & Ulvestad 2001, hereafter HU01).

Table B.1 lists all the properties of the host galaxies of the sample. Data for

Cols. (2)–(8) are taken from the compilation of HU01 and references therein. Distances for a few objects have been updated with more recent estimates (references are indicated in Col. (5)). The median distance of the sample galaxies is 25.7 ± 17.7 Mpc. The nearest galaxy is NGC 185 (one of the companions of M 31) at $D = 0.64$ Mpc and the farthest is NGC 5548 at $D = 70.2$ Mpc, so only the local universe is sampled.

2.2.1 The X-ray data

Other than the ~ 250 ks of EPIC Guaranteed Time for the distance-limited sample of 27 Seyfert galaxies (see Section 2.3), five further public observations available from the XMM-Newton Science Archive (XSA)¹ were analyzed.

The XMM-Newton data reduction and analysis will be discussed in detail in the next section. Here it is important to stress that the objects not belonging to the XMM-Newton sample are NGC 1275, NGC 3516, NGC 3227, NGC 5548 and NGC 7479.

To complement the X-ray information on the whole sample, a search in the literature for observations with previous X-ray observatories (operating in the 2-10 keV energy range) has also been carried out. ASCA observations have been found for 8 further objects, references for those data taken from the literature are given in Table B.2, except for NGC 3982 and NGC 4235 for which ASCA fluxes have been derived in this work. Adding all these data, 47 sources out of 60 objects have X-ray data available.

The CIAO software was used for the Chandra data analysis and to perform the data processing and calibration². Starting from level 1 files, new level 2 event files were generated. Pixel randomization introduced by the CXC (Chandra X-ray observatory Center) and standard data processing (SDP) were applied to avoid the instrumental "gridded" appearance of the data and any possible aliasing effects associated with this spatial grid. Finally, the light curves were examined in order to clean the datasets for periods of anomalous background rates.

Most observations have been taken in the standard mode that allows a read-out mode of the full chip every 3.2s. For many bright sources in the sample more than

¹<http://xmm.esac.esa.int/xsa>

²All the data processing have been carried out following analysis threads on the Chandra web site: <http://cxc.harvard.edu/ciao/threads/index.html>

one observation is often available. In this case, the data set without gratings was chosen and, in order to minimize pile-up effects, the data set with 1/8 or 1/2 chip sub-array mode.

It is worth recalling here that the final results of such analysis are presented in Table B.2. Finally, for the vast majority of the objects not included in the *XMM-Newton* sample, the X-ray data available were not of high quality. This was expected since many of the objects included in the present sample were already known to be quite faint. Nonetheless, the possibility to create a sample quite populated for which the X-ray luminosity is known for almost all the sources, open the opportunity to perform some kind of tests that are hampered by the small number of objects included in the *XMM-Newton* sample.

2.3 The XMM-Newton sample

This sample is drawn from the *X-CfA* sample introduced in the previous section and contains only the nearest 30 AGNs which are within a distance of 22 Mpc. This choice has been done to ensure the formation of a complete sample of Seyfert galaxies that is expected to be, at the same time, completely un-biased.

Three of the originally included galaxies have been excluded from the present analysis, namely NGC 185 (see §2.2 for a brief discussion on this topic for this object as well as for NGC 4395 and NGC 4579), the Seyfert 1.9 galaxy NGC 3982 for lack of available *XMM-Newton* data at the time of writing, and the Seyfert 1.9 galaxy NGC 4168 which no longer meets the distance criterion³.

The final sample consists of 27 Seyfert galaxies which include 9 type 1s (specifically type 1.5) and 18 type 2s. (Here, the “type 2” category is defined to include type 1.9 as well, because the broad $H\alpha$ line is very hard to detect in spectra having low signal-to-noise ratios; moreover, such nuclei may be largely obscured, as are many of the “pure” Seyfert 2s.) The sample properties are listed in Table C.1.

Observation dates, exposure times, and filters used during the observations are listed in Table C.2. The raw observation data files (ODFs) were reduced and analyzed using the standard Science Analysis System (SAS) software package (Saxton 2002) with associated calibration files. The *eproc* and *emproc* tasks were used for

³Its original distance measurement ($D = 16.8$ Mpc; Tully 1988) has been updated recently to $D = 31.7$ Mpc (Caldwell, Rose, & Concannon 2003).

the pipeline processing of the ODFs to generate the corresponding event files and remove dead and hot pixels. Time intervals with very high background rates were identified in light curves at energy >10 keV and removed. Only patterns ≤ 12 for “MOS” and ≤ 4 for “pn” were considered in the analysis and a standard selection filter of FLAG=0 was applied.

2.3.1 Spatial and Timing Analysis

Images and light curves were analyzed in the 0.5–2 keV (soft) and 2–10 keV (hard) energy bands, for MOS and pn separately. Despite the short exposures (as low as ~ 5 ks; see Table C.2), all targets are detected with a minimum of 20 counts per detector in either the soft or the hard energy band. Flux limits reached are on the order of $F_{(0.5-2keV)} \approx 10^{-14}$ erg cm $^{-2}$ s $^{-1}$ and $F_{(2-10keV)} \approx 10^{-13}$ erg cm $^{-2}$ s $^{-1}$. These flux limits translate into minimum luminosities detectable of $\sim 10^{38}$ erg s $^{-1}$ and $\sim 10^{39}$ erg s $^{-1}$ for the nearest and farthest Seyferts, respectively.

It was found that 25 out of 27 sources, and in particular all type 1 Seyferts, have a compact dominant nucleus coincident with the optical nuclear position reported in Table 1. The only sources that did not display a dominant nucleus are NGC 1058 and NGC 4472, for which upper limits are calculated.

Adopting the classification scheme proposed by Ho et al. (2001), which separates the morphologies in four classes (according to the predominance of the nuclear emission with respect to the surrounding structures), turned-out that the most common X-ray morphology is that of a single compact nucleus centered on the position of the optical nucleus ($\sim 60\%$ of the sources), followed by those having a nucleus comparable in brightness to off-nuclear sources in the galaxy ($\sim 25\%$), and a few percent have their nuclei embedded in diffuse soft emission or no core emission. There is also good agreement between the *XMM-Newton* and *Chandra* classifications, which guarantees that the *XMM-Newton* point-spread function (PSF) is effective enough to exclude contamination from off-nuclear sources.

Analysis of the soft and hard X-ray light curves indicates that most sources do not exhibit significant flux variations, except for the few brightest Seyfert 1 galaxies (i.e., NGC 3227, NGC 4051, NGC 4151, NGC 4395). However, this is not inconsistent with the expectation that low luminosity sources should exhibit higher variability amplitude (Nandra et al. 1997) because, given the low statistics,

flux variations up to a factor of a few cannot be excluded for most sources. Any potential spectral variations is thus ignored here and only the source *average* X-ray spectra is the subject of this study. This assumption should, however, be kept in mind.

2.3.2 Spectral Analysis

Source spectra were extracted from circular regions with radii of 50'' and 25'' for sources brighter and fainter than $F_{(0.5-10keV)} \approx 10^{-13}$ erg cm⁻² s⁻¹, respectively. These extraction regions correspond to energy encircled fractions of ~90% and ~80%, respectively. When available, the *Chandra* images have been checked for possible contamination due to off-nuclear sources or diffuse emission unresolved by *XMM-Newton*. Sources which may have been affected by this type of contamination are marked with “+” (only soft) or “‡” (both soft plus hard) in Table C.3, which lists the best-fit spectral parameters. The background was estimated using standard blank-sky files or, when unusually high (as in the case of NGC 5033), locally from source-free circular regions placed in offset positions close to the source.

Spectral channels were binned to a minimum of 20 counts per bin and spectra were fitted using data from the three CCD detectors (MOS1/2 and pn) simultaneously. The pn normalization is fixed to 1, while the MOS1/2 normalizations are left free to vary in the range 0.95–1.05 to account for the remaining calibration uncertainties in their cross-normalizations⁴. Statistical errors are in any case typically much larger than current calibration uncertainties. Data were fitted in the range 0.3–10 keV for MOS1/2 and 0.5–10 keV for the pn.

Spectral analysis was performed to first identify the underlying continuum when possible, and then additional components and features were included to best reproduce the data. Hence, each spectrum was initially fitted with a single model consisting of a power law plus absorption fixed at the Galactic value as quoted in column (2) of Table C.3, plus intrinsic absorption as quoted in column (3).

In many cases this simple parametrization is not sufficient to model the whole 0.3–10 keV spectrum. Residuals often show, for example, a soft excess on top of the (absorbed or non-absorbed) power law. The soft-excess component is clearly

⁴See http://xmm.vilspa.esa.es/external/xmm_sw_cal/calib/index.shtml

more complex than a single power law, often exhibiting emission or absorption structures, or both. The soft excess is fitted here using a simple, and approximate, description/parameterization in terms of a scattered power-law component (with index given in column (5)) plus a thermal plasma model (with temperature kT given in column (6), and metallicity fixed to the solar value). The possible presence of a narrow emission line centered at 6.4 keV originating from neutral iron has also been checked, and modeled with a single Gaussian line (with equivalent width, EW, given in column (7)). Best-fit spectral parameters are reported in Table C.3. Errors given in the table are calculated at 90% confidence for two interesting parameters ($\Delta\chi^2 = 4.61$), and a single-digit approximation was applied.

It is stressed that some source spectra, in particular those with high-quality statistics, do clearly require more complex modeling of the continuum and additional narrow absorption and/or emission features than used above in this simplified procedure. For example, NGC 3227, NGC 4051, NGC 4151, NGC 4395, and NGC 5273 show additional continuum curvatures in the residuals which indicate either multiple or ionized absorption. The same is true for NGC 1068 and NGC 4051 for which a reflection continuum in the data is likely to be significant. Other sources such as NGC 1068, NGC 3031, NGC 3079, NGC 4051, NGC 4151, and NGC 5273 also show evidence for additional absorption and/or emission structures at soft and/or hard energies. Given the purpose of this work (to obtain a proper, uniform, average description of the spectra in terms of absorption, photon-index continuum, flux, and Fe K line intensity), it was not attempted to fit all these extra components in a systematic way.

Chapter 3

Testing the UM using the X-ray continuum

The data collected and handled as described in §2 have been used to infer basic X-ray properties of the Seyfert galaxies in the local Universe. In particular, here, I will focus on the average X-ray properties starting from the spectral parameters and on their usage to test the UM.

It is worth noting here that the sample used to derive such informations are the *BeppoSAX* and *XMM-Newton* ones, because of the, on average, good statistics in the observations of the single objects.

3.1 The methods of analysis of the *BeppoSAX* data

The origin of the X-ray photons from AGN are thought to be due to Comptonization of optical-UV radiation, coming from the accretion disk and Comptonized by the e^- in the hot corona that sandwiches the disk (Haardt & Maraschi 1991; Haardt 1993, Poutanen & Svensson 1996, Czerny et al. 2003a). The mechanism is assumed to be, at least at the zero-th order, very similar in each Seyfert galaxy. Under this hypothesis, the differences between the X-ray spectra of different objects are supposed to be mainly due to two kind of factors: i) the time-dependent state of the emitting source; ii) the intervening matter that imprints on the emerging spectrum the features typical of its physical state. In such a scenario, the observations of many sources can be regarded as the long-term monitoring of a

single source. On the other hand, it is also true that the contrary has some comparison in the literature: e.g. time sparse observations of a single source in different states can resemble observations of objects with completely different spectral properties. This is the case, for example, of the narrow line Seyfert 1 NGC 4051 that displayed variations in flux/luminosity by a factor of ~ 100 (Guainazzi et al 1998) associated with strong variations of the spectral shape ($\Gamma \sim 0.5-2.4$; Guainazzi et al. 1998; Turner et al. 1999; Ponti et al. 2006, but see also Crenshaw & Kraemer (2007) for a different interpretation of this spectral behavior in terms of variable ionized absorption). To calculate the mean X-ray properties of the sources included in this work I treated the multiple observations of single sources separately: i.e. I assumed different observations of the same source as if they were observations of different sources.

This method, in principle, is expected to work properly for all those quantities which are supposed to vary in accordance with the state of activity of the central nucleus. For example, the photon index Γ is known to vary with the AGN flux state (Lee et al. 2000; Shih, Iwasawa & Fabian 2002, Ponti et al. 2006) and the high-energy cut-off (E_c) is linked with the temperature of the corona and thus expected to be variable (Haardt, Maraschi & Ghisellini 1997). On the contrary this method is not expected to work properly when constant components are considered. This could be the case, for instance, of the cold absorption assumed to be due to the putative dusty torus (Antonucci 1993). Thus, for this component, the average value recorded for each source should be used. Nonetheless, these components also were observed to vary in a number of objects (see for example the case of NGC 4151, De Rosa et al. 2007 or Risaliti, Elvis & Nicastro 2002). Moreover, the constancy of the properties of the cold absorption is predicted under the hypothesis of a continuous distribution of the matter that forms the torus. On the contrary, if the torus is formed of blobs/clouds (Elitzur & Shlosman 2006), variability in the measurements of the absorbing column is expected. For both these observational and theoretical reasons the N_H measured in each single observation were treated separately.

In between these two cases are the properties of the emission $FeK\alpha$ line. *BeppoSAX* had a too low sensitivity to detect the relativistically broadened component of this feature in a large number of sources. Thus only the narrow line has been detected in the vast majority of the objects included in the original catalog. This component is supposed to originate far from the SMBH, at least at ~ 1000 Schwarzschild radii

(Mattson & Weaver 2004), i.e. very likely at the inner edge of the torus (Nandra 2006). At these distances from the SMBH, the relativistic effects are negligible. Thus, in principle, the parameters that describe the line should be regarded as stable. Nonetheless the properties of the narrow FeK α line were also observed to vary with its line energy centroid changes between ~ 6.4 keV (neutral iron) and ~ 6.9 keV (H-like iron) showing different ionization states. Moreover, the equivalent width (EW) of this component is not only a function of the intensity of the line itself, but it is also directly linked to the underlying variable continuum emitted in the regions close to the SMBH. This makes EW a variable quantity. The parameters of the emission FeK α line were thus treated as variable ones in order to test its origin, and not averaged when objects were observed more than once.

Table 3.1: General characteristics of the data analyzed here. The number of detections and censored data are reported for the interesting parameters for the whole sample of objects (columns 2 and 3), for the Seyfert 1 galaxies (columns 4 and 5), and for the Seyfert 2 objects (column 6 and 7). The 90% confidence interval limits were used for censored data and the detected values were defined if determined with a 99% confidence level

Parameter	Tot. Sample		Seyfert 1		Seyfert 2	
	Det.	Cens.	Det.	Cens.	Det.	Cens.
N_H	83	80	31	53	52	27
EW	129	7	66	4	63	3
R	68	18	46	9	22	9
E_c	33	51	27	26	6	25

Finally, in a number of cases it was necessary to deal with censored data (see Table 3.1). To manage these data properly, the ASURV software (Feigelson & Nel-

son 1985; Isobe et al. 1986) was used. In particular, to establish if the distributions of parameters of type I and type II objects were drawn from different parent populations, the Peto & Prentice generalized Wilcoxon test (Feigelson & Nelson 1985) has been used while to calculate the mean values considering also the censored data the Kaplan-Meier estimator was used. To establish the presence of correlations between different quantities, both the Spearman's ρ and the generalized Kendall's τ methods were applied. The linear regressions were calculated using the Buckley-James and Schmitt's methods. In the following, two quantities are considered as drawn from different parent populations when the probability of false rejection of the null hypothesis (same parent population) is $P_{null} \leq 1\%$. Similarly, one accepts that there is a correlation between two given quantities when the probability of an absence of correlation remains lower than 1%.

In Table 3.2 the results for the whole set of observations and for the two classes of Seyferts are reported as well as the probability that Seyfert 1 and 2 are drawn from the same parent populations. The histograms of the distributions of the interesting parameters for the entire sample of objects (first column) and for type I (second column) and type II (third column) are reported in Figure 3.1.

3.2 The X-ray continuum parameters to test the UM

A Kolmogorov-Smirnov test performed on the distributions of photon index Γ obtained for the *XMM-Newton* test gives a probability of ~ 0.43 , consistent with the same parent population, i.e. there is not a clear case to exclude that the two populations of AGN are drawn from intrinsically different parent distributions. This is a simple example on how the X-ray data can be used to test the UM.

The UM for AGN (Antonucci 1993), in fact, predicts that Γ , R , and E_c are observables independent of the inclination angle, thus the two classes of Seyfert galaxies should display very similar characteristics. This is confirmed by the analysis of the *BeppoSAX* sample. In particular, there are no hints that the distributions of photon index Γ for the two types of Seyfert are drawn from different parent populations ($P_{null} \sim 90\%$). Moreover, the photon-index peaks, for both classes, between 1.8-1.9 in agreement with the two-phase models for the production of the X-ray in Seyfert galaxies that predict $\Gamma \sim 1.5-2.5$ (Haardt & Maraschi 1991; Haardt 1993; Haardt, Maraschi & Ghisellini 1997). Few objects have extremely flat spec-

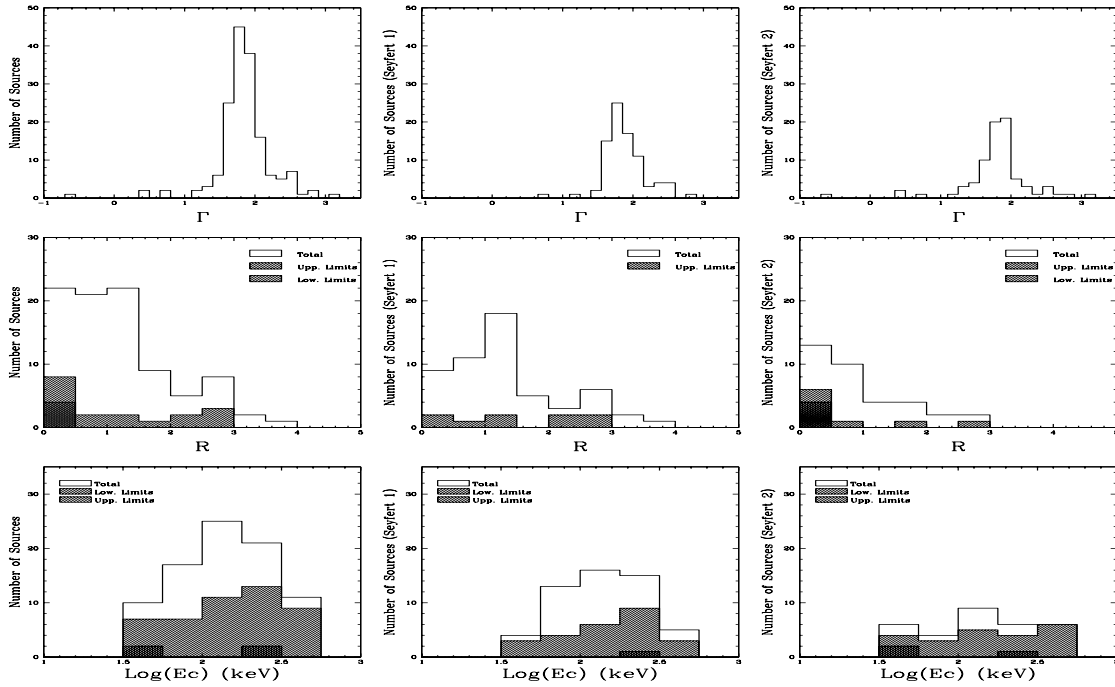


Figure 3.1: Photon index Γ (*first row*), R (*second row*) and E_c (*third row*) in units of cm^{-2} distributions for the whole dataset (*left column*), for type I objects (*center column*), and for type II objects (*right column*).

tra with $\Gamma \leq 1$. Type II objects that show such hard X-ray spectra are supposed to be Compton-thick sources for which, in the 2-10 keV band, only the reflected/flat spectrum is observable. This is the case for NGC 2273 which displays the harder X-ray spectrum. This source was first classified as a Compton-thick object by Maiolino et al. (1998). The Seyfert 1s with flattest spectra are NGC 4151 that is known to have a hard spectrum with complex and variable absorption (De Rosa et al. 2007) and Mrk 231 (classified as a type I AGN by Farrah et al. 2003).

The latter source shows a very hard X-ray spectrum with $\Gamma \sim 0.7$. This source is also classified as a BAL QSO (Smith et al. 1995). A recent spectral analysis in the X-ray band of this source was presented in Braitto et al. (2004). By combining *XMM-Newton* and *BeppoSAX* data, these authors speculated that the spectrum of the source below ~ 10 keV is reflection dominated, thus presenting a case that is difficult to reconcile with the UM of AGN. Moreover, Mrk 231 is an ultra-luminous infra-red galaxy. These sources display strong starburst activity that can

dominate the total X-ray luminosity of the galaxy (see Franceschini et al. 2003 and Ptak et al. 2003 for details on this topic) although in Mrk 231 at least 60% of the observed 0.5-10 keV flux seems to be due to the AGN component (Braitto et al. 2004).

Table 3.2: Mean spectral properties obtained with the *BeppoSAX* sample. Col. I: Spectral parameter; Col. II: Seyfert 1 mean value; Col.III: Seyfert 2 mean value; Col. IV: Probability that Seyfert 1 and Seyfert 2 are drawn from the same parent populations.

Parameter	Tot.	Seyfert 1	Seyfert 2	P_{null}
Γ	1.84 ± 0.03	1.89 ± 0.03	1.80 ± 0.05	90%
R	1.01 ± 0.09	1.23 ± 0.11	0.87 ± 0.14	5%
Ec [†]	287 ± 24	230 ± 22	376 ± 42	5%
N_H^{\ddagger}	31.7 ± 9.1	3.66 ± 2.34	61.3 ± 18.0	$\leq 0.1\%$

[†] in units of eV; [‡] in units of 10^{22} cm^{-2}

Less conclusive results are obtained for R and Ec. In both cases, the probability of false rejection of the null hypothesis (the two distributions are drawn from same parent populations, in accordance with the UM predictions), is $P_{null} \sim 5\%$. However, both type I and II objects lie in the same range of R and Ec. In particular, the distribution of R for type I objects is dominated by a peak of detections between $R \sim 1-1.2$ due to the contribution of a few sources observed several times (e.g. NGC 5548, IC 4329a). This has probably introduced a systematic effect not smeared-out by the relatively small number of useful observations (i.e, the ones for which R and Ec have been estimated). On the other hand, the result on Ec is most probably polluted by the large number of lower limits for Seyfert 2. If the same test is performed only on the detections it is obtained that $P_{null} \sim 35\%$, making impossible to assess that the two samples are drawn from two different populations.

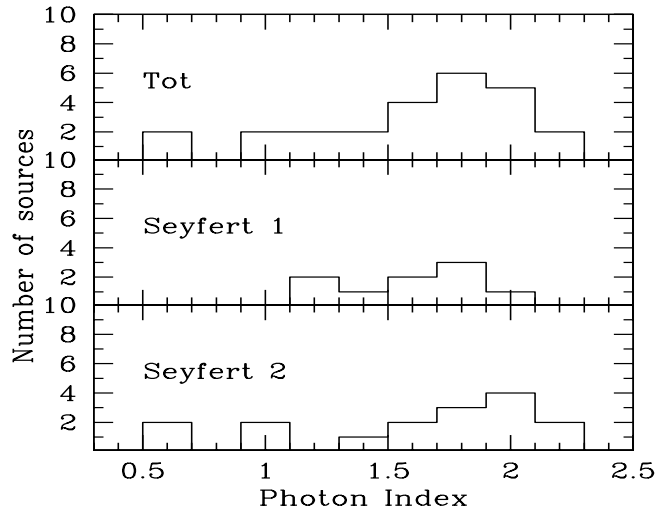


Figure 3.2: Distribution of the observed photon index for the *XMM-Newton* sample. The upper panel refers to the entire sample, the middle panel to the type I objects and the lower panel to the type II Seyferts.

These results are, at a first glance, only partially confirmed with the *XMM-Newton* sample. For the objects included in this last list, in fact, it is obtained that $0.5 < \Gamma < 2.3$ (the value $\Gamma = 2.7$ for NGC 4472 is excluded here because it is due to diffuse emission from the galaxy) The weighted mean for the total sample is $\Gamma \approx 1.60 \pm 0.04$, with a dispersion $\sigma \approx 0.44$. The distribution for type 1 objects (Figure 3.2) has a mean value of 1.56 ± 0.04 and a dispersion $\sigma \approx 0.24$.

It is, nonetheless, worth considering here that the *XMM-Newton* data analyzed here have been fit with simpler models that does not include, for example, the reflection component. This consideration alone could in principle explain the on average flatter spectrum observed by *XMM-Newton*. Moreover, as it will be pointed out in the next section, the distribution of the photon index in the *XMM-Newton* sample is significantly altered by the presence of a number of Compton-thick objects that apparently display extremely flat spectra.

In fact, the rather flat ($\Gamma \lesssim 1.5$) spectrum of 4 (out of 9) type 1 objects can be ascribed to either the presence of a warm absorber, a complex absorber, and/or a reflection component, all of which produce a flattening of the continuum. The distribution of Γ for type 2 objects (lower panel of Fig. 2.2) is somewhat broader.

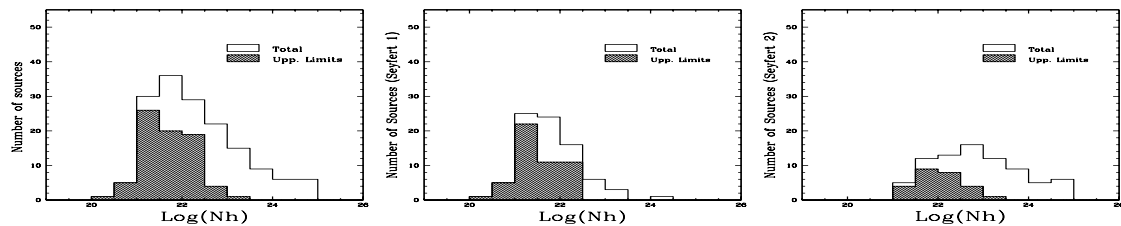


Figure 3.3: N_H (in units of cm^{-2}) distributions for the whole dataset (*left column*), for type I objects (*center column*), and for type II objects (*right column*).

The weighted mean for this class is 1.61 ± 0.06 with a dispersion of ~ 0.5 .

3.3 The average absorption properties

The *BeppoSAX* data are unambiguously in accordance with UM predictions for the absorbing column¹. In this case the statistical tests confirm that Seyfert 1 and Seyfert 2 display very different absorption characteristics with the type II objects being more heavily absorbed than Seyfert 1 (Table 3.2, Figures 3.3 and 3.4). Again, it is noticeable that a few type I objects show high column densities (up to $\sim 10^{24} \text{ cm}^{-2}$) and some Seyfert 2 have low columns (down to 10^{21} cm^{-2}). These are not new results: the high column of NGC 4151 ($\sim 5 \times 10^{22}$, De Rosa et al. 2007) is well known. The highest column measured in a Seyfert 1 is detected during the June 9, 1998 observation of NGC 4051. During this observation the source appeared “switched-off” and only a pure reflection component was measured (Guainazzi et al. 1998). The spectral fit degenerated between two solutions, one in which the source was purely reflection-dominated ($R \geq 7$) and a second one in which a direct component was visible but highly absorbed. The latter scenario was slightly preferred from a pure statistical point of view when the 2-200 keV band is considered, and, for homogeneity, entered in the catalog. Nonetheless, when the entire *BeppoSAX* band (0.1-200 keV) is considered, the reflection scheme is

¹A number of objects in the *BeppoSAX* sample show upper-limits to the absorbing column of the order of $\sim 10^{22} \text{ cm}^{-2}$. This is a selection effect induced by the energy band considered using only MECS and PDS data. The low-energy cut-off due to such a column (10^{22} cm^{-2}) peaks at $E \sim 2 \text{ keV}$ and only for those objects with good statistics it is possible to infer upper limits on the N_H below 10^{22} cm^{-2} . This is most probably responsible for the high value obtained for the average N_H in type I objects.

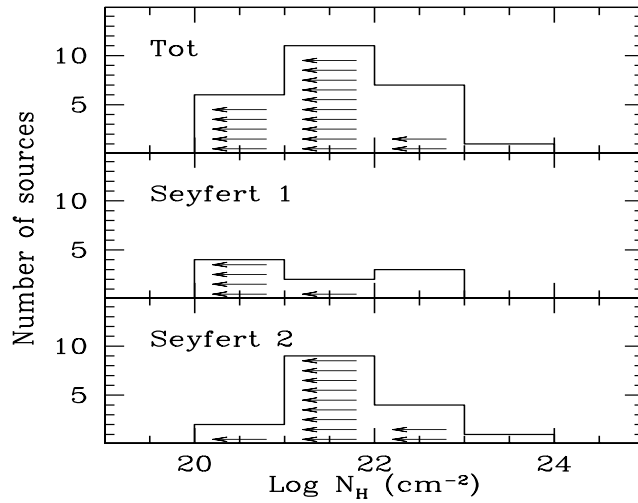


Figure 3.4: Distribution of the observed absorbing columns for the *XMM-Newton* sample. The upper panel refers to the entire sample, the middle panel to the type I objects and the lower panel to the type II Seyferts.

preferred (Guainazzi et al. 1998).

The heterogeneity of the *BeppoSAX* sample prevents to define the average absorption properties of the Seyfert galaxies, the absorption column being the element that separates the two classes of AGN. Thus, to deeply investigate this topic, i.e. the intrinsic distribution of absorption column, an unbiased sample of objects must be used. In this case, it's the *XMM-Newton* sample.

The observed total distribution in the *XMM-Newton* sample varies over the range of Galactic absorptions ($N_H \approx 10^{20} \text{ cm}^{-2}$) to high column densities ($N_H \lesssim 10^{24} \text{ cm}^{-2}$), with most of the measurements being upper-limits of $N_H \approx 10^{21-22} \text{ cm}^{-2}$ (Figure 3.4).

As already said, type 1 objects are known to be less absorbed than type 2s, but three of them show a column density higher than 10^{22} cm^{-2} . The nature of the absorbing material in these objects is likely associated with highly ionized gas (NGC 3516, Netzer et al. 2002) and/or to dense and variable absorbing columns (NGC 3227, Lamer, Uttley, & McHardy 2003; NGC 4151, Puccetti et al. 2003).

Past hard X-ray surveys of Seyfert 2 galaxies have revealed that the column density distribution of this class is significantly shifted toward large columns; most

($\sim 75\%$) of type 2 Seyferts are heavily obscured, with $N_H > 10^{23} \text{ cm}^{-2}$ (Risaliti et al. 1999). The distribution observed here and shown in the lower (left side) panel of Figure 3.4 apparently deviates from past results, containing mostly mildly absorbed objects. However, this distribution does not take into account the possible presence of heavily absorbed sources, not recognised as such because of the absence of a low energy cut-off.

3.4 Identification of highly absorbed sources in the *XMM-Newton* sample

The differences measured in §3.2 between type I and type II objects within the *XMM-Newton* sample in terms of Γ , could well be due to the presence of an unmodeled reflection component (see §3.2, Figure 3.2), but also, in part or totally, to the inability to directly measure heavily absorbed sources. In the hard band, the effective area of the pn peaks at energies around 5–6 keV and has an exponential roll-over at higher energies. This implies that the data are only weakly sensitive to measurements of absorption columns of $N_H \gtrsim 10^{23} \text{ cm}^{-2}$. In particular, in Compton-thick sources with $N_H > 10^{24} \text{ cm}^{-2}$, the transmitted component is completely suppressed below 10 keV and the spectrum observed in the 2–10 keV band is dominated by flattened reprocessed components from a cold and/or warm scatterer (Matt et al. 2000). The galaxy may, thus, be erroneously classified as a source with a flat spectral shape, low absorption and, thus, low luminosity while actually being intrinsically steep, heavily obscured, and luminous (see, for example, the prototypical case of the Seyfert 2 galaxy NGC 1068; Matt et al. 1997, Iwasawa, Fabian & Matt 1997).

To take these factors into account, three independent tools were applied to unveil the presence of heavy obscuration: (i) X-ray spectral diagnostics such as flat slope and large Fe K α EW; (ii) flux diagnostic diagrams; and (iii) the N_H vs. $F_{2-10\text{keV}}/F_{[\text{O III}]}$ diagram.

In three type 2 objects (NGC 1068, NGC 3079, and NGC 5194), the EW of the detected iron K line is higher than ~ 1 keV. Such a high value of the EW is expected in highly obscured objects since it is measured against a much-depressed continuum ($N_H \approx 10^{23}\text{--}10^{24} \text{ cm}^{-2}$; Leahy & Creighton 1993) or against a pure

reflection component ($N_H > 10^{24-25} \text{ cm}^{-2}$; Makishima 1986, Bassani et al. 1999).

In 2 Seyfert 2 galaxies (NGC 2685 and NGC 3486), the photon index is rather flat ($\lesssim 1$) and may also be indicative of Compton-thick sources. However, the lack of any strong line makes this criterion alone not sufficient to classify the sources as Compton-thick candidates. In total, the spectral analysis is able to directly assess three candidate Compton-thick sources, namely NGC 1068, NGC 3079, and NGC 5194. This is consistent with studies which have been able to obtain hard ($E > 10 \text{ keV}$) X-ray spectra of these sources with *BeppoSAX* (Matt et al. 1997, Iyomoto et al. 2001, Fukazawa et al. 2001).

Another way of evaluating the true amount of absorption is through flux diagnostic diagrams (e.g., Bassani et al. 1999, Panessa & Bassani 2002, Panessa 2004, Guainazzi et al. 2005b). These make use of independent indicators of the intrinsic brightness of the source such as the [O III] $\lambda 5007$ flux and the infrared emission, to be compared with the hard X-ray flux.

By studying a large sample of Seyfert 2 galaxies, Bassani et al. (1999) have found that the ratio $F_{2-10\text{keV}}/F_{[\text{OIII}]}$ is effective in separating Compton-thin from Compton-thick sources, the latter having ratios lower than ~ 1 . This is because the [OIII] flux is considered to be a good isotropic indicator; it is mostly produced far from the nucleus, in the NLR, by photoionizing photons from the AGN. Applying this criterion to this sample, and using the [OIII] measurements reported in HFS97, 5 Compton-thick sources have been identified, i.e. with $F_{2-10\text{keV}}/F_{[\text{OIII}]} < 1$: NGC 676, NGC 1068, NGC 3079, NGC 3185, and NGC 5194. Of note is the fact that the three candidates Compton-thick with a strong line are confirmed.

The effectiveness of identifying Compton-thick vs. Compton-thin sources through the ratio $F_{2-10\text{keV}}/F_{[\text{OIII}]}$ is also exemplified by the third diagnostics: the N_H vs. $F_{2-10\text{keV}}/F_{[\text{OIII}]}$ diagram shown in Fig. 3.5. Assuming, as mentioned above, that the [OIII] luminosity is an isotropic indicator of the intrinsic luminosity, one expects that the ratio of $F_{2-10\text{keV}}/F_{[\text{OIII}]}$ decreases as N_H increases, following a path as indicated by the dashed region in Fig. 3.5. The relation was obtained assuming that the observed $F_{2-10\text{keV}}$ changes according to the N_H value given on the ordinate, and starting from the average $F_{2-10\text{keV}}/F_{[\text{OIII}]}$ ratio observed in type 1 Seyferts and assuming a 1% scattered component. The width of the shaded area (from lower left to upper right) was drawn considering the lower and higher $F_{2-10\text{keV}}/F_{[\text{OIII}]}$ ratios obtained for the type 1 objects of the present sample. The shaded region

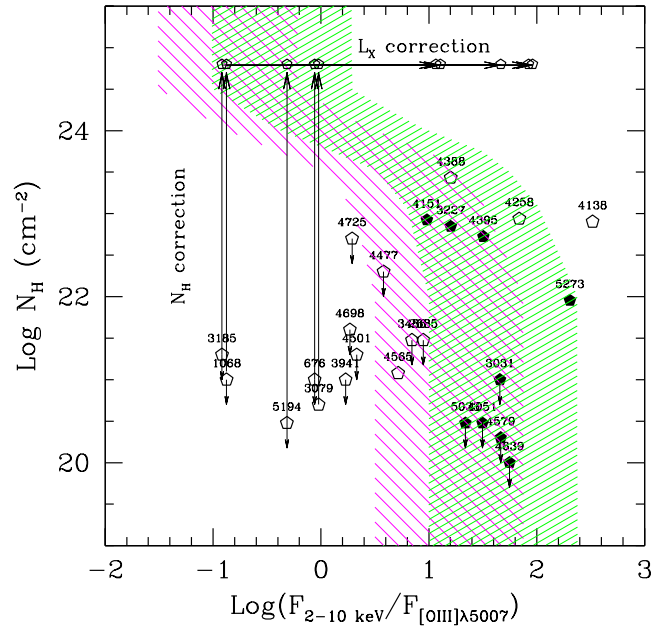


Figure 3.5: Diagram of the absorbing column density N_H versus the ratio between the observed 2–10 keV flux and the reddening-corrected [O III] flux taken from Panessa (2004). Filled polygons are type 1 Seyferts and open polygons are type 2 Seyferts. The shaded region (lower-left to upper-right diagonals) indicates the expected correlation under the assumption that $L_{2-10\text{keV}}$ is absorbed by the N_H reported on the ordinate, starting from the average $F_{\text{HX}}/F_{[\text{O III}]}$ ratio observed in type 1 Seyfert galaxies and by assuming a 1% reflected component. Also, the shaded region (upper-left to lower-right diagonals) obtained by Maiolino et al. (1998) is shown.

(from upper left to lower right) obtained by Maiolino et al. (1998) is also shown for comparison and is consistent with the present results, though slightly shifted to lower flux ratios.

Table 3.3: Compton-thick/thin Seyfert 2 candidates

Name	$\Gamma_{2-10\text{ keV}}$	$\text{EW}_{\text{Fe K}}$	Flux diag.	Thick?
(1)	(2)	(3)	(4)	(5)
NGC 676			Thick	√
NGC 1058			Thick/SB	?
NGC 1068	Thick	Thick	Thick	√
NGC 2685	Thick		Thin	?
NGC 3079		Thick	Thick	√
NGC 3185			Thick	√
NGC 3486	Thick		Thick/SB	?
NGC 3941			Thin	×
NGC 4138	Thick	Thin	Thin	×
NGC 4258	Thick	Thin	Thin	×
NGC 4388		Thin	Thin	×
NGC 4472			Thin	?
NGC 4477			Thin	×
NGC 4501	Thin		Thin	×
NGC 4565		Thin	Thin	×
NGC 4698			Thin	×
NGC 4725			Thin	×
NGC 5194		Thick	Thick	√

Notes: “Thick” = Compton-thick candidate, “Thin” = Compton-thin candidate, “SB” = starburst candidate on the basis of spectral diagnostics (cols. 2 and 3) and flux diagnostics (col. 4). Final classification (col. 5): “√” = Compton-thick candidates, “×” = Compton-thin candidate, and “?” = classification uncertain (likely to contain a starburst, but CT nature cannot be excluded).

Compton-thick AGNs should occupy the *observed* low N_H and low $F_{2-10\text{keV}}/F_{[\text{O III}]}$ part of the diagram, but after correction for their *intrinsic* high N_H , they should occupy the high N_H and low $F_{2-10\text{keV}}/F_{[\text{O III}]}$ region of the predicted distribution (as indicated by the arrows in Fig. 3.5). It was found that this is indeed the case for the previously identified Compton-thick objects of this sample (NGC 676, NGC 1068,

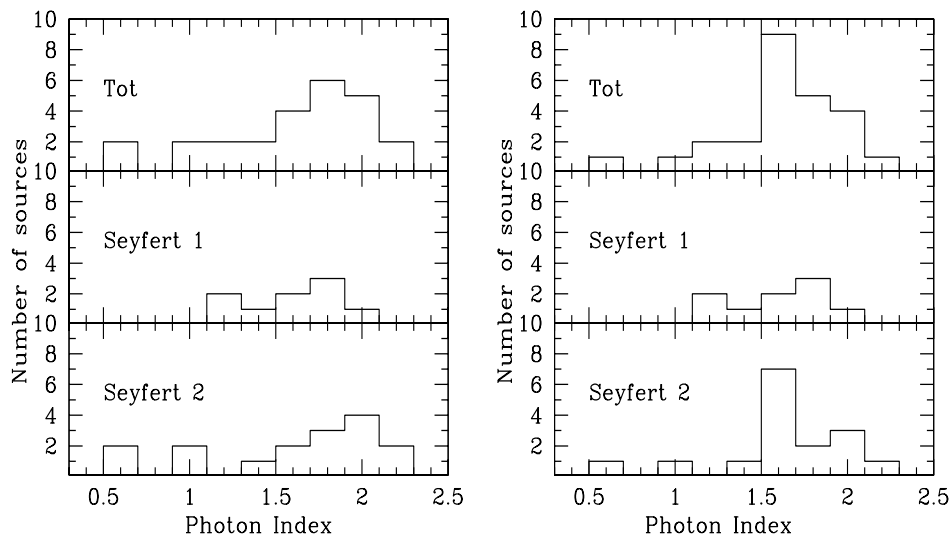


Figure 3.6: Distribution of the photon index before (left panel, see Figure 3.2) and after (right) correction for Compton-thick candidates for which a value of $\Gamma=1.62$ is assumed (see text for details).

NGC 3079, NGC 3185, and NGC 5194). Other sources (NGC 3941, NGC 4698, and NGC 4501) are located in the same area of the plot, but no independent confirmation to classify them as secure Compton-thick candidates were found. Moreover, they have $F_{2-10\text{keV}}/F_{[\text{O III}]}$ ratios exceeding 1, in the Compton-thin regime. Interestingly, two of these sources (NGC 4698 and NGC 4501) have been identified in the literature as “anomalous” cases of Seyfert 2 galaxies with no intrinsic absorption (Georgantopoulos & Zezas 2003, Terashima et al. 2002).

By combining the X-ray spectral properties and the diagnostic diagrams using isotropic indicators, Compton-thin and Compton-thick objects have been identified as indicated in Table 3.3. In total, a subsample of 5 Compton-thick candidate objects have been confidently recognized (5 from diagnostic diagrams, 3 of which have direct spectral information as well).

It is worth considering that once the bona-fide Compton-thick sources have been picked-up, the obtained distributions of photon index and absorbing columns move to average properties in agreement with what measured with the *BeppoSAX* sample and with the literature (see Figures 3.6 and 3.7, Turner et al. 1987, Risaliti et al. 1999).

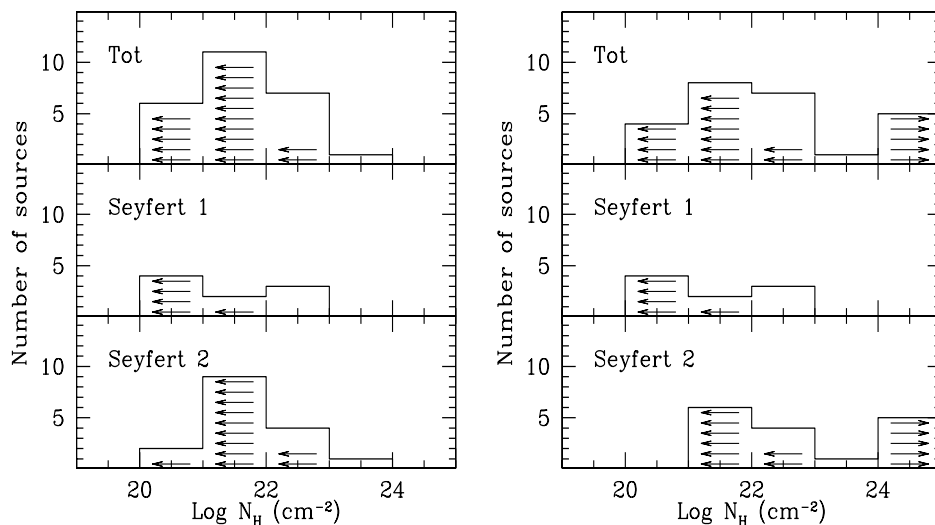


Figure 3.7: Distribution of the absorption column densities before (left, see Figure 3.4) and after (right) correction for Compton-thick candidates. Upper and lower limits are indicated with arrows.

3.5 The origin of the narrow component of the FeK α line

A Gaussian iron K emission line has been detected in 8 out of 9 type 1s and in 6 out of 18 type 2s included in the *XMM-Newton* sample. Their mean equivalent widths are $\approx 215 \pm 80$ eV and $\approx 700 \pm 220$ eV, respectively, which are consistent with previous works (Nandra et al. 1997, Turner et al. 1997) when the large errors and dispersions are taken into account. The larger rate of detected lines in type 1s with respect to type 2s is at first surprising but is consistent with the fact that type 1s are typically brighter in the sample. As mentioned in §2.3.2, the present estimates are to be taken as only rough parameterizations because they do not take into account in detail of the multiple lines often present (i.e. in NGC1068, NGC3031, NGC4579), nor the possibility of line broadening (NGC3031, NGC4051, NGC4151, NGC4395) or variability.

Here I will focus on the *BeppoSAX* sample analysis since it is the largest reservoir of data available to me to study the origin of such a component.

Wherever originated, the FeK α line is produced by reprocessing the primary X-ray emission in matter surrounding the source of hard photons. In the frame-

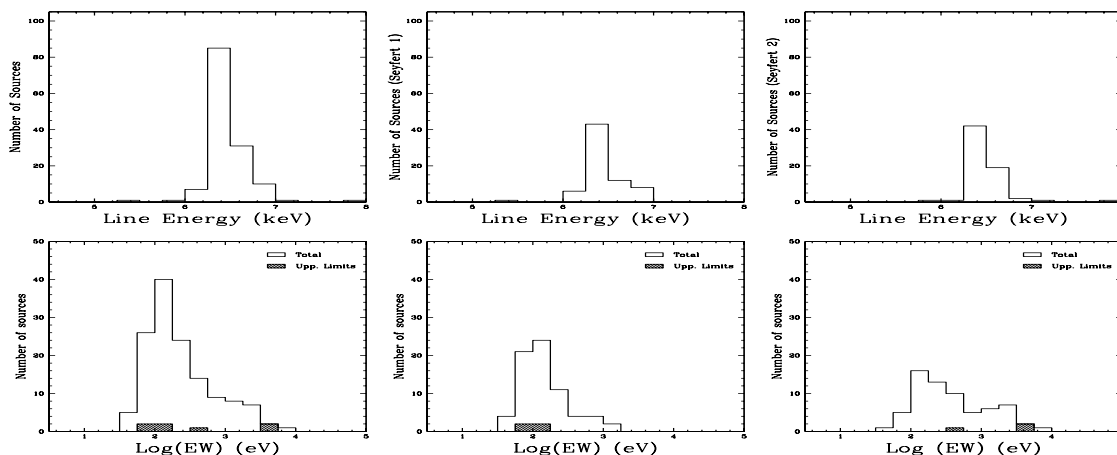


Figure 3.8: Distribution of the FeK α emission line energy centroid (*first row*) and of its EW (*second row*). Distributions for the whole sample of observations (*left panel*), for the type I objects (*center panel*) and for type II objects (*right panel*).

work of the UM, the origin of this component can be placed in a number of regions such as the accretion disk, the dusty torus, and the broad-line regions (even if this last hypothesis is disfavored by the recent results obtained with the *XMM-Newton* and *Chandra* observatories and presented in Nandra 2006). If the line originates in the disk close to the SMBH, relativistic effects that broaden the resulting line are expected. For the vast majority of the sources included in the *BeppoSAX* sample, only narrow components of such features were detected and only in a few cases broad emission lines (e.g. IC 4329a) or relativistically blurred features were detected (for example in MCG-6-30-15). Nonetheless, the number of objects/observations included in this sample is large enough to allow a deep investigation of the origin of the FeK α emission line.

As shown in Figure 3.8 (first row), the line energy centroid is peaked at ~ 6.4 - 6.5 keV (see also Table 3.4) in both type I and II objects. The centroid is slightly above 6.4 keV but, considering the energy resolution of the instrument at these energies (~ 200 eV FWHM, Boella et al. 1997), the results obtained here are in agreement with the line being mainly produced in cold or nearly cold matter (ionization state below FeXVII), i.e. in both type I and II objects, by matter in the same physical state. However, a well known difference between the two classes of objects is the EW of the narrow FeK α line in type II objects, which shows stronger

features than type I objects (see second row of Figure 3.8 and Table 3.4, Bassani et al 1999, Risaliti et al. 1999). As shown in the central panel of Figure 3.8, the Seyfert 1s peak at $EW_{FeK\alpha} \sim 100-200$ eV while the type II have a broader distribution with a hard tail that reaches values well above 1 keV. Also few Seyfert 1 have large values of EW of the FeK α line (above 300-400 eV). The large EW tail of the Seyfert 1 distribution is composed mainly of objects in which the broad components of the FeK α line are detected such as in MCG-6-30-15, Mrk 841 and IC 4329a. The Seyfert 1 with largest EW is NGC 4051 during the June 9, 1998 observation when its spectrum was due to pure reflection (Guainazzi et al. 1998).

Table 3.4: Mean properties of the FeK α emission line. Col. I: spectral parameter; Col. II mean value for the whole sample; Col. III: mean value for Seyfert 1; Col. IV: mean value for Seyfert 2. Col. V: Probability that the parameters of type I and type II objects are drawn from the same parent population.

Parameter	Tot.	Seyfert 1 [†]	Seyfert 2 [†]	P_{null}
$E_{FeK\alpha}$ [†]	6.49±0.02	6.46±0.03	6.51±0.03	32%
$EW_{FeK\alpha}$ [‡]	448±67	222±33	693±195	≤1%

[†] in units of keV; [‡] in units of eV

The larger FeK α EW in Seyfert 2 galaxies is in agreement with the UM (Antonucci 1993). If the origin of this component is indeed located in the dusty torus, than the line EW has to be correlated with the absorber column density. This is indeed what is observed also in this sample (see Figure 3.9, upper panel). Moreover, the Spearman ρ and Kendall's τ tests indicate that a correlation between the FeK α EW and the N_H is highly probable for type II objects ($P_{null} \leq 0.1\%$), i.e. for that sources for which I can have direct evidence of the torus absorbing column. The robustness of the N_H estimates have been tested by correlating it with the model independent indicator offered by the ratio of the observed fluxes at 2-10 and 20-100

keV respectively (left panel of Figure 3.9). The two quantities are strongly correlated (generalized Spearman ρ and Kendal τ tests give $P_{null} \leq 0.1\%$) with only a few exceptions: the pure Compton-thick sources which are located in the diagram below the majority of the sources. This effect is expected since the absorbing column can affect the X-ray radiation below ~ 10 keV while at harder energies the radiation pierces the matter for columns $\leq 3\text{-}5 \times 10^{24}$ cm^{-2} . Otherwise, the Compton absorption dominates and also photons with energy above 10 keV are stopped since the Klein-Nishina regime is reached (see §3.4).

As stated above, when the EW of the $\text{FeK}\alpha$ emission line is tested against the measured N_H (upper panel of Figure 3.9) a result in good agreement with what is predicted by theoretical models is obtained (Makishima 1986; Leahy & Creighton 1993). The majority of the sources, in fact, behave as expected if the line is produced by the absorbing matter that depresses the direct continuum (Makishima 1986). All the known Compton-thick sources are located at low N_H and high EW, in accordance with previous results (Bassani et al. 1999, Risaliti et al. 1999). As an additional test, the EW of the $\text{FeK}\alpha$ line has been plotted versus the $F_{2-10\text{keV}}/F_{20-100\text{keV}}$ ratio. As expected (see right panel of Figure 3.9), a good correlation ($P_{null} \leq 0.1\%$ according to generalized Spearman ρ and Kendall τ tests) is obtained.

These results thus confirm that the properties of the $\text{FeK}\alpha$ line agree with the expectations of the UM for AGN. Nonetheless, this is not the only information about the iron line. In recent papers (Iwasawa & Taniguchi 1993; Page, O'Brien et al. 2004, Grandi, Malaguti & Fiacchi 2006; Bianchi et al. 2007) it has been claimed that a X-ray *Baldwineffect* (or Iwasawa-Taniguchi effect) is present in AGN when the $\text{FeK}\alpha$ intensity is probed against the 2-10 keV luminosity. Here this effect is tested considering for the first time both the 2-10 keV and the 20-100 keV luminosities.

A strong correlation ($P_{null} \leq 0.1\%$ using Spearman ρ and generalized Kendal τ test) is found when the EW of the $\text{FeK}\alpha$ line is plotted both against the observed 2-10 keV (panel (a) of Figure 3.10) and 20-100 keV (panel (c) of Figure 3.10) keV luminosities. The nature of these correlations, however, is not straightforward, especially for the 2-10 keV luminosity. In this energy band the effect of the absorber is very important. As previously demonstrated, the EW of the iron line correlates with N_H , but stronger absorbing columns imply lower fluxes. Moreover, when the

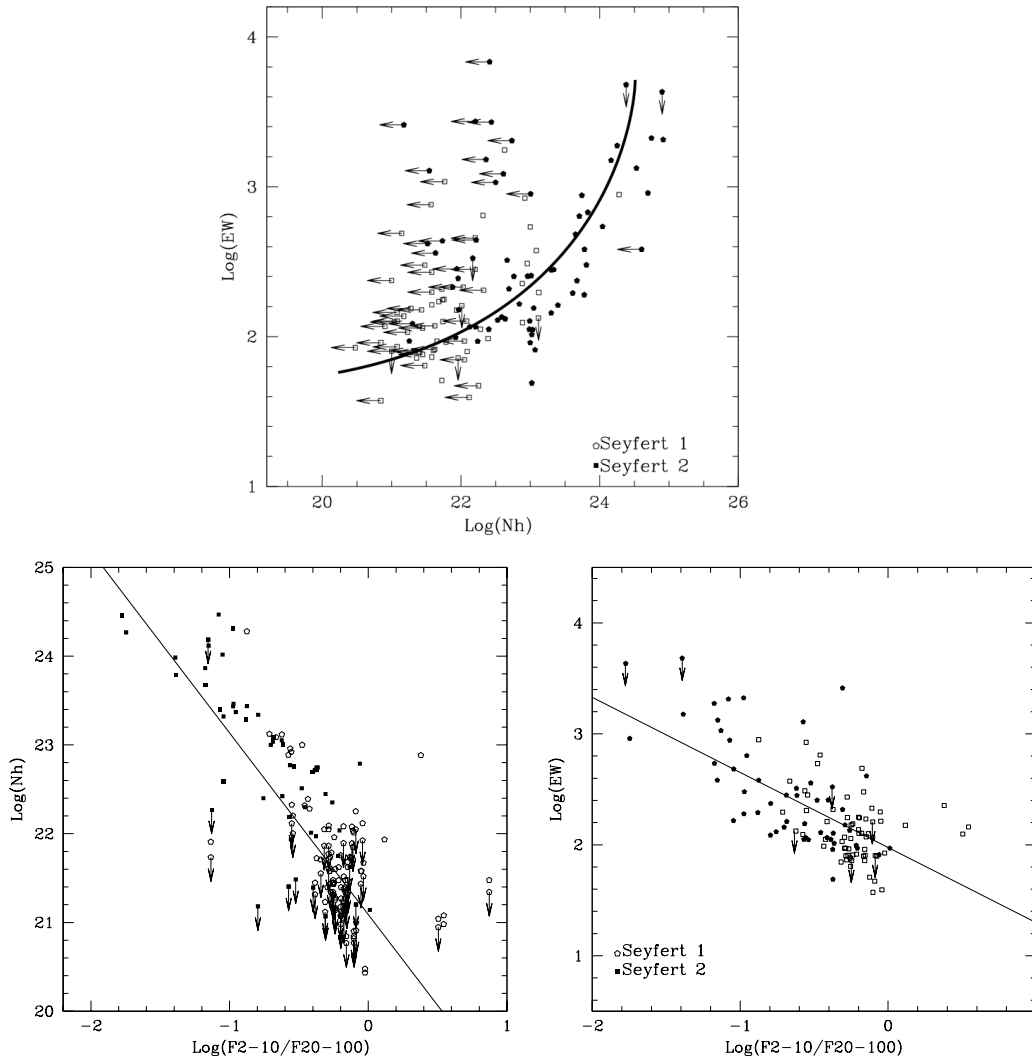


Figure 3.9: *Upper panel:* $\text{Log}(EW_{FeK\alpha})$ vs. $\text{Log}(N_H)$. As expected, the sources are divided in two families: the ones that follow the expectations if the FeK α line is produced in the absorption matter and the candidate Compton-thick ones that display low absorption and large EW. The solid line indicates the prediction by Makishima (1986). *Left panel:* $\text{Log}(F_{2-10keV}/F_{20-100keV})$ vs. $\text{Log}(N_H)$. The two quantities are correlated as expected since the 2-10 keV band is strongly affected by the absorption while the 20-100 band is almost free from absorption. The solid line is the best fit obtained with linear regression methods *Right Panel:* $\text{Log}(EW_{FeK\alpha})$ vs. $\text{Log}(F_{2-10keV}/F_{20-100keV})$. The two quantities are strongly correlated ($P_{null} \leq 0.01$). The ratio between X-ray fluxes is a model independent indicator of the absorption affecting the low energy band. Thus, this correlation strongly indicates that the narrow component of FeK α line in emission is indeed produced by the same matter responsible for the absorption. The solid line is the linear regression obtained using Buckley-James method (Isobe et al. 1986).

relation between the FeK α line EW and the 2-10 keV flux is investigated (panel (b) of Figure 3.10), it is found that the two quantities are correlated ($P_{null} \leq 1\%$). This is explainable only in terms of instrumental effects, since the sensitivity of the instruments to narrow features decreases with the source's flux. Thus, to be detected in faint objects, the FeK α line must be strong enough. Since the original sample is limited to the local Universe, this correlation in flux acts, at least partially, also in the EW vs $L_{2-10keV}$ relation.

This N_H effect should be negligible when the 20-100 keV band is considered. In fact, in this case, one expects to find a correlation between the observed 20-100 keV luminosity and the EW of the FeK α line only in the most extreme cases, i.e. for the “pure Compton thick” objects. Apart from NGC 1068, these sources are too weak to be detected by the PDS, thus unable to drive the relation observed in plot (c) of Figure 3.10. Moreover, panel (e) of Figure 3.10 indicates that the EW of the iron line is not related to the 20-100 keV flux thus excluding that the “Baldwin effect” measured using the 20-100 keV band is due to instrumental selection effect as it happens for the $F_{2-10keV}$. On the other hand, in the 20-100 keV band the reflection-hump at $\sim 30-40$ keV contributes to the observed flux. If the origin of the FeK α line is due to the same matter responsible of the reflection, one should expect that the EW of the iron line should increase as the reflection component augments the 20-100 keV flux (i.e. the iron line EW should correlate with the 20-100 keV flux). Thus, the net contribution of the reflection component should act in the opposite direction to that observed (i.e. larger iron line EW at smaller 20-100 keV flux). If the two classes of Seyfert galaxies are analyzed separately it is obtained that a strong correlation is found for Seyfert 1 ($P_{null} \leq 0.1\%$ using both Spearman ρ and generalized Kendal τ tests, panel (d) of Figure 3.10) while no correlation is evident for type II objects ($P_{null} \sim 80\%$).

This result is not unexpected since the EW of the obscured sources are boosted by the suppression of part of the underlying continuum. To conclude, the presence of a X-ray Baldwin effect for Seyfert 1 is unambiguously confirmed by the present data if the $L_{20-100keV}$ is considered and it has the following relation:

$$\text{Log(EW)} = -(0.22 \pm 0.05) \times \text{Log}(L_{20-100}) + 11.91 \pm 2.52. \quad (1)$$

The slope of the relation found in this work is in agreement with that previously

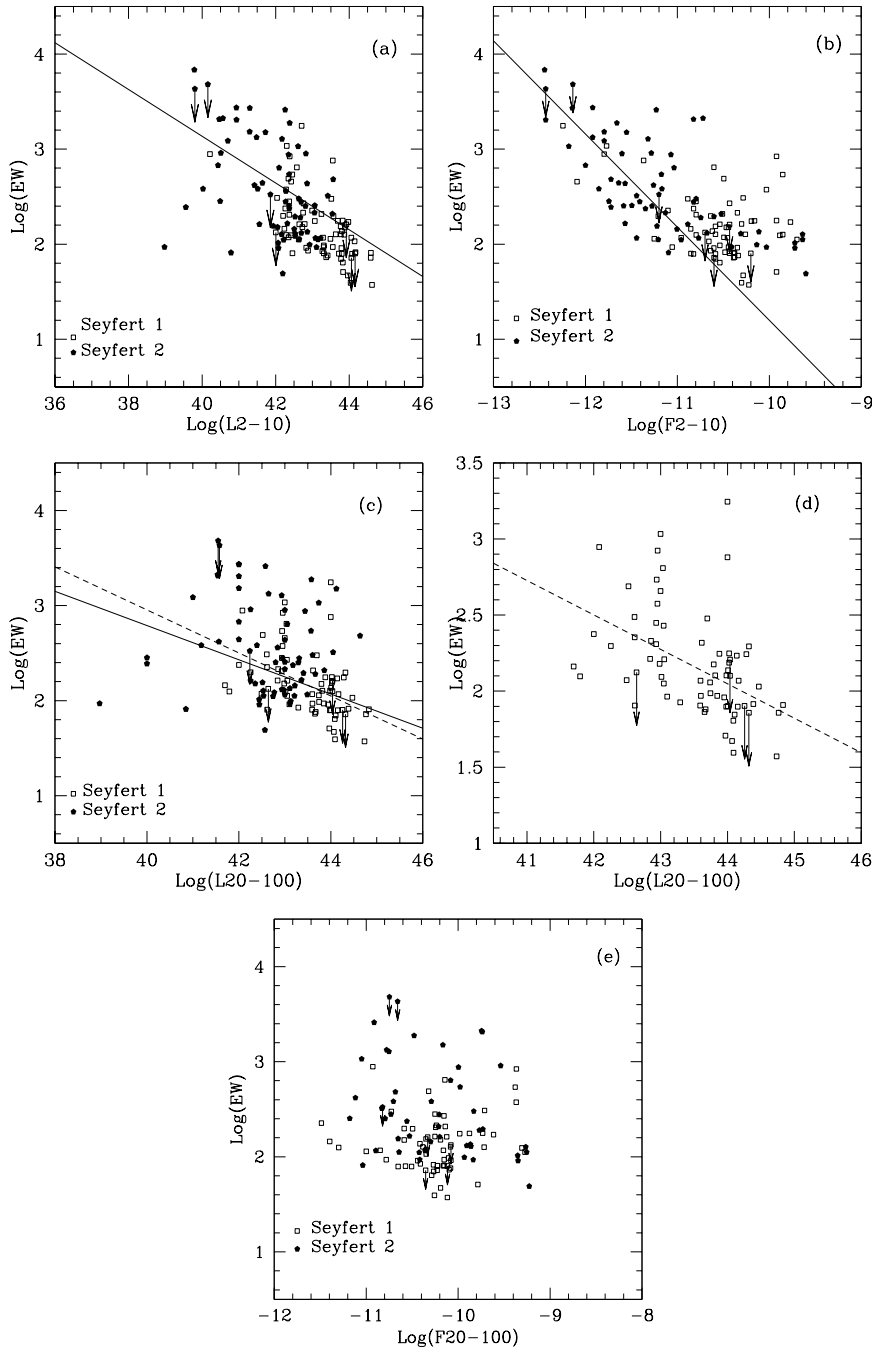


Figure 3.10: *Panel (a):* $\text{Log}(EW_{FeK\alpha})$ vs. $L_{2-10,observed}$. *Panel (b):* $\text{Log}(EW_{FeK\alpha})$ vs. $F_{2-10,observed}$. *Panel (c):* $\text{Log}(EW_{FeK\alpha})$ vs. $L_{20-100,observed}$. *Panel (d):* The same as panel (c) but only for Seyfert 1 objects. *Panel (e):* $\text{Log}(EW_{FeK\alpha})$ vs. $F_{20-100,observed}$. Solid lines in panel (a), (b), and (c) are the linear regressions obtained for the whole sample of observations. The dashed line in panels (c) and (e) is the linear regression obtained considering only type I objects. As visible in panel (b) the less scattered relation is obtained considering the 2-10 keV observed flux. The relation is linear, as expected if the correlation is due to selection effects, i.e. considering that in faint objects only large EW were detectable by the MECS instruments on-board *BeppoSAX*.

obtained by Page et al. (2004) ($EW_{\alpha}(L_{2-10})^{-0.17\pm 0.08}$) using a sample containing both radio-quiet and radio-loud objects. The present result is also consistent with that found by Zhou & Wang (2005) (who used a sample containing both radio-quiet and radio-loud objects finding $EW_{\alpha}(L_{2-10})^{-0.15\pm 0.05}$) and Bianchi et al. (2007) (who used only radio-quiet objects obtaining $EW_{\alpha}(L_{2-10})^{0.17\pm 0.03}$). On the contrary, Jiang, Wang & Wang (2006), excluding the radio-loud AGN from a sample similar to the one used by Page et al. (2004), found that $EW_{\alpha}(L_{2-10})^{0.10\pm 0.05}$. It is worth recalling here, that the the present sample is composed of both radio-loud and radio quiet sources. In particular, it contains 7 radio-loud Seyfert 1, and only for 5 of them are the 20-100 and iron line data available. Nonetheless, the presence of these sources in the sample does not affect the $FeK\alpha$ EW vs. L_{20-100} relation ($EW_{\alpha}(L_{2-10})^{0.21\pm 0.05}$ excluding radio-loud type I objects).

The origin of the X-ray *Baldwineffect* is unclear. In the light bending scenario (Miniutti & Fabian 2004) the height of the source above the accretion disk determines the degree of beaming along the equatorial plane of the high energy emission. Because of relativistic effects, the closer the source is to the disk, the greater will be the fraction of X-rays beamed in the equatorial plane (i.e. towards the disk) and correspondingly lower will be the observed flux. Thus, the EW of the relativistically blurred $FeK\alpha$ line produced in the inner regions of the disk and the EW of the narrow iron line produced in the outer parts of the disk would appear enhanced in low-state sources.

On the contrary, Page et al. (2004) speculated that this effect could indicate that luminous sources are surrounded by dusty tori with lower covering factor thus pointings towards a torus origin of most of the narrow $FeK\alpha$ lines. The present work supports this view. The $FeK\alpha$ line EW of the iron line correlates with the observed N_H as predicted by theory (Makishima 1986; Leahy & Creighton 1993; Ghisellini, Haardt & Matt 1994). Moreover, the case of the extremely low state of NGC 4051 (Guainazzi et al. 1998) included in this dataset also seems to point in this direction. The very large EW of the narrow $FeK\alpha$ line recorded in this observation is typical of Compton-thick type II objects, but the line does not show evidence of relativistic broadening due to the contribution of the inner orbits of the accretion disk.

3.6 Summary of the results obtained testing the UM

The average properties of Seyfert galaxies in the local Universe have been here investigated, analyzing the *BeppoSAX* and *XMM-Newton* samples. The main results may be summarized as follow:

- the average slope of the power-law is 1.84 ± 0.03 for the entire *BeppoSAX* sample of objects. Considering the two families of AGN separately, $\Gamma = 1.89 \pm 0.03$ for type I objects (including Seyfert 1, 1.2 and 1.5) while $\Gamma = 1.80 \pm 0.05$ for type II objects (including Seyfert 1.8, 1.9 and 2). The observed values are slightly flatter if the *XMM-Sample* is considered, but see §3.2 for a discussion on this topic. No significant differences have been observed between the two types of Seyfert galaxies;
- the average value of the relative reflected-to-direct normalization parameter R obtained using the *BeppoSAX* sample is 1.01 ± 0.09 with a slight difference between the two classes of Seyfert galaxies ($R = 1.23 \pm 0.11$ for type I objects and $R = 0.87 \pm 0.14$ for the type II ones). No significant differences have been observed between the two types of Seyfert galaxies;
- the high energy cut-off was measured in the entire *BeppoSAX* sample to be $E_c = 287 \pm 24$ ($E_c = 230 \pm 22$ keV for Seyfert 1 and $E_c = 376 \pm 42$ keV for Seyferts 2). No significant differences have been observed between the two types of Seyfert galaxies;
- as expected and as known from previous works, the absorbing column is very different in the two classes of objects. Considering the *BeppoSAX* sample, one obtains, on average, $N_H \sim 3.66 \times 10^{22} \text{ cm}^{-2}$ for type I and $N_H \sim 6.13 \times 10^{23} \text{ cm}^{-2}$ for type II AGN. It is worth considering here, however, that the high mean value obtained for Seyfert 1 is caused by a selection effect induced by the energy coverage of the MECS+PDS instruments (2-100 keV). Moreover, if one considers the *XMM-Newton* sample, it is obtained that $\sim 30\text{--}50\%$ of type II Seyfert galaxies are Compton-thick in agreement with what found by Risaliti et al. 1999.
- evidence of a X-ray Baldwin effect is found in Seyfert 1 galaxies included in the *BeppoSAX* sample and when the EW of the FeK α line is plotted against

the 20-100 keV luminosity.

These results are well in agreement with the basic assumptions of the UM for AGN (Antonucci 1993). No differences are measured in the observables that are supposed to be isotropic while the absorbing column seems to be the only discriminator between the different types of Seyfert galaxies. This is reflected also in the properties of the FeK α line. No difference is measured in the line centroid (see Table 3.4) between the two classes of Seyfert galaxies. Type II objects, however, display more intense features (EW=222 \pm 33 eV for Seyfert 1 and EW=693 \pm 195 eV for Seyfert 2). The physical origin of the X-ray “Baldwin effect” here measured for Seyfert 1 using the 20-100 luminosity is unclear. Both light bending (Miniutti & Fabian 2004) and torus models (Page et al. 2004) are consistent with the present data even if the strong relation of the FeK α line EW in type II objects with the absorption column indicates that most of the narrow line component should be due to the torus.

Finally, considering the *XMM-Newton* sample one can infer that the Seyfert galaxies as a whole possess the entire range of N_H , from 10^{20} cm $^{-2}$ to 10^{24} cm $^{-2}$, fairly continuously. This is similar to what was found in the deepest X-ray surveys available to date (Mateos et al. 2005), and it is consistent with local absorption distributions adopted by, e.g., La Franca et al. (2005) to fit the hard X-ray luminosity functions of AGNs.

Chapter 4

The X-ray emission mechanism

Figure 4.1 (see next page) shows the 2-10 keV luminosity distributions recorded for the *XMM-Newton* sample. It is worth recalling here that this sample is supposed to be un-biased and complete. Thus it is assumed to represent the *intrinsic* picture of the Seyfert galaxies in the local Universe.

As such, it is quite surprising that, despite the corrections for the known CT sources (i.e. the sources for which the observed emission is heavily depressed by the intervening and obscuring matter), there are sources extremely weak with $L_{2-10keV} \sim 10^{38}$ erg s⁻¹. It is worth noting here that this luminosity is of the order of what expected for neutron stars accreting at the Eddington limit while the mass of the accretors considered here ranges between 10^6 - $10^8 M_{\odot}$ (see table b.2). This evidence clearly indicates that the efficiency of the emission mechanism can be extremely low as, for example, happens for ADAF-like accretion systems.

Here, the origin of the X-ray photons is investigated trying to discriminate the emission mechanism effectively working and its efficiency. To do that, I will take advantage of the *BeppoSAX* and *X-CfA* samples since they are numerous enough to allow good statistical tests. Moreover, I will take advantage of a multi-frequency approach.

4.1 The emission mechanism

In §3.5 it has been shown how the selection effects may introduce unphysical correlations between observables obtained studying the X-ray spectra of nearby

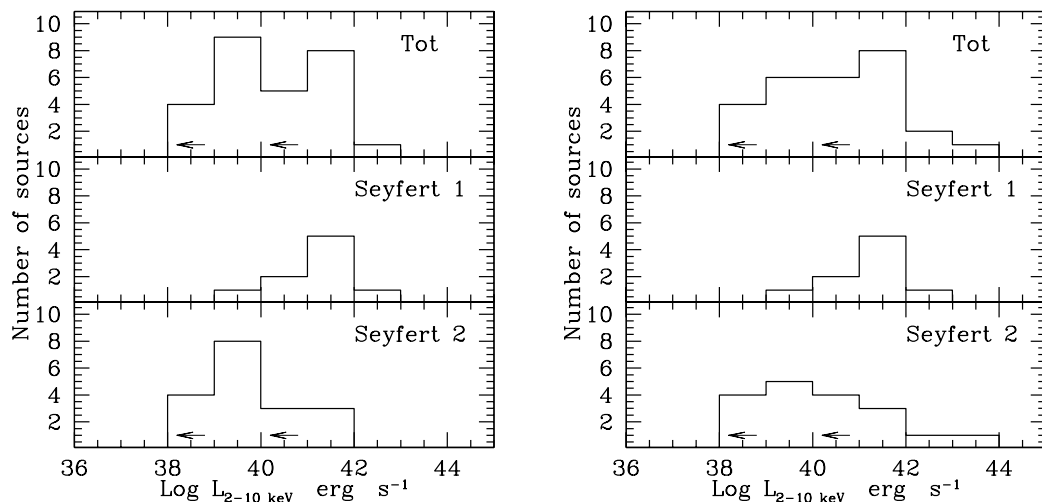


Figure 4.1: Distribution of the 2–10 keV luminosities before (left) and after (right) correction for Compton-thick candidates (after Table 3.3). Upper limits have been indicated with arrows.

Seyfert galaxies. False correlations may be also caused by the degeneracy between parameters during the fitting procedures. This is the case, for example, of the photon index with the column density for low statistics observations. In that case, one could obtain similar descriptions of the observed spectrum with *flat* (small Γ) and low N_H power-law and/or with a *steep* (large Γ) and highly absorbed power-law. The same could happen for the determination of R and E_c , since R introduces in the spectrum a bump peaking between 20–40 keV and declining at higher energies where the E_c may appear. To check if the results presented here are affected by such effects, the correlations between these parameters have been studied and the results are presented in Figure 4.2.

The left panel of Figure 4.2 shows how, on average, the estimate of Γ is not affected by the simultaneous determination of the absorbing column. No trend is observed between Γ and N_H . Obviously, this does not imply that this is true for each single source included in the original sample. On the other hand, this is an expected result since the broad band of *BeppoSAX* should reduce this spurious effect. Similar results are obtained also when the Γ vs. E_c , and R vs. E_c (center panel of Figure 4.2) relations are investigated. In these cases the Spearman ρ and Kendall's τ tests do not support the existence of a relation between these quantities

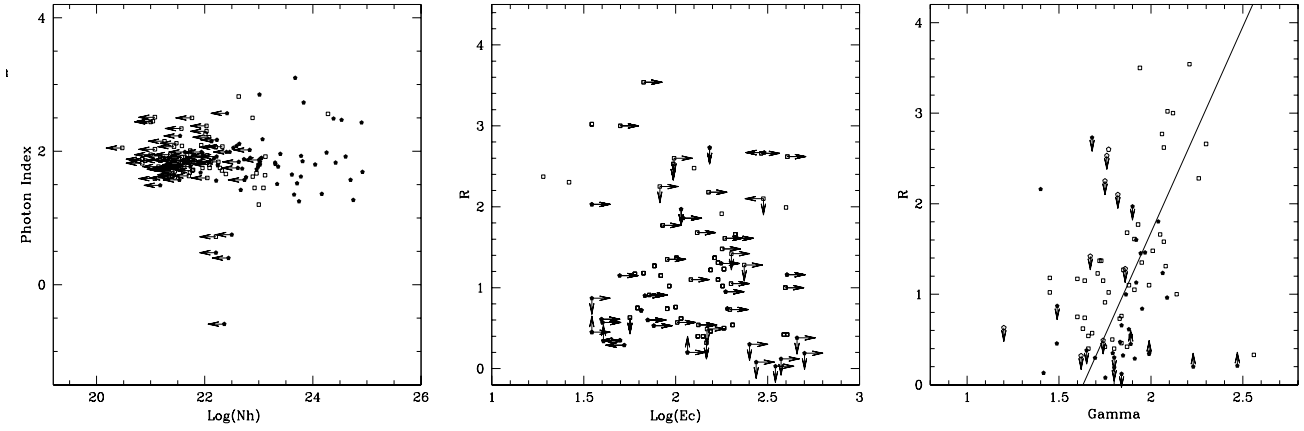


Figure 4.2: *Left panel:* Photon index Γ plotted versus the measured N_H (in units of cm^2). No significant trend relating these two quantities is found; *center panel:* R vs. E_c (in units keV), no correlation is found between these quantities; *right panel* R vs. Γ . The two quantities are correlated with a high significance level ($P_{null} \leq 1\%$). The line is the linear regression best fit.

($P_{null} \sim 15\%$). All these indications suggest that, if any, the possible degeneracy in the fitting procedure did not introduce strong spurious relations between the spectral parameters.

However a strong correlation ($P_{null} \leq 0.01\%$) is recorded between Γ and R (that are linked by the following relation):

$$R = (4.54 \pm 1.15) \times \Gamma - (7.41 \pm 4.51) \quad (2)$$

It is hard to determine if this correlation is the result of a systematic effect since it is possible that these two quantities degenerate in the fitting procedure. A flat power-law with small reflection could be described also by a steep power-law plus strong reflection. The absence of similar correlations between Γ and E_c and R vs. E_c seems to suggest that this correlation is real.

A similar relation was previously found using *Ginga* and *RXTE* data (Zdziarski, Lubinski, & Smith 1999; Gilfanov, Churazov & Revnivtsev 1999). Zdziarski, Lubinski, & Smith (1999) interpreted this as evidence of thermal Comptonization as the origin of X-rays providing that the optical-UV seed photons were mainly produced by the same material responsible for the reflected component. In this case

the cooling rate of the hot corona is directly linked to the power-law slope. But the cooling rate is also related to the angle subtended by the reflector. This result is also in agreement with predictions of models that consider mildly relativistic outflows driven by magnetic flares (Beloborodov 1999). In general, Merloni et al. (2006) demonstrated that any geometry in which the hot, X-ray emitting plasma is photon starved (i.e. geometries of the accreting systems in which the accretion disk is only partially covered by the Comptonizing plasma such as patchy coronae, inner ADAF plus outer disks etc.) will produce hard X-ray spectra, little soft thermal emission and a weak reflection component. On the other hand, geometries corresponding to a very large covering fractions of the cold phase have strong soft emission, softer spectra and strong reflection fractions (Collin-Souffrin et al. 1996). Thus, moving along the Γ vs. R relation implies moving from lower to higher accreting systems.

The findings on the emission mechanism based on the data of the *BeppoSAX* sample may be, thus, summarized as follow:

1. the accretion region is characterized by the presence of cold matter most probably due to cold gas (see the detection of reflecting matter §3);
2. the Γ vs. R relation left space to mixed systems in which the accretion flow switch from standard accretion disk to ADAF modes in the inner regions of low luminosity objects.

4.2 The multiwavelength characteristics of the *X-CfA* sample

As stated at the beginning of §4, the objects included in the *X-CfA* sample¹ have been detected down to $L_{2-10keV} \sim 10^{38}$ erg s⁻¹. Nonetheless, since the detection of an X-ray nucleus in almost all the sources, it is possible to assess that there is a strong evidence in favour of the presence of an AGN even at very low luminosities.

¹It is worth recalling here that the *XMM-Newton* sample for which the 2-10 keV luminosity distribution is presented in Figure 4.1 is a sub-sample of the *X-CfA* sample.

4.3 Picking-up Compton-thick and Starburst dominated objects

As shown in §3.4, within X-ray selected samples of Seyfert galaxies can be present deeply absorbed objects not classified as such from the X-ray modelling: i.e. the so-called Compton-thick ones. To catch these sources into the CfA sample, I have taken advantage of the same powerful diagnostic tool described in §3.4 (Bassani et al. 1999) adding also the diagnostic indicator introduced by Panessa & Bassani (2002) to pick-up the sources with strong starburst contribution.

A flux diagram is presented in Fig. 4.3. All far-infrared fluxes are based on IRAS data derived from HFS97. The $[OIII]\lambda 5007$ flux of each galaxy has been corrected for extinction (HFS97). Type I objects are plotted as filled polygons, type II as empty polygons and 'mixed Seyferts' as crosses. Compton thick candidates, as discussed below, have been marked with stars. Discriminating values, chosen for SB (starburst), Compton thick and Compton thin regions, are given as in Panessa & Bassani (2002).

Most of the sources of both types lie in the AGN region and only a small fraction are located at the boundary between AGN and Starburst. Indeed, the X-ray analysis of most of the CfA sample objects has shown that they host an AGN (Panessa 2002). The positions of the few borderline objects in the diagram of Figure 4.3 could be due to the low IRAS angular resolution², i.e. the presence of enhanced star-forming regions in the host galaxy may contribute significantly to increase the IR flux in these Seyferts; this translates into $F_{[OIII]}/F_{IR}$ ratios smaller than that of the AGN alone. For example, NGC 5033 is known to host bright HII regions in the inner parts of its spiral arms (Pérez García & Rodríguez Espinosa 1998); in NGC 4639 (González-Delgado et al. 1997) as well as in NGC 4725 (Sandage & Bedke 1994) many bright HII regions have been observed, while NGC 3031 is known to host a very strong underlying stellar continuum (Alonso-Herrero et al. 2000).

As shown in §3.4, to identify Compton thick sources, the $F_X/F_{[OIII]}$ ratio has been considered: the most populated region is that of Compton thin AGN where all broad line Seyferts and 17 type II objects are located while the remaining Seyfert

²Note that infrared data have been taken using a beam size of $\sim 8'$, while optical and X-ray data are derived using much smaller apertures, i.e. $\sim 1''$ and $\sim 2''$ - $25''$ respectively.

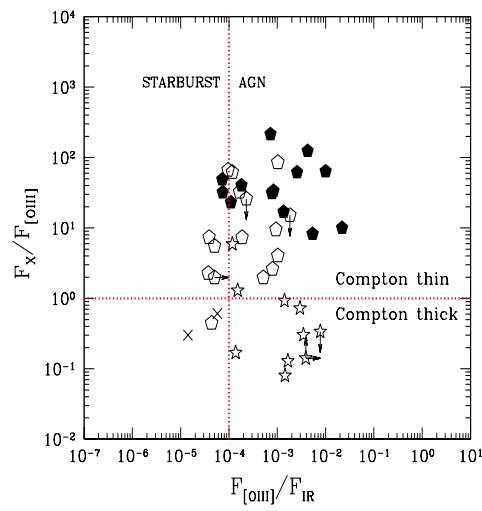


Figure 4.3: $F_X/F_{[OIII]}$ vs. $F_{[OIII]}/F_{IR}$ diagram. Compton thin, Compton thick and starburst regions have been separated by dashed lines. Type 1 objects are plotted as filled polygons, type 2 as empty polygons, 'mixed Seyfert' objects as crosses and Compton thick candidates as stars.

2 galaxies lay in the Compton thick region. As a matter of fact, four out of six known Compton thick sources, namely NGC 1068, NGC 1667, NGC 2273 and NGC 5194, occupy this region confirming the reliability of this diagnostic diagram, while NGC 3079, a Compton thick source, is above the Compton thick boundary, probably because of the presence of filaments in its nuclear region whose emission contributes significantly in the 0.1-6.5 keV range (Cecil et al. 2002). There is a group of Compton-thick source candidates, namely NGC 676, NGC 1167, NGC 3185, NGC 3982 and NGC 7743, for which X-ray spectral analysis alone cannot draw a conclusion. No FIR data are available for NGC 3489 (not in the plot), which has been here classified as Compton thick from its $F_X/F_{[OIII]}$ ratio (0.63).

Objects with an uncertain behaviour constitute a small fraction of the Seyfert 2 sample (7 out of 34, marked with a "?" in Table B.2). Most of these objects, placed on the SB region of the diagram, may even not contain an AGN. Actually, NGC 1058, NGC 3627 and NGC 3486 only have upper limits in X-rays.

In summary, a sub-sample of 11 secure Compton thick candidates have been recognized (they have been marked with a \checkmark in Col. 6 of Table B.2); these objects are all Compton thick according to the flux diagnostic diagram and in five cases this indication is supported by a strong Fe line of a > 1 keV equivalent width, i.e. NGC 1068 (Matt et al. 1997), NGC 1667 (Bassani et al. 1999), NGC 2273 (Maiolino et al. 1998), NGC 3079 (Cecil et al. 2002) and NGC 5194 (Terashima & Wilson 2001)³.

These tools have revealed that the fraction of objects which may be affected by Compton thick obscuration among type 2 Seyferts ranges from 30% (if only the secure Compton thick sources are considered) up to 50% (if also objects with an uncertain behaviour are Compton thick sources) in agreement with previous estimates available for a flux-limited sample (Risaliti et al. 1999).

The X-ray luminosities of Compton thin sources (both type I and type II Seyferts) have been corrected for the column density measured from the 2-10 keV spectra. Assuming that all the secure candidates are actually Compton thick, then their intrinsic column density should be higher than $\sim 10^{24}$ cm⁻². This prevents any possibility to directly measure the intrinsic X-ray luminosity in the 2-10 keV band, since the latter is completely blocked by the absorbing matter and the observer can only

³Note that in the other six cases, the non detection of an Fe line could be due to the poor statistics of the X-ray spectra.

measure a reflected/scattered component, if any. Therefore, to estimate the intrinsic X-ray luminosity, the observed one has been incremented by a factor of 60. This value has been obtained by means of the $F_{2-10keV}/F_{[OIII]}$ ratio: the mean value of this ratio has been calculated for our type 1 objects ($\text{Log } \langle F_{2-10keV}/F_{[OIII]} \rangle \sim 1.74 \pm 0.49$) and for the five known CT sources ($\text{Log } \langle F_{2-10keV}/F_{[OIII]} \rangle \sim -0.03 \pm 0.07$). The difference between these mean values can be considered as an approximate value of the correction factor when estimating the intrinsic luminosity of the Compton thick sources, i.e., $\langle F_{2-10keV}/F_{[OIII]} \rangle_{Type1} / \langle F_{2-10keV}/F_{[OIII]} \rangle_{Type2,CTthick} \sim 60$, hereafter I refer to CT corrected X-ray luminosities. In Table B.2, X-ray luminosities for the sample sources have been corrected for the intrinsic absorption measured from their X-ray spectra, while for Compton thick candidates, it was applied the above correction factor. Although the latter should be considered as an indicative value, it is however in tune with what observed with BeppoSAX in Circinus Galaxy (Matt et al. 1999) and NGC 4945 (Guainazzi et al. 2000). Moreover, in the case of NGC 1068, Iwasawa, Fabian, & Matt (1997) estimate the intrinsic luminosity to be in the range of $10^{43} - 10^{44}$ erg/s which is a factor of 100-1000 higher than the observed luminosity. This large correction factor is also theoretically justified by the torus model proposed by Ghisellini, Haardt & Matt (1994), in which they derive, a correction factor ranging from 100 to 2×10^3 depending on the amount of absorption and on the viewing angle with respect to the obscuring torus. Finally, it is worth noticing that before correcting the X-ray luminosity for the Compton thick sources, type I and type II Seyfert galaxies show a different distribution in luminosities (with KS test $P_{null}=0.001$), type II objects have lower luminosities than type I objects. After correcting for Compton thick sources, the KS probability is reduced to 0.05.

4.4 The X-rays and the Optical emission line characteristics

A convincing way to investigate the activity of the central source is through the observed correlations between X-ray and optical emission line luminosities since a proportionality between these quantities is expected in AGN. In luminous sources strong correlations between H_α , H_β , $[OIII]_{\lambda 5007}$ luminosities and X-ray

luminosities have already been found (Elvis, Soltan & Keel 1984, Ward et al. 1988, Mulchaey et al. 1994).

It is worth investigating whether this correlation holds in the present samples as well, and, in particular, in the *X-CfA* sample since it is expected to be complete and it is known to reach the low luminosities recorded also in the *XMM-Newton* sample (that is an *X-CfA* sub-sample). This kind of analysis can be used to further test whether the same physical processes occurring in luminous AGN are also in action in their low luminosity counterparts.

To characterize quantitatively an apparent correlation between two properties of the sample under study I apply a linear regression statistical procedure. Here I have used the EM (Expectation-Maximization) algorithm since it deals with censored data; this algorithm, as the other used for the analysis of the spectral parameters of the *BeppoSAX* sample, is implemented in the ASURV package (Isobe, Feigelson & Nelson 1986).

Table 4.1 shows the statistical properties of the correlations. As usual, the sample has been grouped in sub-classes (type I and type II); here quasar samples (as described below) have been added to the analysis.

4.4.1 X-ray vs. H_{α} luminosity

A strong positive correlation between the X-ray and the H_{α} emission line luminosity has been widely observed in classical AGN, such as Seyferts and quasars (Ward et al. 1988) and in low luminosity AGN, such as LINERs (Terashima, Ho & Ptak 2000, Ho et al. 2001). It has been shown that this correlation is not an artifact of distance effects. Typical ratios observed in bright objects are $\text{Log}(L_X/L_{H\alpha}) \sim 1-2$, supporting the idea that optical emission lines arise in gas photoionized by the central nucleus.

In Fig. 4.4 the logarithm of the 2-10 keV luminosity has been plotted versus the $\log L_{H\alpha}$, the latter including both the narrow and broad (if present) components of the line, corrected for extinction due to the Galaxy and to the narrow-line region (Ho, Filippenko & Sargent 1997). The X-ray luminosities are from this work (Table B.2) without (left panel) and with (right panel) correction applied to Compton thick candidates. A sample of low- z quasars from Ward et al. (1988) has also been included to compare our results with high luminosity objects (luminosities have

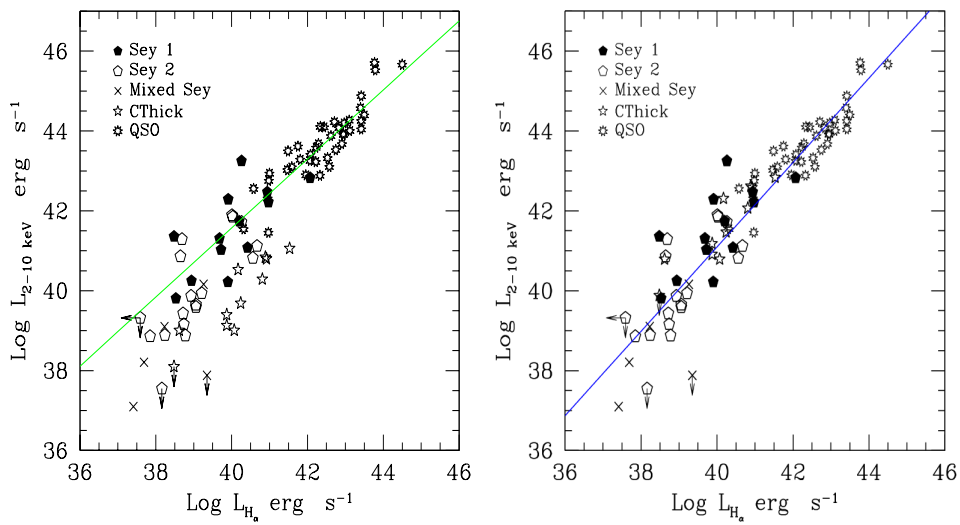


Figure 4.4: Left panel: Log of 2-10 keV luminosity versus log of H_{α} luminosity (narrow+broad components) corrected for the Galactic and NLR extinction. The dotted line shows the best fit linear regression obtained by fitting type I Seyferts and low- z quasars from Ward et al. (1988). Right panel: the same plot using the 'Compton thick' corrected luminosity. The solid line shows best fit linear regression line obtained by fitting the total sample of Seyfert galaxies and the low- z quasars. Filled polygons are type I Seyfert, open polygon sare type II Seyfert, 'mixed Seyfert' objects are indicated as crosses, Compton thick candidates are stars and low- z quasars are 'rounded-stars'.

been adjusted to $H_0 = 75 \text{ km s}^{-1} \text{ Mpc}^{-1}$). Each class of AGN has been marked with different symbols: filled polygons are type I Seyfert, open polygons are type II Seyferts, crosses are 'mixed Seyferts', stars are the Compton thick candidates and rounded-stars are low- z quasar objects.

First, I checked whether a correlation is present among our Seyfert sample. As reported in Table 4.1, a strong correlation is found in the sample. I fitted type I Seyferts and low- z quasar objects in order to compare objects with broad+narrow component of the H_α line. The solid line in the left panel of Figure 4.3 represents the best-fit linear regression line obtained here. This correlation is highly significant (Spearman's $\rho=0.93$), although type I Seyferts in the CfA sample show a larger scatter than the low- z quasars. Note that the X-ray and H_α data have not been taken simultaneously. Consequently, the strong X-ray flux variability observed in most type Seyfert Is (see for example the cases of NGC3516, Guainazzi et al. 2001; NGC 4051, Guainazzi et al. 1998, Lamer et al. 2003 and Ponti et al. 2006; NGC4151, Czerny et al. 2003b, NGC4395, Iwasawa et al. 2000) is a likely source of scatter. At lower luminosities, Seyfert 2 galaxies and 'mixed Seyferts' show $L_X/L_{H\alpha}$ ratios lower than type I and low- z quasars. Note, however, that here type I objects which have both narrow and broad H_α line components are compared Seyfert 2 galaxies which lack the broad H_α component.

On the right panel of Figure 4.4, the 2-10 keV luminosity of Compton thick candidates has been corrected. Again, the solid line is the best-fit regression line obtained by fitting the total Seyfert sample and the low- z quasar sample. This regression line is consistent with that found by Ho et al. (2001) using the same low- z quasar sample and a sample of LLAGN observed with *Chandra*.

The correction in the X-ray luminosity of CT sources significantly reduces the scatter at low luminosities and the inclusion of type II Seyferts in the calculation of the regression line results in a steeper slope with respect to those of type I and low- z quasars. The steepening of the regression line is probably enhanced by those Compton thin type 2 objects at low luminosities, which show an optical excess emission with respect to the X-ray luminosity. The latter could be due to the contribution given by a circumnuclear starburst to the $H\alpha$ emission which is more important in low luminosity sources than in high luminosity ones, where the emission is completely dominated by the AGN.

The same correlation using fluxes is shown in Fig. 4.5 ($\rho=0.78$, $P_{null} < 0.001$)

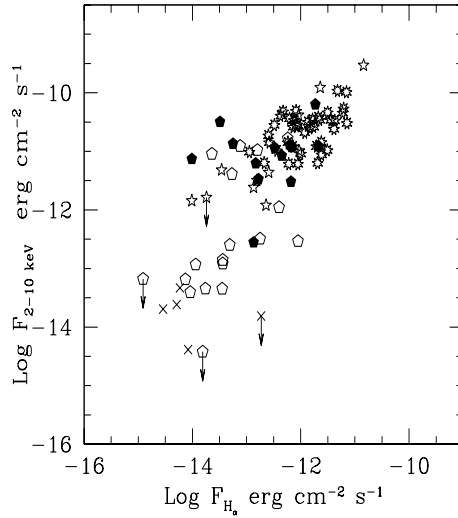


Figure 4.5: Correlation between 2-10 keV versus H_α fluxes. H_α narrow+broad components are corrected for the Galactic and NLR extinction. Symbols as in Fig. 4.4

strongly supporting that the luminosity-luminosity correlation is not due to distance effects.

It is remarkable that the present sample traces the $L_X - L_{H\alpha}$ relation for luminosities typical of luminous AGN ($10^{41} - 10^{43} \text{ erg s}^{-1}$) down to low luminosities typical of LINERs ($10^{37} - 10^{40} \text{ erg s}^{-1}$). The strong correlation observed between $L_X - L_{H\alpha}$ suggests that the dominant ionization source in our sample is photoionization by an AGN and that optical/UV photons are somehow linked to the X-ray emission. A few objects at 2-10 keV luminosities of $\sim 10^{38} \text{ erg sec}^{-1}$ appear to be systematically under the correlation. Three out of four of these sources are actually those classified as 'mixed Seyfert', i.e. NGC 2683, NGC 3627 and NGC 6503; moreover for NGC 1058 and NGC 3627 only an upper limit to the X-ray luminosity is available.

If the ionization mechanism of the emission lines is due to or enhanced by hot stars or shocks, the resulting $L_X/L_{H\alpha}$ ratio is expected to be accordingly smaller compared to those of AGN. Indeed, Pérez-Olea & Colina (1996) have shown how the $L_X/L_{H\alpha}$ ratio in AGN is larger than in starbursts up to a factor of ~ 100 inde-

pendently on the intrinsic luminosity or activity level. This could be a possible scenario for these sources which, from the diagnostic diagrams (Figure 4.3), have been recognized as our most probable starburst candidates. However the presence of a very faint/heavily obscured AGN in such objects cannot be ruled out. These objects could be what have been defined as 'Elusive AGN' (Maiolino et al. 2003), i.e. objects in which the nucleus is heavily obscured and there are no optical evidences for the presence of an AGN.

4.4.2 X-ray vs. $[\text{OIII}]_{\lambda 5007}$ luminosity

As previously discussed in §3.4 and §4.2, the $[\text{OIII}]_{\lambda 5007}$ emission line is thought to be an isotropic indicator in the UM scenario and should, therefore, be representative of the intrinsic power of the central engine. Although the properties of $[\text{OIII}]_{\lambda 5007}$ have been widely investigated in the literature, the L_X vs. $L_{[\text{OIII}]}$ correlation itself has been poorly studied. Mulchaey et al. (1994) have found a strong correlation between the emission line flux and the observed UV continuum in type I Seyferts, while no correlation was observed in type II Seyferts. This finding is in agreement with the torus model, where the UV photons are scattered while the line emission is produced by a directly viewed component. However these authors made use of an heterogeneous sample and did not take into account the presence of Compton thick sources. More recently, Heckman et al. (2005) have found that L_X and $L_{[\text{OIII}]}$ are well correlated in a sample of hard X-ray selected AGN (both type I and type II). They also found that for a sample of $[\text{OIII}]$ flux selected sources, the correlation L_X vs. $L_{[\text{OIII}]}$ for type I objects is consistent with that found in the type I hard X-ray sample. However, the type II objects spread a much wider range in the luminosity ratio and many of them are very weak in hard X-rays.

In Fig. 4.6 the 2-10 keV luminosity (without correction for Compton thick sources, left panel, and with correction, right panel) measured for the CfA sources is plotted versus their $[\text{OIII}]_{\lambda 5007}$ luminosity (corrected for the Galactic and NLR extinction, Ho, Filippenko & Sargent 1997). Two comparison samples of bright AGN have been included in the analysis chosen for having both X-rays and $[\text{OIII}]_{\lambda 5007}$ fluxes available: 1) a sample of luminous type 1 Seyfert galaxies (hereafter QSO) from Mulchaey et al. (1994); 2) a sample of PG quasars (hereafter PG) from Alonso-Herrero et al. (1997) (luminosities have been adjusted to $H_0 = 75 \text{ km s}^{-1}$

Table 4.1: Correlation statistics in luminosities

Variables (1)	Sample (2)	N (3)	X(ul) (4)	Y(ul) (5)	rho (6)	Prob. (7)	a (8)	b (9)
Log L_X vs Log $L_{H\alpha}$	Tot	47	1	4	0.82	<0.001	1.20±0.12	-6.82±4.82
Log L_X vs Log $L_{H\alpha}$	S1	13	0	0	0.68	0.019	0.74±0.21	12.12±8.34
Log L_X vs Log $L_{H\alpha}$	S2	34	1	4	0.83	<0.001	1.28±0.14	-10.04±5.61
Log L_X vs Log $L_{H\alpha}$	Tot+QSO ^a	87	1	4	0.95	<0.001	1.06±0.04	-1.14±1.78
Log L_X vs Log $L_{H\alpha}$	S1+QSO ^a	53	0	0	0.93	<0.001	0.86±0.05	6.98±2.08
Log L_X vs Log $L_{[OIII]}$	Tot	45	1	4	0.88	<0.001	1.22±0.11	-7.55±4.33
Log L_X vs Log $L_{[OIII]}$	S1	13	0	0	0.93	<0.001	0.86±0.09	6.99±3.51
Log L_X vs Log $L_{[OIII]}$	S2	32	1	4	0.86	<0.001	1.34±0.15	-12.32±5.80
Log L_X vs Log $L_{[OIII]}$	Tot+QSO ^b	66	1	4	0.93	<0.001	1.22±0.06	-7.34±2.53
Log L_X vs Log $L_{[OIII]}$	S1+QSO ^b	34	0	0	0.83	<0.001	0.95±0.07	3.87±2.76

Notes: Statistical properties of the 'Compton thick' corrected 2-10 keV X-ray luminosity versus H_α and [OIII] λ 5007 luminosities; Col. (1): Variables X and Y; Col. (2): Subsample considered: Tot = total Seyfert sample, S1 = Seyfert 1 galaxies, S2 = Seyfert 2 galaxies; QSO^a= low-z quasars (Ward et al. 1988); QSO^b= bright type 1 Seyfert (Mulchaey et al 1994) + PG quasars (Alonso-Herrero et al. 1997); Col. (3): number of objects; Col. (4)-(5): Number of upper limits in variable X and Y; Col. (6-7) Spearman's rho correlation coefficient and the associated probability P for accepting the null hypothesis that there is no correlation; Col. (8)-(9): Correlation coefficient of the best fit linear regression line calculated using EM algorithm (Isobe, Feigelson & Nelson 1986), $Y=a \times X + b$.

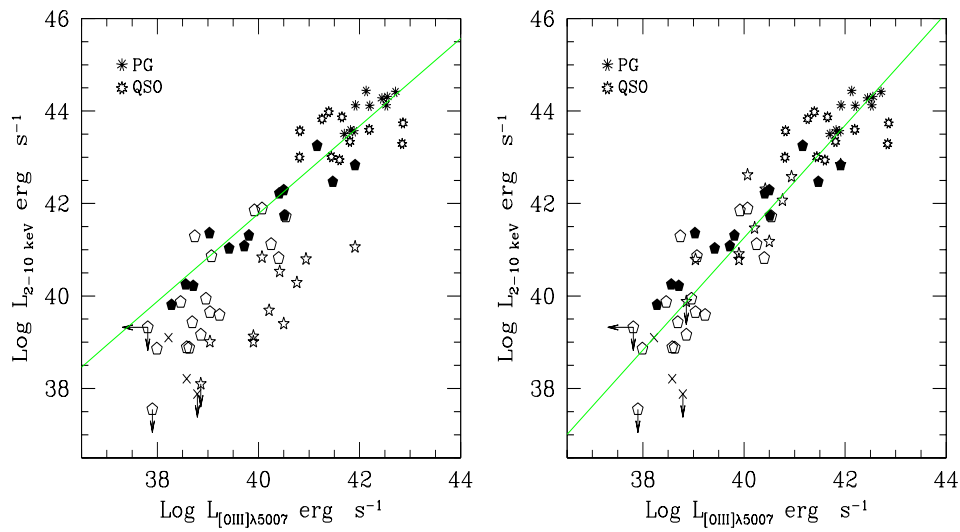


Figure 4.6: Left panel: Log of 2-10 keV luminosity versus log of $[OIII]_{\lambda 5007}$ luminosity corrected for the Galactic and NLR extinction. The solid line shows the best fit linear regression line obtained by fitting type 1 Seyfert, a sample of bright type 1 Seyferts (QSO, Mulchaey et al. 1994) and a sample of PG quasar (PG, Alonso-Herrero et al. 1997). Right panel: the same plot using 'Compton thick' corrected luminosity. The solid line shows our best fit linear regression line for the total sample of Seyfert galaxies, the PG quasars and bright type 1 Seyfert. Symbols are as in Fig. 4.4

Mpc⁻¹). The two chosen samples of luminous AGN are not meant to be complete and biases against low luminosity objects are probably introduced. However the low luminosity ranges are covered by the *X-CfA* sample and they are just taken as representatives of the class of luminous sources.

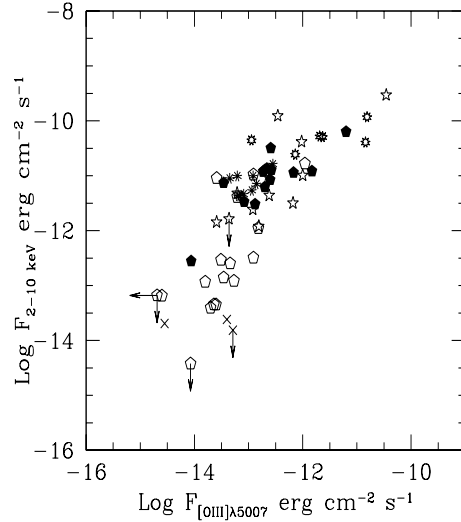


Figure 4.7: Correlation between log of 2-10 keV versus log of [OIII]_{λ5007} fluxes, the latter corrected for the Galactic and NLR extinction.

The solid line in the left panel of Fig. 4.6 is the best fit linear regression line obtained by fitting type I Seyferts, the QSO sample and the PG sample. Contrary to what is obtained in the L_X vs. $L_{H\alpha}$ relation, most of the scatter here is introduced by QSOs, while type I Seyferts of the *X-CfA* sample follow a tighter correlation. There is a clear separation between type I and type II Seyferts. Once I correct the X-ray luminosity assuming the presence of CT sources, the correlation between the two luminosities is tighter as shown in the right panel of Fig. 4.6 in which the best fit linear regression line for the total sample, the QSO and PG samples is overplotted. As also found in the L_X vs. $L_{H\alpha}$ correlation, the slope of the regression line is steeper with respect to those obtained for only type I and low-*z* quasars. At low luminosities, a possible contribution by a circumnuclear starburst to the [OIII] emission could explain the excess of the [OIII] luminosity with respect to the X-ray one observed in a few sources. Actually, at very low luminosities, the same sources

which lay below the correlation in the X-ray vs H_α plot, lay also below the L_X vs. $L_{[OIII]}$ relation (e.g., NGC 1058, NGC 2683 and NGC 3627). The X-ray versus [OIII] correlation still holds in the flux-flux plot of Fig. 4.7 ($\rho=0.78$, $P_{null} < 0.001$). As for the H_α luminosity, also the $[OIII]_{\lambda 5007}$ flux appears to be a good tracer of the AGN power, and both correlations are good tools to estimate the expected X-ray luminosity. The following relations are obtained for $X-CfA$ sample:

$$\log L_X = (1.06 \pm 0.04) \log L_{H_\alpha} + (-1.14 \pm 1.78)$$

$$\log L_X = (1.22 \pm 0.06) \log L_{[OIII]} + (-7.34 \pm 2.53)$$

4.5 M_{BH} and Eddington ratios for the $X-CfA$ sample

Black hole mass (M_{BH}) estimates are available for 44 out of 47 objects in the $X-CfA$ sample (col 9, Table B.2). The M_{BH} obtained from the literature, have been estimated in different ways from gas, stellar and maser kinematics to reverberation mapping or inferred from the mass-velocity dispersion correlations (Ferrarese 2002, Tremaine et al. 2002). For a group of objects stellar velocity dispersions are available from di Nella et al. (1995), Barth et al. (2002) and McElroy (1995), and the M_{BH} has been here calculated using the Tremaine et al. (2002) relation. All the M_{BH} estimates are reported in Table B.2, with the method used to calculate them and the corresponding reference.

As shown in Fig. 4.8 (left panel), black hole masses are fairly sampled from $\sim 10^5$ to $10^8 M_\odot$ with a peak at $10^{7-8} M_\odot$; this figure further indicates that type I and type II Seyferts show a similar distribution. Woo & Urry (2002) presented a large compilation of black hole masses, for an heterogeneous sample of 234 AGN, ranging from $\sim 10^6$ to $\sim 10^{10} M_\odot$. From a comparison of different methods in estimating M_{BH} , they found that M_{BH} values estimated from reverberation mapping and stellar velocity dispersion are those more reliable. Uncertainties in M_{BH} estimates for the $X-CfA$ sample are probably introduced by the scatter in the mass-velocity dispersion correlations and are typically of the order of 0.3-0.5 dex. I refer to the above mentioned papers for a detailed description of the different methods used to estimate M_{BH} and the relative errors associated to these measurements.

The L_{Bol}/L_{Edd} ratio distribution is plotted in the right panel of Fig. 4.8. To calculate the bolometric luminosity I have assumed that $L_{Bol}/L_{2-10keV} \sim 30$. The latter

value is typical of luminous AGN, being normally in the range of 25-30 (Risaliti & Elvis 2004, Elvis et al. 1994). However, it must be kept in mind that the bolometric luminosity here is just a multiple of the X-ray luminosity, while it really depends on the shape of the spectral energy distribution which could differ among high and low luminosity AGN (Ho 1999, Marconi et al. 2004); actually, in LLAGN, the observed $L_{Bol}/L_{2-10keV}$ ratio ranges from 3 to 16 (Ho 1999). The L_{Bol}/L_{Edd} ratio distribution for the total Seyfert sample covers a wide range of Eddington ratios going down to 10^{-7} . If a $L_{Bol}/L_{2-10keV}$ ratio of 10 is considered, then Eddington ratios would be a factor of 3 lower than those in Fig. 4.8. The distribution of type I objects has been marked with a shaded region. It is interesting to note that a Kolmogorov-Smirnov test gives a probability of 0.01 for the type I and type II sub-samples of being drawn from the same parent population, suggesting that type II objects are accreting at lower Eddington ratios with respect to type I Seyfert galaxies. However, there are some caveats to take into account: i) the KS probability of the type I and type II X-ray luminosity distribution is 0.05, consequently affecting the bolometric luminosity distributions; ii) as already pointed out, the bolometric correction could be not a constant, depending for example on luminosity and therefore could change from object to object; iii) objects with an uncertain behaviour, those in which the star-formation probably dominates, have been included in the type II class. As a matter of fact, if 'mixed Seyferts' are excluded from the type II sub-sample, the KS probability of the L_{Bol}/L_{Edd} ratio distributions is 0.05. Moreover, it is possible that with the present data I am not able to detect all the absorbed low luminosity type 2s, e.g. Compton thick sources not recognized to be such by the diagnostic tools and/or objects with part of the X-ray emission absorbed by parsec scale clumpy material detected in a low N_H state (see §3.4, and the case of NGC 4388, Elvis et al. 2004).

However, if a trend of type II Seyfert galaxies having lower Eddington ratios than type I ones is present, this would have several interesting implications: for example it would nicely confirm a model proposed by Nicastro (2000) that relates the formation of the broad emission lines of active galactic nuclei to the accretion rates, i.e. for very low accretion rates the BLR would no longer exist. More data are needed to have a complete sample and statistically confirm these findings.

In Fig. 4.9, Compton thick corrected X-ray luminosities have been plotted against black hole mass. No correlation is found between these two parameters.

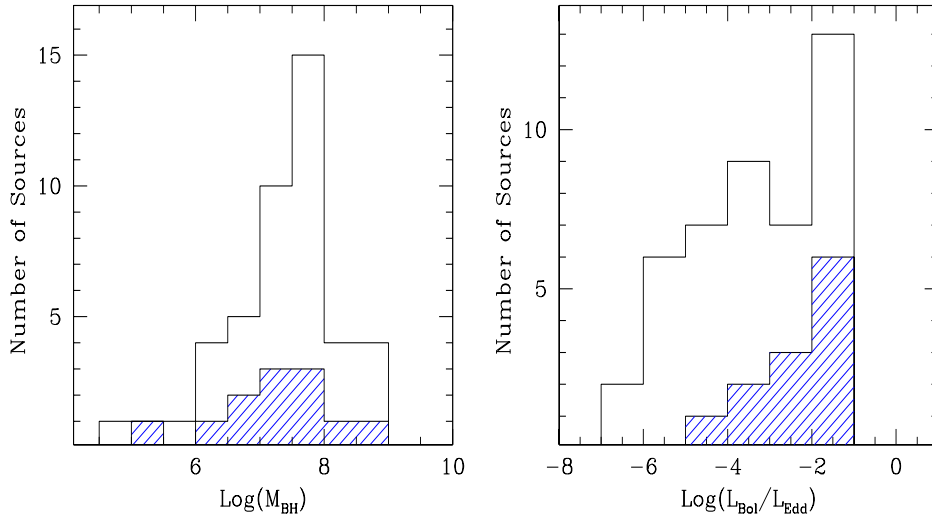


Figure 4.8: Left panel: Distribution of the log of black hole masses in unit of solar masses . Right panel: Distribution of the log of L_{Bol}/L_{Edd} ratio, assuming that $L_{Bol}/L_X \sim 30$. In both panels the shaded areas represent the distribution of type 1 Seyferts only.

The same considerations can be applied when H_α and [OIII] luminosities are plotted against M_{BH} , i.e. no correlation with M_{BH} is observed, which is an expected result given the correlation of these quantities with the X-ray luminosity. Some previous studies found a correlation between the AGN luminosity and M_{BH} (Koratkar & Gaskell 1991, Kaspi et al. 2000), however this result is in agreement with that found by Pellegrini (2005) for a sample of SMBH in the local universe for which Chandra nuclear luminosities were available. Also Woo & Urry (2002) found no correlation between bolometric luminosity and black hole masses. Interestingly, neither is radio emission correlated to black hole mass in nearby nuclei (Ho 2002).

I have over-plotted L_X as a function of M_{BH} for Eddington ratios of 1.0, 0.01 and 10^{-4} (solid lines in Fig. 4.9). Woo & Urry (2002) have shown that bright local AGN normally show Eddington ratios which span three orders of magnitude down to $L_{Bol}/L_{Edd} \sim 10^{-3}$, while at higher redshifts the Eddington ratios distribution is narrower, i.e. L_{Bol}/L_{Edd} peaks at around 1/3 with a dispersion of 0.3 dex rms, as recently shown by Kollmeier et al. (2005) for a sample of AGN discovered in the AGES Survey covering a redshift range of 0.3-4. Indeed, most of the X -

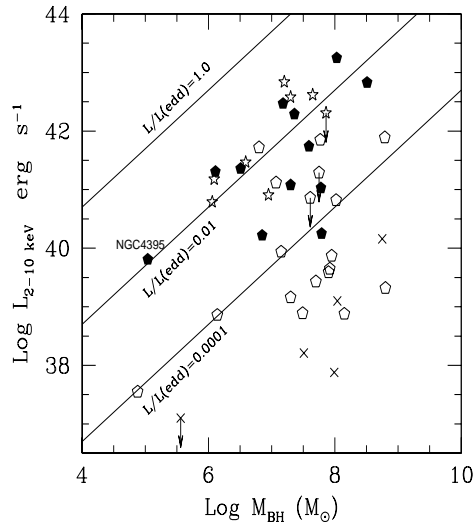


Figure 4.9: Log of 2-10 keV luminosity versus log of black hole mass (symbols as in fig 4.6). Compton thick candidates are plotted as stars. The solid lines show the $L_{2-10keV}$ as a function of the black hole mass for Eddington ratios of 1.0 and 0.01.

CfA sources are radiating at very low Eddington ratios if compared with luminous AGN. The low Eddington ratios observed here are even lower if the bolometric correction considered is that of LLAGN. At such low Eddington ratios, radiatively inefficient accretion is normally invoked as the putative mechanism for the production of the observed emission.

For example, in Merloni et al. (2003) the $L_{2-10keV}/L_{Edd}$ ratio for a heterogeneous sample of AGN and stellar masses black holes ranges from 1 to 10^{-8} . These authors delineate a range of $L_{2-10keV}/L_{Edd}$ ratios in which the accretion mode changes from a radiatively efficient to a radiatively inefficient one below 10^{-3} and above ~ 0.7 . According to these claims, most of our sources would be powered by radiatively inefficient accretion. Finally, note that in Fig. 4.9 Compton thick sources populate the upper part of the plot, at higher Eddington ratios, while only one source has $L_{Bol}/L_{Edd} \lesssim 10^{-3}$; this is probably a selection effect, since Compton thick sources with an observed $L_{2-10keV} \lesssim 10^{38}$ erg s $^{-1}$ would probably be undetectable in X-rays.

4.6 Summary of the results obtained on the emission mechanism

The intrinsic nuclear X-ray luminosities of the Seyfert galaxies in the local Universe span nearly five orders of magnitude, down to 10^{38} erg/s in the 2-10 keV energy range.

After taking into account the presence of Compton thick objects in which the nuclear emission is heavily reduced by absorbing material, strong correlation between X-ray and optical line emission luminosities were found. This suggests a link between the X-ray emission and the ionization radiation which holds also at very low luminosities. In luminous AGN, the UV/optical radiation has the form of a "big blue bump" feature (Elvis et al. 1994), commonly modelled by a geometrically thin accretion disk working in a radiatively efficient regime (Shakura & Sunyaev 1973) while the X-ray emission is produced by Comptonization of soft photons in a hot corona (Haardt & Maraschi 1991). On the other hand, it has been shown that some LLAGN lack this "big blue bump" feature (Ho 1999). Such observational evidence combined with the low Eddington ratios commonly observed in LLAGN, has lead many authors to invoke advection-dominated accretion flow models (ADAF, Narayan & Yi 1994) and their variants to model their spectral shape.

As a matter of fact, ADAF models work in a radiatively inefficient regime at sub-Eddington ratios ($L < 0.01-0.1L_{Edd}$) and can reproduce the lack of UV excess observed in the SED of LLAGN. However, also radiatively efficient standard accretion disks are stable at low Eddington ratios down to $L \sim 10^{-6}L_{Edd}$ (Park & Ostriker 2001) and can reproduce the shape of the LLAGN SED since the temperatures of a multi-colour disk scale with $\dot{m}^{1/4}$ (Ptak et al. 2004).

Moreover, the Γ vs. R relation obtained for the *BeppoSAX* sample makes plausible a scenario in which the two mechanism co-exist with different relative importance depending on the accretion rate (Merloni 2006). In this scenario, in fact, the accretion disk is able to deeply penetrate the hot phase (corona or ADAF flow) that surrounds the SMBH. Being so, the emission is dominated by the standard "two-phase" X-ray emission. On the contrary, when the accretion rate decreases, the hot-phase no more surrounds the accretion disk that cannot reaches the innermost regions and the X-ray emission is dominated the ADAF component.

Here it was also found that the X-ray versus optical emission line correlations scale with luminosity, so that low luminosity Seyfert galaxies appear to be a scaled-down version of classical AGN. The observed optical emission line spectra suggest that the amount of UV radiation produced is sufficient to ionize the NLR. However, if Seyfert galaxies with very low luminosities in the $X-CfA$ sample actually lack a "big blue bump" feature, as sometimes observed in LLAGN, then an additional source of UV photons must be invoked which means that the AGN UV photons are not the only contributors to the ionizing radiation, i.e. radiation produced in circumnuclear starburst could contribute significantly to the observed emission line fluxes.

A similar scenario has been proposed by Contini (2004) for NGC 4579, in which both line and continuum emission are explained by a composite model which accounts for the presence of an AGN, a jet which interacts with the ISM creating shocks, a starburst of different ages and HII regions. Moreover, some authors have shown that the observed emission line ratios in AGN may be produced by both a thermal or a non-thermal optical/UV continuum (Keel & Miller 1983, Martins et al. 2003). Indeed, to constrain the spectral shape of these sources and compare it with theoretical models, it is necessary to properly subtract UV/optical data for the Galactic emission and have multi-waveband observations.

In summary, the results obtained on this topic can be listed as follow:

- a highly significant Γ vs. R relation was found using the *BeppoSAX* sample, thus implying that the thermal Comptonization is present in the core of Seyfert galaxies to produce X-rays;
- both L_X vs. $L_{H\alpha}$ and L_X vs. $L_{[OIII]}$ correlations are highly significant in the $X-CfA$ sample, indicating that the X-ray emission and the UV ionizing radiation are linked.
- Both correlations scale with luminosity, i.e. they have similar slopes of more powerful objects, suggesting that low luminosity Seyfert galaxies are powered by the same physical processes which operate in brighter AGN such as QSOs.
- No correlation is found between nuclear luminosity and M_{BH} in agreement with some previous studies (Woo & Urry 2002, Pellegrini et al. 2005).

- L/L_{Edd} ratios span three order of magnitudes down to $L_{Bol}/L_{Edd} \sim 10^{-7}$, indicating that most of our sources are accreting at very low Eddington ratios.

Overall our results suggest that Seyfert nuclei in our sample are consistent with being a scaled-down version of luminous AGN, except for a small fraction of objects having luminosities in the $10^{37} - 10^{38}$ erg s⁻¹ range and which show evidences of stellar processes as the underlying agent responsible for the activity.

Chapter 5

Key study objects: i) Mrk 509

In the previous sections it was tested that, at least at the zero-th order, the UM is a valid geometrical framework within which we can interpret the observational evidences obtained in studying the Seyfert galaxies. I also obtained indications (§3 and §4) that a cold accretion disk could extend, at least in the brightest sources, close to the last stable orbits. Thus I must expect that the relativistic effects predicted to occur in such conditions (see §1.3.3 and §1.4.3), have to be detected. I should also expect that these effects can be used to trace the flow dynamics around the SMBH. Nonetheless, it must be recalled here that recent results indicated that the matter flow close to the SMBH is not limited to the accretion disk. Several detections of red- and blue-shifted resonant absorption lines and of shifted emission lines obtained in the recent past, strongly support the idea that, close to SMBH, radial motions both in in- and out-flows must be present.

To study such phenomena, here I focused on three well defined case studies: Mrk 509, NGC 3783 and IRAS 13197-1627. The first two objects are type I Seyfert galaxies while the latter is a Seyfert 1.8 (i.e. a type II object). These objects were chosen since in their X-ray data were already observed hints of ionized absorption lines (MKN 509, NGC 3783, IRAS 13197-1627, Dadina et al. 2005, Reeves et al 2004, Dadina & Cappi 2004), hints of variability of the broad and gravitationally redshifted component of the Fe K line (NGC 3783, De Marco et al. 2006), evidences of variability of the narrow resonant Fe absorption line (MKN 509, Dadina et al. 2005), and traces of extreme reflection and/or absorption properties (IRAs 13197-1627, Dadina & Cappi 2004). In few words, the three sources

showed both evidences of extreme relativistic effects in the X-ray band where the iron line is expected to be observed and/or in the reflection continuum.

5.1 The case of Mrk 509

Mrk 509 ($z=0.034397$) is the brightest Seyfert 1 of the hard (2–100 keV) X-ray sky (Malizia et al. 1999; Revnivtsev et al. 2004; Sazonov et al. 2007) that is not strongly affected by a warm absorber component (Pounds et al. 2001; Yaqoob et al. 2003). The HETG observation confirms the presence of a narrow component of the Fe K line with an equivalent width (EW) of 50 eV (Yaqoob et al. 2004). The presence of a second ionized component of the Fe K line at 6.7–6.9 keV has been claimed by Pounds et al. (2001) who fitted this feature using a relativistic profile. Page et al. (2003) showed that the same spectral feature was consistent with a simple Compton reflection component from distant material. The broad-band spectrum and, in particular, the soft excess, have been fitted by De Rosa et al. (2004) with a reflection component from a ionized disc in addition to a neutral reflection component. Finally, Dadina et al. (2005) found evidence of absorption due to transient, relativistically red–blue–shifted ionized matter.

Here I present the spectral and variability analysis of the complex Fe K band of Mrk 509, using the whole set of *XMM-Newton* and observations.

Section 5.2 describes the observations and the data reduction. In Sect. 5.3 the spectral analysis of the EPIC-pn data of the Fe K band (using phenomenological models) is presented. In Sect. 5.3.3, to check for the presence of an absorption line, the EPIC-MOS data have also been considered. In Sect. 5.3.4 the spectral variability analysis, within the *XMM-Newton* observations, is presented. Sect. 5.4 describes the spectral analysis of the Fe K band of the summed (XIS0+XIS3) data and the detailed comparison with the spectrum accumulated during the *XMM-Newton* observations. In Sect. 5.4.1 the HXD-pin data are introduced in order to estimate the amount of reflection continuum present in the source spectrum. Finally, a more physically self-consistent fit of the EPIC spectra of all the EPIC instruments (EPIC-pn plus the two EPIC-MOS) is investigated in Sect. 5.5. The results of this analysis are discussed in Sect. 6, followed by conclusions in Sect. 7.

5.2 Observations and data reduction

Mrk 509 was observed 5 times by *XMM-Newton* on 2000–10–25, 2001–04–20, 2005–10–16, 2005–10–20 and 2006–04–25. All the observations were performed with the EPIC–pn CCD camera operating in small window observing mode and with the thin filter applied. The total pn observation time is of about 260 ks. Since the live–time of the pn CCD in small window mode is 71 per cent, the net exposure of the summed spectrum is of about 180 ks. The analysis has been made with the SAS software (version 7.1.0), starting from the ODF files. Single and double events are selected for the pn data, while only single events are used for the MOS camera because of a slight pile–up effect. For the pn data I checked that the results obtained using only single events (that allow a superior energy resolution) are consistent with those from the MOS, finding good agreement. The source and background photons are extracted from a region of 40 arcsec within the same CCD of the source both for the pn and MOS data. Response matrices were generated using the SAS tasks RMFGEN and ARFGEN.

observed Mrk 509 four times on 2006–04–25, 2006–10–14, 2006–11–15 and 2006–11–27. The last *XMM-Newton* and the first observations overlap over a period of ~ 25 ks. Event files from version 2.0.6.13 of the pipeline processing were used and spectra were extracted using XSELECT. Response matrices and ancillary response files were generated for each XIS using XISRMMFGEN and XISSIMARFGEN version 2007–05–14. The XIS1 camera data are not considered here because of the relatively low effective area in the Fe K energy interval, while the XIS2 is unavailable for observations performed after November 2006. I used the data obtained during the overlapping interval to check whether the EPIC pn and MOS data on one hand and the XIS0 and XIS3 data on the other hand are consistent within the inter–calibration uncertainties. I found an overall good agreement between the data from the two satellites, the parameters related to the main iron emission features and the power–law continuum being the same within the errors (except for the XIS2 camera above 8 keV). The total XIS observation time is about 108 ks. The source and background photons are extracted from a region of 4.3 arcmin within the same CCD of the source. For the HXD/PIN, instrumental background spectra and response matrices provided by the HXD instrument team have been used. An additional component accounting for the CXB has been included in the spectral fits

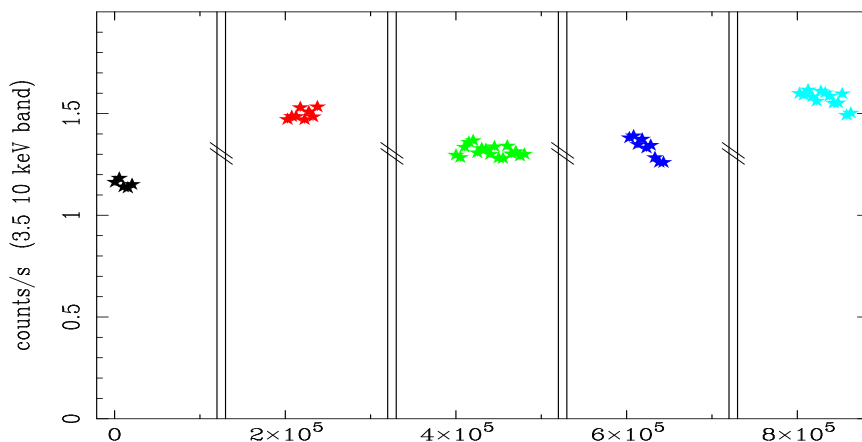


Figure 5.1: 3.5–10 keV EPIC-pn light curves of the *XMM-Newton* observations. The abscissa shows the observation time in seconds. The time between the different observations is arbitrary. The black, red, green, blue and light blue show the light curves during the 2000–10–25, 2001–04–20, 2005–10–16, 2005–10–20 and 2006–04–25 observations, respectively.

of the PIN data.

All spectral fits were performed using the Xspec software (version 12.3.0) and include neutral Galactic absorption ($4.2 \times 10^{20} \text{ cm}^{-2}$; Dickey & Lockman 1990), the energies are rest frame if not specified otherwise, and the errors are reported at the 90 per cent confidence level for one interesting parameter (Avni 1976). The sum of the spectra has been performed with the MATHPHA, ADDRMF and ADDARF tools within the HEASOFT package (version 6.1).

5.3 Fe K band emission of Mrk 509: the *XMM-Newton* data

The primary goal of this investigation is the study of the Fe K line band; therefore, in order to avoid the effects of the warm absorber (although not strong; Yaqoob et al. 2003; Smith et al. 2007) and of the soft excess, I concentrate on the analysis of the data in the 3.5–10 keV band only.

Figure 5.1 shows the source light curve in the 3.5–10 keV energy band obtained from the *XMM-Newton* pointings. Mrk 509 shows variations of the order of ~ 30 per cent over the different observations, while almost no variability is detected within each observation. Only during the fourth observation the source shows sig-

nificant variability, with a mean fractional rms of about 0.04.

I start the analysis of the *XMM-Newton* data considering the spectra from the EPIC-pn camera only (including the EPIC-MOS data only when a check of the significance of a feature is required; see Sect. 3.3). I have fitted a simple power law model to the 3.5–10 keV data and found that the spectral index steepens with increasing flux. It goes from 1.54 ± 0.03 to 1.72 ± 0.03 for fluxes of 2.5×10^{-11} and 3.3×10^{-11} erg cm⁻² s⁻¹, respectively (3.0×10^{-11} – 4.3×10^{-11} erg cm⁻² s⁻¹, in the 2–10 keV band).

I firstly phenomenologically fitted the Fe K complex of each single observation with a series of emission-absorption lines (see also §5.3.3) and checked that the results on the parameters of Fe K complex obtained in each observation are consistent within the errors (not a surprising result in light of the low statistics of the single spectra and weakness of the ionized features; see §5.3.4). Hence, I concluded that the continuum variations do not strongly affect the observed shape of the narrow-band emission/absorption structures in the Fe K band. Thus, in order to improve the signal-to-noise ratio and thus to detail the fine structures of the Fe K band, the spectra of all the *XMM-Newton* observations have been summed (see §5.3.4 for the study of the source spectral variability). The summed mean EPIC-pn spectrum has been grouped in order to have at least 1000 counts in each data bin. Moreover, this binning criterion ensures to have at least 30 data-points per keV in the 4–7 keV band, where the Fe K α complex is expected to contribute. This guarantees a good sampling of the energy resolution of the instrument and the possibility of fully exploiting the spectral potentials of the EPIC instruments. Figure 5.2 shows the ratio between the data and the best-fit power law. The energy band used during the fit has been restricted to 3.5–5 and 8–10 keV, in order to avoid the Fe K band, hence measuring the underlying continuum.

The resulting best-fit power-law continuum has a photon index of 1.63 ± 0.01 and very well reproduces the source emission ($\chi^2=170.0$ for 163 degrees of freedom, dof) outside the Fe K band. The inclusion of the Fe K band shows that other components are necessary to reproduce it ($\chi^2=753.9$ for 307 dof). The bad statistical result is explained by the presence of clear spectral complexity in the 6–7 keV band.

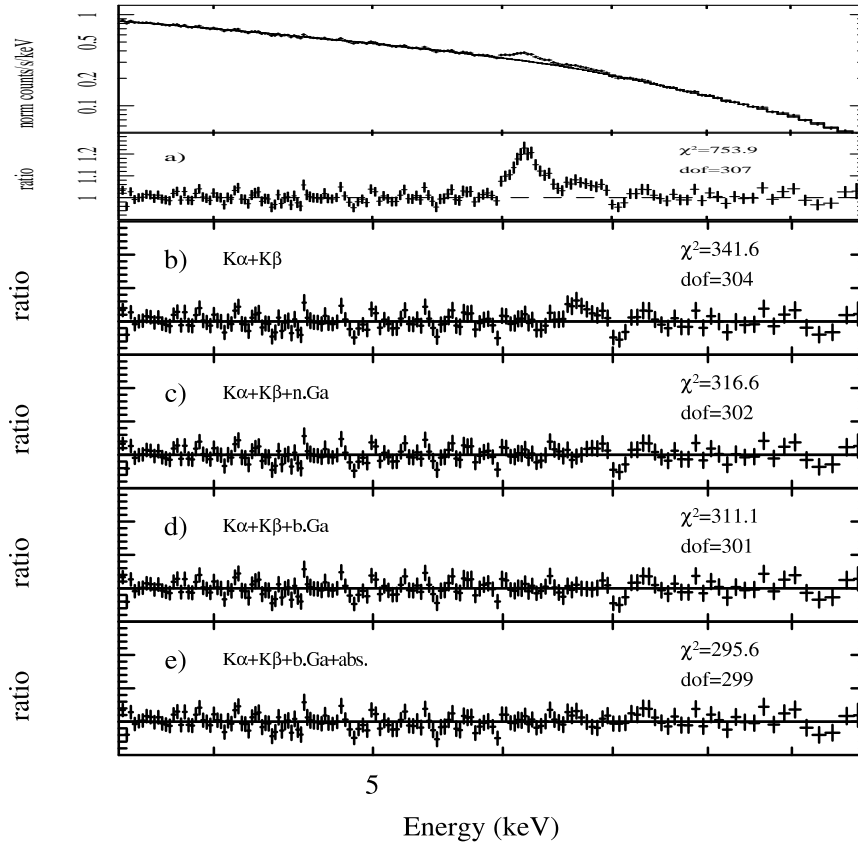


Figure 5.2: (*Upper panel*) Observed-frame 3.5–10 keV summed XMM-Newton EPIC-pn spectrum fitted in the 3.5–5 and 8–10 keV band with a power law. (*Panel a*) Data/model ratio. This ratio shows a clear evidence for a neutral Fe K emission line and further emission from ionized Fe, as well as other complexities around 7 keV. (*Panel b*) Data/model ratio when two resolved emission lines (for the Fe $K\alpha$ and $K\beta$) are included in the spectral fitting. Strong residuals are still present, indicative of ionized Fe K emission, while no residual emission redward of the neutral Fe K line appears. (*Panel c*) Data/model ratio when a narrow emission line is included in the model to reproduce the ionized emission. (*Panel d*) Same as panel c, but with a single broad emission line instead of a narrow line. In both cases (panel c and d), an absorption feature is present around 7 keV. (*Panel e*) Data/model ratio when an absorption component (modeled using *xstar*) and a relativistic ionized line are added to the power law and the emission from neutral Fe K.

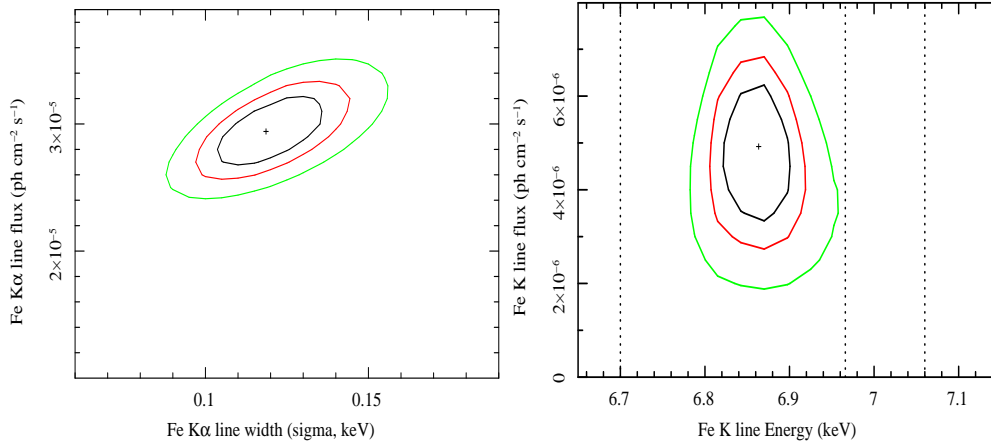


Figure 5.3: (*Left panel*) Contour plot of the sigma vs. intensity of the neutral Fe K line. (*Right panel*) Contour plot of the energy vs. intensity of the narrow line used to fit the ionized Fe K emission. The narrow line energy is not consistent with emission from Fe XXV (neither with the forbidden at 6.64 keV, nor with the resonant at 6.7 keV), Fe XXVI or Fe K β , whose energy is indicated by the vertical dotted lines (from left to right).

5.3.1 The 6.4 keV emission line

Panel a of Figure 5.2 shows the clear evidence for a prominent emission line, consistent with a neutral Fe K α line at 6.4 keV. I therefore added a Gaussian emission line to the model, obtaining a very significant improvement of the fit ($\Delta\chi^2=392.1$ for the addition of 3 d.o.f.). The best-fit energy of the line is 6.42 ± 0.02 keV, consistent with emission from neutral or slightly ionised material. The line has an equivalent width of 69 ± 8 eV and is clearly resolved ($\sigma=0.12\pm 0.02$ keV), as shown by the contour plot in the left panel of Figure 5.3.

The residuals in panel b of Fig. 5.2 show no excess redward of this emission line, which could have been indicative of emission from relativistically redshifted neutral material.

5.3.2 The ionized Fe K emission line

An excess is, however, present in the range 6.5–7 keV (Fig. 5.2, panel a). If modeled with a Fe K β component with the expected energy (fixed at 7.06 keV)

and forced to have an intensity of 0.15 of the $K\alpha$ (Palmeri et al. 2003; Basko 1978; Molendi et al. 2003) and a width equal to the Fe $K\alpha$ line (i.e. assuming that the $K\alpha$ and $K\beta$ line originate from one and the same material), the fit improves significantly ($\Delta\chi^2=20.3$). Nonetheless, significant residuals are still present in the 6.5–6.9 keV band (panel b of Fig.5.2). If this further excess is modelled with a narrow Gaussian line ($\Delta\chi^2=25$ for 2 additional d.o.f.), the feature ($EW=12\pm 4$ eV) is found to peak at $E=6.86\pm 0.04$ keV (see panel c of Figure 5.2 and right panel of Fig. 5.3). Thus, the energy centroid is not consistent with the line being produced by either Fe XXV or Fe XXVI (right panel of Fig. 5.3) in a scattering medium distant from the X-rays source (Bianchi et al. 2002; 2004). The higher energy transition of the Fe XXV complex is the "resonant line" expected at 6.7 keV (see e.g. Bianchi et al. 2005b). Thus, to save this interpretation, it is required that the photo-ionized gas has a significant blueshift (~ 5700 km/s, if the line is associated to Fe XXV) or redshift (~ 4500 km/s, for Fe XXVI). Then, instead of fitting the ionized excess with a single line, I fitted it with two narrow lines forcing their energies to be 6.7 and 6.96 keV. The fit clearly worsens ($\chi^2=326.7$ for 302 dof, corresponding to a $\Delta\chi^2 = -10.1$ for the same d.o.f.).

However, if the gas is allowed to be outflowing, the fit improves ($\Delta\chi^2=4.3$ for the addition of 1 new parameter; $\chi^2=312.3$ for 301 dof; the EW are 8.9 and 12.4 eV for the Fe XXV and Fe XXVI lines, respectively) as respect to the single narrow emission line and it results to have a common velocity of 3500^{+1900}_{-1200} km/s.

Alternatively, the excess could be produced by a single broad line coming from matter quite close to the source of high-energy photons (in this case the Fe K emission is composed by Fe $K\alpha+\beta$ plus another Fe K line). Leaving the width of the line free to vary, the fit improves, with $\chi^2=311.1$ (panel d Figure 5.2) and $\Delta\chi^2$ of 5.5, with respect to the single narrow ionized emission line fit, and $\Delta\chi^2$ of 1.3 for the same dof with respect to the best-fit model with two narrow ionized lines. The resulting broad ionized Fe K line has $EW=23\pm 9$ eV and $\sigma=0.14^{+0.13}_{-0.08}$ keV. The best-fit energy of the line does not change significantly ($E=6.86^{+0.08}_{-0.16}$ keV); however, in this case the emission is consistent (at the 99 per cent confidence level) with either Fe XXV or Fe XXVI. Although the statistical improvement is not highly significant, in the following I will consider that the ~ 6.8 –6.9 keV excess is indeed associated with a resolved emission line.

5.3.3 Ionized absorption?

The *XMM-Newton* data display a narrow absorption feature at $E \sim 7$ keV (observed frame; see Figure 5.2, panel d). Since this feature is very close to the broad excess discussed in the previous section, its significance and intensity are degenerate with the broad emission-line parameters. In order to gain some insight, the broad emission-line parameters have been fixed at the best-fit values obtained before the addition of a narrow (σ fixed at 1 eV) Gaussian absorption line component. In this case, the line is significant at the ~ 99 per cent confidence level (dashed contours of Fig. 5.4; $\Delta\chi^2 = 15.5$ for 2 additional parameters; see also panel e of Fig. 2). Once the MOS data¹ are added, the significance of this feature increases to 99.9 per cent (solid contours of Fig. 5.4), in both cases, of a broad and of a narrow ionized emission line. The best fit energy and EW of the line are $E = 7.28^{+0.03}_{-0.02}$ keV and $EW = -14.9^{+5.2}_{-5.5}$ eV, $E = 7.33^{+0.03}_{-0.04}$ keV and $EW = -13.1^{+5.9}_{-2.9}$ eV, in the pn alone and in the pn+MOS, respectively.

5.3.4 Time resolved spectral variability and total rms spectrum

To measure possible variations in the Fe K band, the mean EPIC-pn spectra of each of the 5 *XMM-Newton* observations have been studied. The spectra are fitted with the same model composed by a power law plus three emission lines for the Fe $K\alpha$, $K\beta$ (with the width fixed at the best-fit value, $\sigma = 0.12$ keV) and the broad ionized Fe K line. The low statistics of the spectra of the single observations prevents us from the detection of significant spectral variability of the weak ionised emission/absorption lines. The neutral Fe K line is better constrained and its EW is found to be anti-correlated with the level of the continuum, as expected for a constant line.

A different, more sensitive, way to detect an excess of spectral variability is the total rms function. The upper panel of Fig. 5.5 displays the shape of the summed spectrum in the Fe K line band. The lower panel shows the total rms spectrum (Revnivtsev et al. 1999; Papadakis et al. 2005) calculated with time bins of ~ 4.5

¹The shapes of the emission/absorption lines in the MOS instruments appear slightly narrower, although consistent with the values obtained with the pn instrument.

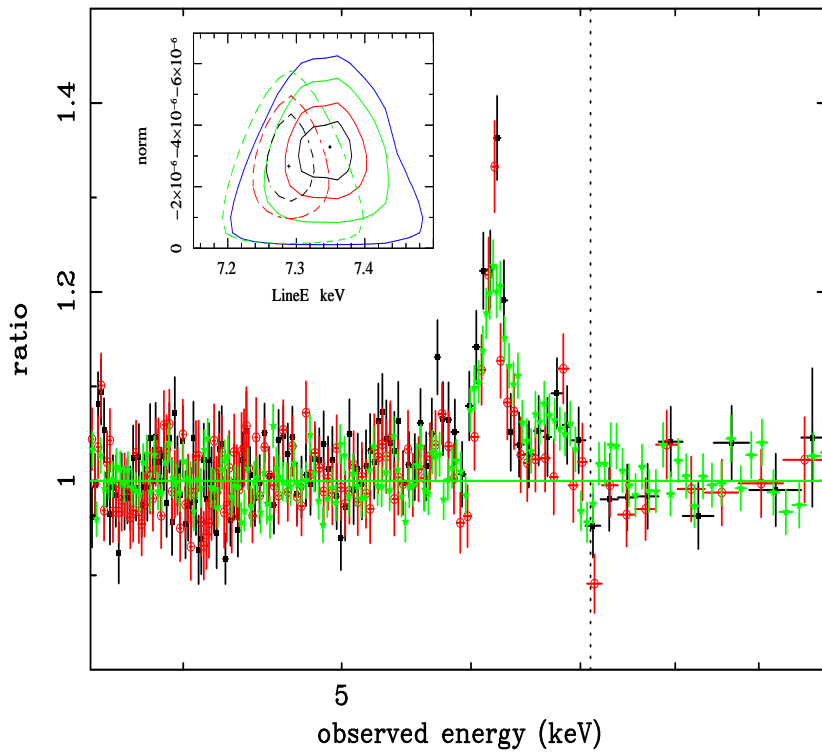


Figure 5.4: Superposition of the pn (green), MOS1 (black) and MOS2 (red) summed spectra of all the *XMM-Newton* observations. The data are fitted, in the 3.5–5 and 8–10 keV bands with a power law, absorbed by Galactic material. The same structures are present in the three spectra. In particular, a narrow drop of emission is present in all the instruments at the same energy (see vertical dotted line). (*Inset panel*) Confidence contour plot of the intensity vs. energy of the narrow unresolved ionized absorption when using the pn data alone (dashed contours) and including the MOS data as well (solid contours). The lines indicate the 68.3 (black), 90 (red), 99 (green) and 99.9 (blue) per cent confidence levels.

ks. The total rms is defined by the formula:

$$RMS(E) = \frac{\sqrt{S^2(E) - \langle \sigma_{err}^2 \rangle}}{\Delta E * arf(E)} \quad (5.1)$$

where S^2 is the source variance in a given energy interval ΔE ; $\langle \sigma_{err}^2 \rangle$ is the scatter introduced by the Poissonian noise and arf is the telescope effective area convolved with the response matrix². This function shows the spectrum of the varying component only, in which any constant component is removed and has been computed by using the different *XMM-Newton* observations as if they were contiguous. The total rms spectrum may be reproduced by a power law with a spectral index of 2.13 ($\chi^2=46.4$ for 43 dof). Thus, the variable component is steeper than the observed power law in the mean spectrum, in agreement with the mentioned observed steepening of the photon index (Γ) with flux. The Γ -flux correlation is commonly observed in Seyfert galaxies and has been interpreted as being due to the flux-correlated variations of the power-law slope produced in a corona above an accretion disc and related to the changes in the input soft seed photons (e.g. Haardt, Maraschi & Ghisellini 1997; Maraschi & Haardt 1997; Poutanen & Fabian 1999; Zdziarski et al. 2003). These models predict the presence of a pivot point, that would correspond to a minimum in the total rms spectrum. The observation of a perfect power law shape (see Fig. 5.5) indicates that the pivot point (if present) has to be outside the 3–10 keV energy band. On the other hand, the slope-flux behaviour can be explained in terms of a two-component model (McHardy, Papadakis & Uttley 1998; Shih, Iwasawa & Fabian 2002) in which a constant-slope power law varies in normalization only, while a harder component remains approximately constant, hardening the spectral slope at low flux levels only, when it becomes prominent in the hard band. In this scenario the spectral index of the variable component is equal to the one of the total rms spectrum, that is $\Gamma=2.13$.

Moreover, at the energy of the neutral and ionized Fe K line components there is no hints of variability (Figure 5.5), in agreement with these components being constant, while an indication for an excess of variability is present around 6.7 keV.

²The total rms spectrum provides the intrinsic source spectrum of the variable component. Nevertheless, we can only measure the variance as observed through the instrument. Thus, the sharp features in the source spectrum, as well as the effects of the features on the effective area, are broadened by the instrumental spectral resolution. For this reason, to obtain the total rms spectrum, we must take into account the convolution of the effective area with the spectral response.

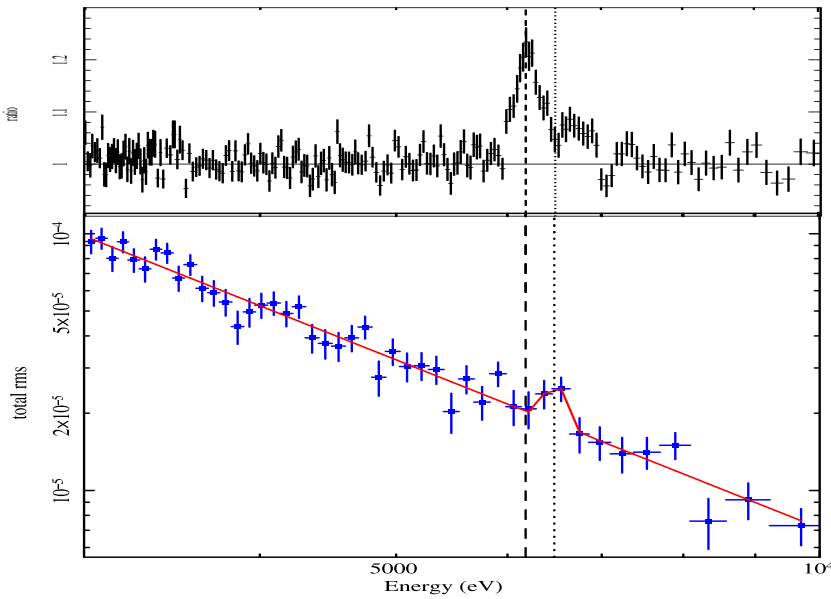


Figure 5.5: *Lower panel:* Total rms variability spectrum of the *XMM-Newton* observations. The data (blue crosses) show the spectrum of the variable component. The best-fit model is a power law with spectral index $\Gamma=2.18$ (red line) plus a Gaussian emission line (improving the fit by $\Delta\chi^2$ of 8.9 for the addition of 2 parameters). The dashed line highlights the centroid energy of the neutral Fe $K\alpha$ line, while the dotted line is placed at the maximum of the variability excess, modeled with the Gaussian emission line. The excess variability energy corresponds to a drop of emission of the real spectrum.

To compute the significance of this variability feature, a narrow Gaussian line has been added to the modelling of the total rms spectrum. The best-fit energy of the additional line is 6.69 keV, with a σ fixed at the instrumental energy resolution, while the resulting $\Delta\chi^2$ is 8.9 for the addition of 2 parameters (that corresponds to an F-test significance of 98.8 per cent). Introducing the line, the continuum spectral index steepens to $\Gamma \sim 2.18$. The dashed line in Figure 5.5 highlights the centroid energy of the neutral Fe $K\alpha$ line, while the dotted line (at ~ 6.7 keV, rest frame) is placed at the maximum of the variability excess. This energy corresponds to a drop of emission in the real spectrum, as I shall discuss in more detail in Section 5.5.

5.4 The view of the Fe K band emission

As mentioned in §5.5.2, the source was also observed with Suzaku. The first 25 ks observation is simultaneous with the last *XMM-Newton* pointing. The source spectra of all the instruments are in very good agreement, during the simultaneous observation. The spectrum is also consistent with the presence of the emission and absorption lines, as observed in the mean *XMM-Newton* spectrum, nevertheless, due to the low statistics of the 25 ks spectrum and the weakness of the ionized features, it is not possible to perform a detailed comparison. Only the presence of the strong Fe $K\alpha$ line can be investigated, the ionized emission and absorption lines are not constrained in the 25 ks exposure.

Also during the 4 pointings, Mrk 509 has shown little variability, with flux changes lower than 10–15 per cent, hampering any spectral variability study. Figure 5.6 shows the *XMM-Newton* (black) and XIS0+XIS3 (red) summed mean spectra. The data were fitted, in the 3.5–5 and 7.5–10 keV bands, with a simple power law and Galactic absorption: the ratio of the data to the best fit model is shown in Figure 5.6. The source emission varied between the *XMM-Newton* and the observations. The best-fit spectral index and the 3.5–10 keV band fluxes are: $\Gamma=1.63\pm0.01$ and $\Gamma=1.71\pm0.02$ and 2.63×10^{-11} and 3.11×10^{-11} ergs cm^{-2} s^{-1} , during the *XMM-Newton* and observations, respectively. The neutral and ionized Fe K emission lines appear constant, while some differences are present at 6.7 keV, the same energy where the *XMM-Newton* data were suggesting an increase of variability. Other more subtle differences appears at ~ 7 keV, where the absorption line imprints its presence in the *XMM-Newton* data only.

The spectrum of Mrk 509 shows, in good agreement with the *XMM-Newton* one, a resolved neutral Fe K line smoothly joining with a higher energy excess, most likely due to ionized iron emission (see Fig. 5.6). Given that no absorption lines around 6.7 keV or 7.3 keV are present in the data, the spectrum may be useful to infer the properties of the emission lines more clearly.

The XIS0+XIS3 summed spectrum has been fitted in the 3.5–10 keV band with a power law plus two resolved Gaussian emission lines to reproduce the emission from Fe $K\alpha+\beta$. The parameters of the Fe $K\alpha$ line are free to vary, while the Fe $K\beta$ ones are constrained as in §5.3.2. This fit leaves large residuals ($\chi^2=1379.8$ for 1337 dof) in the Fe K band. In this respect, it is difficult to describe the >6.5 keV

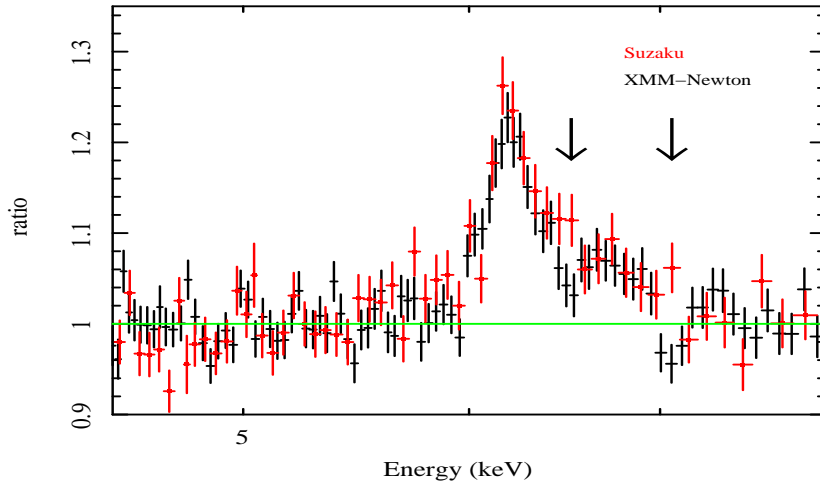


Figure 5.6: *XMM-Newton* (black) and *XIS0+XIS3* (red) summed mean spectra. The data are fitted, in the 3.5–5 and 7.5–10 keV bands, with a simple power law, absorbed by Galactic material, and the ratio of the data to the best fit model is shown. The arrows mark absorption features in the spectrum.

excess with a single narrow ionized Fe line (either due to Fe XXV or Fe XXVI). In fact, although the addition of a narrow line is significant ($\Delta\chi^2=20.1$ for 2 more parameters), it leaves residuals in the Fe K band. This remaining excess can be reproduced ($\Delta\chi^2=5.9$ for 1 more parameter), in a photoionized gas scenario, by a blend of two unresolved ionized lines, requiring three emission lines to fit the Fe K band (FeK $\alpha+\beta$, Fe XXV and Fe XXVI). In this case, such as in the analysis of the *XMM-Newton* mean spectrum, a blueshift of this component is suggested ($v=2600^{+2800}_{-2000}$ km s $^{-1}$). However, the best-fit model (this scenario is strengthened by the lack of narrow peaks) suggests that the excess may be in fact associated with a broad ionized Fe line (over which the ~ 6.7 keV and ~ 7.3 keV absorption lines are most likely superimposed, but during the *XMM-Newton* observation only). In fact considering a broad Fe line instead of the two narrow lines I obtain an improvement of $\Delta\chi^2=9.7$ for the same dof (see Table 5.1, model A).

	3.5–10 keV	BEST-FIT	SPECTRA						
Suzaku									
	Γ	pl norm ^a	$E_{Neut.}$ keV	$\sigma_{Neut.}$ keV	$A_{Neut.}{}^b$ (EW) ^c	$E_{Ion.}$ keV	$\sigma_{Ion./r_{in}}$ keV/ r_g	$A_{Ion.}{}^b$ (EW) ^c	χ^2/dof
A	1.72±0.02	1.12±0.02	6.42±0.03	<0.06	1.7±0.5 (32)	6.54±0.09	0.40±0.1	4.6±1.2 (90)	1344/1340
B	1.72±0.02	1.12±0.02	6.42±0.02	<0.07	2.1±0.5 (40)	6.61±0.08	24±10	3.4±0.8 (79)	1346/1340
Self-consistent model									
<i>XMM-Newton</i>									
	Γ	pl norm ^a	$E_{Neut.}$ keV	$\sigma_{Neut.}$ keV	$A_{Neut.}{}^b$	Incl. deg	ξ erg cm s ⁻¹	$A_{Ref1.Ion.}{}^b$	
C	1.70±0.01	0.92±0.04	6.41±0.01	0.07±0.01	2.2±0.3	47±2	11 ⁺²⁰⁰ ₋₇	0.9 ^{+3.0} _{-0.5}	
	$N_H{}^d$	log(ξ)	z	χ^2/dof					
	5.8 ^{+5.2} _{-4.8}	5.15 ^{+1.25} _{-0.52}	-0.0484 ^{+0.012} _{-0.013}	894.3/876					

Table 5.1: *Top panel:* Best-fit values of the summed spectra (XIS0+XIS3) of all observations fitted in the 3.5–10 keV band. Both model A and B include a power law and two Gaussian lines $K\alpha+\beta$ to fit the 6.4 keV excess. In addition to this baseline model, either another Gaussian component (Model A) or a *DISKLINE* profile (Model B) have been added to reproduce the ionized line, respectively. In Table the best-fit power law spectral index (Γ) and normalization as well as the Fe $K\alpha$ energy, width and normalization are reported for model A and B. The energy, width and normalization are reported when a Gaussian profile for the ionized Fe K line is considered (Model A), while the best fit energy, inner radius and normalization are presented when a *DISKLINE* profile is fitted (Model B). Standard disc reflectivity index, outer disc radius and disc inclination of $\alpha = 3$, $r_{out} = 400 r_g$ and 30° have been assumed for the relativistic profile. *Bottom panel:* Best fit results of the summed *XMM-Newton* EPIC-pn and EPIC-MOS data of Mrk 509 (fitted in the 3.5–10 keV band). The model ($wabs*zxipcf*(pow+zgaus+zgaus+pextrav+kdblur*(reflion))$) consists of: i) a power law; ii) two Gaussian emission lines for the Fe $K\alpha$ and $K\beta$ emission (this latter has energy is fixed to the expected value, 7.06 keV, intensity and width tied to the $K\alpha$ values); iii) a neutral reflection continuum component (*pextrav* in Xspec) with $R=1$ (value broadly consistent with the pin constraints and the values previously observed; De Rosa et al. 2004), Solar abundance and high energy cut off of the illuminating power law at 100 keV; iv) a ionized disc reflection spectrum (*reflion* model; Ross & Fabian 2005) with the disc inner and outer radii and the emissivity of 6, 400 r_g and -3 , respectively. The best fit disc inclination and ionization and the normalization of the disc reflection component are shown; v) an ionized absorption component (*zxipcf*) totally covering the nuclear source. The best fit column density, ionization parameter and outflow velocity are reported. a) In units of 10^{-2} photons keV⁻¹ cm⁻² s⁻¹ at 1 keV; b) In units of 10^{-5} photons cm⁻² s⁻¹; c) In units of eV; d) In units of 10^{22} atoms cm⁻².

Thus, the data indicate that the broad excess at 6.5–6.6 keV is indeed due to a broad line rather than a blend of narrow ionized Fe lines. Since broad lines may arise because of relativistic effects in the inner regions of the accretion flow, we tested this hypothesis by fitting the excess at 6.5–6.6 keV with a *diskline* profile. The statistics of the spectrum is not such to allow us to constrain all the parameters of the ionized *diskline* model. Thus, the disc reflectivity index has been fixed at the standard value ($\alpha = -3$, where the emissivity is proportional to r^α), the outer disc radius and inclinations to 400 gravitational radii (r_g) and 30° , respectively. The broad line is consistent with being produced in the accretion disc (Table 5.1, Model B); however, the emission from the innermost part of the disc is not required, the lower limit on the inner disc radius being 10–15 r_g . As clear from Fig. 5.6, the data do not require any ionized Fe K absorption structures.

In order to quantify the differences between the and *XMM-Newton* spectra (and, in particular, the reality of the absorption structures at 6.7 and 7.3 keV appearing in the *XMM-Newton* spectrum only) I fixed all the parameters of the model (apart from the intensity and spectral index of the direct power law) and fit the *XMM-Newton* data with that model. This corresponds to assuming that the intrinsic line shapes do not vary between the two observations. Then, a narrow Gaussian line has been added to the *XMM-Newton* model to estimate the significance of the putative absorption structures. The improvement in the spectral fitting is evident, as indicated by the $\Delta\chi^2=28.3$ and 22 in the case of a line at $E=6.72\pm 0.04$ keV and $E=7.29\pm 0.04$ keV, respectively. The presence of these spectral features only in the *XMM-Newton* observations is thus indicative of variability at energies ~ 6.6 – 6.7 and ~ 7.3 keV.

5.4.1 The *Suzaku pin* data to constrain the reflection fraction

I add the *pin* data to measure the amount of reflection continuum. and obtain that the *pin* data provide a good quality spectrum up to 50 keV. The model used involves a direct power law plus a neutral reflection component (*pe xrav* model in *Xspec*; Magdziarz & Zdziarski 1995) plus the Fe $K\alpha+\beta$ resolved lines and a broad (DISKLINE) component of the line. As for model B fix some of the parameters of the DISKLINE profile (disc inclination= 30° , $r_{out}=400 r_g$ and $\alpha=-3$). Moreover I assume a high-energy cut off of 100 keV and Solar abundance. Thus, by fitting the

3–50 keV band data, I obtained a reflection fraction $R = 0.4_{-0.2}^{+0.6}$ and a spectral index $\Gamma = 1.76_{-0.03}^{+0.12}$. The total EW of the emission lines above the reflected continuum (about 1.2 keV) is broadly consistent with the theoretical expectations (Matt et al. 1996) and with what observed in CT Seyfert 2 galaxies, where the primary continuum is absorbed and only the reflection is observed. Nevertheless, also for this source, as already known from previous studies (Zdziarski et al. 1999), the spectral index and the reflection fraction are degenerate and strongly depend on the energy band considered. In fact, if the 2–10 keV band is considered, the reflection fraction increases, resulting to be $R = 1.1_{-0.5}^{+0.2}$ and the power-law photon index of $\Gamma = 1.88_{-0.02}^{+0.03}$. The total EW of the Fe emission lines above the reflected continuum are about 750 eV. Again these values are broadly in agreement with expectations (Matt et al. 1996).

5.5 A physically self-consistent fit: possible origin of the spectral features

The analysis of the *XMM-Newton* and data shows evidence for the presence of: i) a resolved, although not very broad, ($\sigma \sim 0.12$ keV) neutral Fe $K\alpha$ line and associated Fe $K\beta$ emission; ii) an ionized Fe K emission line inconsistent with emission from a distant scattering material at rest and most likely produced in the accretion disc; iii) an absorption line at ~ 7.3 keV, present in the summed spectrum of all *XMM-Newton* observations only; iv) an indication for an enhancement of variability - both by considering the *XMM-Newton* data alone and by comparison between the two data sets - at ~ 6.7 keV that could be either due to the high variability of the red wing of the broad ionized Fe K line, possibly associated with a variation of the ionisation of the disc, or to a second ionized absorption line.

These emission/absorption components are partially inter-connected to each other given the limited CCD resolution onboard *XMM-Newton* and . Thus, the *XMM-Newton* (both the pn and MOS in the 3.5–10 keV energy band) have been fit again with a model containing components that better describe the physical processes occurring in the AGN. In particular, I consider two Gaussian lines for the Fe $K\alpha$ and $K\beta$ emission plus a neutral reflection component (*pexrav* in *xspec*) with a reflection fraction $R = 1$ (consistent with the constraints given by the pin data).

The Fe $K\alpha$ line has an equivalent width of 1 keV above the reflection continuum. Moreover, the broad ionized Fe K line is now fit with a fully self-consistent relativistic ionised disc reflection component (*relion* model in *Xspec*; Ross & Fabian 2005, convolved with a *LAOR* kernel; *KDBLUR* in *Xspec*).

The statistics prevents us from constraining the parameters of the relativistic profile. Standard values for the relativistic profile are assumed, with the disc inner and outer radii and the emissivity of 6, 400 r_g , and -3 , respectively. Finally, the ~ 7.3 keV absorption line has been fitted with a photoionised absorption model (*zxcipcf* model in *Xspec*; Miller et al. 2007; Reeves et al. 2008; Model C, Table 1), assuming a total covering factor.

Table 5.1 shows the best-fit parameters. Once the presence of the reflection continuum is taken into account, the power law slope becomes steeper ($\Gamma=1.70\pm 0.01$, $\Delta\Gamma \sim 0.07$) as compared to the fit with a simple power law and emission absorption lines (see §5.3). The best fit energy of the neutral Fe $K\alpha$ line is $E=6.41\pm 0.01$ keV, consistent with being produced by neutral material, and results to be narrower ($\sigma=0.07\pm 0.01$ keV) than in the previous fits. The ionized emission line is fitted with a ionized disc reflection model. The only free parameters of such a component are the inclination and ionisation parameter of the disc that result to be $47\pm 2^\circ$ and $\xi=11_{-7}^{+200}$ erg cm s $^{-1}$ (Model C, Table 1). The material producing the 7.3 keV absorption feature in the *XMM-Newton* data has to be highly ionized, as also indicated by the absence of a strong continuum curvature. In fact, the best ionization parameter is $\log(\xi)=5.15_{-0.52}^{+1.25}$ and the column density $N_H = 5.8_{-4.8}^{+5.2} \times 10^{22}$ cm $^{-2}$. Nevertheless the observed energy of the absorption feature does not correspond to any strong absorption features, thus there is evidence for this absorption component to be outflowing with a shift $v = -0.0484_{-0.013}^{+0.012} c$ ($\sim 14000_{-4200}^{+3600}$ km s $^{-1}$). The resulting χ^2 is 894.3 for 876 dof.

5.6 Discussion

This study clearly shows that long exposures are needed to disentangle the different emitting/absorbing components contributing to the shape-variability of the Fe K complex in Seyfert galaxies. Here, the origin of both neutral and ionized emission and absorption Fe lines in Mrk 509 are discussed recalling that they allow to have insights in the innermost regions of the accretion flow.

5.6.1 Neutral/lowly ionized Fe emission line

Once the broad ionized line is fitted, the width of the Fe $K\alpha$ line lowers to a value of 72 ± 11 eV (see Fig. 5.3) that corresponds to a $\text{FWHM}(\text{Fe } K\alpha) = 8000\pm 1300$ km s^{-1} (see Model C, Table 5.1). This value is slightly higher than that measured by Yaqoob & Padmanabhan (2004) with a ~ 50 ks HETG observation (2820^{+2680}_{-2800} km s^{-1}). The FWHM of the Fe $K\alpha$ line is larger than the width of the $H\beta$ line ($\text{FWHM}(H\beta) = 3430\pm 240$ km s^{-1} ; Peterson et al. 2004; Marziani et al. 2003), indicating that the Fe line is produced closer to the center than the optical BLR and the torus; I note that a wide range of FWHM values is observed for the BLR and the Fe K lines in local Seyfert galaxies (Nandra 2006). However, the UV and soft X-ray spectra of Mrk 509 show evidence for the presence of broad emission lines with FWHM of 11000 km s^{-1} (Kriss et al. 2000). The origin of these UV and soft-X lines is still highly debated, nevertheless they may indicate that the BLR region is stratified, i.e. that these lines are not produced in the optical BLR but in the inner part of a stratified BLR region (see also Kaastra et al. 2002; Costantini et al. 2007), possibly as close as $2000 r_g$ from the center (about 0.012 pc, being the mass of the black hole in Mrk 509 $M_{BH} \approx 1.43\pm 0.12 \times 10^8 M_\odot$ Peterson et al. 2004; Marziani et al. 2003). Nevertheless, if the line is produced in the innermost part of a stratified BLR, it would require either a higher covering fraction or a higher column density than generally derived from the optical and ultraviolet bands. Simulations by Leahy & Creighton (1993) show that about 70 per cent of the sky, as seen by the central source, has to be covered in order to produce the Fe $K\alpha$ line, if the broad line clouds have column densities of about 10^{23} cm^{-2} , while the typical values for the BLR clouds covering fractions are of the order of 10–25 per cent (Davidson & Netzer 1979; Goad & Koratkar 1998). Alternatively, the Fe $K\alpha$ line may be produced by reflection by the outer part of the accretion disc.

5.6.2 Ionized Fe emission lines

The spectrum of Mrk 509 shows emission from ionized iron, consistent with either Fe XXV or Fe XXVI, implying photoionized gas outflowing or inflowing respectively. Alternatively, the ionized Fe K emission may be produced by reflection from the inner part of the accretion disc.

In fact, both the *XMM-Newton* and the *data* are consistent with the two sce-

narios, even if a slightly better fit ($\Delta\chi^2=5.5$ and 9.7 for *XMM-Newton* and , respectively) is obtained in the case of broad line. Moreover in the case of narrow emission lines the emitting gas should have a significant outflow (for Fe XXV, $v\sim 3500$ and 2600 km s⁻¹ for *XMM-Newton* and , respectively) or inflow (for Fe XXVI, $v\sim 4500$ km s⁻¹) with velocities higher than what generally observed (Reynolds et al. 2004; Longinotti et al. 2007; but see also Bianchi et al. 2008 that detect an outflow of $v=900^{+500}_{-700}$ km s⁻¹). On the other hand, the high radiative efficiency of the source ($\eta=0.12$; Woo & Urry 2002) suggests that the accretion disc is stable down to the innermost regions around the BH, where the reflection component should be shaped by relativistic effects. For these reasons, although an outflowing emitting gas is not excluded, the broad line interpretation seems favoured. In fact, the profile of the line is compatible with being shaped by relativistic effects, consistent with its origin being in the surface of an accretion disc, in vicinity of a black hole. Nevertheless, the width of the line is not a compelling evidence. The observed broadening of the line can be reproduced also with the Comptonization process occurring in the upper layer of the ionized accretion disc. Moreover, it must be kept in mind that the main evidences for the presence of a broad Fe K line comes from the mean summed spectrum. The process of summing spectra, although is a powerful way to extract information, might be dangerous in presence of spectral variability and when applied to observations taken many years apart. Thus, the final answer on the origin of these ionized lines will be obtained with either a higher resolution observation or with significantly longer *XMM-Newton* exposures.

5.6.3 Ionized Fe absorption lines

The *XMM-Newton* data indicate the presence of a highly ionized absorption component, the best fit column density being $N_H=5.8^{+5.2}_{-4.8}\times 10^{22}$ cm⁻² and ionization $\log(\xi)=5.15^{+1.25}_{-0.52}$. Moreover, fitting the absorption with this model, it results that the absorber has to be blueshifted by $0.0484^{+0.012}_{-0.013}$ c. The blueshift corresponds to an outflow velocity of ~ 14000 km s⁻¹. The structure implies a significant blueshift if the absorber is located in the core of Mrk 509 but, considering the systemic velocity of the galaxy, its energy is also consistent with a local absorber (McKernan et al. 2004; 2005; Risaliti et al. 2005; Young et al. 2005; Miniutti et al. 2007; but see also Reeves et al. 2008). Nevertheless, the observed variabil-

ity between the *XMM-Newton* and observations points towards an origin within Mrk 509.

An hint of variability is observed around 6.7 keV both in the *XMM-Newton* data and by comparing the *XMM-Newton* and spectra. This could be due in principle to variability in the red wing of the ionized emission line. However, the total rms spectrum shows a peak of variability that is consistent with being narrow, thus it may suggest an alternative explanation. Indeed, the observed difference between the *XMM-Newton* and Fe K line shapes could be due to a further ionized absorption component, present only the *XMM-Newton* observations, with a column density $N_H = 5.4^{+4.8}_{-4.4} \times 10^{21} \text{ cm}^{-2}$ and ionization parameter $\log(\xi) = 2.04^{+0.43}_{-0.60}$. When the structure at 6.7 keV is fitted with such a component, an absorption structure appears around 7.3 keV, nevertheless its equivalent width is not strong enough to reproduce the total absorption feature; moreover, it appears at slightly different energy, not completely fitting the ~ 7.3 keV line. Thus, the absorption structures at 6.7 and the one at 7.3 keV may be connected and they may be indicative of another absorption screen. If this further lower ionization absorption component is present, different absorption feature would be expected (due to the low ionization and high column density) at lower energies. Smith et al. (2007) analyzed the RGS data and detected two absorption components with physical parameters similar ($\log(\xi) = 2.14^{+0.19}_{-0.12}$ and $3.26^{+0.18}_{-0.27}$; $N_H = 0.75^{+0.19}_{-0.11}$ and $5.5^{+1.3}_{-1.4} \times 10^{21} \text{ cm}^{-2}$) to the ones inferred here, strengthening this interpretation.

The observation of highly ionized matter in the core of Mrk 509 is in line with its high BH mass and accretion rate. In fact, the Eddington limit the radiation pressure equals the gravitational pull, however the densities of the matter lowers with the BH mass (Shakura & Sunyaev 1976). Thus the ionization of the material surrounding high accretion rate and BH mass AGNs, such as Mrk 509, should be higher than normal. If true, however, this hypothesis needs far better X-ray data than the (indeed excellent) ones used here.

5.7 Conclusions

The Fe K band of Mrk 509 shows a rich variety of emission/absorption components. The *XMM-Newton* and data shows evidence for the presence of:

- a resolved, although not very broad, ($\sigma \sim 0.07$ keV) neutral Fe $K\alpha$ line and associated Fe $K\beta$ emission. The width of the line suggests that the 6.4 keV line is produced in the outer part of the accretion disc (the broad line region or torus emission seem unlikely). The measured reflection fraction is consistent in this case with the intensity of the line, while a covering factor or column density higher than generally observed would be required if the line were produced in the BLR or the torus;
- both the *Chandra* and the *XMM-Newton* data show an excess due to ionized Fe K emission. Both datasets show a superior fit when a broad ionized line coming from the central parts of the accretion disc is considered. The data are inconsistent with narrow emission from a distant scattering material at rest, while it can not be excluded if the gas is outflowing ($v \sim 3500$ km s⁻¹);
- both EPIC-pn and MOS data show an absorption line at ~ 7.3 keV, present in the summed spectrum of all *XMM-Newton* observations only. This component confirms the presence of highly ionized, outflowing ($v \sim 14000$ km s⁻¹), gas along the line of sight. The comparison between *XMM-Newton* and *Chandra* suggests a variability of this component;
- a hint of an enhancement of variability - both by considering the *XMM-Newton* data alone and by comparison between the two data sets - at ~ 6.7 keV that could be either due to the high variability of the red wing of the broad ionized Fe K line, possibly associated with a variation of the ionisation of the disc, or to a second ionized absorption line.

Chapter 6

Key study objects: ii) NGC 3783

NGC 3783 has been taken as example of objects in which multiple warm absorbers can mimic the broad iron line feature (Reeves et al. 2004), contrary to the initial claim of the presence of a broad iron line emission using ASCA data (Nandra et al. 1997). However, the recent study by De Marco et al. (2006) found evidence for a transient excess feature in the 5–6 keV energy band, interpreted as a redshifted component of the Fe K line. This result is also supported by a variability study by O’Neill & Nandra (2006), who examined rms variability spectra of a sample of bright active galaxies observed with *XMM-Newton*. Given the above considerations, all the *XMM-Newton* observations of NGC 3783 have been re-examined so as to perform a comprehensive study of the iron line temporal evolution, on the shortest possible time-scale.

6.1 *XMM-Newton* observations

XMM-Newton observed NGC 3783 on 2000 December 28–29 and on 2001 December 17–21. The first observation (ID 0112210101) has a duration of ~40 ks while the second (ID 0112210201 and ID 0112210501, hereafter observation 2001a and 2001b respectively) lasts over two complete orbits for a total duration of ~270 ks. Only the EPIC pn data are used in the following analysis because of the high sensitivity in the Fe K band. The EPIC pn camera was operated in the Small Window mode with the Medium filter both during the 2000 and the 2001 observations. The live time fraction is thus 0.7. The data were reduced using the

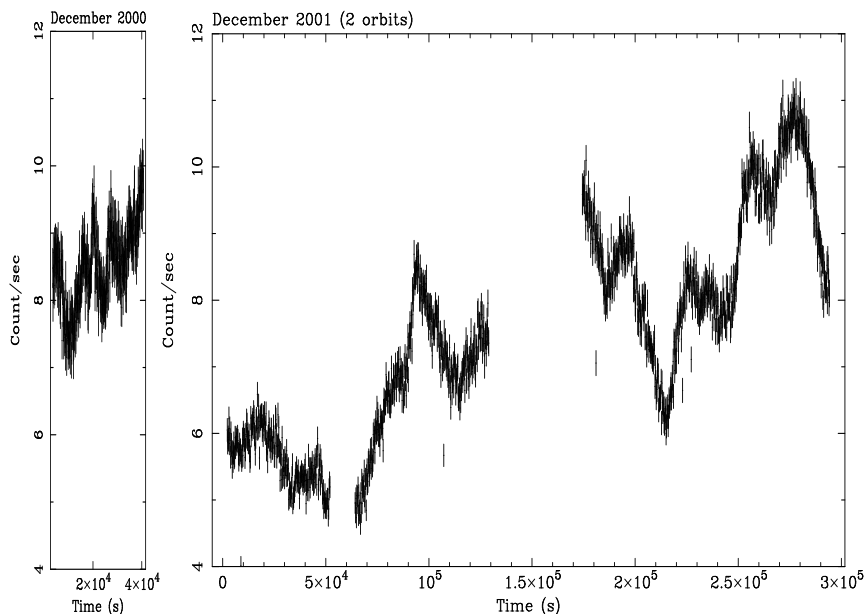


Figure 6.1: The X-ray light curves of NGC 3783 in the 0.3–10 keV band. *Left panel*: light curve of the 2000 observation. *Right panel*: light curves of the 2001a and 2001b observations.

XMM-SAS v. 6.5.0 software while the analysis was carried on using the *lheasoft* v. 5.0 package. High background time intervals were excluded from the analysis. The useful exposure time intervals are listed in Tab. 1, together with the mean 0.3–10 keV count rate for each observation. Only single and double events were selected. Source photons were collected from a circular region of 56 arcsec radius, while the background data were extracted from rectangular, nearly source-free regions on the detector. The background is assumed to be constant throughout the useful exposure. The 0.3–10 keV light curves are shown in Fig. 6.1 for each observation.

6.2 Data analysis

6.2.1 Spectral features of interest and selection of the energy resolution

The time-averaged spectrum was analyzed using the XSPEC v. 11.2 software package. For simplicity, I limited the analysis to the 4–9 keV band. In this energy band, I checked that the complex and highly ionized warm absorber (with $\log \xi$

Obs. ID	Date	Duration (ks)	Exposure (ks)	$\langle CR \rangle$ (c/s)
0112210101	2000 Dec 28–29	40.412	35	8.5
0112210201	2001 Dec 17–19	137.818	115	6.5
0112210501	2001 Dec 19–21	137.815	120	8.5

Table 6.1: Date, duration, useful exposure and mean EPIC pn 0.3–10 keV count rate for each *XMM-Newton* observation of NGC 3783.

and N_H up to $\sim 2.9 \text{ erg cm s}^{-1}$ and $5 \times 10^{22} \text{ cm}^{-2}$, Reeves et al. 2004) shall not affect the conclusions below. The residuals against a simple power-law plus cold absorption continuum model for the 2001b observation, the longest continuous dataset available, are shown in Fig. 6.2. In this fit the Fe K energy band (i.e. 5–7 keV) was excluded and the best fit parameters are $(2.5 \pm 0.6) \times 10^{22} \text{ cm}^{-2}$ and 1.81 ± 0.04 , for the absorber column density and power-law slope respectively.

Four excess emission features are identified: the main Fe $K\alpha$ core at ~ 6.4 keV, a wing to the line core at around 6 keV, a peak at ~ 7 keV (possibly Fe $K\beta$) and a narrow peak at ~ 5.4 keV. Moreover two absorption features at ~ 6.7 keV and ~ 7.6 keV have been also picked-up. When fitted with Gaussian emission and absorption lines, all these features are significant at more than $\sim 99\%$ confidence level. Similar results were also obtained by a detailed analysis with more complex models (Reeves et al. 2004). I will focus here on the analysis of the features variability properties.

The application of the excess map technique to the identified absorption features did not give significant results, thus, in the following, I will focus on the analysis of emission features variability only. The 2001a observation has been divided into two parts because of the gap in the data between $t \sim 5 \times 10^4$ s and $t \sim 6 \times 10^4$ s. Since all the selected spectral features are comparable to the CCD spectral resolution, I chose 100 eV for the energy resolution of the excess maps.

6.2.2 Selection of the time resolution

In choosing the time resolution for the excess maps, it was looked for the best trade-off between getting a sufficiently short time-scale, in order to oversample

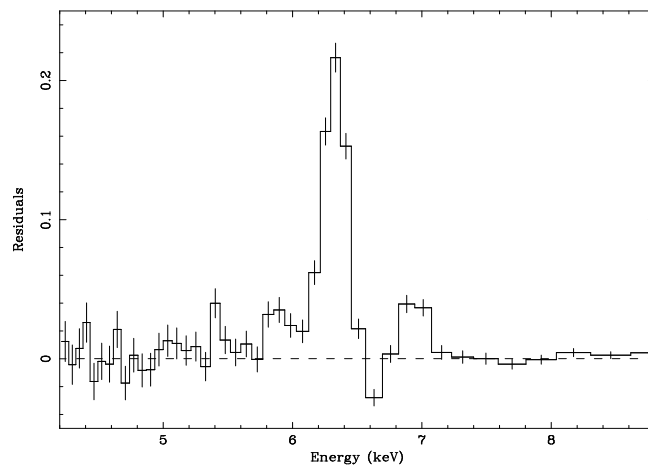


Figure 6.2: The 4–9 keV residuals against a simple power-law plus cold absorption continuum model for the spectrum of NGC 3783 during the 2001b observation. The data are obtained from EPIC pn.

variability, and keeping enough counts in each energy resolution bin. It was first considered the 2001b observation, having the longest and continuous exposure. Spectra were extracted during different time intervals (1 ks, 2.5 ks and 5 ks) around the local minimum flux state at $t \sim 215$ ks. The required condition is that each 100 eV energy bin in the 4–9 keV band has to contain at least 50 counts. At the time resolution of 2.5 ks I got ~ 90 counts per energy bin at the energies of the red feature (5.3–5.4 keV), and ~ 80 counts per energy bin in the wing feature energy band (5.8–6.1 keV). Moreover, for a $10^7 M_{\odot}$ black hole we expect the Keplerian orbital period to be $\sim 10^4$ s at a radius of $10 r_g$. Thus, selecting 2.5 ks as the excess maps time resolution, enables to completely oversample this typical time-scale. This choice of time resolution, optimized for the 2001b observation, was extended to the 2000 and 2001a data.

6.3 Excess emission maps

Energy spectra for a duration of the chosen exposure time (2.5 ks) are extracted in time sequence. 14 spectra are obtained from the 2000 observation, 46 and 48 spectra are obtained from 2001a and 2001b observations respectively. For each spectrum the continuum is determined and subtracted. The residuals in counts

Feature	Energy band (keV)	$\langle I \rangle$ ($10^{-5} \text{ ph s}^{-1} \text{ cm}^{-2}$)
red	5.3–5.4	0.6
wing	5.8–6.1	2
core ($K\alpha$)	6.2–6.5	5.3
$K\beta$	6.8–7.1	1.2
Red+Wing	5.3–6.1	3.2

Table 6.2: Spectral features of interest in the 4–9 keV band with the selected band-passes and mean intensity.

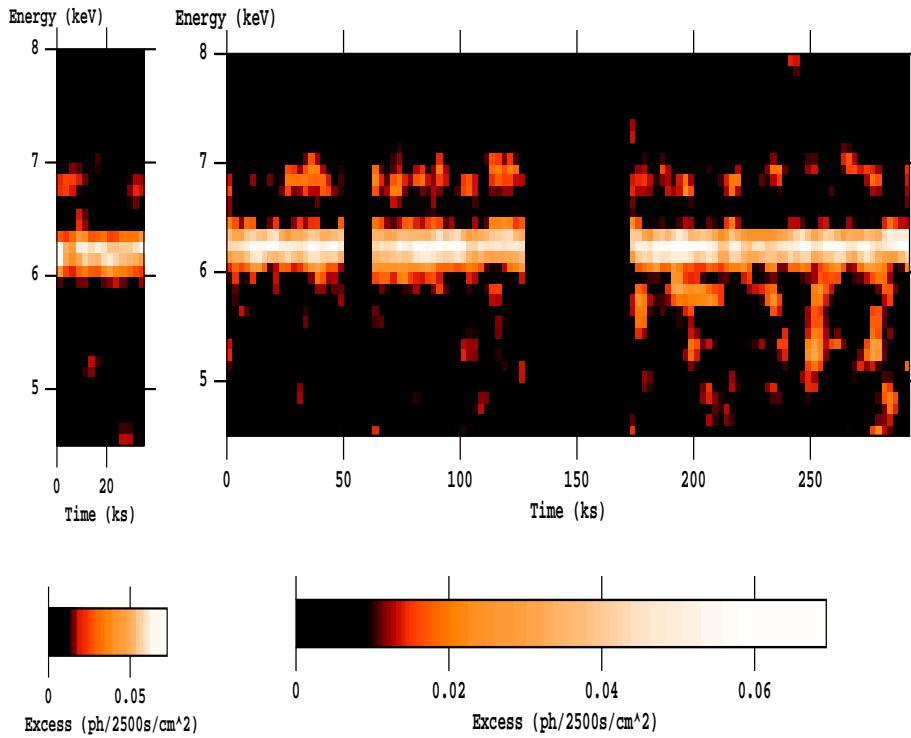


Figure 6.3: The excess emission maps of the 4–9 keV band in the time-energy plane at 2.5 ks time resolution. The images have been smoothed. Since the 6.4 keV line core is very strong and stable, the color map is adjusted to saturate the line core and allow lower surface brightness features to be visible. *Left panel*: excess emission map from the 2000 observation. *Right panel*: excess emission map from the 2001a and 2001b observations.

unit are corrected for the detector response and put together in time sequence to construct an image in the time-energy plane.

6.3.1 Continuum subtraction

The continuum model is assumed to be always a simple absorbed power-law, throughout all the observations. For each spectrum the energy band of the observed spectral features (i.e. 5–7 keV) is excluded during the continuum fit. The 4–5 keV and 7–9 keV data are rebinned so that each channel contains more than 50 counts to enable the use of the χ^2 minimization process when performing spectral fitting and to ensure that the high energy end of the data (7–9 keV) have enough statistical weight. Because of the chosen low energy bound (4 keV), the fit is not sensitive to cold absorption. Thus the cold absorption column density is fixed to the time-averaged spectrum value ($N_H \simeq 2.5 \times 10^{22} \text{ cm}^{-2}$). Each 4–9 keV spectrum at 100 eV energy resolution is then fitted with its best-fit continuum model and residuals are used to construct the excess emission map in the time-energy plane.

Once all the continuum spectral fits have been done, it was checked if continuum changes could affect the measurements of the line fluxes. The mean power-law slopes during the three observations are 1.85, 1.75 and 1.79 respectively, with standard deviations of 0.08, 0.1 and 0.09. The power-law slopes are indeed quite constant, consistent with values obtained from the mean spectrum (§3.1), which result in a very marginal effect ($< 0.1\%$) in the flux measurement of the narrow features I found here. These power-law continuum slopes are also in agreement with those previously found in observations using other instruments with overlapping spectral coverage, like *BeppoSAX* (De Rosa et al. 2002), *ASCA*, *RXTE* and *Chandra* (Kaspi et al. 2001).

6.3.2 Image smoothing

As discussed in Iwasawa, Miniutti & Fabian (2004), if the data are acquired continuously and the characteristic time-scale of any variation in a feature of interest is longer than the sampling time (i.e. the time resolution), it is possible to suppress random noise between neighboring pixels by applying a low-pass filter. Here it was used a circular Gaussian filter with $\sigma=0.85$ pixel (200 eV in energy and 5 ks in time, FWHM). The Gaussian-filtered images of the excess map for each ob-

ervation are shown in Fig. 6.3. Systematic variations are observed in the 5.3–5.4 keV and in the 5.8–6.1 keV energy bands of the 2001b observation. However, the image filtering can slightly smear these narrow features and reduce their intensity.

6.4 Results

6.4.1 Light curves of the individual spectral features

Light curves of the four emission features are extracted from filtered images of the excess map. The selected band-passes are listed in Tab. 2. During the image filtering process individual pixels lose their independence to the neighbouring ones. This means that a simple counting statistics is inappropriate for estimating the features light curves errors. For this reason the estimation of the errors has been done by extensive Monte Carlo simulations. 1000 simulations were implemented following the same procedure in making the excess map images. In the simulations all the spectral features parameters and the power-law slope are assumed to be constant, while letting the power-law normalization vary according to the 0.3–10 keV light curve. Light curves of individual spectral features have been extracted from each simulation and their mean values and variances recorded. The square root of the mean of the variances (i.e. the dispersion) has been regarded as the light curves error. In Fig. 6.4 the emission features light curves for the 2001a and 2001b observations are shown. The 2000 observation light curves are not reported because they do not show any sign of variability. The most intense variations are registered in the light curves of the red ($E=5.3\text{--}5.4$ keV) and wing ($E=5.8\text{--}6.1$ keV) features during the 2001b observation. The observed peaks seem to follow the same kind of variability pattern and, as shown in more details below, appear to be in phase with the continuum emission. In order to check the significance of the observed variability both real and simulated data light curves were extracted in the entire 5.3–6.1 keV band, i.e. of the red+wing structure. The χ^2 values were then probed against a constant hypothesis for the real data and the 1000 simulations; equivalent results can be derived comparing the variances directly. Only 73 of 1000 simulations show variability at the same or larger level than the real data, therefore the variability confidence level was of 93%.

The light curves of the excess emission features in the 5–6 keV energy band (red,

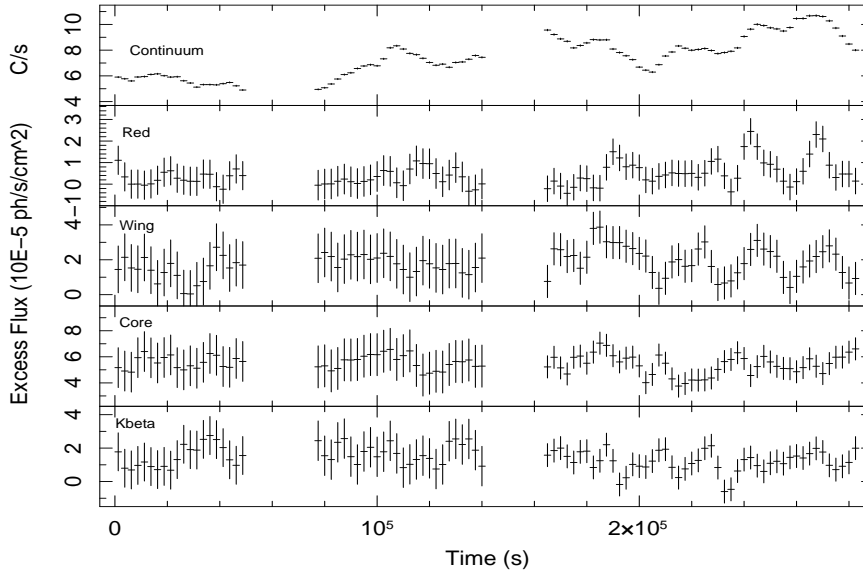


Figure 6.4: The light curves of the total 0.3–10 keV continuum flux and of the four spectral features (Tab. 2) extracted from the excess maps of the 2001a and 2001b observations (Fig. 6.3, Right panel), with errors computed from simulations. The time resolution is 2.5 ks.

wing and red+wing) seem to show a variability pattern with a recurrence of the flux peaks on time-scales of 27 ks. Thus it was investigated how it is likely to occur by chance applying a method that makes use of the 1000 Monte Carlo simulations. The real data light curve was folded with the interval of 27 ks and fitted with a constant, obtaining a $\chi_r^2 = 88$ for 19 degrees of freedom. The same was done to the simulated red+wing light curves but, this time, folding in $n = 9$ trial periods, from 17 to 37 ks at intervals of 2.5 ks, and recorded the χ_i^2 values. If N is the total number of simulated red+wing light curves for which $\chi_i^2 \geq \chi_r^2$, the confidence level can be derived as $(1 - \frac{N}{1000-n})$. Only $N = 54$ of the simulated red+wing light curves folded at the trial periods show chi-square values greater than the real one. Therefore, it can be derived a confidence level for the recurrence pattern on the 27 ks time scale of 99.4%.

Finally, the continuum above 7 keV (which carries the photons eventually responsible for the Fe line production) was checked founding that it varies following the same pattern of the 0.3–10 keV band (Fig. 6.4, Top panel).

6.4.2 Correlation with the continuum light curve

In the 0.3–10 keV light curve of observation 2001b (Fig. 6.5, Upper panel) flux variations of $\sim 30\%$ are visible with four peaks separated by approximately equal time intervals. Given such peculiar time series shape, I focused on this observation and searched for some typical time-scale in the variability pattern. Thus, I applied the *efsearch* task (in *Xronos*), which searches for periodicities in a time series calculating the maximum chi-square of the folded light curve over a range of periods. A typical time-scale for variability of 26.6 ± 2.2 ks was found. The underlying long-term variability trend was then removed by subtracting a 4th degree polynomial to the 0.3–10 keV continuum light curve (see Fig 6.5, Middle panel). The polynomial has been determined using the *lcurve* task (in *Xronos*), which makes use of the least-square technique. Applying again the *efsearch* task, a typical time-scale for short-term variability of ~ 27.4 ks¹ was found.

The peaks observed in the continuum light curve seem to appear at the same times at which those observed in the wing and red light curves do. In order to look for some correlation between the continuum and the 5.3–6.1 keV (red+wing) feature flux, it was calculated the cross correlation function (CCF) between the two time series where the input continuum light curve is the de-trended one. It is reported in Fig. 6.6 as a function of time delay, measured with respect to the continuum flux variations. No delay is evident, with an estimated error at the peak of 2.5 ks. The continuum and red+wing fluxes seem to show a correlation, with peak value 0.7. To estimate the significance of the correlation the CCFs was then computed between the continuum and the simulated red+wing light curves. If N is the number of simulated light curves which have a higher cross correlation than the real one, the significance of the correlation is $(1 - N/1000)$. Applying this method, a confidence level greater than 99.9% was found.

6.4.3 High/Low flux state line profiles

Looking at the “red+wing” light curve (Fig. 6.5, Lower panel) I constructed two spectra from the integrated high and low flux intervals to verify the variability

¹It should be noted that the variability PSD study of this *XMM-Newton* dataset by Markowitz (2005) suggests an excess of power around 4×10^{-5} Hz (corresponding to about 25 ks) during the 2001b observation (square symbols in his Fig. 6.3).

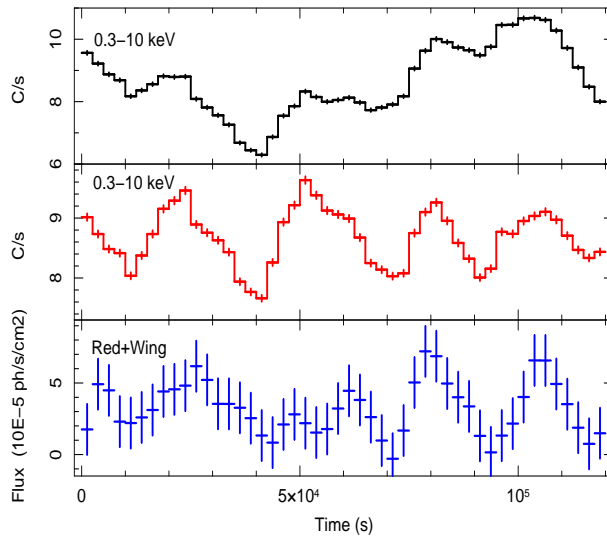


Figure 6.5: *Upper panel:* The 0.3–10 keV light curve of NGC 3783 during 2001b observation at 2.5 ks time resolution. *Middle panel:* The 0.3–10 keV light curve of NGC 3783 during the 2001b observation after subtraction of a 4th degree polynomial (long-term variations) at 2.5 ks time resolution. *Lower panel:* The 5.3–6.1 keV (‘red+wing energy band’) light curve extracted from the excess emission map of the 2001b observation (Fig. 6.3, Right panel) at 2.5 ks time resolution.

in this energy band. The line profiles are shown in Fig. 6.7 where the ratio between the data and a simple power-law plus cold absorption model is shown. While the 6.4 keV and 6.9 keV features remain the same, a small increase of counts is visible in the 5.3–5.4 keV and 5.8–6.1 keV bands in the high flux state. Adding an emission Gaussian model to the simple power law plus Gaussian line (at the Fe K α energy) model in the high flux state integrated spectra improves the χ^2 of 18. Thus the significance of the excess is $\sim 99.9\%$.

6.5 The deduced scenario for NGC 3783

The most remarkable result of this analysis is the detection of redshifted (5.3–6.1 keV) Fe K emission and of its variability. The redshifted emission appears to respond only to the shorter ~ 27 ks time-scale modulation and shows a good correlation with the continuum with a time-lag consistent with zero within the errors ($\Delta\tau \sim 1.25$ ks). This indicates that the continuum modulation on this time interval

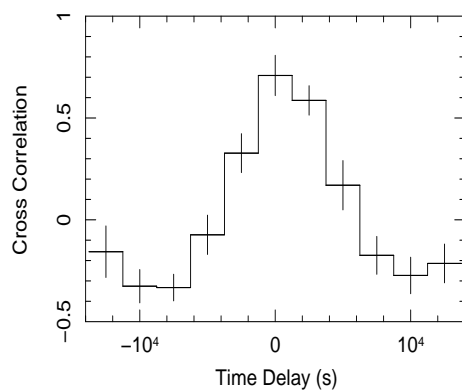


Figure 6.6: The cross correlation function calculated between the de-trended 0.3–10 keV continuum light curve and the 5.3–6.1 keV feature (red+wing) light curve.

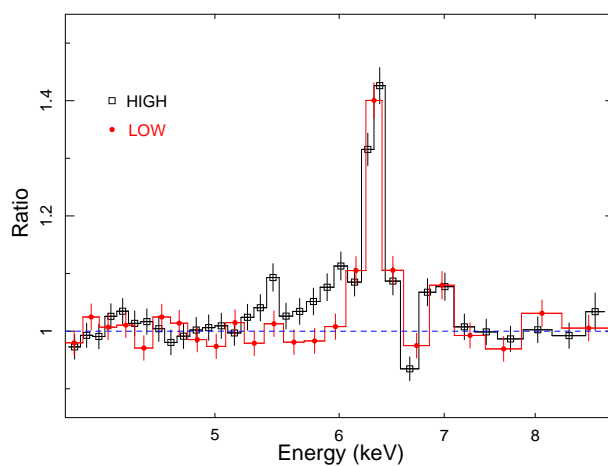


Figure 6.7: The Fe K line profile during the High flux (open squares) and the Low flux (solid circles) phases of the 5.3–6.1 keV feature. The ratios are computed against the best-fitting continuum model. The energies are in the observer frame.

is likely to induce Fe K emission from dense material close to the black hole (which explains the observed redshift of the emission feature); moreover the lack of time-lags implies that the distance between the sites of continuum and line production is smaller than $c\Delta\tau \sim 4 \times 10^{13} \text{ cm} \sim 8 r_g$ (for the black hole mass given above). We are therefore most likely observing emission from the innermost accretion flow in both the continuum and line emission (corona and disc).

As discussed above, the variability time-scale suggests that we are looking at emission from around $\sim 9\text{--}10 r_g$. As a consistency check, I thus fit the time-averaged spectrum by including a *diskline* component to account for the redshifted features. I forced the emission region to be an annulus of $\Delta r = 0.5 r_g$ with uniform emissivity because the purpose of this test is to assess the approximate location of the line-emitting region. Good fits are obtained with an almost face-on disc ($i = 11 \pm 4^\circ$) and an annulus at $9\text{--}15 r_g$ depending on the assumed Fe line rest-frame energy (from neutral at 6.4 keV to highly ionized at 6.97 keV). For all cases I tested, the statistical improvement is of $\Delta\chi^2 \sim 16$ for 3 additional degrees of freedom, corresponding to a confidence level of 99.7%. This fit shows that the detected redshifted Fe line emission is indeed consistent in shape with being produced around $10 r_g$, where the disc orbital period is of the order of 27 ks, which agrees well with the correlated (and zero-lag) variability of the two components.

The interpretation of this results is not straightforward, however. The quasi-sinusoidal modulations of the continuum and line emission (see Fig. 6.5) would suggest the presence of a localized co-rotating flare above the accretion disc which irradiates a small spot on its surface. The intensity modulations (Fig. 6.5) would then be produced by Doppler beaming effects (acting on both the flare and spot emission, i.e. on both continuum and line) and the characteristic time-scale of 27 ks would be identified with the orbital period (because of gravitational time dilation, the period measured by an observer on the disc at $10 r_g$ would be shorter by $\sim 10\%$). As demonstrated above, a flare/spot system orbiting the black hole at $\sim 10 r_g$ would also produce a time-averaged line profile in agreement with the observations. However, such a model makes definite prediction on the Fe line energy modulation within one orbital period. In this framework, the orbiting spot on the accretion disc would also give rise to energy modulations of the Fe line due to the Doppler effect and such energy modulation is barely seen in the data (see Fig. 6.3). It must be stressed that the adopted time resolution (2.5 ks) is good

enough to detect energy modulations with a characteristic 27 ks time-scale. This has been demonstrated with *XMM-Newton* in the case of NGC 3516, where the modulation occurs on a very similar time-scale (Iwasawa et al. 2004; see also Dovčiak et al. 2004 for theoretical models). Therefore, the lack of Fe line energy modulation disfavors the orbiting flare/spot interpretation for NGC 3783.

However, a variability time-scale of the order of the orbital one at a given radius does not necessarily imply the motion of a point-like X-ray source. In fact, since the orbital time-scale is the fastest at a given disc radius, and since the observed time-scale of ~ 27 ks corresponds to the orbital period at $\sim 10 r_g$, one could argue that the data only imply that the X-ray variability likely originates from within $\sim 10 r_g$. The apparent recurrence in the X-ray continuum modulation may not necessarily be related to a real physical periodicity, especially considering the limited length of the observation (only four putative cycles are detected).

A possible explanation for the observed behaviour is that the X-ray continuum source(s) (located within $\sim 10 r_g$ from the center) irradiates the whole accretion disc, but only a ring-like structure around $10 r_g$ is responsible for the fluorescent Fe emission. This is possible if the bulk of the accretion disc is so highly ionized that little Fe line is produced, while an over-dense (and therefore lower ionization) structure is responsible for the fluorescent emission. Such an over-dense region could have an approximate ring-like geometry if it is for instance associated with a spiral-wave density perturbation. In this case, the Fe emitting region is extended in the azimuthal direction and there is not need of strong energy modulation with time, whatever the origin of the continuum modulation. The spiral density distributions could result from the ordered magnetic fields in the inner region of the disc and the energy dissipation (via e.g. magnetic reconnection) could be enhanced there, thereby providing a common site for the production of the X-ray continuum and the Fe line (e.g. Machida & Matsumoto 2003).

On the other hand, if the apparent recurrence is in fact real, it is worth noting that the continuous theoretical effort in understanding the origin of quasi-periodic oscillations (QPO) in neutron star and black hole systems provides a wealth of mechanisms inducing quasi-periodic variability, although none is firmly established (Psaltis 2001; Kato 2001; Rezzolla et al. 2003; Lee et al. 2004; Zycki & Sobolewska 2005 and many others). A connection between QPO phase and Fe line intensity has been previously claimed in the Galactic black hole GRS 1915+105

(Miller & Homan 2005). Although in this case, the presence of a QPO cannot be claimed because of the very small number of detected cycles, the analogy is suggestive. In the case of GRS 1915+105, Miller & Homan consider that a warp in the inner disc, possibly due to Lense-Thirring precession, may produce the observed QPO-Fe line connection (e.g. Markovic & Lamb 1998). However, to produce the observed $\sim 15\%$ rms variability in the X-ray lightcurve, the black hole spin axis should be inclined with respect to the line of sight by at least 60° (which is at odds with the inclination estimate of $11 \pm 4^\circ$ and with the Seyfert 1 nature of NGC 3783), and the tilt precession angle should be larger than 20° – 30° (Schnittman, Homan, Miller 2006). Both requirements make it highly unlikely that Lense-Thirring precession can successfully account for the observed modulations in NGC 3783.

While the origin of the coherent intensity modulation still remains unclear, the correlated variation of the continuum and line emission and the Fe line shape are consistent with an emission site at $\sim 10 r_g$. Moreover, the fact that the iron line variability responds to the 27 ks time-scale modulation only implies that this short time-scale variation is somehow detached from the long-term variability. The latter may be associated with perturbations in the accretion disc propagating inwards from outer radii and modulating the X-ray emitting region (Lyubarskii 1997), while the former seems to genuinely originate in the inner disc.

Chapter 7

Key study objects: iii) IRAS 13197-1627

IRAS 13197–1627 (also MCG–03-34-064, $z=0.01654$) is a *warm* ($f_{25\mu m}/f_{60\mu m} \sim 0.48$) and luminous IR–galaxy with $L_{IR}=L(8-1000 \mu m)=1.7 \times 10^{11} L_{\odot}$ (Sanders et al. 2003). It was first classified as a moderately reddened Seyfert 2 by Osterbrock and de Robertis (1985) & de Robertis, Hutchings & Pitts (1998). However, as pointed out by these authors, the source has peculiar emission–line properties: in particular its $H\alpha$, $[O_I]$, $[N_{II}]$, and $[S_{II}]$ are both exceptionally broad for Seyfert 2 galaxies (with FWHMs from 480 km s^{-1} to 860 km s^{-1}) and asymmetric, with excess flux blue–wards of their centres. In the UV, most of the lines are broad at the level seen in the Optical, and C_{IV} as a width comparable to those typically measured in Seyfert 1 galaxies. Agüero et al (1994) were able to disentangle broad and narrow components of the $H\alpha$ and $H\beta$ lines which led to a Seyfert 1.8 classification. A broad component to $H\alpha$ was also detected by Young et al (1996) in polarised light. Signatures of the presence of Wolf–Rayet stars have been reported by Cid Fernandes et al (2004) who also estimate that about 25 per cent of the stellar population is relatively young (less than 25 Myr). Extended Radio emission is also detected with a linear extension of about 280 pc, almost aligned with the host galaxy major axis (Schmitt et al. 2001a; 2001b) while the 1.4 GHz luminosity is $1.6 \times 10^{30} \text{ erg s}^{-1} \text{ Hz}^{-1}$ (Condon et al. 1996).

In the X–rays, the source was first observed with ASCA in 1995 revealing a very steep spectral shape (photon index $\Gamma \simeq 3$), a large absorbing column density

$N_H \approx 6 \div 8 \times 10^{23} \text{ cm}^{-2}$, a narrow Fe emission line at 6.4 keV, and a *soft excess* component emerging below about 2 keV (Ueno 1997). A *BeppoSAX* observation was obtained in 1998 and was first published by Risaliti (2002) in a statistical study of 20 bright Seyfert 2 galaxies. A variation in the absorbing column density between the *ASCA* and the *BeppoSAX* observations was later suggested by Risaliti, Elvis & Nicastro (2002). A more detailed analysis of the *BeppoSAX* data was presented by Dadina & Cappi (2004). The absorbing column was found to be dependent on the adopted spectral model so that the column density variation could not be confirmed (this topic will be discussed in the next sections). The better quality, broadband *BeppoSAX* data also revealed spectral complexity that could be modelled in terms of a partial covering scenario or of a reflection-dominated model in which X-ray reflection from the accretion disc dominates the hard spectral shape. In both cases, Dadina & Cappi estimated an intrinsic 2–10 keV luminosity of $\sim 2 \times 10^{44} \text{ erg s}^{-1}$, making IRAS 13197–1627 the nearest and brightest type-1.8 quasar known to date. An absorption line at $\sim 7.5 \text{ keV}$ was also detected and, if interpreted as He-like Fe resonant absorption, the line energy implies an outflow with a velocity of the order of 0.1 c.

7.1 The XMM–Newton observation and first-look analysis

IRAS 13197–1627 was observed by *XMM–Newton* on 2005 January 24 for a total exposure of 45 ks. The data have been processed starting from the ODF files with the *XMM–Newton* SAS software (version 6.5.0). Source spectra and light curves of the EPIC cameras were extracted from circular regions centred on the source, while background products were extracted from off-set regions close to the source. I remind here that the background region of the pn camera has to be taken as close to the centre as possible to avoid contamination from the strong spatially dependent fluorescent Cu $K\alpha$ emission line originating from the electronics board mounted below the pn CCD which would result in a spurious absorption line around 8 keV in the (background subtracted) source spectrum. With the adopted choice of the background extraction region, such contamination is negligible. After filtering for periods of high background the net exposure is 37 ks in the pn cam-

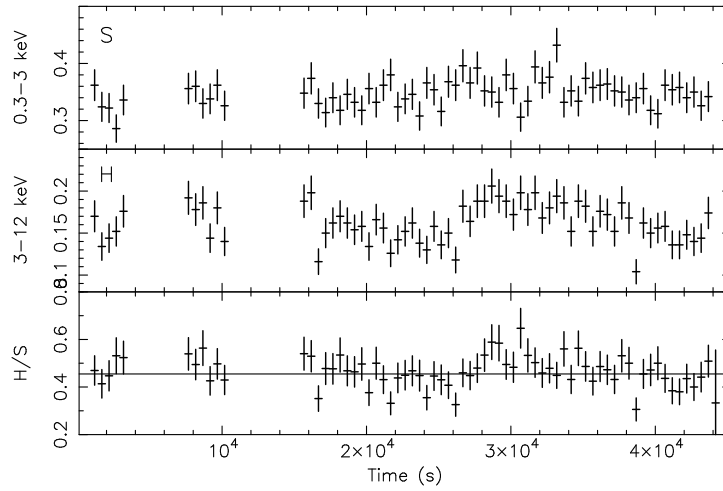


Figure 7.1: Soft (S: 0.3–3 keV) and a hard (H: 3–12 keV) EPIC–pn source light curve together with the resulting hardness ratio (bottom panel). As revealed by fitting a constant to the data, the hard band is more variable than the soft one ($\chi_r^2 = 1.65$ vs. $\chi_r^2 = 0.85$ for 67 dof). However, the hardness ratio is still consistent with a constant value throughout the observation.

era and 39 ks (43 ks) in the MOS 1 (MOS 2) detectors. The EPIC spectra were grouped to have at least 20 counts per bin to ensure the validity of χ^2 statistical analysis. The RGS were operated in the standard spectroscopy mode and standard data reduction was performed resulting in a net exposure of about 43 ks in the RGS detectors.

In Figure 7.1 the background–subtracted source light curves in a soft (S: 0.3–3 keV) and a hard (H: 3–12 keV) energy band are shown: these curves were obtained after removal the residual background flares. No strong variability is seen in the soft band and a fit with a constant is very satisfactory ($\chi_r^2 \simeq 0.85$ for 67 dof). More fluctuations are present in the hard band ($\chi_r^2 = 1.65$). In the bottom panel, it is plotted the hardness ratio and it is compared with the best–fitting constant value producing an acceptable fit with $\chi_r^2 = 1.1$. Given the limited evidence for spectral variability, in the following only the time–averaged spectrum of the source is considered. The broadband EPIC–pn spectrum of IRAS 13197–1627 is shown in Figure 7.2. The MOS data are not shown for visual clarity and agree very well

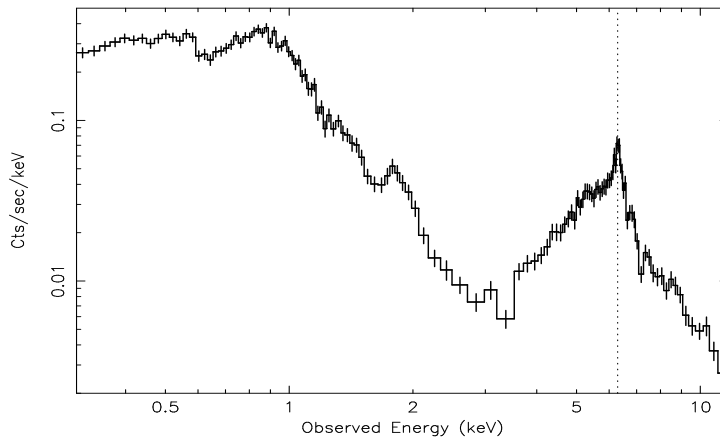


Figure 7.2: The broadband (0.3–12 keV) EPIC–pn spectrum of IRAS 13197–1627. The spectrum exhibits strong curvature in the hard band which is a clear sign of absorption by a substantial column of gas in the line of sight. Fe emission is detected at 6.4 keV in the rest–frame (vertical dotted line) together with a deep absorption edge at 7 keV. A soft excess is present below ~ 3 keV and is characterised by a bump around 0.9 keV. Data have been rebinned for visual clarity.

with the pn. The main features of the spectrum are i) strong curvature in the hard band with a ~ 3 –4 keV low–energy cut–off and a deep spectral drop around 7 keV where the Fe absorption edge is expected; ii) a clear narrow Fe emission feature at 6.4 keV (vertical dotted line in Figure 7.2); iii) a soft excess emerging below 2–3 keV which seems structured rather than smooth, especially around 0.9–1 keV. In this thesis I adopt standard cosmology parameters ($H_0 = 75 \text{ km s}^{-1}$, $\Lambda_0 = 0.73$, and $q_0 = 0$).

7.2 The 2–12 keV spectrum of IRAS 13197–1627

In the analysis, joint fits to the EPIC–pn and MOS (1 and 2) cameras were considered. The pn data are considered up to 12 keV, while for the MOS the analysis is limited up to 9.5 keV due to the lack of signal–to–noise above that energy. As a first attempt to describe the hard spectrum above 2 keV, it is first used a simple model in which a power law is absorbed by neutral matter at the redshift of the source (the ZWABS model in XSPEC). A second power law component emerging at soft energies, to account for the soft excess, is also included. The two

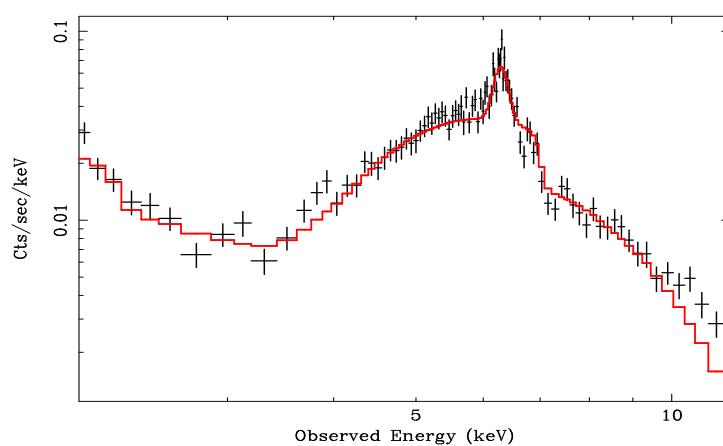


Figure 7.3: The 2–12 keV pn spectrum is shown together with a simple model (solid line) comprising a power law absorbed by a column density of $\sim 6.2 \times 10^{23} \text{ cm}^{-2}$ of neutral matter at the redshift of the source and a resolved ($\sigma \sim 90 \text{ eV}$) Gaussian emission line at 6.4 keV. Only the pn data are shown but all spectral analysis is performed simultaneously with the MOS data as well. Notice several residuals: absorption structures are seen around 6.8 keV and 7.1 keV. Moreover the model systematically underestimates the data in the 5–6 keV band and above 10 keV. In the Figure, data have been rebinned for visual clarity.

power law slopes (Γ_h and Γ_s respectively) are allowed to be different. The observed Fe line at 6.4 keV is modelled with a Gaussian emission line with width, energy, and normalisation free to vary. All subsequent fits include Galactic absorption with column density fixed at its nominal value ($5.8 \times 10^{20} \text{ cm}^{-2}$, Dickey & Lockman 1990).

With this simple model, an acceptable fit to the 2–12 keV data is obtained with $\chi^2 = 519$ for 447 degrees of freedom (d.o.f.). The hard power law has a slope $\Gamma_h = 2.9 \pm 0.4$, marginally consistent with the soft one ($\Gamma_s = 2.4 \pm 0.4$). The ratio of the soft to the hard power law normalisations is of about 1–2 per cent only. The neutral absorber affects the hard band above ~ 3 keV and is Compton–thin with a column density of $6.2 \pm 0.5 \times 10^{23} \text{ cm}^{-2}$.

The Fe emission line is clearly detected ($\Delta\chi^2 = 160$ for 2 more free parameters) and has an energy of 6.40 ± 0.02 keV indicating an origin in neutral matter. The line has an observed equivalent width (EW) of 140 ± 20 eV when computed with respect to the unabsorbed continuum, to be compared with the theoretical prediction of 80 eV for a line transmitted through the observed column density (e.g. Matt 2002). Thus, the Compton–thin absorber (if solar Fe abundance is assumed) is not sufficient to explain the strength of the Fe line and the issue is examined in a more detailed analysis in the next Section.

The Fe line width is $\sigma = 90_{-20}^{+40}$ eV, significantly broader than the EPIC cameras spectral resolution (~ 40 eV in σ). The measured Fe line width corresponds to a FWHM = $1.21_{-0.33}^{+0.44} \times 10^4$ km/s. Under the assumption that the line emitting gas is gravitationally bound and that gas motion occurs in randomly oriented circular orbits, the line width places the emitting gas *within* 2×10^3 gravitational radii ($r_g = GM/c^2$) from the central black hole (Krolik 2001). If the line, as is likely, is transmitted through the Compton–thin absorber, the line width would place the absorber much closer to the nucleus than often thought (e.g. Galactic discs, Maiolino & Rieke 1995; dust lanes, Malkan, Gorijn & Tam 1998; Guainazzi, Matt & Perola 2005; starburst clouds, Weaver 2001; see also Lamastra, Perola & Matt 2006). However, a much closer location of the absorbing gas, consistent with the measured line width, has been proposed by e.g. Elvis (2000; 2004). The case for an absorber located close to the nucleus is particularly compelling in NCG 1365 (Risaliti et al. 2005) in which rapid transitions between Compton–thin and Compton–thick absorption have been observed. On the other hand, as it will be discussed below, the

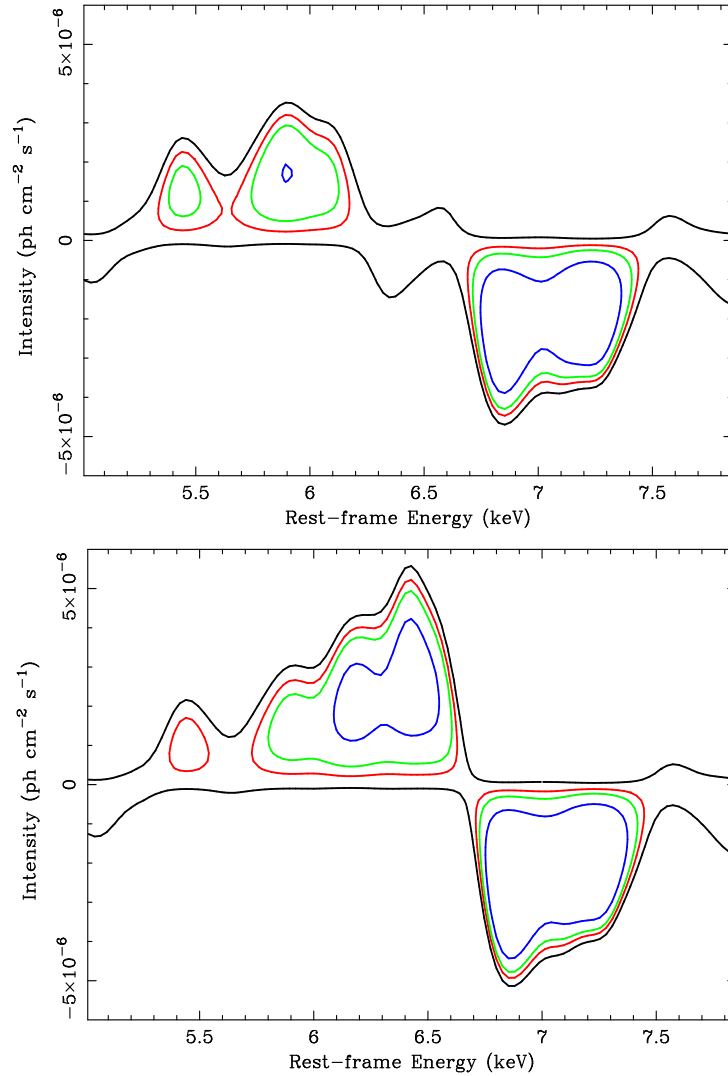


Figure 7.4: **Top:** A Gaussian line is added to the baseline model and its energy and normalisation are varied. The contours represent an improvement of $\Delta\chi^2 = -1, -2.3, -4.61, -9.21$ in fitting the joint pn-MOS data. The $\Delta\chi^2 = -1$ contour (outermost) is shown as a reference of the best-fitting continuum model. **Bottom:** In this case the Fe K α line of the baseline model is forced to be unresolved. The shape of the residuals strongly suggests the presence of X-ray reflection from the disc (broad Fe emission line and broad Fe absorption edge).

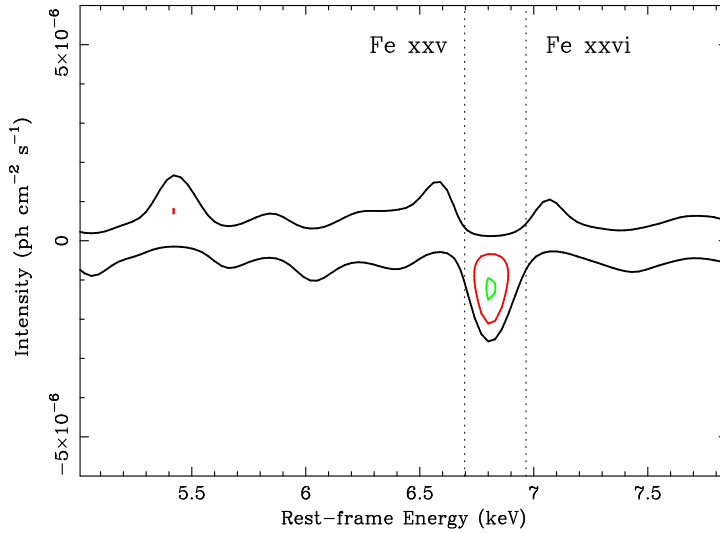


Figure 7.5: Same as in Figure 7.4, but now for the best-fitting model comprising Compton-thin absorption and reflection from the accretion disc, both with slightly super-solar Fe abundance (see text for details). The only remaining residual is a narrow absorption line at 6.8 keV. The rest-frame energies of the closest transitions (Fe_{xxv} and Fe_{xxvi} resonant absorption) are shown as vertical lines.

observed Fe line width could be due to an unmodelled broader component to the Fe line profile.

Although this simple spectral model (hereafter the “baseline model”) provides a reasonable description of the hard spectrum, several residuals are present as shown in Figure 7.3. Two absorption features are seen around 6.8 keV and 7.1 keV, while positive residuals are left at high energy (above 10 keV) and in the 5–6 keV band where the model seems to systematically underestimate the data. As a first check for the significance of the residuals, an unresolved Gaussian line is added to the baseline model, varying its energy in the 4–8 keV range and its normalisation in the $\pm 1 \times 10^{-5}$ ph cm⁻¹ s⁻¹ range, and the χ^2 improvement is recorded (see Miniutti & Fabian 2006 for more details). The results are presented in the top panel of Figure 7.4 where the 68, 90, and 99 per cent confidence contour levels are shown both for the additional Gaussian line rest-frame energy and intensity in the most relevant band around the Fe K complex. The outermost line shows the $\Delta\chi^2 = -1$ contour as reference.

Although the contours should not be taken as a precise significance test, they indicate the relative importance of the residuals. Figure 7.4 clearly reveals both positive and negative residuals on the red and blue side respectively of the Fe $K\alpha$ line (6.4 keV). If the Fe $K\alpha$ emission line in the best-fitting model is forced to be narrow (i.e. unresolved, as in most Compton–thin sources), the bottom panel figure is obtained, where the positive residuals are very reminiscent of X–ray reflection from the accretion disc resulting in a skewed and broad Fe emission line and Fe absorption edge. With the caveats mentioned above, the significance of the whole structure seem to be higher than 99 per cent. A more detailed spectral modelling of these absorption and emission features is presented below.

7.2.1 X–ray reflection from the accretion disc and Fe ν resonant absorption

The shape of the residuals in Figure 7.4 strongly suggests that both the positive and negative residuals could be accounted for by a reflection component from the accretion disc. Thus, a relativistically blurred reflection spectrum has been added. It is worth considering here that the used model for the reflection computes the continuum and emission lines self-consistently (from Ross & Fabian 2005). The model free parameters are the ionization parameter ξ , the illuminating power law slope, the normalisation, and the Fe abundance. To test whether the Fe abundance is different from solar, it is let free to vary, replacing the Compton–thin absorber model with one which allows to vary the Fe abundance (ZVFEABS). The Fe abundance in the two models is forced to be the same. The illuminating power law slope is forced to have the same photon index as the hard power law continuum. The relativistic blurring is obtained by using a LAOR kernel in which the emissivity profile is fixed at its standard value ($\epsilon = r^{-3}$), the outer disc radius at $400 r_g$, while the inner disc radius and observer inclination are free parameters. The reflection spectrum is absorbed by the same column density as the continuum.

This model allows to obtain a very significant improvement with respect to the previous model, with $\Delta\chi^2 = 63$ for 5 more free parameters ($\chi^2 = 456$ for 442 dof). Since the reflection model does not include emission from Ni (see Ross & Fabian 2005), a Gaussian emission line with energy between 7.4 keV and 7.6 keV is added and to it is applied the same relativistic blurring as for the reflection spectrum,

Table 7.1: The best-fitting parameters from joint fits to the 2–12 keV (pn) and 2–9.5 keV (MOS) spectrum of IRAS 13197–1627 ($\chi^2 = 442$ for 438 dof).

Parameter	Value	F-test
Continuum		
Γ_h	2.5 ± 0.3	
N_h [10^{-3} ph cm $^{-2}$ s $^{-1}$]	$5.7^{+1.6}_{-1.9}$	
Γ_s	2.1 ± 0.4	
N_s [10^{-5} ph cm $^{-2}$ s $^{-1}$]	8.2 ± 4.8	
Absorption		> 99.99%
N_H [10^{23} cm $^{-2}$]	3.9 ± 0.4	
Fe abundance		99.8%
A_{Fe} [solar]	1.5 ± 0.3	
Transmitted Fe Kα line		> 99.99%
E [keV]	6.40 ± 0.02	
σ [eV]	< 85	
EW [eV]	105 ± 18	
Disc reflection		99.8%
ξ [erg cm s $^{-1}$]	< 60	
E_{Ni} [keV]	7.5 ± 0.06	94.8%
EW_{Ni} [eV]	60 ± 40	
R	10 ± 3	
r_{in} [$r_g = GM/c^2$]	7^{+7}_{-5}	99.1%
i [degrees]	27 ± 17	
Fexxv absorption line		98.1%
E [keV]	$6.81^{+0.08}_{-0.06}$	
EW [eV]	-50 ± 30	
Flux and Luminosity		
F_{2-10} [10^{-12} erg cm $^{-2}$ s $^{-1}$]	2.1 ± 0.2	
L_{2-10}^{obs} [10^{43} erg s $^{-1}$]	0.7 ± 0.2	
L_{2-10}^{est} [10^{43} erg s $^{-1}$]	$4.2^{+2.8}_{-2.2}$	

The EW of the Fe K α emission line is computed with respect to the unabsorbed continuum assuming it is transmitted and not absorbed. If the line is assumed to be absorbed by the same column as the continuum its EW is 160 ± 70 eV. The F-test results are obtained by removing the relevant component from the model and by re-fitting the data. The F-test corresponding to r_{in} in the *Disc reflection* section is relative to the relativistic blurring kernel, i.e. it provides the significance of the relativistic effects.

obtaining a marginal improvement of $\Delta\chi^2 = 6$ for 2 more free parameters. Before discussing the best-fit parameters, here it is considered again the procedure used to produce Figure 7.4 on this best-fitting model to search for any other possible residual (see Figure 7.5). The X-ray reflection from the disc accounted for all positive and negative residuals (compare Figure 7.5 with Figure 7.4) except what appears to be an absorption line at ~ 6.8 keV whose significance can be roughly estimated to be between 90 and 99 per cent.

A further narrow Gaussian absorption line is then added to the spectral model finding a marginal improvement of $\Delta\chi^2 = 8$ for 2 more free parameters (98.1 per cent significance level according to the F-test) for a line energy of $6.81^{+0.08}_{-0.06}$ keV with equivalent width of -50 ± 30 eV and a final statistics of $\chi^2 = 442$ for 438 dof. The absorption line energy suggests an origin in resonant absorption due to Fe_{xxv} or Fe_{xxvi} (see e.g. Bianchi et al. 2005b) but is inconsistent with the expected rest-frame energies (weighted mean of 6.697 keV and 6.966 keV respectively). If Fe_{xxv} is assumed, the line energy indicates an outflow velocity of 5061^{+3600}_{-2700} km s⁻¹.

It should be stressed that the inferred outflow velocity is remarkably similar to the systemic velocity of the galaxy. IRAS 13197–1627 is at redshift $z=0.016541$ which corresponds to a receding velocity of 4959 km s⁻¹. Such a coincidence raises the possibility that the line has a local origin (i.e. Galactic) as it was recently suggested by McKernan, Yaqoob & Reynolds (2004; 2005) for the cases of extreme relativistic outflows inferred from X-ray spectroscopy in several AGNs (see e.g. Pounds et al 2003; Reeves, O’Brien, & Ward 2003).

The data, residuals, and best-fitting model are shown in the two panels of Figure 7.6. I include the Ni emission line from the disc and the 6.8 keV absorption line in the final model, but it must be stressed again that they are respectively detected at about the 95 and 98 per cent level only. The best-fitting parameters are reported in Table 7.1 where it is also computed the F-test significance for the most important spectral components obtained by re-fitting the data after having excluded the relevant component. In the case of the disc reflection component, the F-test is computed for the overall blurred reflection (99.8%), for the addition of the Ni emission line (94.8%), and for the relativistic blurring only (99.1%) separately.

The most important result is that we infer a very strong (and nearly neutral) reflection component from the accretion disc which dominates the hard spectrum. Notice also that the transmitted Fe line width is now only an upper limit, consistent

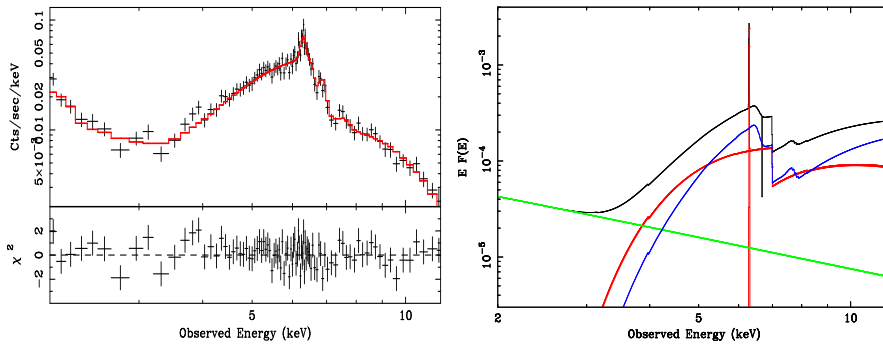


Figure 7.6: In the top panel I show the result of our best-fitting model in the 2–12 keV band (see Table 1). Only the pn data are shown for clarity. In the bottom panel, I show the model components.

with an absorber far away from the nucleus. The transmitted Fe line equivalent width is also slightly reduced because of the broad Fe line associated with the disc reflection component. Part of the hard curvature is now due to the disc reflection component which results in a slightly smaller column density of the absorber. As for the disc parameters, the inner disc radius is consistent with both a spinning and a non-spinning black hole, while the inclination is relatively poorly constrained.

The large value of the reflection fraction $R = 10 \pm 3$ (where $R = \Omega/2\pi$ and Ω is the solid angle subtended by the reflector) is unusual and the resulting reflection-dominated spectrum has consequences on luminosity estimates of the nuclear emission. If the spectrum is indeed reflection-dominated, the intrinsic AGN luminosity is much higher than the observed one. For this reason, in Table 7.1 I report two different measures of the 2–10 keV luminosity, with two different meanings. The first one is the absorption-corrected observed luminosity (L_{2-10}^{obs}), while the second is the estimated intrinsic luminosity of the AGN (L_{2-10}^{est}): this is the absorption-corrected luminosity of the direct AGN emission (the hard power law continuum) multiplied by the reflection fraction i.e. the observed AGN luminosity plus the luminosity needed to produce the reflection spectrum I measured. It is clearly a model-dependent, but in my opinion meaningful, estimate.

7.2.2 A partial covering alternative

In previous analysis of the *BeppoSAX* observation, Dadina & Cappi (2004) pointed out that, besides the Compton–thin absorber, the *BeppoSAX* hard spectrum could be described either in terms of a strong and dominant X–ray reflection component from the disc or in terms of a partial covering model. Their partial–covering solution was an attempt to describe the 5–6 keV and >10 keV positive residuals seen in Fig 4 (and visible in the *BeppoSAX* data as well) with the curvature produced by a high–column ($\sim 5 \times 10^{24} \text{ cm}^{-2}$) absorber. Motivated by that study, I also considered a similar model and allowed the Fe abundance of the Compton–thin absorber and of the partial coverer to vary, but forcing it of course to be the same. I also include the 6.8 keV absorption line. However, the partial covering best–fit is statistically worse than the *reflection dominated* best–fit model with $\chi^2 = 470$ for 442 dof (to be compared with $\chi^2 = 442$ for 438 dof). The partial–coverer has $N_H \simeq 5 \times 10^{24} \text{ cm}^{-2}$ and a covering fraction of about 97 per cent, while the Compton–thin absorber parameters are consistent with those reported in Table 7.1. The partial coverer accounts for the residuals above 10 keV (see Figure 7.3) but not for the positive residuals in the 5–6 keV band and the absorption structure around 7 keV is only poorly modelled (see Figure 7.4).

7.3 The previous *ASCA* and *BeppoSAX* observations

IRAS 13197–1627 has been observed twice previously in X–rays, in July 1995 by *ASCA* in the 0.5–10 keV band for 37 ks (Ueno 1997), and in July 1998 by *BeppoSAX* in the 0.5–100 keV band for 44 ks, reduced to 20 ks above 10 keV (Risaliti 2002; Dadina & Cappi 2004). The *ASCA* data were retrieved from the Tartarus database and the event files were processed as standard and verified to give consistent results with the products obtained by Tartarus team. I used data from the SIS 0 and 1 and from the GIS 2 and 3 detectors and performed joint fit to the X–ray spectra in the 2–10 keV band. The *BeppoSAX* data were retrieved from the *BeppoSAX* Science Data Centre and event files were processed as standard. The final MECS and PDS spectra were found to be in excellent agreement with those from the automated pipeline (available on–line).

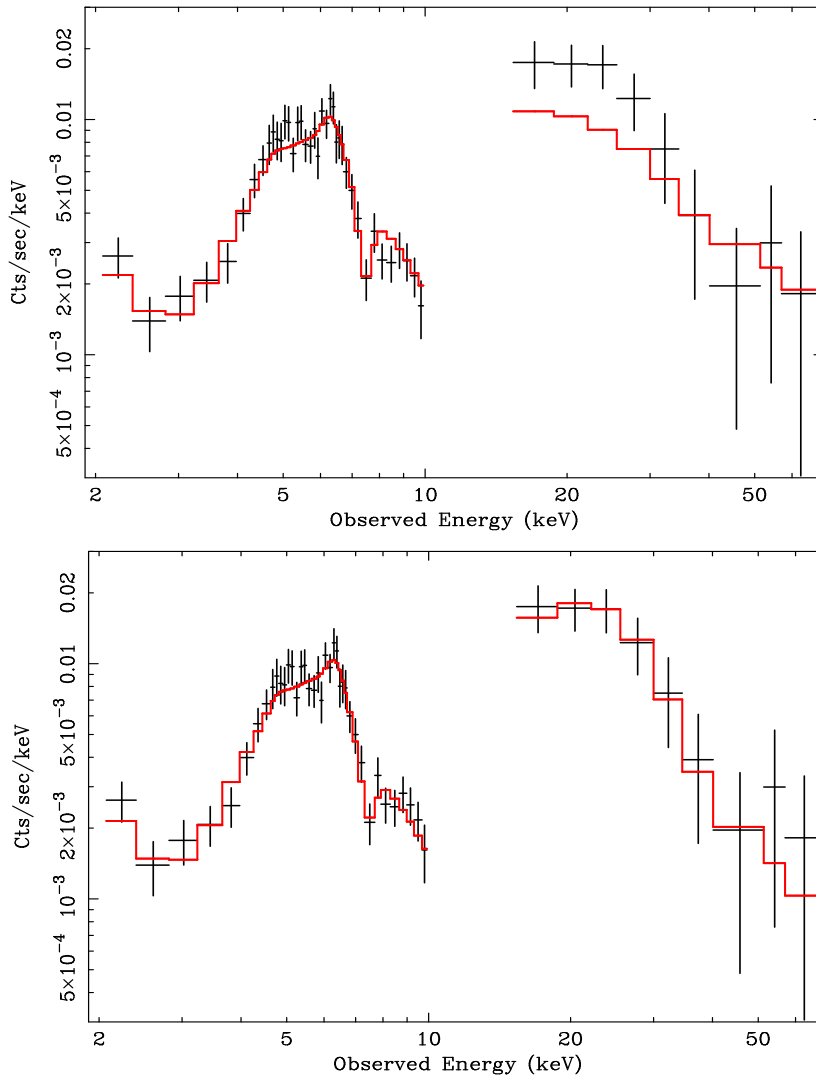


Figure 7.7: In the top panel I show the baseline *XMM-Newton* model applied to the *BeppoSAX* data (MECS and PDS detectors). The fit is acceptable but large residuals are seen around 20–30 keV where reflection is expected to dominate. In the bottom panel, I add the disc reflection component, i.e. I apply the *XMM-Newton* best-fitting model to the *BeppoSAX* data.

7.3.1 Confirming the reflection-dominated spectrum with *BeppoSAX*

Besides the broad Fe line and edge, the X-ray reflection model predicts the presence of a strong Compton hump around 20–30 keV. The previous *BeppoSAX* observation can thus be used to confirm the detection of the Compton hump in the high-energy PDS detector. Thus I first apply to the 2–80 keV *BeppoSAX* data the baseline model (no disc reflection). As already reported by Dadina & Cappi (2004) an absorption line is tentatively detected at 7.5 ± 0.2 keV, while none is seen at 6.8 keV. If related to resonant absorption from Fe xxv (Fe xxvi), the energy of the line implies an outflow of at least 27000 (13000) km s⁻¹. I confirm this result and add that the line is detected only marginally (at the 98 per cent level) but if true, its presence could indicate that an outflow with variable velocity on long timescales is indeed present in IRAS 13197–1627.

The *BeppoSAX* data and baseline (plus absorption line) best-fitting model are shown in the top panel of Figure 7.7. The fit is acceptable ($\chi^2 = 76$ for 69 dof), but clear residuals are left around 20–30 keV, where reflection is expected to dominate. I thus consider the *XMM-Newton* best-fitting model comprising the X-ray reflection component from the disc. Given the poorer quality of the data, the Fe abundance, inner disc radius, inclination and Ni emission line energy were fixed to the best-fitting *XMM-Newton* values and the *BeppoSAX* data were fit with the other parameters free to vary. The result is shown in the bottom panel of Figure 7.7 and shows that the X-ray reflection component is required by the PDS data. The final fit is good with $\chi^2 = 52$ for 66 d.o.f., significantly better than the baseline model one. *BeppoSAX* measures a reflection fraction of $R = 11 \pm 2$, consistent with the *XMM-Newton* one ($R = 10 \pm 3$).

7.3.2 Long-term spectral variability

I have studied the long-term spectral variability of IRAS 13197–1627 by using the three available X-ray observations with the goal of determining i) changes in the continuum slope, column density of the absorber, and narrow Fe line flux, and ii) variability of the two main spectral components, namely the continuum power law and the disc reflection. I mention here that, based on literature results from *ASCA* (Ueno 1997) and on the Risaliti (2002) analysis of the *BeppoSAX* data, Risaliti, Elvis & Nicastro (2002) have pointed out that a long-term variability in

Table 7.2: The best-fitting model to the *XMM-Newton* data is applied to the previous *ASCA* (2–10 keV) and *BeppoSAX* (2–80 keV) observations. I report the most relevant best-fitting parameters and the resulting statistics (χ^2/dof). For the *BeppoSAX* (*XMM-Newton*) observation, the baseline model also comprises a ~ 7.5 keV (~ 6.8 keV) absorption line.

Parameter.	ASCA	BeppoSAX	XMM-Newton
	(1995)	(1998)	(2005)
Γ_h	$2.6^{+0.5}_{-0.7}$	$2.2^{+0.7}_{-0.4}$	2.5 ± 0.3
N_H	$4.3^{+1.3}_{-0.7}$	3.7 ± 0.8	3.9 ± 0.4
E_{Fe}	6.5 ± 0.1	6.4 ± 0.1	6.40 ± 0.02
N_{Fe}	6.5 ± 0.9	6.8 ± 0.8	6.2 ± 0.4
F_{cont}	9.2 ± 1.6	11.4 ± 1.3	$6.8^{+1.9}_{-2.3}$
F_{refl}	7.0 ± 2.7	8.0 ± 1.1	3.9 ± 0.8
Best Fit	156/150	52/66	442/438
Baseline	165/153	76/69	505/445

The column density of the absorber (N_H) is in units of 10^{23} cm^{-2} and the Fe line energy (E_{Fe}) is in keV. The Fe line normalisation (N_{Fe}) is in units of 10^{-6} $\text{ph cm}^{-2} \text{s}^{-1}$. The continuum and reflection fluxes (F_{cont} and F_{refl}) are unabsorbed and given in the 2–10 keV band in units of 10^{-12} $\text{erg cm}^{-2} \text{s}^{-1}$.

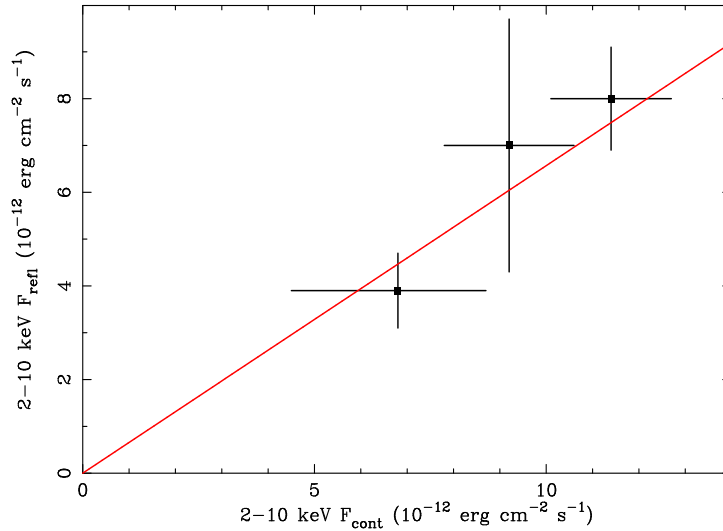


Figure 7.8: The 2–10 keV reflection flux is plotted against the 2–10 keV continuum flux from the three available observations. This demonstrates that the reflection component responds to the continuum long-term variability within the errors. As a reference the best-fitting linear relationship is shown.

the absorbing column density could be claimed in IRAS 13197–1627, which would be consistent with a clumpy absorbing medium close to the central engine.

I applied the best-fit model to the *ASCA* spectrum as well and the results are reported in Table 7.2 for the three observations. The source observed (i.e. absorbed) 2–10 keV flux was low during the *XMM-Newton* observation ($2.1 \pm 0.2 \times 10^{-12}$ erg cm^{-2} s^{-1}), about a factor 2 higher during the *BeppoSAX* one ($4.7 \pm 0.7 \times 10^{-12}$ erg cm^{-2} s^{-1}), and intermediate during the *ASCA* pointing ($3.5 \pm 0.9 \times 10^{-12}$ erg cm^{-2} s^{-1}). Table 7.2 shows that the hard power law photon index, the column density of the Compton-thin absorber, and the transmitted Fe line normalisation are all consistent with being the same in the three observations. I conclude that the data collected so far are consistent with the flux variability occurring at constant spectral slope and absorption, meaning that we have no observational evidence to support the conclusion that the absorber is located relatively close to the central engine (although it cannot be excluded).

As for the variability of the continuum and reflection components, it is found that they are consistent with being correlated. This is shown in Figure 7.8 where

the 2–10 keV flux of the reflection component is plotted against the 2–10 keV flux of the continuum (both unabsorbed). The origin of the reflection-dominated spectrum and of its variability are discussed below.

7.4 Origin of the reflection-dominated spectrum

The most remarkable result of this analysis is the presence of a dominant reflection component from the accretion disc with a reflection fraction of $R = 10 \pm 3$. In other words, the hard X-ray spectrum of IRAS 13197–1627 is largely reflection-dominated. Since reflection comes from the inner accretion disc, and since most of the accretion power has to be radiated from there (or in a corona above it), it is very difficult to imagine a situation in which the spectrum is reflection-dominated because absorption covers the direct continuum X-ray source and not the inner disc. I tried anyway a spectral model in which the hard power law and the reflection component are absorbed by different column densities to check whether this could help explaining the large reflection fraction. However, we did not find any statistical improvement and, more importantly, the two column densities turned out to be consistent with each other and with the value reported in Table 7.1.

One possibility is that the large observed reflection fraction is due to strong gravity effects. If the primary emitting source of X-rays is located only a few r_g from the black hole, light bending focus the continuum towards the accretion disc (and black hole) dramatically reducing the primary continuum at infinity and enhancing the reflection fraction up to the very large observed values (see the light bending model proposed by Miniutti et al. 2003; Miniutti & Fabian 2004; see also Fabian et al 2005; Ponti et al 2006; Miniutti et al 2006 for recent applications). As for the variability, the model was devised to reproduce large continuum variation with no or little reflection variability (as observed e.g. in MCG–6-30-15, see Fabian & Vaughan 2003; Miniutti et al 2006). The model successfully reproduces this behaviour for sources with R between ~ 1 and $\sim 3 - 4$ (such as MCG–6-30-15), while it predicts a correlated variability for reflection-dominated sources with $R > 3 - 4$. Thus, in the present case, the continuum/reflection correlated variability (see Figure 7.8) is consistent with the model (since $R \sim 10$). However, a correlation between disc reflection and continuum is expected in any simple disc reflection model and is not specific of the light bending one. The main advantage of the

model is that the large reflection fraction is naturally explained.

As recently pointed out by Merloni et al. (2006), reflection-dominated spectra could also be produced from discs which are subject to instabilities making both density and heating rate in the inner disc inhomogeneous. If the clouds generated by the inhomogeneous flow have high effective optical depth, steep spectra ($\Gamma \sim 2.4$) emerge and they are associated with a dominant reflection component, in good agreement with our analysis. It is a natural consequence of this model that some of the inner-disc clouds responsible for the X-ray reflection would be seen in absorption with a range of column densities (say $10^{23} - 10^{25} \text{ cm}^{-2}$). Given the location of the clouds (few innermost r_g) short-timescale variability in absorption has to be expected and could be used to disentangle between the two models in future longer observations. At the present time, here there is no evidence for absorption variability (notice that the Compton-thin absorber detected here has nothing to do with this scenario since the transmitted Fe line is too narrow to be produced in the inner-disc).

Chapter 8

Overview on the obtained results

The main goal of this dissertation has been probing physical conditions of matter in the inner pc of nearby Seyfert galaxies. The results obtained on the different topic touched for this thesis have been summarized and discussed at the end of the due chapters. Here, a general overview of the obtained results is presented.

The Seyfert galaxies are the closest AGN known. As such they can be possibly used to test the physical properties of the entire class of AGN, supposing that all AGN are similar, independently from distance.

To investigate the general properties of nearby Seyfert galaxies I took advantage of different methods of analysis. In particular I used three different samples of objects, that, despite frequent overlaps, have been thought to be tuned to tackle different topics: the heterogeneous *BeppoSAX* sample (see §2.1) was thought to be optimized to test the average hard X-ray ($E \geq 10$ keV) properties of nearby Seyfert galaxies; the *X-CfA* (see §2.2) was thought to be optimized to compare the properties of LLAGN to the ones at higher luminosity and, thus, to test the emission mechanism; the *XMM-Newton* (§2.3) sample was extracted from the *X-CfA* sample so as to be sure to have a truly unbiased and well defined sample of objects to test the average properties of Seyfert galaxies.

The three samples were also used to test the validity of the UM of AGN (Antonucci 1993). It is important to stress here that the UM, despite being only little more than a geometrical scenario, is a fundamental keytool to model the synthesis of the CXB (Comastri et al. 1995, Gilli et al. 2001, 2007). These models, on the other hand, put important constraints to the scenarios describing the evolution and

co-evolution of SMBH with their host galaxies (see Marconi et al. 2004).

One of the structures assumed to be present in the UM is the accretion disk. As introduced in §1, it is assumed to be formed by the infalling matter that is driven onto the SMBH while the disk, thanks to viscosity, drives outwards the angular momentum. This structure is *needed* for this reason but also to explain the BBB observed in many type I objects (see §1). It's presence was also *used* to develop the most popular models for the production of X-ray photons, the so called *two-phase* models (Haardt 1991, Haardt & Maraschi 1991, 1993).

Nonetheless, the presence of such a structure intrinsically implies that relativistic effects due to the interaction between the high-energy emission and the matter that reach the last stable orbits around the SMBH (Fabian 2000, Miniutti & Fabian 2004) must occur. As such, X-rays may also be used to probe general relativity in AGN. Here these effects have been studied focusing on three case study objects (namely Mrk 509, NGC 3783 and IRAS 13197-1627). These objects were chosen since they were known to display in their X-ray spectrum evidences of radial motions in the form of shifted resonant absorption X-ray lines. Thus, accretion and possibly other types of flowing matter were supposed to co-exist in these objects.

8.1 The UM

The UM has been positively tested taking advantage of the X-ray data collected both with *BeppoSAX* and *XMM-Newton* and no major departure have been observed with respect to the predictions/expectations of the UM itself.

The UM has been tested also using the E_c and R , two quantities that have been available for such studies only since the completion of the *BeppoSAX* archive of pointed observations (§3.2). In particular, type I and II objects do not differ significantly on the spectral shape if the absorption due to the *dusty torus* is accounted for (see §3.2, 3.3 and 3.4). On average, the X-ray spectrum is well modeled by a power-law with a spectral index $\Gamma \sim 1.9$, $E_c \sim 200-300$ keV and $R \sim 1$. It is worth considering here that the value of E_c can suffer the contribution of the large number of lower limits (with values generally higher than 200-300 keV) measured with *BeppoSAX*. As such, the average value is probably not fully representative of the intrinsic distribution of such quantity in the nearby Seyfert galaxies. Nonetheless, it must be recalled here, that the *BeppoSAX* sample is, *ab origine* a heterogeneous

sample of objects (see §3.2).

On the other hand, the average spectral parameters obtained for the *XMM-Newton* sample are slightly different ($\Gamma=1.62\pm0.3$) from the ones obtained for the *BeppoSAX* sample. In particular, the *flatter* spectra measured by *XMM-Newton* is most probably due, and in any case certainly *polluted*, by the fact that the latter data cannot ensure the detection of a reflection component and, being considered between 0.1-10 keV (the *BeppoSAX* data were considered between 2-100 keV) they also suffered for a poor treatment of the contribution from a *warm absorber*. Both these effects can *mimic* flat spectra if not properly accounted for. The major advantage of the *XMM-Newton* sample is the fact that it allows to investigate the intrinsic distribution of absorbing columns. It has been found that Seyfert galaxies as a whole exhibit absorption columns in the entire range of N_H , from 10^{20} cm⁻² to 10^{24} cm⁻², fairly continuously and that 30-50% of the type II objects are Compton-thick (see §3.3 and 3.4).

Moreover, also the origin of the FeK α emission line has been tested using the *BeppoSAX* sample. The results are well in agreement with a *dusty torus* origin of such a spectral feature. This scenario is directly confirmed for type II objects where a direct correlation is measured between the absorbing column and the EW of the emission line. Type I and II sources are on the same relations both in the EW vs. N_H and EW vs. $F_{2-10keV}/F_{20-100keV}$ (see fig. 3.9) thus indicating that also in type I sources the narrow component of the iron line comes from the matter constituting the *dusty torus* (see §3.5).

Finally, the Iwasawa-Taniguchi effect is confirmed for type I objects considering the 20-100 keV luminosity. Assuming that the narrow FeK α emission line is indeed produced in *dusty torus*, this seems to indicate that the torus covering fraction of the sky as seen by the X-ray source decreases as the source's luminosity increases (see §3.5).

8.2 The emission mechanism

The standard scenario in which X-ray photons are produced by thermal Comptonization of seed UV photons coming from an accretion disk has been, at least at the zero-th order, confirmed by the measurement of a significant relation between R and Γ . As discussed (§4.1), this relation naturally emerges if different

accretion rates are considered or, in other words, if it is supposed that the accretion disk penetrates the central corona at different depths (Merloni et al. 2006). Thus, highly accreting systems have accretion disks that can penetrate deeply into the inner corona/ADAF phase and are thus dominated by the standard *two phases* emission mechanism while in low accreting systems the disk cannot extend deeply into the corona/ADAF phase reducing the efficiency of the system.

This is consistent with what found for the study of the well defined *X-CfA* sample of Seyfert galaxies (type I, type II and 'mixed Seyfert', see §2.2). The analysis of such sample has proven that the intrinsic X-ray luminosity of nearby Seyfert galaxies can span between 10^{38-43} erg s⁻¹, i.e. covering a huge range of accretion rates. The less efficient systems are supposed to host ADAF systems. Moreover, the study of the *X-CfA* sample has also proven the existence of correlations between optical lines and X-ray luminosity in the entire range of L_X covered by the sample. These relations are similar to the ones obtained if high-L objects are considered. Thus the emission mechanism must be similar in the luminous and weak systems.

A possible scenario is that the ADAF and *two phase* mechanism co-exist with different relative importance moving from low-to-high accretion systems (as suggested by the Γ vs. R relation). The present data require that no abrupt transition between the two regimes is present.

8.3 Matter flows close to SMBHs

The study of the three samples of objects presented here has highlighted that the matter form an accretion disk before disappearing onto the SMBH hosted at the center of the galaxies. This was expected since the formulation of the UM.

Nonetheless, the study of the 'case study sources' has demonstrated that in some sources matter can reach down to the inner orbits around SMBH and thus, extreme relativistic effects, such as *light bending* can be recorded and used to probe the general relativity theory around SMBH (this is the case for IRAS 13197-1627). Moreover, in some cases (e.g NGC 3783) matter can accrete via spiraling in the last orbits. In this case, a modulation between the continuum emission and the red wing of the relativistically broadened FeK α emission line can be observed. In Mrk 509, it was observed that the narrow component of the iron line is

most probably produced in the outer parts of the accretion disk while also a faint relativistically broadened FeK emission line is observed.

Apart from a sometimes questioned existence of an accretion disk, all these evidences demonstrate that little is known about the flow patterns of gas in the innermost regions close to the black-holes in AGNs. It must be recalled here, however that probing the gas kinematics (velocities) and, most importantly, dynamics (accelerations) around black holes is a fundamental requisite if we want to understand the sources geometry and energy generation mechanism, i.e. the accretion mode.

The analysis of the 'case study objects' demonstrated that the accretion flow can significantly differ between the objects when it is inspected with appropriate details. For instance the accretion disk seems to have different characteristics between the three objects (stable down to last stable orbit in a Kerr system for IRAS 13197-1627, formed by spiral arms in the inner $\sim 10-30 r_g$ in NGC 3783 and *barely detectable* in Mrk 509).

Moreover blueshifted resonant absorption lines have been detected in the three objects, most likely produced by outflowing matter. This seems to indicate that, around SMBH, there is matter that does not remain in the disk and moves with velocities as large as $v \sim 0.01-0.4c$. Whether this matter forms a wind or blobs is still unknown as well as the real significance of the measured absorption lines. Nonetheless, if confirmed, these phenomena are of outstanding interest because they offer new potential to probe the dynamics of innermost regions of accretion flows, to tackle the formation of ejecta/jets and to place constraints on the rate of kinetic energy injected by AGNs into the ISM and IGM. Future high energy missions (such as the planned Simbol-X and IXO) will likely allow an exciting step forward in our understanding of the flow dynamics around black holes and the formation of the highest velocity outflows.

Appendix A

The BeppoSAX data

Table A.1: List of the sources analyzed in this thesis. Col. I: Object Name; Col. II and III: Right ascension and declination (Equinox 2000); Col. IV: Redshift; Col. V: Seyfert type; Col. VI: Radio class.

Obj. name	R.a.	Dec.	Redshift	Obj. type	Class
MARK 335	00 06 19.50	+20 12 11.0	0.025	S1.2	RQ ¹
IRAS 00198-792	00 21 53.80	-79 10 08.0	0.073	S2	RQ ²
TON S180	00 57 20.20	-22 22 56.0	0.062	S1n	RQ ³
Tololo 109-383	01 11 27.70	-38 05 01.0	0.011	S2	RQ ⁴
MARK 1152	01 13 50.10	-14 50 45.0	0.052	S1.5	RQ ⁴
F 9	01 23 45.80	-58 48 21.0	0.046	S1.2	RQ ³
NGC 526A	01 23 54.40	-35 03 56.0	0.019	S1.9	RQ ⁴
NGC 985	02 34 37.80	-08 47 15.0	0.043	S1.5	RQ ⁴
ESO 198-G24	02 38 19.70	-52 11 32.0	0.045	S1.0	RQ ^{3,5}
NGC 1052	02 41 04.80	-08 15 20.8	0.005	S2	RQ ⁴
NGC 1068	02 42 40.70	-00 00 47.0	0.003	S2	RQ ⁴
3C 78	03 08 26.20	+04 06 39.0	0.029	S1	RL ⁶
MARK 1073	03 15 01.40	+42 02 09.0	0.023	S2	RQ ⁷
MARK 609	03 25 25.36	-06 08 37.9	0.034	S1.8	RQ ⁴
3C 88	03 27 54.20	+02 33 42.0	0.003	S2	RQ ⁴
NGC 1365	03 33 36.60	-36 08 17.0	0.006	S1.8	RQ ²
NGC 1358	03 33 39.70	-05 05 22.0	0.013	S2	RQ ⁴
NGC 1386	03 36 45.40	-35 59 57.0	0.002	S2	RQ ⁴
3C 111.0	04 18 21.30	+38 01 35.0	0.048	S1	RL ⁸
3C 120	04 33 11.10	+05 21 15.0	0.033	S1.5	RL ⁴

continued on next page

continued from previous page

Obj. name	R.a.	Dec.	Redshift	Obj. type	Class
UGC 3134	04 41 48.20	-01 18 07.0	0.029	S2	RQ ⁹
ESO 033-G02	04 55 58.80	-75 32 28.0	0.019	S2	RQ ²
IRAS 05189-252	05 21 01.40	-25 21 45.0	0.042	S2	RQ ²
NGC 2110	05 52 11.40	-07 27 23.0	0.007	S2	RQ ⁴
MCG 8-11-11	05 54 53.60	+46 26 21.0	0.020	S1.5	RQ ⁴
H 0557-385	05 58 02.10	-38 20 05.0	0.034	S1.2	RQ ¹⁰
MARK 3	06 15 36.30	+71 02 15.0	0.014	S2	RQ ⁴
NGC 2273	06 50 08.70	+60 50 45.0	0.006	S2	RQ ⁴
MARK 6	06 52 12.30	+74 25 38.0	0.019	S1.5	RQ ⁴
MCG-5-18-2	07 16 31.20	-29 19 28.0	0.005	S2	RQ ¹¹
MARK 1210	08 04 05.90	+05 06 50.0	0.013	S2	RQ
MCG-1-24-12	09 20 46.25	-08 03 22.1	0.020	S2	RQ
MARK 110	09 25 12.90	+52 17 11.0	0.036	S1.5	RQ ⁴
NGC 2992	09 45 42.00	-14 19 35.0	0.008	S1.9	RQ ⁴
MCG-5-23-16	09 47 40.20	-30 56 54.0	0.008	S2	RQ ¹²
M 81	09 55 33.17	+69 03 55.0	0.0001	S1.8	RQ
NGC 3081	09 59 29.60	-22 49 34.0	0.007	S2	RQ ⁴
NGC 3079	10 01 58.50	+55 40 50.0	0.004	S2	I ⁴
NGC 3147	10 16 53.20	+73 24 02.0	0.010	S2	RQ ¹³
NGC 3281	10 31 52.10	-34 51 13.0	0.011	S2	RQ ⁴
RE J1034+393	10 34 38.60	+39 38 29.0	0.042	S1n	RQ ¹⁴
NGC 3393	10 48 23.40	-25 09 44.0	0.012	S2	RQ ¹⁵
NGC 3516	11 06 47.40	+72 34 07.0	0.009	S1.5	RQ ⁴
IRAS 11058-113	11 08 20.30	-11 48 11.0	0.054	S2	RQ ¹⁶
NGC 3627	11 20 15.03	+12 59 29.6	0.002	S2	RQ ¹⁷
NGC 3660	11 23 32.20	-08 39 30.0	0.011	S2	RQ ¹¹
NGC 3783	11 39 01.80	-37 44 19.0	0.009	S1.5	RQ ⁴
NGC 3998	11 57 56.11	+55 27 12.7	0.003	S1	RQ ⁴
NGC 4051	12 03 09.60	+44 31 53.0	0.002	S1n	RQ ⁴
NGC 4151	12 10 32.50	+39 24 21.0	0.003	S1.5	RQ ⁴
MARK 766	12 18 26.70	+29 48 47.0	0.012	S1.5	RQ ¹⁸
NGC 4258	12 18 57.50	+47 18 14.0	0.002	S2	RQ ⁴
NGC 4261	12 19 23.22	+05 49 30.8	0.007	S2	RL ¹⁹
MARK 205	12 21 44.10	+75 18 38.0	0.070	S1.0	RQ ⁴
NGC 4388	12 25 46.70	+12 39 41.0	0.008	S2	RQ ⁴
NGC 4507	12 35 36.50	-39 54 33.0	0.012	S2	RQ ⁴
NGC 4579	12 37 43.52	+11 49 05.5	0.005	S1.9	RQ ⁴
NGC 4593	12 39 39.40	-05 20 39.0	0.009	S1.0	RQ ⁴
M 104	12 39 59.30	-11 37 23.0	0.002	S1.9	RQ ¹⁹
IC 3639	12 40 52.90	-36 45 21.0	0.011	S2	RQ ¹⁹
M 94	12 50 53.06	+41 07 13.6	0.001	S2	RQ ¹⁷
MARK 231	12 56 14.20	+56 52 25.0	0.041	S1.0	I ⁴

continued on next page

continued from previous page

Obj. name	R.a.	Dec.	Redshift	Obj. type	Class
NGC 4826	12 56 43.76	+21 40 51.9	0.001	S2	RQ ⁴
NGC 4941	13 04 13.10	-05 33 06.0	0.003	S2	RQ ⁴
NGC 4939	13 04 14.30	-10 20 23.0	0.010	S2	RQ ²⁰
NGC 4945	13 05 27.50	-49 28 05.6	0.002	S2	RQ ²¹
IRAS 13197-162	13 22 24.50	-16 43 42.0	0.017	S2	RQ ¹⁸
IRAS 13224-380	13 25 19.20	-38 24 54.0	0.065	S1n	RQ ¹⁴
Centaurus A	13 25 27.62	-43 01 08.8	0.002	S2	RL ²²
M 51	13 29 52.40	+47 11 41.0	0.001	S2	RQ ²³
MCG-6-30-15	13 35 53.40	-34 17 48.0	0.008	S1.5	RQ ¹⁸
NGC 5252	13 38 15.90	+04 32 33.0	0.022	S2	RQ ⁴
MARK 266SW	13 38 17.30	+48 16 34.0	0.028	S2	RQ ⁴
IC 4329A	13 49 19.30	-30 18 34.0	0.016	S1.2	RQ ⁴
MARK 463E	13 56 02.89	+18 22 19.0	0.050	S2	RQ ¹⁷
Circinus	14 13 09.80	-65 20 17.0	0.001	S2	RQ ⁴
NGC 5506	14 13 14.80	-03 12 26.0	0.007	S2	RQ ⁴
NGC 5548	14 17 59.60	+25 08 13.0	0.017	S1.5	RQ ⁴
NGC 5643	14 32 40.70	-44 10 28.0	0.003	S2	RQ ⁴
NGC 5674	14 33 52.30	+05 27 30.0	0.025	S1.9	RQ ⁴
NPM1G-14.0541	14 37 38.40	-15 00 23.0	0.081	S1	RQ ²⁴
MARK 478	14 42 07.50	+35 26 23.0	0.077	S1n	RQ ⁴
IRAS 14454-434	14 48 42.50	-43 55 52.0	0.037	S2	RQ ¹⁰
NGC 5793	14 59 27.50	-16 41 51.0	0.011	S2	RL ²⁵
MARK 841	15 04 01.20	+10 26 16.0	0.036	S1.5	RQ ⁴
NGC 6251	16 32 32.10	+82 32 17.0	0.024	S2	RL ⁴
NGC 6212	16 43 23.10	+39 48 24.0	0.030	S1	RQ ⁴
NGC 6240	16 52 58.90	+02 24 03.0	0.024	S2	RQ ⁴
NGC 6300	17 16 59.20	-62 49 05.0	0.003	S2	RQ ⁴
3C 382.0	18 35 03.40	+32 41 47.0	0.059	S1.0	RL ⁴
F 49	18 36 58.30	-59 24 09.0	0.019	S1.9	RQ ⁴
ESO 103-G35	18 38 20.50	-65 25 39.0	0.013	S1.9	RQ ¹⁰
3C 390.3	18 42 09.00	+79 46 17.0	0.057	S1.5	RL ⁴
H 1846-786	18 47 01.70	-78 31 59.0	0.074	S1.2	RQ ⁷⁵
ESO 141-G55	19 21 14.30	-58 40 13.0	0.037	S1.2	RQ ¹⁰
Cygnus A	19 59 28.30	+40 44 02.0	0.056	S1.9	RL ²⁶
IRAS 20051-111	20 07 51.30	-11 08 34.5	0.031	S?	RQ ⁵
IRAS 20210+112	20 23 25.60	+11 31 34.0	0.056	S2	RQ ²⁴
MARK 509	20 44 09.70	-10 43 24.0	0.035	S1.5	RQ ⁴
S5 2116+81	21 14 01.60	+82 04 47.0	0.086	S1.0	RL ²⁷
PKS 2153-69	21 57 05.80	-69 41 23.0	0.028	S2	RL ¹⁰
NGC 7172	22 02 01.90	-31 52 08.0	0.008	S2	RQ ¹⁸
IRAS 22017+031	22 04 19.20	+03 33 51.0	0.066	S2	RQ ¹⁸
NGC 7213	22 09 16.25	-47 10 00.0	0.06	S1.5	RQ ¹⁸

continued on next page

continued from previous page

Obj. name	R.a.	Dec.	Redshift	Obj. type	Class
3C 445.0	22 23 49.70	-02 06 13.0	0.057	S1.5	RL ⁴
NGC 7314	22 35 46.10	-26 03 02.0	0.005	S1.9	RQ ⁴
AKN 564	22 42 39.30	+29 43 32.0	0.025	S1n	RQ ¹⁴
MR 2251-178	22 54 05.90	-17 34 55.0	0.068	S1.5	RQ ⁴
NGC 7469	23 03 15.60	+08 52 26.0	0.017	S1.5	RQ ⁴
MARK 926	23 04 43.50	-08 41 08.0	0.047	S1.5	RQ ⁴
NGC 7582	23 18 23.50	-42 22 14.0	0.005	S1	RQ ⁴
NGC 7674	23 27 56.70	+08 46 44.0	0.029	S2	RQ ⁴
NGC 7679	23 28 46.60	+03 30 42.0	0.016	S2	RQ ⁷

¹Barvainis et al. (2005); ²Roy et al. (1994); ³Yuan et al. (1998); ⁴Xu et al. (1999); ⁵No radio-data available in literature; ⁶Yee & Oke (1978); ⁷Marx et al. (1994); ⁸Petre et al. (1984); ⁹Condon et al. (2002); ¹⁰Brindle et al. (1990); ¹¹Morganti et al. (1999); ¹²Nagar et al. (1999); ¹³Ulvestad & Ho (2001); ¹⁴Wang et al. (2004); ¹⁵Yun et al. (2001); ¹⁶Roy et al. (1998); ¹⁷Condon & Broderick (1991); ¹⁸Thean et al. (2000); ¹⁹Chiaberge et al. (2002); ²⁰Giuricin et al. (1990); ²¹Colbert et al. (1996); ²²Harris & Krawczynski (2002); ²³Rush et al. (1996); ²⁴Yun et al. (2001); ²⁵Baan & Klöckner (2006); ²⁶Perley et al. (1984); ²⁷Taylor et al. (1996)

RL, radio loud object; RQ, radio quiet object; I, intermediate object.

Table A.2: Observations Log. Col. I: Object name; Col. II: Observation date; Col. III: MECS exposure in ks; Col. IV: PDS exposure in ks; Col. V: MECS detection significance in the 2-10 keV band express in terms of standard deviation; Col. VI: PDS detection significance in the 20-100 keV band express in terms of standard deviations. In parentheses, values concerning the 20-50 keV band for those sources that are not detected in the 15-100 keV band.

Name	Start date	MECS exp.	PDS exp.	2-10 keV sig.	20-100 (20-50) keV sig.
		ks	ks	σ	σ
MARK 335	1998-12-10	86.7	42.6	90.3	2.75 (3.0)

continued on next page

continued from previous page

Name	Start date	MECS exp.	PDS exp.	2-10 keV sig.	20-100 (20-50) keV sig.
		ks	ks	σ	σ
IRAS 00198-7926	1997-12-20	20.2	9.5	S 1.33	1.44
TON S180	1996-12-03	24.7	10.7	44.2	neg.
Tololo 0109-383	1999-07-26	65.0	32.2	20.9	4.92
MARK 1152	2000-01-04	79.1	39.7	70.1	2.31 (3.1)
F 9	1996-09-25	94.1	40.8	206	11.2
NGC 526A	1998-12-31	93.2	44.2	128	12.9
NGC 985	1999-08-20	95.0	44.0	119	9.00
ESO 198-G24-a	2001-01-23	143	62.2	161	11.1
ESO 198-G24-b	2001-07-05	97.0	44.4	97.2	8.40
NGC 1052	2000-01-11	63.9	30.0	43.0	5.22
NGC 1068-a	1996-12-30	101	62.5	83.7	7.15
NGC 1068-b	1998-01-11	37.3	17.7	47.6	2.57 (2.32)
3C 78	1997-01-07	19.4	9.44	18.9	0.81 (0.52)
MARK 1073	1999-02-15	58.9	28.1	cont.	cont.
MARK 609-a	2000-01-20	18.1	8.26	16.7	0.63 (0.83)
MARK 609-b	2000-02-14	2.34	1.08	0.38	0.46 (neg.)
MARK 609-c	2000-03-04	28.3	13.1	28.3	0.20 (0.13)
3C 88	1999-02-03	42.7	20.6	9.68	neg. (neg.)
NGC 1365	1997-08-12	27.6	13.0	30.2	9.0
NGC 1358	2000-02-08	33.7	16.6	4.31	2.92 (2.69)
NGC 1386	1996-12-10	30.1	13.6	9.86	cont.
3C 111.0	1998-03-08	69.6	33.0	137	11.8
3C 120	1997-09-20	77.9	35.8	207	18.0
UGC 3134	2001-09-14	25.9	13.1	38.0	2.92 (3.42)
ESO 033-G02	2001-04-20	106	50.0	81.1	9.99
IRAS 05189-2524	1999-10-03	42.1	19.4	36.6	1.75 (3.35)
NGC 2110	1997-10-12	83.9	38.7	155	18.5
MCG 8-11-011	1998-10-07	74.9	36.2	220	24.7
H 0557-385-a	2000-12-19	29.3	14.8	107	7.65
H 0557-385-b	2001-01-26	14.2	5.8	81.6	7.83
MARK 3	1997-04-16	113	44.8	9E+3	40.0
NGC 2273	1997-02-22	24.0	9.9	16.4	0.9 (0.85)
MARK 6	1999-09-14	109	52.0	163	19.5
MCG-5-18-002	1997-11-21	8.9	3.5	neg.	1.33 (1.21)
MARK 1210	2001-05-05	95.3	41.3	82.6	17.6
MCG-1-24-12	2001-05-15	75.7	35.4	81.9	12.1
MARK 110-a	2000-05-23	35.7	15.7	107	8.91
MARK 110-b	2000-11-02	41.4	18.6	97.3	7.42
MARK 110-c	2001-04-02	31.2	15.2	55.9	3.10
NGC 2992-a	1997-12-01	72.0	33.2	67.3	4.98
NGC 2992-b	1998-11-25	59.2	27.1	219	31.3
MCG-5-23-16	1998-04-24	77.0	32.5	277	41.0

continued on next page

continued from previous page

Name	Start date	MECS exp.	PDS exp.	2-10 keV sig.	20-100 (20-50) keV sig.
		ks	ks	σ	σ
M 81	1998-04-06	100	36.6	217	9.69
NGC 3081	1996-12-20	15.3	2.0	13.1	neg. (neg.)
NGC 3079-a	2000-05-26	44.6	20.1	10.6	3.75
NGC 3079-b	2001-03-28	36.4	16.4	11.0	5.08
NGC 3147	1997-11-15	34.4	16.3	27.8	0.37 (0.40)
NGC 3281	2000-05-20	71.3	35.0	33.5	20.7
RE J1034+396	1997-04-18	43.0	19.5	27.8	0.95 (1.19)
NGC 3393	1997-01-08	14.6	7.2	8.88	2.52 (1.94)
NGC 3516-a	1996-11-08	55.7	20.8	144	16.2
NGC 3516-b	1997-03-11	57.6	21.7	208	21.2
NGC 3516-c	2001-04-10	87.4	39.9	164	26.4
NGC 3516-d	2001-11-09	171	64.1	159	24.1
NGC 3516-e	2001-11-19	64.9	23.1	98	16.7
NGC 3516-f	2001-11-28	48.9	19.6	116	14.0
IRAS 11058-1131-a	1998-05-29	35.4	16.6	5.21	0.45 (0.42)
IRAS 11058-1131-b	1998-12-09	27.7	12.8	4.25	neg. (neg)
NGC 3627	1998-12-18	47.6	22.2	17.1	neg. (neg.)
NGC 3660	2001-06-05	78.0	36.0	42.8	7.42
NGC 3783	1998-06-06	154	70.4	333	41.8
NGC 3998	1999-06-29	76.9	38.0	105	5.51
NGC 4051-a	1998-05-09	69.2	33.0	26.8	3.86
NGC 4051-b	1998-06-28	11.6	9.0	51.4	7.30
NGC 4151-a	1996-07-06	73.6	35.2	718	123
NGC 4151-b	1996-12-04	24.3	11.2	166	65.8
NGC 4151-c	1996-12-06	23.5	10.8	162	64.5
NGC 4151-d	1999-01-04	83.4	38.5	296	142
NGC 4151-e	2000-12-22	18.6	8.8	93.0	26.6
NGC 4151-f	2001-12-18	115	53.3	481	152
MARK 766-a	1997-05-17	78.1	34.2	139	cont.
MARK 766-b	2001-05-20	81.8	38.0	156	cont.
NGC 4258	1998-12-19	99.6	46.9	84.0	4.14
NGC 4261	2000-12-27	67.4	32.6	25	1.44 (0.59)
MARK 205-a	1997-03-12	47.0	6.6	46.0	1.98 (1.11)
MARK 205-b	2001-12-21	166	70.5	146	7.38
MARK 205-c	2002-01-05	32.7	12.6	52.9	3.57
NGC 4388-a	1999-01-09	67.9	51.2	108	60.0
NGC 4388-b	2000-01-03	28.3	14.6	42.7	15.2
NGC 4507-a	1997-12-26	55.2	27.0	78.8	39.8
NGC 4507-b	1998-07-02	41.4	20.1	47.2	21.9
NGC 4507-c	1999-01-13	31.4	17.0	56.3	27.8
NGC 4579	2001-06-17	102	47.7	78.8	2.68 (4.72)
NGC 4593	1997-12-31	84.2	38.5	192	20.8

continued on next page

continued from previous page

Name	Start date	MECS exp.	PDS exp.	2-10 keV sig.	20-100 (20-50) keV sig.
		ks	ks	σ	σ
M 104	2000-06-29	72.1	32.8	36.3	1.46 (1.88)
IC 3639	1998-06-30	83.3	38.8	10.7	neg. (neg.)
M 94	2000-12-29	76.2	34.7	36.9	1.52 (0.91)
MARK 231	2001-12-29	144	71.3	24.4	2.79 (4.0)
NGC 4826	2001-06-26	90.0	41.8	6.5	neg. (neg.)
NGC 4941	1997-01-22	28.6	12.6	15.44	1.17 (1.67)
NGC 4939	1997-01-27	33.1	14.7	24.0	3.25
NGC 4945	1999-07-01	93.8	43.8	70.5	82.3
IRAS 13197-1627	1998-07-22	43.8	18.6	36.7	6.31
IRAS 13224-3809-a	1998-01-29	47.0	10.2	10.4	neg. (neg.)
IRAS 13224-3809-b	1998-06-29	14.9	6.9	3.93	neg. (neg.)
Cen A-a	1997-02-27	33.4	14.9	283	70.2
Cen A-b	1998-01-16	54.2	23.0	344	120
Cen A-c	1999-07-10	38.8	17.8	280	102
Cen A-d	1999-08-02	36.1	16.1	245	79.4
Cen A-e	200-01-08	34.0	17.9	260	105
M 51	2000-01-18	97.0	44.9	36.2	5.63
MCG -6-30-15-a	1996-07-29	183	85.7	407	25.4
MCG -6-30-15-b	2001-07-31	72.9	49.6	189	21.6
NGC 5252	1998-01-20	61.3	29.2	34.0	2.10 (3.00)
MARK 266SW	1998-12-29	40.7	20.1	10.4	0.12 (0.11)
IC 4329A-a	1998-01-02	81.9	37.6	355	54.9
IC 4329A-b	1998-07-17	40.0	18.3	203	27.6
IC 4329A-c	1998-07-21	37.8	17.8	237	33.8
IC 4329A-d	1998-07-27	47.0	11.2	196	24.6
IC 4329A-e	2001-01-31	32.5	16.4	251	41.2
MARK 463-a	1998-07-03	5.3	2.2	n.d	n.d
MARK 463-b	1998-07-05	28.4	13.0	7.68	0.87 (0.68)
MARK 463-c	1998-07-28	53.2	23.5	13.4	1.47 (1.26)
Circinus-a	2001-01-07	138	63.2	130	63.4
Circinus-b	1998-03-13	52.0	38.0	96.2	52.7
NGC 5506-a	1997-01-30	39.4	17.0	205	25.6
NGC 5506-b	1998-01-14	39.0	17.5	166	27.9
NGC 5506-c	2001-02-01	78.0	37.9	248	44.4
NGC 5548-a	1997-08-14	88.3	19.2	186	14.8
NGC 5548-b	1997-08-16	91.0	40.6	194	21.1
NGC 5548-c	1997-08-19	85.3	38.1	191	21.6
NGC 5548-d	1997-08-21	48.8	21.7	128	16.4
NGC 5548-e	1999-12-10	88.3	42.9	218	29.2
NGC 5548-f	2001-07-08	99.0	48.0	208	28.1
NGC 5643	1997-03-01	10.4	4.4	14.4	0.28 (0.16)
NGC 5674	2000-02-12	45.0	20.8	44.5	4.83

continued on next page

continued from previous page

Name	Start date	MECS exp.	PDS exp.	2-10 keV sig.	20-100 (20-50) keV sig.
		ks	ks	σ	σ
NPM1G-14.0541	2001-07-18	23.5	11.1	n.d.	1.21 (1.28)
MARK 478	2000-08-09	53.3	24.5	50.2	neg. (neg.)
IRAS 14454-4343	1997-03-02	24.0	12.8	4.27	1.25 (2.84)
NGC 5793	2001-07-25	78.8	36.4	n.d.	cont.
MARK 841-a	1999-07-30	87.8	41.5	116	6.47
MARK 841-b	2001-01-11	90.3	40.6	138	8.97
NGC 6251	2001-07-19	80.9	36.2	65.3	3.82
NGC 6212	1999-02-19	25.9	13.0	38.0	2.93 (3.42)
NGC 6240	1998-08-14	119	57.2	43.2	11.6
NGC 6300	1999-08-28	86.3	38.6	89.1	20.6
3C 382.0	1998-09-20	85.6	41.6	251	25.8
F 49	2000-03-31	116	59.4	171	4.80
ESO 103-G35	1997-10-14	14.4	5.9	40.2	7.00
3C 390.3	1997-01-09	101	45.7	190	14.9
H 1846-786	2001-03-08	34.5	17.9	57.8	3.92
ESO 141-G55	1999-11-01	89.0	39.2	161	13.5
Cygnus A	1999-10-27	73.1	34.1	216	24.0
IRAS 20051-1117	2001-10-29	56.1	24.4	36.6	2.12 (3.55)
IRAS 20210+1121	1996-10-02	39.2	18.6	14.4	1.07 (3.0)
MARK 509-a	1998-05-18	51.9	24.1	180	16.2
MARK 509-b	1998-10-11	36.0	17.0	166	15.8
MARK 509-c	2000-11-03	41.3	18.8	117	12.0
MARK 509-d	2000-11-08	38.1	17.6	105	12.1
MARK 509-e	2000-11-18	39.9	17.8	108	8.85
MARK 509-f	2000-11-24	33.1	14.6	100	10.1
S5 2116+81-a	1998-04-29	28.9	13.3	73.4	4.52
S5 2116+81-b	1998-10-12	19.7	10.5	52.3	4.47
PKS 2153-69	1996-09-29	16.9	6.9	45.3	1.18 (1.88)
NGC 7172-a	1996-10-14	39.2	17.3	73.6	7.52
NGC 7172-b	1997-11-06	49.4	21.1	47.9	4.99
IRAS 22017+0319	1997-11-28	47.6	22.2	36.7	2.69 (3.53)
NGC 7213-a	1999-05-30	46.8	56.0	119	18.0
NGC 7213-b	1999-11-23	14.9	33.6	64.7	14.4
NGC 7213-c	2000-05-03	45.9	30.8	136	16.7
NGC 7213-d	2001-05-27	61.6	37.9	113	10.0
3C 445.0	1999-11-30	99.9	46.4	67.2	9.03
NGC 7314	1999-06-08	90.0	42.6	155	16.9
AKN 564-a	1997-11-14	26.2	12.2	73.8	1.29 (1.37)
AKN 564-b	1998-06-12	29.2	12.5	80.1	1.85 (3.0)
AKN 564-c	1998-11-22	46.8	21.5	96.8	3.04
MR 2251-178-a	1998-06-14	82.7	40.9	197	18.9
MR 2251-178-b	1998-11-12	71.6	35.1	185	18.9

continued on next page

continued from previous page

Name	Start date	MECS exp.	PDS exp.	2-10 keV sig.	20-100 (20-50) keV sig.
		ks	ks	σ	σ
NGC 7469	1999-11-23	250	122	341	24.9
MARK 926	2000-12-01	25.0	46.1	98.6	20.0
NGC 7582	1998-11-09	56.4	26.1	93.9	21.8
NGC 7674	1996-11-25	116	51.2	35.0	1.96 (3.0)
NGC 7679	1998-12-06	90.9	45.3	77.3	4.25

neg., negative PDS counts in the background subtracted data;

cont., PDS counts most probably contaminated by other sources in the FOV.

[8pt]

Table A.3: Best-fit spectral parameter. Col. I: Observation name; Col. II: Total absorber Col. density; Col. III: Photon index; Col. IV: Energy centroid of the emission FeK α line; Col. V; EW of the emission line; Col. VI: Reflection parameter R; Col. VII: High-energy cut-off; Col. VIII: 2-10 keV flux; Col. IX: 2-10 keV observed luminosity; Col. X: 20-100 keV flux. Upper limits (3σ confidence level) have been calculated following the method presented in Sect. 3.3; Col. XI: 20-100 keV observed luminosity.

Name	N_H 10^{20}cm^{-2}	Γ	E_{line} keV	EW_{Line} eV	R	E_c keV	$F_{2-10keV}$ $\text{erg s}^{-1} \text{cm}^{-2}$	$L_{2-10keV}$ erg s^{-1}	$F_{20-100keV}$ $\text{erg s}^{-1} \text{cm}^{-2}$	$L_{20-100keV}$ erg s^{-1}
MARK 335 ¹	$7.66^{+1.55}_{-2.22}$	$2.50^{+0.16}_{-0.23}$	$6.35^{+0.08}_{-0.10}$	226^{+80}_{-81}			7.85E-12	9.75E+42	3.26E-12	4.09E+42
TonS 180	≤ 0.37	$2.34^{+0.17}_{-0.11}$	$6.89^{+0.36}_{-0.40}$	759^{+500}_{-431}			4.34E-12	3.57E+43	$\leq 1.57\text{E-}11$	$\leq 1.37\text{E+}44$
Tololo 109	339^{+500}_{-88}	$2.47^{+0.53}_{-2.70}$	$6.56^{+0.09}_{-0.09}$	1330^{+351}_{-362}	≥ 0.21		1.16E-12	3.02E+41	1.67E-11	4.43E+42
MARK 1152	≤ 0.28	$1.70^{+0.09}_{-0.06}$	$6.33^{+0.60}_{-0.32}$	114^{+88}_{-87}			5.62E-12	3.10E+43	1.00E-11	5.50E+43
Fairall 9 ¹	≤ 0.00	$2.14^{+0.19}_{-0.09}$	$6.81^{+0.17}_{-0.18}$	79^{+61}_{-48}	$1.00^{+4.30}_{-0.73}$	≥ 395	2.65E-11	1.20E+44	3.12E-11	1.42E+44
NGC 526a	$1.63^{+0.21}_{-0.21}$	$1.56^{+0.06}_{-0.06}$	$6.49^{+0.15}_{-0.16}$	116^{+45}_{-45}			1.73E-11	1.21E+43	4.37E-11	3.07E+43
NGC 985	$1.23^{+0.31}_{-0.28}$	$1.75^{+0.20}_{-0.14}$	$6.40^{+0.25}_{-0.27}$	$79.7^{+49.9}_{-51.1}$	$0.91^{+0.94}_{-0.81}$	≥ 72	1.42E-11	5.24E+43	2.68E-11	1.01E+44
ESO198-G24-a	≤ 0.25	$1.76^{+0.29}_{-0.09}$	$6.31^{+0.19}_{-0.29}$	79^{+42}_{-42}	≤ 2.53	97^{+312}_{-58}	1.50E-11	6.28E+43	2.23E-11	9.59E+43
ESO198-G24-b	≤ 1.12	$1.94^{+0.40}_{-0.27}$	$6.92^{+0.35}_{-0.17}$	$93.2^{+101}_{-72.8}$	$3.50^{+3.51}_{-2.00}$	≥ 45.7	8.80E-12	3.59E+43	1.65E-11	7.03E+43

continued on next page

continued from previous page

Name	N_H 10^{20}cm^{-2}	Γ	E_{line} keV	EW_{Line} eV	R	E_c keV	$F_{2-10keV}$ $\text{erg s}^{-1} \text{cm}^{-2}$	$L_{2-10keV}$ erg s^{-1}	$F_{20-100keV}$ $\text{erg s}^{-1} \text{cm}^{-2}$	$L_{20-100keV}$ erg s^{-1}
NGC 1052	$21.8^{+4.80}_{-5.30}$	$1.51^{+0.28}_{-0.27}$	$6.51^{+0.17}_{-0.17}$	280^{+153}_{-160}	$0.15^{+3.72}_{-0.12}$		3.89E-12	1.86E+42	1.86E-11	8.93E+42
NGC 1068-a ²	≤ 0.35	$2.23^{+0.14}_{-0.21}$	$6.48^{+0.03}_{-0.04}$	1280^{+357}_{-240}	≥ 0.20	≥ 116	4.84E-12	1.49E+42	1.77E-11	8.53E+42
NGC 1068-b ²	≤ 0.15	$1.49^{+0.07}_{-0.07}$	$6.53^{+0.04}_{-0.04}$	2590^{+300}_{-300}	≤ 0.87	≥ 35	5.88E-12	1.81E+42	1.22E-11	3.78E+42
3C 78	≤ 0.58	$2.50^{+0.34}_{-0.30}$	$6.24^{+0.24}_{-0.18}$	1080^{+597}_{-605}			1.70E-12	2.02E+42	$\leq 1.65\text{E-}11$	$\leq 1.96\text{E+}43$
MARK 609-a	≤ 10.1	$1.87^{+0.50}_{-0.41}$	$7.84^{+0.50}_{-0.30}$	896^{+577}_{-546}			2.55E-12	6.63E+42	$\leq 1.75\text{E-}11$	$\leq 4.55\text{E+}43$
MARK 609-c	≤ 0.54	$1.77^{+0.21}_{-0.15}$	$6.76^{+0.35}_{-0.40}$	435^{+302}_{-303}			2.70E-12	7.16E+42	$\leq 1.44\text{E-}11$	$\leq 3.82\text{E+}43$
3c88	≤ 1.68	$2.17^{+0.90}_{-0.50}$					3.31E-13	6.00E+42	$\leq 1.19\text{E-}11$	$\leq 2.15\text{E+}44$
NGC 1365	$60.5^{+17.3}_{-11.4}$	$1.93^{+0.09}_{-0.39}$	$6.21^{+0.09}_{-0.14}$	382^{+277}_{-195}	$1.86^{+1.77}_{-0.74}$	≥ 110	6.83E-12	3.25E+41	5.12E-11	2.47E+42
NGC 1386	≤ 2.59	$2.57^{+1.19}_{-0.82}$	$6.31^{+0.15}_{-0.16}$	6820^{+2380}_{-2395}			3.57E-13	6.16E+39	cont.	cont.
3C111	$0.91^{+0.24}_{-0.29}$	$1.75^{+0.13}_{-0.18}$	$6.40^{+0.00}_{-0.00}$	≤ 72	≤ 2.25	≥ 82	2.50E-11	1.15E+44	4.43E-11	2.09E+44
3C120	≤ 1.31	$1.85^{+0.09}_{-0.12}$	$6.25^{+0.25}_{-0.28}$	$39.3^{+11.6}_{-29.7}$	$1.27^{+1.50}_{-0.70}$	76.6^{+94}_{-30}	4.99E-11	1.09E+44	5.52E-11	1.23E+44
UGC 3134	≤ 0.34	$1.57^{+0.12}_{-0.11}$					5.19E-12	9.22E+42	1.26E-11	2.24E+43
ESO33-G02 ¹	$2.52^{+0.35}_{-0.41}$	$1.99^{+0.18}_{-0.17}$	$6.42^{+0.19}_{-0.30}$	112^{+211}_{-82}	$0.61^{+0.62}_{-0.42}$		6.19E-12	4.35E+42	2.28E-11	1.62E+43
IRAS05189	$10.3^{+1.40}_{-1.41}$	$2.85^{+0.33}_{-0.14}$	$6.50^{+0.24}_{-0.20}$	255^{+171}_{-168}			3.21E-12	1.16E+43	$\leq 1.22\text{E-}11$	$\leq 4.41\text{E+}43$

continued on next page

continued from previous page

Name	N_H 10^{20}cm^{-2}	Γ	E_{line} keV	EW_{Line} eV	R	E_c keV	$F_{2-10keV}$ $\text{erg s}^{-1} \text{cm}^{-2}$	$L_{2-10keV}$ erg s^{-1}	$F_{20-100keV}$ $\text{erg s}^{-1} \text{cm}^{-2}$	$L_{20-100keV}$ erg s^{-1}
NGC 2110	$4.92^{+0.74}_{-0.68}$	$1.74^{+0.20}_{-0.13}$	$6.41^{+0.07}_{-0.14}$	208^{+47}_{-51}	$0.60^{+1.38}_{-0.57}$	≥ 70.5	3.00E-11	3.49E+43	6.15E-11	7.21E+43
MCG 8-11-11	≤ 1.21	$1.80^{+0.10}_{-0.10}$	$6.49^{+0.07}_{-0.07}$	127^{+30}_{-30}	$0.40^{+0.33}_{-0.24}$	141^{+198}_{-53}	5.52E-11	4.33E+43	8.26E-11	6.54E+43
H0557-a	$0.86^{+0.66}_{-0.47}$	$2.09^{+0.44}_{-0.41}$	$6.41^{+0.18}_{-0.18}$	150^{+170}_{-107}	$3.02^{+5.21}_{-1.52}$	35^{+175}_{-20}	3.35E-11	7.66E+43	2.59E-11	6.24E+43
H0557-b ³	$1.03^{+0.40}_{-0.36}$	$2.26^{+0.39}_{-0.22}$	$6.42^{+0.40}_{-0.39}$	≤ 161	$2.28^{+5.20}_{-1.30}$	≥ 155	3.65E-11	8.38E+43	4.66E-11	1.09E+44
MARK 3	$110^{+8.00}_{-8.00}$	$1.80^{+0.05}_{-0.17}$	$6.39^{+0.03}_{-0.11}$	542^{+145}_{-86}	$0.95^{+0.16}_{-0.18}$	≥ 187	6.73E-12	2.32E+42	1.05E-10	3.71E+43
NGC 2273	≤ 1.61	$0.48^{+0.46}_{-0.32}$	$6.42^{+0.08}_{-0.09}$	2730^{+587}_{-612}			1.24E-12	8.55E+40	$\leq 1.62\text{E-}11$	$\leq 1.12\text{E+}42$
MARK 6	$2.46^{+0.20}_{-0.21}$	$1.66^{+0.09}_{-0.08}$	$6.38^{+0.11}_{-0.14}$	97^{+33}_{-33}	$0.54^{+0.53}_{-0.44}$	≥ 133	2.91E-11	2.05E+43	7.85E-11	5.57E+43
MARK 1210	$20.0^{+0.79}_{-2.22}$	$1.83^{+0.07}_{-0.18}$	$6.48^{+0.14}_{-0.16}$	144^{+59}_{-61}	$1.34^{+0.70}_{-0.33}$	≥ 107	9.91E-12	3.20E+42	5.03E-11	1.65E+43
MCG-1-24-12	$6.94^{+0.22}_{-0.54}$	$1.90^{+0.20}_{-0.11}$	$6.38^{+0.12}_{-0.12}$	165^{+54}_{-54}	$1.49^{1.08}_{0.93}$	≥ 420	2.68E-12	2.08E+42	2.96E-11	2.31E+43
MARK 110-a	≤ 0.07	$1.82^{+0.03}_{-0.03}$	$6.63^{+0.39}_{-0.25}$	91^{+61}_{-63}			2.52E-11	6.18E+43	3.63E-11	8.91E+43
MARK 110-b	≤ 0.25	$1.76^{+0.06}_{-0.06}$					2.09E-11	5.13E+43	3.28E-11	8.04E+43
MARK 110-c	≤ 0.59	$1.71^{+0.12}_{-0.11}$					8.83E-12	2.16E+43	1.67E-11	4.07E+43
NGC 2992-a	$1.48^{+0.71}_{-0.48}$	$1.89^{+0.56}_{-0.26}$	$6.44^{+0.11}_{-0.13}$	≤ 333	≥ 0.45	≥ 35	6.30E-12	7.20E+41	1.51E-11	1.73E+42
NGC 2992-b	$0.84^{+0.14}_{-0.13}$	$1.68^{+0.19}_{-0.05}$	$6.49^{+0.11}_{-0.11}$	$99^{+29.2}_{-32.7}$	≤ 2.73	153^{+166}_{-54}	7.34E-11	8.40E+42	1.17E-10	1.34E+43

continued on next page

continued from previous page

Name	N_H 10^{20}cm^{-2}	Γ	E_{line} keV	EW_{Line} eV	R	E_c keV	$F_{2-10keV}$ erg s $^{-1}$ cm $^{-2}$	$L_{2-10keV}$ erg s $^{-1}$	$F_{20-100keV}$ erg s $^{-1}$ cm $^{-2}$	$L_{20-100keV}$ erg s $^{-1}$
MCG-5-23-16	$1.74^{+0.06}_{-0.14}$	$1.79^{+0.07}_{-0.08}$	$6.49^{+0.08}_{-0.08}$	93^{+24}_{-22}	$0.74^{+0.22}_{-0.52}$	191^{+110}_{-60}	9.29E-11	1.29E+43	1.46E-10	1.29E+43
M 81	$0.18^{+0.18}_{-0.14}$	$1.90^{+0.10}_{-0.09}$	$6.83^{+0.14}_{-0.09}$	$93.3^{+36.5}_{-37.4}$	≤ 1.97	$107^{+1200}_{-54.9}$	3.87E-11	9.49E+38	3.82E-11	9.34E+38
NGC 3081	≤ 2.30	$-0.59^{+0.46}_{-0.50}$	$6.39^{+0.12}_{-0.12}$	1520^{+539}_{-536}			1.61E-12	1.96E+41	$\leq 3.17\text{E-}11$	$\leq 3.86\text{E+}42$
NGC 3079-a	795^{+470}_{-400}	$2.43^{+0.50}_{-0.40}$	$6.29^{+0.33}_{-1.85}$	≤ 4300			3.68E-13	6.36E+39	2.20E-11	3.79E+41
NGC 3079-b	241^{+50}_{-44}	$2.49^{+0.51}_{-0.46}$	$5.98^{+1.21}_{-1.98}$	≤ 4800			7.27E-13	1.43E+40	1.79E-11	3.55E+41
NGC 3147	≤ 1.66	$1.92^{+0.42}_{-0.29}$	$6.47^{+0.39}_{-0.29}$	441^{+320}_{-298}			2.26E-12	4.37E+41	$\leq 1.31\text{E-}11$	$\leq 2.53\text{E+}42$
NGC 3281	146^{+27}_{-47}	$1.36^{+0.21}_{-0.48}$	$6.48^{+0.06}_{-0.06}$	1500^{+1260}_{-890}	$0.72^{+1.26}_{-0.38}$	65^{+28}_{-27}	2.80E-12	5.28E+41	6.82E-11	1.32E+44
RE J1034+396	≤ 0.18	$2.15^{+0.17}_{-0.17}$					1.11E-12	4.03E+42	$\leq 1.22\text{E-}11$	$\leq 4.43\text{E+}43$
NGC 3393	≤ 2.75	$0.40^{+0.68}_{-0.75}$	$6.32^{+0.14}_{-0.14}$	2700^{+1060}_{-1080}			7.19E-13	1.98E+41	$\leq 1.85\text{E-}11$	$\leq 5.09\text{E+}42$
NGC 3516-a ¹	$2.08^{+0.29}_{-0.26}$	$1.71^{+0.21}_{-0.10}$	$6.41^{+0.11}_{-0.10}$	644^{+176}_{-126}	$1.23^{+1.86}_{-0.59}$	183^{+547}_{-68}	2.53E-11	3.77E+42	7.18E-11	1.08E+43
NGC 3516-b ¹	$0.61^{+0.28}_{-0.12}$	$1.72^{+0.30}_{-0.08}$	$6.42^{+0.09}_{-0.11}$	$91.9^{+31.3}_{-54.0}$	$1.37^{+1.68}_{-0.59}$	101^{+404}_{-37}	4.53E-11	6.76E+42	8.35E-11	1.25E+43
NGC 3516-c ¹	≤ 0.00	$1.91^{+0.07}_{-0.14}$	$6.36^{+0.08}_{-0.07}$	162^{+39}_{-50}	$1.61^{+1.68}_{-1.05}$	≥ 185	2.93E-11	4.38E+42	7.52E-11	1.13E+43
NGC 3516-d ¹	≤ 1.60	$2.06^{+0.08}_{-0.14}$	$6.44^{+0.05}_{-0.05}$	281^{+50}_{-50}	$2.77^{+3.62}_{-1.14}$	≥ 233	1.56E-11	2.34E+42	5.61E-11	8.59E+42
NGC 3516-e ¹	≤ 2.12	$2.07^{+0.19}_{-0.16}$	$6.45^{+0.08}_{-0.09}$	204^{+54}_{-56}	$2.62^{+2.36}_{-1.13}$	≥ 405	1.58E-11	2.36E+42	5.70E-11	8.56E+42

continued on next page

continued from previous page

Name	N_H 10^{20}cm^{-2}	Γ	E_{line} keV	EW_{Line} eV	R	E_c keV	$F_{2-10keV}$ $\text{erg s}^{-1}\text{ cm}^{-2}$	$L_{2-10keV}$ erg s^{-1}	$F_{20-100keV}$ $\text{erg s}^{-1}\text{ cm}^{-2}$	$L_{20-100keV}$ erg s^{-1}
NGC 3516-f ¹	≤ 0.27	$2.07^{+0.17}_{-0.17}$	$6.33^{+0.19}_{-0.20}$	151^{+47}_{-50}	$1.58^{+1.18}_{-0.82}$	≥ 379	3.56E-11	5.33E+42	6.43E-11	9.67E+42
NGC 3627	≤ 0.90	$1.91^{+0.67}_{-0.23}$					7.62E-13	8.41E+39	$\leq 1.15\text{E-}11$	$\leq 1.27\text{E+}41$
NGC 3660	263^{+98}_{-51}	$1.83^{+0.11}_{-0.11}$					2.36E-12	6.59E+41	2.67E-11	7.79E+42
NGC 3783 ¹	≤ 0.11	$1.79^{+0.14}_{-0.07}$	$6.43^{+0.07}_{-0.10}$	175^{+39}_{-59}	$0.50^{+0.90}_{-0.18}$	183^{+340}_{-53}	6.40E-11	1.17E+43	1.04E-10	1.91E+44
NGC 3998	≤ 0.47	$1.94^{+0.10}_{-0.09}$					1.18E-11	2.04E+40	1.27E-11	2.19E+41
NGC 4051-a	190^{+80}_{-92}	$2.56^{+0.45}_{-0.83}$	$6.42^{+0.12}_{-0.12}$	886^{+3600}_{-614}	$0.33^{+0.66}_{-0.21}$		1.62E-12	1.64E+40	1.18E-11	1.20E+42
NGC 4051-b	≤ 0.28	$1.61^{+0.10}_{-0.13}$					1.86E-11	1.43E+41	4.56E-11	3.50E+41
NGC 4151-a ¹	$8.34^{+1.24}_{-1.47}$	$1.45^{+0.17}_{-0.19}$	$6.16^{+0.06}_{-0.05}$	839^{+123}_{-105}	$1.18^{+0.65}_{-0.54}$	$66.9^{+25.8}_{-16.9}$	1.16E-10	2.42E+42	4.31E-10	9.01E+42
NGC 4151-b ¹	$12.2^{+0.81}_{-0.79}$	$1.45^{+0.12}_{-0.11}$	$6.45^{+0.04}_{-0.04}$	$375^{+73.5}_{-46.1}$	$1.02^{+0.98}_{-0.35}$	$92.3^{+34.8}_{-20.9}$	9.25E-11	1.93E+42	4.28E-10	8.96E+42
NGC 4151-c ¹	$10.0^{+0.82}_{-0.83}$	$1.20^{+0.12}_{-0.12}$	$6.44^{+0.04}_{-0.07}$	540^{+102}_{-80}	≤ 0.63	$56.4^{+14.1}_{-10.1}$	1.36E-10	2.82E+42	4.18E-10	8.73E+42
NGC 4151-d ¹	$7.73^{+1.17}_{-1.13}$	$1.62^{+0.15}_{-0.13}$	$6.39^{+0.04}_{-0.04}$	$124^{+14.3}_{-17.5}$	≤ 0.32	147^{+90}_{-57}	1.29E-10	2.66E+42	4.94E-10	1.03E+43
NGC 4151-e ¹	$9.07^{+1.19}_{-1.34}$	$1.67^{+0.14}_{-0.10}$	$6.46^{+0.08}_{-0.08}$	$307^{+87.9}_{-122}$	≤ 1.42	≥ 201	5.23E-11	1.09E+42	1.94E-10	4.07E+42
NGC 4151-f ¹	$1.91^{+0.45}_{-0.20}$	$1.75^{+0.02}_{-0.02}$	$6.42^{+0.03}_{-0.03}$	$112^{+11.8}_{-11.6}$	$0.42^{+0.13}_{-0.08}$	404^{+195}_{-109}	2.03E-10	4.24E+42	5.34E-10	1.12E+43
MARK 766-a ¹	≤ 0.23	$1.95^{+0.07}_{-0.05}$					1.96E-11	6.44E+42	cont.	cont.

continued on next page

continued from previous page

Name	N_H 10^{20}cm^{-2}	Γ	E_{line} keV	EW_{Line} eV	R	E_c keV	$F_{2-10keV}$ $\text{erg s}^{-1} \text{cm}^{-2}$	$L_{2-10keV}$ erg s^{-1}	$F_{20-100keV}$ $\text{erg s}^{-1} \text{cm}^{-2}$	$L_{20-100keV}$ erg s^{-1}
MARK 766-b ¹	≤ 0.12	$2.03^{+0.06}_{-0.03}$	$6.46^{+0.27}_{-0.19}$	85.5^{+45}_{-47}			2.31E-11	7.60E+42	cont.	cont.
NGC 4258	$11.7^{+1.15}_{-1.15}$	$2.18^{+0.08}_{-0.15}$	$6.57^{+0.21}_{-0.23}$	$81.5^{+64.2}_{-71.2}$			7.99E-12	6.12E+40	9.19E-12	7.05E+40
NGC 4261	≤ 0.27	$1.65^{+0.18}_{-0.17}$					1.11E-12	1.05E+42	$\leq 9.81\text{E-12}$	$\leq 9.28\text{E+42}$
MARK 205-a	≤ 0.15	$1.86^{+0.09}_{-0.09}$					8.36E-12	8.61E+43	$\leq 1.92\text{E-11}$	$\leq 1.98\text{E+44}$
MARK 205-b	≤ 0.08	$1.86^{+0.04}_{-0.03}$	$6.50^{+0.20}_{-0.26}$	117^{+184}_{-47}			1.11E-11	1.14E+44	1.42E-11	1.47E+44
MARK 205-c	≤ 0.18	$1.73^{+0.08}_{-0.07}$					7.49E-12	7.66E+43	1.33E-11	1.36E+44
NGC 4388-a	$40.9^{+2.51}_{-2.00}$	$1.65^{+0.05}_{-0.14}$	$6.45^{+0.05}_{-0.07}$	$195^{+40.2}_{-19}$	≤ 0.38	≥ 457	2.50E-11	3.37E+42	1.86E-10	2.54E+43
NGC 4388-b	$51.0^{+7.61}_{-6.80}$	$1.52^{+0.12}_{-0.13}$	$6.37^{+0.06}_{-0.07}$	636^{+163}_{-143}		≥ 135	9.24E-12	1.24E+42	8.29E-11	1.13E+43
NGC 4507-a	$60^{+7.2}_{-7.1}$	$1.62^{+0.18}_{-0.22}$	$6.41^{+0.01}_{-0.10}$	190^{+57}_{-59}	$0.54^{+0.24}_{-0.20}$	152^{+350}_{-70}	1.78E-11	4.70E+42	1.70E-10	4.60E+43
NGC 4507-b	$55.4^{+16.2}_{-13.1}$	$1.25^{+0.42}_{-0.43}$	$6.43^{+0.07}_{-0.07}$	875^{+285}_{-215}	$2.67^{+3.34}_{-2.44}$	≤ 303	8.47E-12	2.24E+42	1.01E-10	2.75E+43
NGC 4507-c	$64.5^{+5.9}_{-6.2}$	$1.85^{+0.06}_{-0.16}$	$6.57^{+0.11}_{-0.12}$	301^{+88}_{-89}	$0.90^{+0.19}_{-0.26}$	≥ 68	1.61E-11	4.26E+42	1.48E-10	4.01E+43
NGC 4579	≤ 0.33	$1.80^{+0.11}_{-0.07}$	$6.66^{+0.13}_{-0.13}$	417^{+159}_{-143}			5.52E-12	2.66E+41	7.65E-12	3.68E+41
NGC 4593	≤ 0.38	$1.91^{+0.10}_{-0.09}$	$6.43^{+0.12}_{-0.12}$	269^{+123}_{-160}	$1.05^{+2.60}_{-0.47}$	≥ 200	3.66E-11	5.74E+42	7.02E-11	1.11E+43
M 104	≤ 0.87	$1.99^{+0.27}_{-0.17}$	$6.54^{+0.44}_{-0.30}$	283^{+240}_{-238}			1.80E-12	3.10E+40	$\leq 2.58\text{E-12}$	$\leq 4.40\text{E+40}$

continued on next page

continued from previous page

Name	N_H 10^{20}cm^{-2}	Γ	E_{line} keV	EW_{Line} eV	R	E_c keV	$F_{2-10keV}$ $\text{erg s}^{-1} \text{cm}^{-2}$	$L_{2-10keV}$ erg s^{-1}	$F_{20-100keV}$ $\text{erg s}^{-1} \text{cm}^{-2}$	$L_{20-100keV}$ erg s^{-1}
IC3639	≤ 5.43	$1.57^{+1.05}_{-0.74}$	$6.46^{+0.22}_{-0.22}$	2030^{+890}_{-920}			3.70E-13	8.63E+40	$\leq 9.12\text{E-}12$	$\leq 2.13\text{E+}42$
M94	$0.91^{+0.74}_{-0.69}$	$1.97^{+0.23}_{-0.25}$	$6.69^{+0.34}_{-0.33}$	245^{+224}_{-216}			1.89E-12	3.61E+39	$\leq 9.56\text{E-}12$	$\leq 1.82\text{E+}40$
MARK 231	≤ 1.61	$0.72^{+0.33}_{-0.18}$	$5.28^{+0.20}_{-0.13}$	455^{+209}_{-212}			8.13E-13	2.65E+42	$\leq 7.06\text{E-}12$	$\leq 2.30\text{E+}43$
NGC 4826	≤ 4.26	$1.84^{+2.00}_{-0.73}$					1.53E-13	2.93E+38	$\leq 8.84\text{E-}12$	$\leq 16.9\text{E+}40$
NGC 4941	67.4^{+28}_{-12}	$2.73^{+0.95}_{-0.52}$	$6.41^{+0.17}_{-0.14}$	675^{+507}_{-349}			1.03E-12	2.71E+40	$\leq 3.85\text{E-}11$	$\leq 1.37\text{E+}42$
NGC 4939	$45.0^{+17.8}_{-15.2}$	$1.35^{+0.35}_{-0.43}$	$6.65^{+0.16}_{-0.17}$	481^{+286}_{-248}			1.94E-12	3.67E+43	2.08E-11	4.33E+44
NGC 4945	496^{+55}_{-46}	$1.57^{+0.09}_{-0.08}$	$6.50^{+0.04}_{-0.07}$	909^{+180}_{-155}		122^{+41}_{-26}	5.21E-12	3.23E+40	2.90E-10	1.80E+42
IRAS13197 ¹	$47.1^{+6.80}_{-6.80}$	$3.10^{+0.41}_{-0.30}$	$6.42^{+0.13}_{-0.12}$	236^{+275}_{-126}			4.49E-12	2.35E+42	2.77E-11	1.50E+43
IRAS13224-a	$4.25^{+4.45}_{-4.18}$	$2.82^{+0.89}_{-1.06}$	$6.88^{+0.62}_{-0.33}$	1760^{+1920}_{-1330}			5.73E-13	5.07E+42	$\leq 1.60\text{E-}11$	$\leq 1.42\text{E+}44$
CenA-a	$10.5^{+0.02}_{-0.04}$	$1.80^{+0.03}_{-0.02}$	$6.43^{+0.07}_{-0.07}$	103^{+17}_{-18}	≤ 0.30	≥ 252	1.89E-10	1.17E+42	4.44E-10	2.76E+42
CenA-b	$10.5^{+0.06}_{-0.07}$	$1.84^{+0.02}_{-0.07}$	$6.49^{+0.09}_{-0.08}$	49^{+14}_{-14}	≤ 0.12	≥ 374	2.52E-10	1.56E+42	5.94E-10	3.69E+42
CenA-c	$9.82^{+0.03}_{-0.04}$	$1.80^{+0.02}_{-0.04}$	$6.57^{+0.03}_{-0.04}$	127^{+18}_{-18}	≤ 0.19	≥ 500	2.34E-10	1.45E+42	5.44E-10	3.38E+42
CenA-d	$9.97^{+0.03}_{-0.04}$	$1.80^{+0.04}_{-0.05}$	$6.47^{+0.08}_{-0.09}$	91^{+21}_{-22}	≤ 0.08	≥ 274	1.92E-10	1.19E+42	4.49E-10	2.79E+42
CenA-e	$9.69^{+0.03}_{-0.04}$	$1.77^{+0.02}_{-0.05}$	$6.52^{+0.05}_{-0.05}$	112^{+18}_{-18}	≤ 0.03	≥ 349	2.30E-10	1.42E+43	5.56E-10	3.45E+42

continued on next page

continued from previous page

Name	N_H 10^{20}cm^{-2}	Γ	E_{line} keV	EW_{Line} eV	R	E_c keV	$F_{2-10keV}$ $\text{erg s}^{-1} \text{cm}^{-2}$	$L_{2-10keV}$ erg s^{-1}	$F_{20-100keV}$ $\text{erg s}^{-1} \text{cm}^{-2}$	$L_{20-100keV}$ erg s^{-1}
M 51	≥ 403	$1.92^{+0.11}_{-0.11}$	$6.50^{+0.19}_{-0.19}$	382^{+263}_{-251}			$1.38\text{E-}12$	$1.06\text{E+}40$	$1.98\text{E-}11$	$1.52\text{E+}41$
MCG-6-30-15 -a ³	$0.38^{+0.14}_{-0.07}$	$2.08^{+0.12}_{-0.05}$	$6.90^{+0.09}_{-0.24}$	163^{+58}_{-43}	$1.31^{+0.62}_{-0.31}$	170^{+240}_{-53}	$5.02\text{E-}11$	$6.22\text{E+}42$	$5.59\text{E-}11$	$6.95\text{E+}42$
MCG-6-30-15 -b ³	≤ 1.08	$2.30^{+0.14}_{-0.10}$	$6.10^{+0.89}_{-0.30}$	$214^{+88}_{-93.4}$	$2.66^{+0.80}_{-0.75}$	≥ 292	$4.51\text{E-}11$	$5.57\text{E+}42$	$5.80\text{E-}11$	$7.19\text{E+}42$
NGC 5252	$9.15^{+2.85}_{-3.15}$	$1.73^{+0.30}_{-0.33}$	$6.46^{+0.19}_{-0.21}$	253^{+165}_{-168}			$2.56\text{E-}12$	$2.32\text{E+}42$	$6.63\text{E-}12$	$6.30\text{E+}42$
MARK 266	$5.32^{+6.65}_{-4.43}$	$1.88^{+1.12}_{-0.46}$					$5.32\text{E-}13$	$8.12\text{E+}41$	$\leq 1.20\text{E-}11$	$\leq 18.3\text{E+}43$
IC4329a-a ³	$0.55^{+0.09}_{-0.08}$	$1.87^{+0.05}_{-0.04}$	$6.48^{+0.13}_{-0.12}$	126^{+43}_{-35}	$0.42^{+0.11}_{-0.33}$	388^{+580}_{-160}	$1.36\text{E-}10$	$7.42\text{E+}43$	$1.92\text{E-}10$	$1.09\text{E+}44$
IC4329a-b ³	$0.54^{+0.21}_{-0.16}$	$2.01^{+0.06}_{-0.15}$	$6.60^{+0.19}_{-0.26}$	176^{+139}_{-85}	$1.48^{+1.46}_{-0.80}$	≥ 179	$6.89\text{E-}11$	$4.92\text{E+}43$	$1.33\text{E-}10$	$7.59\text{E+}43$
IC4329a-c ³	$0.53^{+0.26}_{-0.14}$	$1.84^{+0.17}_{-0.07}$	$6.63^{+0.61}_{-0.27}$	51^{+27}_{-40}	$0.46^{+1.50}_{-0.18}$	155^{+93}_{-44}	$1.20\text{E-}10$	$6.81\text{E+}43$	$1.64\text{E-}10$	$9.32\text{E+}43$
IC4329a-d ³	$0.57^{+0.22}_{-0.17}$	$1.99^{+0.19}_{-0.08}$	$6.53^{+0.20}_{-0.18}$	177^{+90}_{-94}	$1.10^{+1.90}_{-0.55}$	≥ 121	$1.18\text{E-}10$	$6.67\text{E+}43$	$1.85\text{E-}10$	$1.06\text{E+}44$
IC4329a-e ³	$0.48^{+0.13}_{-0.12}$	$1.89^{+0.08}_{-0.07}$	$6.35^{+0.16}_{-0.25}$	171^{+115}_{-69}	$0.54^{+0.55}_{-0.34}$	204^{+190}_{-70}	$1.69\text{E-}10$	$9.56\text{E+}43$	$2.43\text{E-}10$	$1.38\text{E+}44$
MARK 463-b	≤ 2.89	$1.99^{+1.14}_{-0.58}$					$3.61\text{E-}13$	$1.86\text{E+}42$	$\leq 1.44\text{E-}11$	$\leq 7.43\text{E+}43$
MARK 463-c	≤ 6.77	$2.02^{+1.06}_{-0.84}$					$4.73\text{E-}13$	$2.38\text{E+}42$	$\leq 1.13\text{E-}11$	$\leq 5.82\text{E+}43$
Circ-a ²	825^{+80}_{-75}	$1.69^{+0.13}_{-0.14}$	$6.44^{+0.01}_{-0.01}$	2060^{+69}_{-88}	$0.29^{+0.05}_{-0.04}$	≤ 53	$1.53\text{E-}11$	$2.93\text{E+}40$	$1.83\text{E-}10$	$3.51\text{E+}41$
Circ-b ²	558^{+301}_{-124}	$1.27^{+0.20}_{-0.15}$	$6.48^{+0.01}_{-0.01}$	2110^{+114}_{-124}	$0.35^{+0.39}_{-0.09}$	≤ 50	$1.92\text{E-}11$	$3.68\text{E+}40$	$1.80\text{E-}10$	$3.45\text{E+}41$

continued on next page

continued from previous page

Name	N_H 10^{20}cm^{-2}	Γ	E_{line} keV	EW_{Line} eV	R	E_c keV	$F_{2-10keV}$ $\text{erg s}^{-1} \text{cm}^{-2}$	$L_{2-10keV}$ erg s^{-1}	$F_{20-100keV}$ $\text{erg s}^{-1} \text{cm}^{-2}$	$L_{20-100keV}$ erg s^{-1}
NGC 5506-a	$4.36^{+0.27}_{-0.23}$	$2.11^{+0.14}_{-0.10}$	$6.43^{+0.19}_{-0.11}$	131^{+37}_{-41}	$1.30^{+1.28}_{-0.42}$	≥ 177	2.06E-11	4.99E+42	1.24E-10	8.61E+42
NGC 5506-b	$3.38^{+0.08}_{-0.19}$	$2.05^{+0.09}_{-0.09}$	$6.44^{+0.09}_{-0.09}$	129^{+41}_{-43}	$2.26^{+0.92}_{-0.40}$		4.91E-11	3.40E+42	1.38E-10	9.60E+42
NGC 5506-c	$3.87^{+0.36}_{-2.92}$	$2.08^{+0.13}_{-0.10}$	$6.47^{+0.09}_{-0.09}$	135^{+29}_{-31}	$1.61^{+0.55}_{-0.95}$	≥ 210	7.73E-11	7.27E+42	1.36E-10	1.29E+43
NGC 5548-a	$0.25^{+0.19}_{-0.15}$	$1.63^{+0.09}_{-0.07}$	$6.39^{+0.07}_{-0.07}$	117^{+35}_{-34}	$0.62^{+0.58}_{-0.39}$	107^{+259}_{-45}	3.46E-11	1.95E+43	6.92E-11	3.94E+43
NGC 5548-b	$0.45^{+0.17}_{-0.20}$	$1.87^{+0.12}_{-0.17}$	$6.39^{+0.09}_{-0.09}$	93.1^{+38}_{-33}	$1.68^{+1.00}_{-1.15}$	≥ 131	3.60E-11	2.03E+43	7.05E-11	4.00E+43
NGC 5548-c	$0.22^{+0.23}_{-0.13}$	$1.64^{+0.21}_{-0.12}$	$6.39^{+0.14}_{-0.17}$	$80.3^{+32.5}_{-43.3}$	$0.74^{+1.58}_{-0.47}$	90^{+111}_{-41}	3.65E-11	2.05E+43	6.87E-11	3.91E+43
NGC 5548-d	$0.53^{+0.26}_{-0.25}$	$1.68^{+0.11}_{-0.10}$	$6.49^{+0.07}_{-0.07}$	208^{+47}_{-53}	$0.57^{+0.55}_{-0.35}$	≥ 102	3.14E-11	1.77E+43	7.26E-11	4.12E+43
NGC 5548-e	≤ 0.28	$1.77^{+0.14}_{-0.07}$	$6.40^{+0.15}_{-0.15}$	76^{+39}_{-36}	$1.02^{+1.48}_{-0.64}$	180^{+455}_{-83}	4.59E-11	2.59E+43	8.27E-11	4.70E+43
NGC 5548-f	$0.38^{+0.20}_{-0.19}$	$1.83^{+0.10}_{-0.07}$	$6.35^{+0.10}_{-0.10}$	73^{+28}_{-27}	$0.73^{+0.35}_{-0.35}$	≥ 197	4.17E-11	2.36E+43	8.00E-11	4.53E+43
NGC 5643	≤ 4.10	$1.75^{+0.46}_{-0.63}$	$6.75^{+0.20}_{-0.23}$	1220^{+705}_{-715}			1.64E-12	5.02E+40	$\leq 2.28\text{E-}11$	$\leq 6.98\text{E+}41$
NGC 5674	$5.79^{+0.97}_{-0.96}$	$1.61^{+0.17}_{-0.16}$	$6.36^{+0.13}_{-0.15}$	252^{+116}_{-118}			5.35E-12	6.47E+42	1.61E-11	1.97E+43
MARK 478	≤ 1.08	$2.38^{+0.18}_{-0.17}$					3.77E-12	5.16E+43	cont.	cont.
MARK 841-a ³	≤ 0.30	$2.12^{+0.31}_{-0.10}$	$6.40^{+0.40}_{-0.30}$	300^{+145}_{-250}	$3.00^{+4.32}_{-1.43}$	≥ 50	1.26E-11	3.27E+43	1.88E-11	4.98E+43
MARK 841-b	≤ 1.20	$2.21^{+0.30}_{-0.24}$			$3.54^{+3.21}_{-2.09}$	≥ 67	1.64E-11	4.29E+43	2.05E-11	5.49E+43

continued on next page

continued from previous page

Name	N_H 10^{20}cm^{-2}	Γ	E_{line} keV	EW_{Line} eV	R	E_c keV	$F_{2-10keV}$ $\text{erg s}^{-1} \text{cm}^{-2}$	$L_{2-10keV}$ erg s^{-1}	$F_{20-100keV}$ $\text{erg s}^{-1} \text{cm}^{-2}$	$L_{20-100keV}$ erg s^{-1}
NGC 6251	≤ 0.62	$1.86^{+0.13}_{-0.12}$					4.75E-12	5.87E+42	6.43E-12	7.96E+42
NGC 6212	≤ 0.51	$1.63^{+0.16}_{-0.10}$					5.03E-12	8.95E+42	1.07E-11	1.91E+43
NGC 6240	179^{+40}_{-15}	$1.98^{+0.25}_{-0.16}$	$6.50^{+0.15}_{-0.07}$	1880^{+1590}_{-730}			2.20E-12	2.41E+42	3.32E-11	3.78E+43
NGC 6300	$25^{+1.86}_{-1.56}$	$1.96^{+0.06}_{-0.12}$	$6.26^{+0.23}_{-0.16}$	162^{+53}_{-58}	$1.87^{+0.44}_{-0.31}$		1.27E-11	3.61E+41	6.30E-11	1.80E+42
3C382	≤ 0.07	$1.88^{+0.06}_{-0.04}$	$6.51^{+0.27}_{-0.18}$	$37.3^{+64.3}_{-27.6}$	$1.10^{+0.57}_{-0.80}$	170^{+284}_{-71}	6.01E-11	4.18E+44	7.64E-11	5.43E+44
Fairall 49	$1.34^{+0.15}_{-0.12}$	$2.15^{+0.05}_{-0.05}$	$6.54^{+0.12}_{-0.12}$	116^{+40}_{-40}			3.65E-12	1.68E+43	1.27E-11	1.00E+43
ESO103	$20.2^{+4.52}_{-2.74}$	$1.81^{+0.20}_{-0.10}$	$6.48^{+0.11}_{-0.15}$	278^{+142}_{-129}	$0.57^{+1.81}_{-0.26}$	$0.00^{+0.00}_{-40.0}$	1.52E-11	4.93E+42	6.24E-11	2.05E+43
3C390	≤ 0.17	$1.73^{+0.11}_{-0.05}$	$6.39^{+0.09}_{-0.11}$	$107^{+31.7}_{-32.6}$	$1.37^{+1.13}_{-0.48}$	163^{+822}_{-68}	2.20E-11	1.40E+44	4.50E-11	2.95E+44
H 1846-786	≤ 0.30	$1.86^{+0.10}_{-0.07}$				0.	8.18E-11	9.48E+43	1.14E-11	1.32E+44
ESO141	≤ 0.15	$1.93^{+0.23}_{-0.09}$	$6.45^{+0.09}_{-0.09}$	137^{+48}_{-42}	$1.77^{+2.96}_{-0.71}$	≥ 85.0	2.45E-11	6.35E+43	3.84E-11	1.02E+44
Cyg A	$22.8^{+3.62}_{-2.88}$	$1.77^{+0.08}_{-0.08}$	6.72				1.88E-11	1.12E+44	8.01E-11	5.15E+44
IRAS20051	≤ 0.21	$1.87^{+0.12}_{-0.12}$					2.24E-12	4.02E+42	2.70E-12	4.85E+42
IRAS20210	≤ 3.16	$0.75^{+0.38}_{-0.26}$	$6.74^{+0.18}_{-0.21}$	1070^{+483}_{-513}			6.65E-13	4.08E+42	8.94E-12	5.46E+43
MARK 509-a	≤ 1.79	$1.84^{+0.21}_{-0.07}$	$6.39^{+0.96}_{-0.39}$	47^{+36}_{-23}	$0.76^{+0.79}_{-0.29}$		5.16E-11	9.24E+43	6.45E-11	1.17E+44

continued on next page

continued from previous page

Name	N_H 10^{20}cm^{-2}	Γ	E_{line} keV	EW_{Line} eV	R	E_c keV	$F_{2-10keV}$ $\text{erg s}^{-1} \text{cm}^{-2}$	$L_{2-10keV}$ erg s^{-1}	$F_{20-100keV}$ $\text{erg s}^{-1} \text{cm}^{-2}$	$L_{20-100keV}$ erg s^{-1}
MARK 509-b	≤ 0.10	$1.95^{+0.06}_{-0.08}$	$6.52^{+0.41}_{-0.30}$	≤ 80	$1.35^{+1.05}_{-0.83}$	≥ 90	6.27E-11	1.45E+44	7.67E-11	1.80E+44
MARK 509-c ²	≤ 0.30	$1.74^{+0.23}_{-0.11}$	$6.20^{+0.21}_{-0.23}$	64^{+50}_{-50}	$1.15^{+4.24}_{-0.61}$	83^{+120}_{-33}	2.92E-11	6.73E+43	5.16E-11	1.22E+44
MARK 509-d	≤ 1.12	$1.60^{+0.34}_{-0.21}$	$6.40^{+0.22}_{-0.20}$	70^{+58}_{-54}	$1.17^{+2.37}_{-0.73}$	60^{+71}_{-23}	2.63E-11	6.04E+43	5.43E-11	1.28E+44
MARK 509-e	≤ 0.12	$1.59^{+0.04}_{-0.06}$	$6.74^{+0.23}_{-0.20}$	127^{+62}_{-62}		133^{+389}_{-50}	2.58E-11	5.94E+43	4.13E-11	9.61E+43
MARK 509-f	≤ 0.19	$1.60^{+0.34}_{-0.23}$	$6.19^{+0.27}_{-0.14}$	154^{+62}_{-64}	$0.75^{+1.22}_{-0.55}$	62^{+61}_{-31}	2.56E-11	5.87E+43	4.47E-11	1.06E+44
S52116+81-a	≤ 0.33	$1.76^{+0.10}_{-0.05}$					1.55E-11	2.32E+44	2.40E-11	3.60E+44
S52116+81-b	≤ 0.81	$1.84^{+0.16}_{-0.13}$					1.15E-12	1.74E+44	1.52E-11	2.30E+44
PKS2153-69	≤ 0.76	$1.82^{+0.14}_{0.17}$	$6.50^{+0.20}_{-0.20}$	214^{+161}_{-150}			7.35E-12	1.14E+43	$\leq 1.88\text{E-}11$	$\leq 2.92\text{E+}43$
NGC 7172-a	$10.8^{+1.32}_{-1.31}$	$1.89^{+0.16}_{-0.20}$	$6.50^{+0.21}_{-0.19}$	111^{+98}_{-78}	$0.53^{+3.42}_{-0.32}$	≥ 76	1.14E-11	1.65E+42	3.77E-11	5.53E+42
NGC 7172-b	$11.2^{+1.60}_{-2.59}$	$1.90^{+0.32}_{-0.34}$	$6.55^{+0.33}_{-0.20}$	155^{+129}_{-77}	$2.03^{+5.42}_{-1.51}$	≥ 35	5.96E-12	8.66E+41	2.23E-11	3.27E+42
IRAS22017	$4.64^{+1.16}_{-1.05}$	$1.42^{+0.19}_{-0.16}$	$6.56^{+0.20}_{-0.25}$	323^{+145}_{-150}			3.57E-12	2.62E+43	1.48E-11	1.12E+44
NGC 7213-a ³	≤ 0.14	$1.77^{+0.03}_{-0.04}$	$6.85^{+0.42}_{-0.21}$	489^{+160}_{-156}		≥ 188	3.24E-11	2.24E+42	4.78E-11	3.31E+42
NGC 7213-b	≤ 0.42	$1.86^{+0.15}_{-0.11}$	$6.89^{+0.23}_{-0.32}$	118^{+100}_{-98}	≤ 1.28	≥ 236	3.25E-11	2.25E+42	4.49E-11	3.11E+42
NGC 7213-c	≤ 0.21	$1.74^{+0.06}_{-0.05}$	$6.52^{+0.14}_{-0.32}$	$80.4^{+42.9}_{-44.9}$	≤ 0.49	≥ 148	4.16E-11	2.88E+42	5.95E-11	4.13E+42

continued on next page

continued from previous page

Name	N_H 10^{20}cm^{-2}	Γ	E_{line} keV	EW_{Line} eV	R	E_c keV	$F_{2-10keV}$ $\text{erg s}^{-1} \text{cm}^{-2}$	$L_{2-10keV}$ erg s^{-1}	$F_{20-100keV}$ $\text{erg s}^{-1} \text{cm}^{-2}$	$L_{20-100keV}$ erg s^{-1}
NGC 7213-d	≤ 0.38	$1.82^{+0.15}_{-0.14}$	$6.70^{+0.25}_{-0.21}$	198^{+156}_{-98}	≤ 2.10	≤ 300	$2.31\text{E-}11$	$1.60\text{E+}42$	$2.59\text{E-}11$	$1.80\text{E+}42$
3C 445 ¹	$13.3^{+4.75}_{-9.33}$	$1.92^{+0.31}_{-0.24}$	$6.43^{+0.12}_{-0.12}$	197^{+223}_{-47}			$6.18\text{E-}12$	$3.74\text{E+}43$	$3.20\text{E-}11$	$2.09\text{E+}44$
NGC 7314	$0.93^{+0.25}_{-0.15}$	$1.94^{+0.07}_{-0.08}$	$6.51^{+0.20}_{-0.20}$	151^{+79}_{-61}	$1.16^{+1.26}_{-0.33}$	≥ 403	$2.36\text{E-}11$	$1.13\text{E+}42$	$4.72\text{E-}11$	$2.27\text{E+}42$
AKN 564-a	≤ 0.10	$2.44^{+0.06}_{-0.06}$	$6.37^{+0.28}_{-0.29}$	237^{+130}_{-120}			$1.47\text{E-}11$	$1.83\text{E+}42$	$\leq 1.48\text{E-}11$	$\leq 1.84\text{E+}42$
AKN 564-b	≤ 0.11	$2.45^{+0.06}_{-0.06}$	$6.60^{+0.26}_{-0.38}$	125^{+107}_{-110}			$1.55\text{E-}11$	$1.93\text{E+}42$	$5.03\text{E-}12$	$6.24\text{E+}41$
AKN 564-c	≤ 0.12	$2.51^{+0.05}_{-0.05}$	$6.91^{+0.25}_{-0.35}$	145^{+94}_{-100}			$1.40\text{E-}11$	$1.74\text{E+}42$	$4.02\text{E-}12$	$5.00\text{E+}41$
MR2251-a	$0.23^{+0.15}_{-0.19}$	$1.66^{+0.06}_{-0.11}$	$6.50^{+0.16}_{-0.12}$	72^{+33}_{-32}	$0.40^{+0.61}_{-0.38}$	132^{+130}_{-68}	$4.05\text{E-}11$	$3.86\text{E+}44$	$5.94\text{E-}11$	$5.83\text{E+}44$
MR2251-b	$0.40^{+0.13}_{-0.12}$	$1.69^{+0.04}_{-0.04}$	$6.57^{+0.14}_{-0.12}$	81^{+32}_{-32}			$4.08\text{E-}11$	$3.91\text{E+}44$	$7.06\text{E-}11$	$6.77\text{E+}44$
NGC 7469 ²	≤ 0.03	$2.05^{+0.02}_{-0.03}$	$6.35^{+0.14}_{-0.07}$	$84.3^{+20.2}_{-19.3}$	$1.66^{+0.53}_{-0.43}$	211^{+235}_{-95}	$3.72\text{E-}11$	$1.86\text{E+}43$	$3.89\text{E-}11$	$1.96\text{E+}43$
MARK 926	≤ 0.42	$1.77^{+0.19}_{-0.14}$	$6.54^{+0.63}_{-0.25}$	$82.3^{+156}_{-61.0}$	≤ 2.60	≥ 98	$3.34\text{E-}11$	$1.49\text{E+}44$	$5.39\text{E-}11$	$2.44\text{E+}44$
NGC 7582 ¹	$13.1^{+0.68}_{-1.17}$	$1.64^{+0.42}_{-0.37}$	$6.45^{+0.25}_{-0.32}$	≤ 133	$1.15^{+3.30}_{-0.99}$	≥ 50	$1.95\text{E-}11$	$1.01\text{E+}42$	$8.37\text{E-}11$	$4.37\text{E+}42$
NGC 7674	≤ 0.43	$1.99^{+0.37}_{-0.31}$	$6.51^{+0.12}_{-0.11}$	361^{+135}_{-137}	≥ 0.34	≥ 41	$1.18\text{E-}12$	$1.90\text{E+}42$	$4.03\text{E-}12$	$6.94\text{E+}42$
NGC 7679	≤ 0.20	$1.73^{+0.08}_{-0.05}$	$7.15^{+0.23}_{-0.47}$	$122^{+99.5}_{-101}$	$0.00^{+0.00}_{-0.00}$	$0.00^{+0.00}_{-0.00}$	$1.58\text{E-}12$	$3.39\text{E+}42$	$1.04\text{E-}11$	$5.88\text{E+}42$

continued on next page

continued from previous page

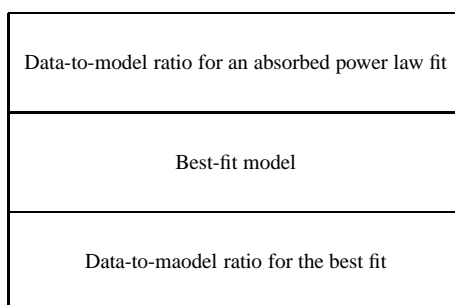
Name	N_H	Γ	E_{line}	EW_{Line}	R	E_c	$F_{2-10keV}$	$L_{2-10keV}$	$F_{20-100keV}$	$L_{20-100keV}$
	10^{20}cm^{-2}		keV	eV		keV	$\text{erg s}^{-1} \text{cm}^{-2}$	erg s^{-1}	$\text{erg s}^{-1} \text{cm}^{-2}$	erg s^{-1}

¹ Complex absorber; ² FeK β emission line is detected; ³ Broad FeK α emission line; *cont.* PDS data contaminated by other sources.

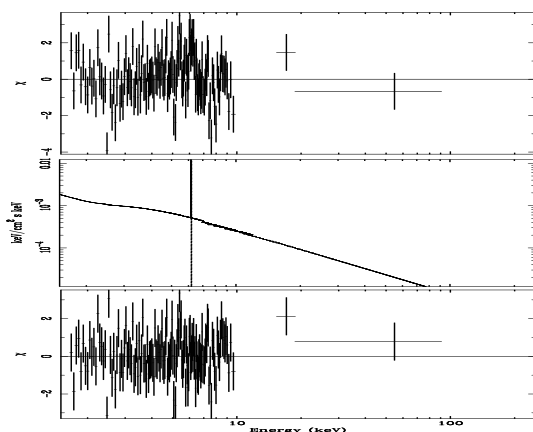
A.1 Atlas of the 2-100 keV spectra

Here the X-ray spectra of the sources are presented. For each source the data-to-model ratio for an absorbed power law fit, the best-fit model and its data-to-model ratio are presented in upper, middle and lower panel respectively (see the scheme below). The data-to-model ratios are expressed in terms of standard deviation.

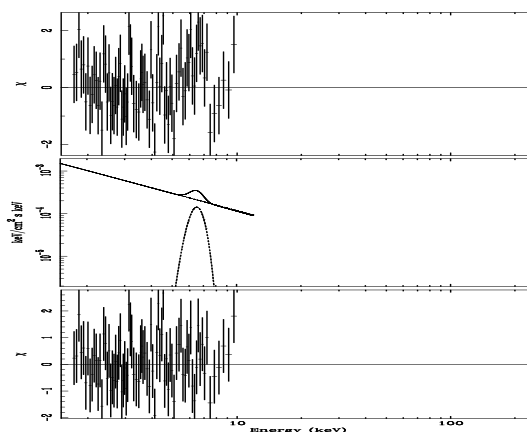
Source Name



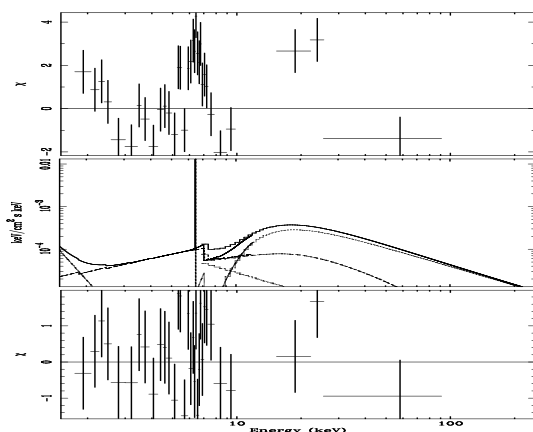
MARK 335



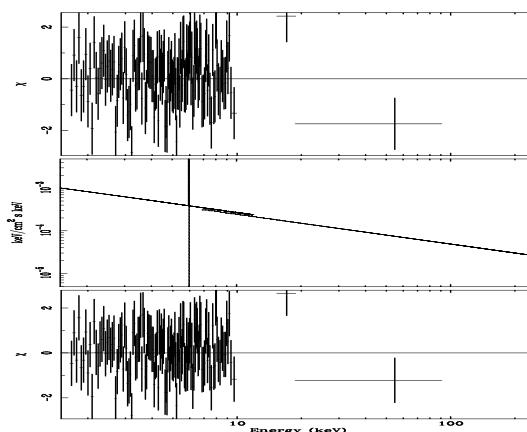
TonS 180



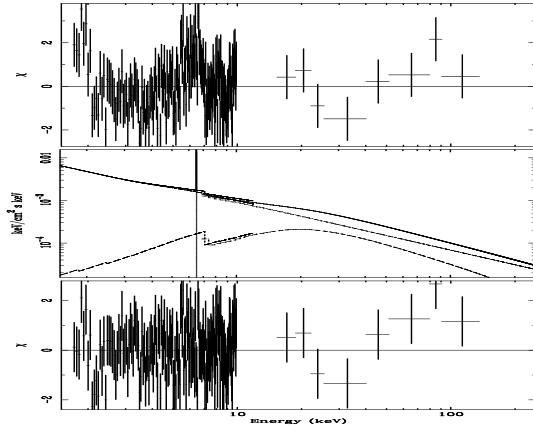
Tololo 109-383



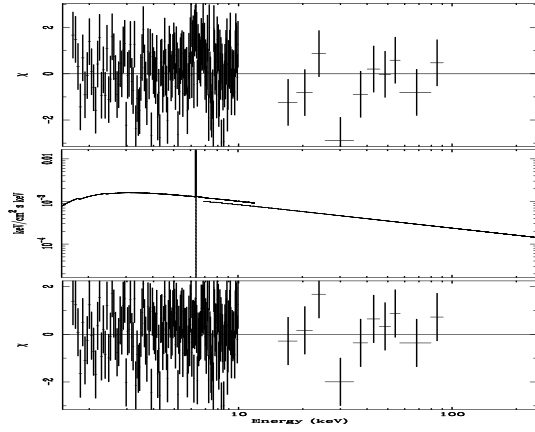
MARK 1152



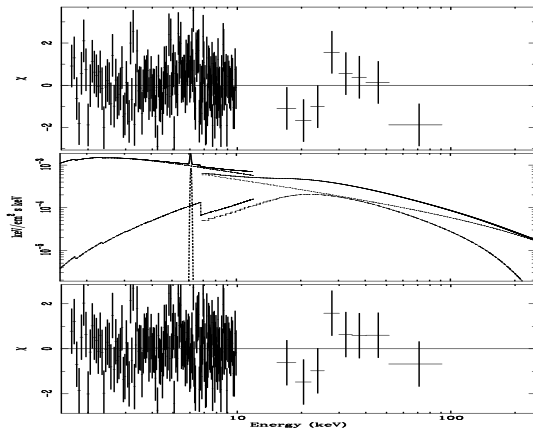
Fairall 9



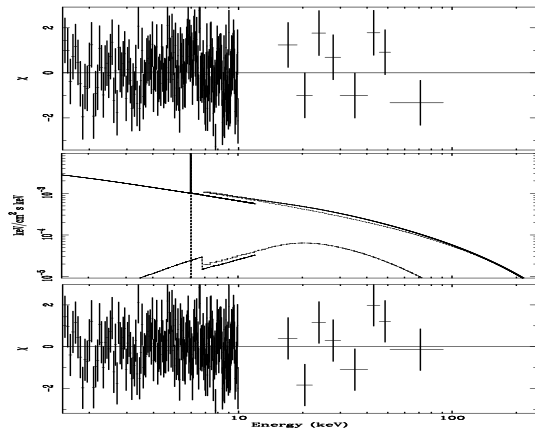
NGC 526a



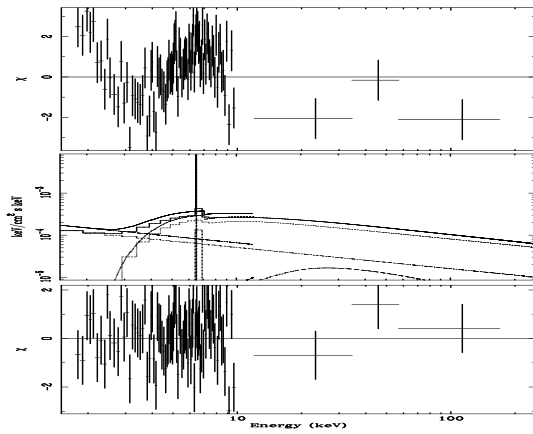
NGC 985



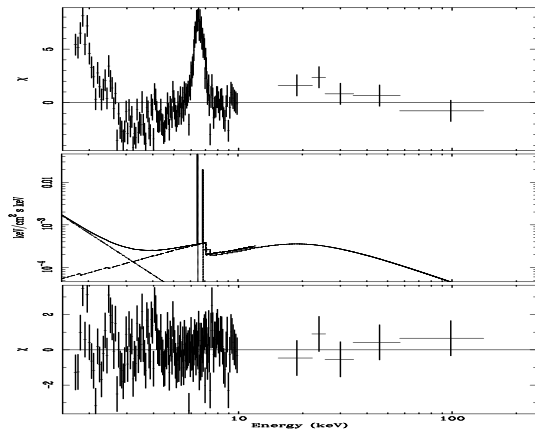
ESO 198-G24



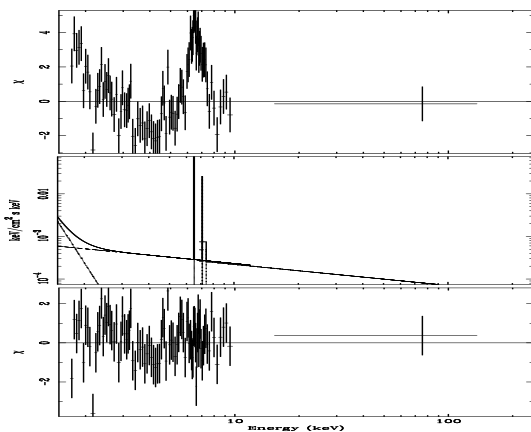
NGC 1052



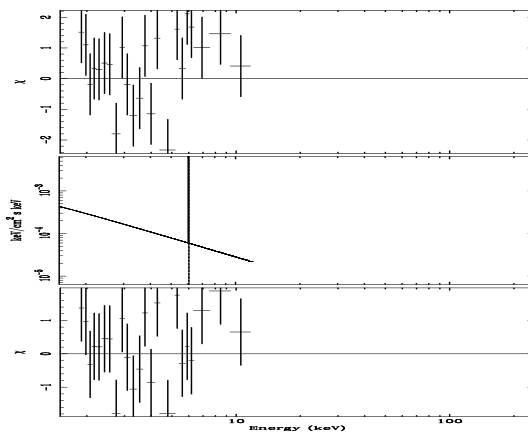
NGC 1068 -a



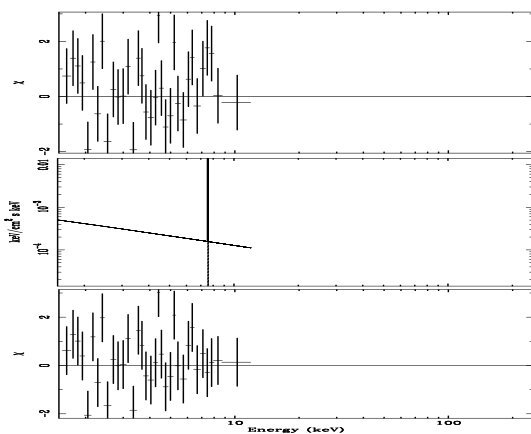
NGC 1068 -b



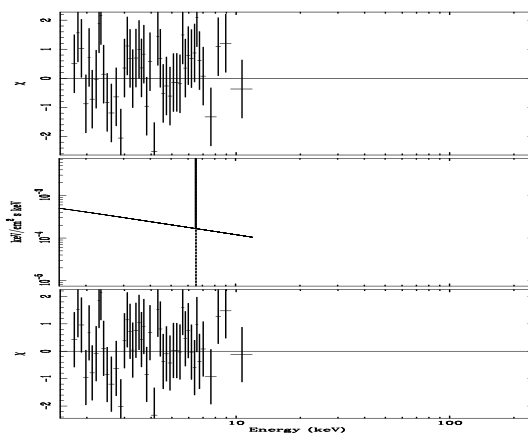
3C 78



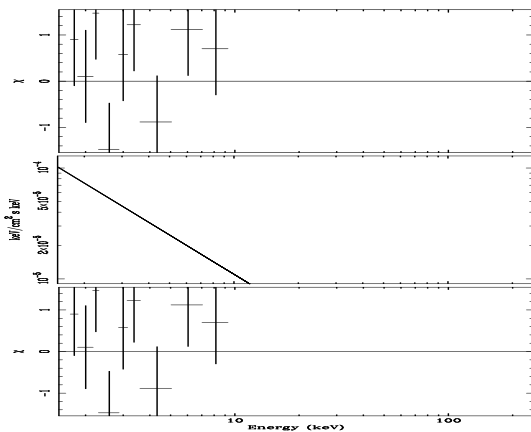
MARK 609 -a



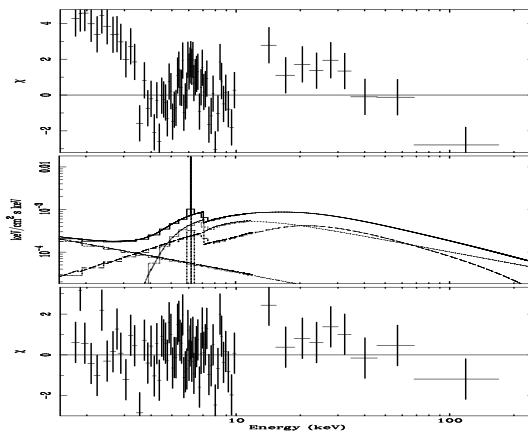
MARK 609 -c



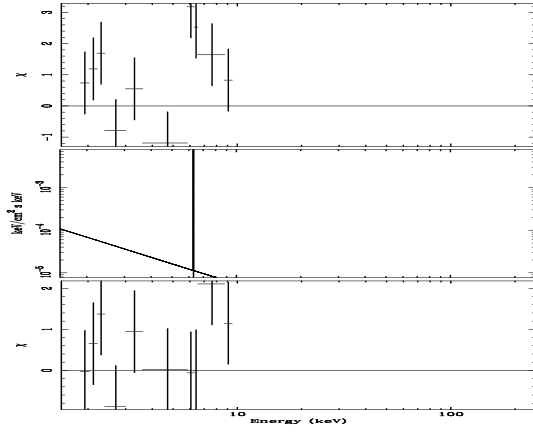
3C 88



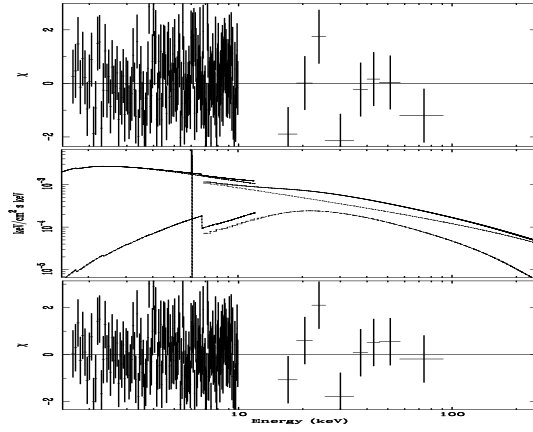
NGC 1365



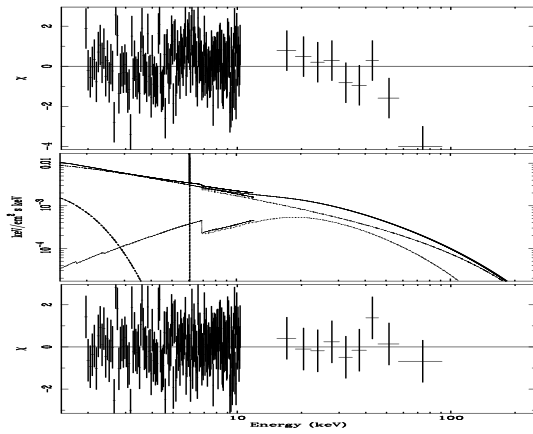
NGC 1386



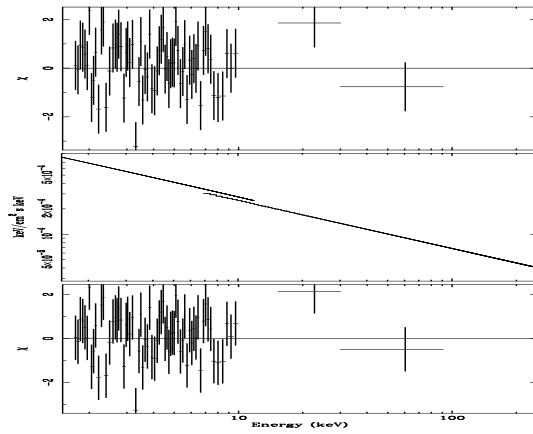
3C 111



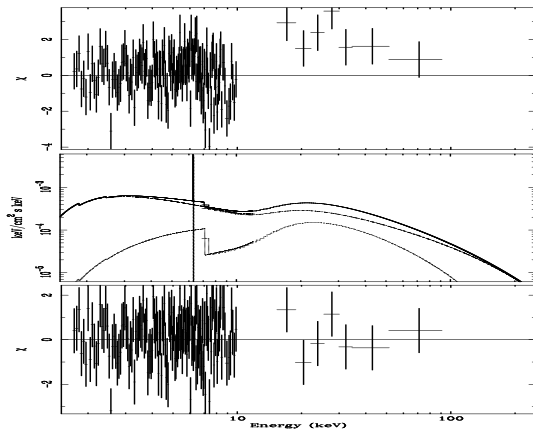
3C 120



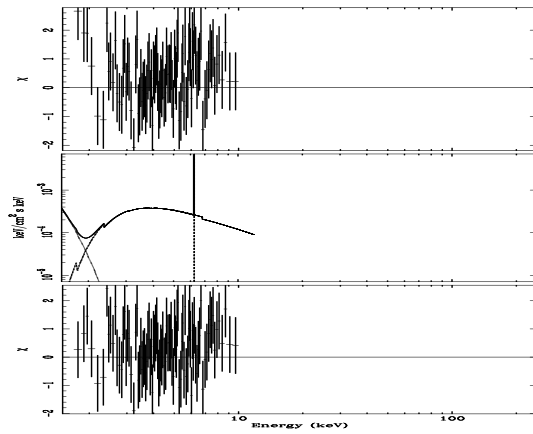
UGC 3134



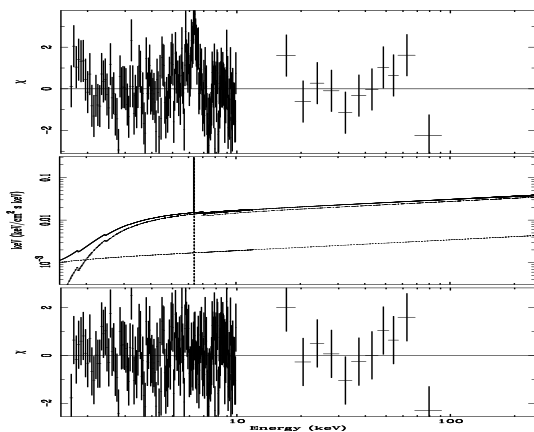
ESO 33-G2



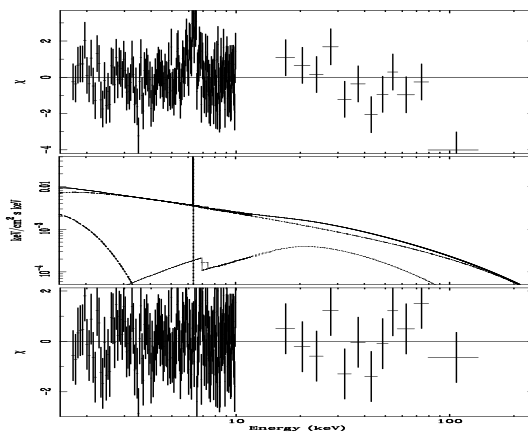
IRAS05189-2524



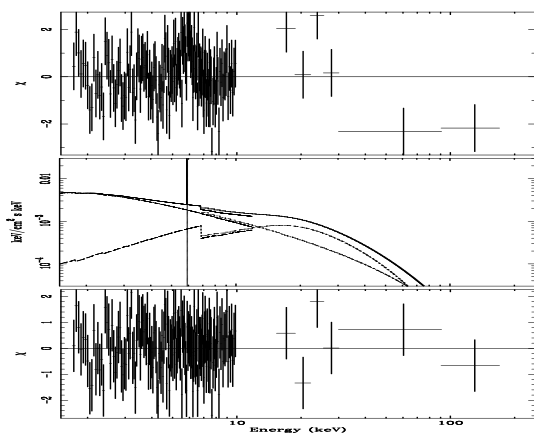
NGC 2110



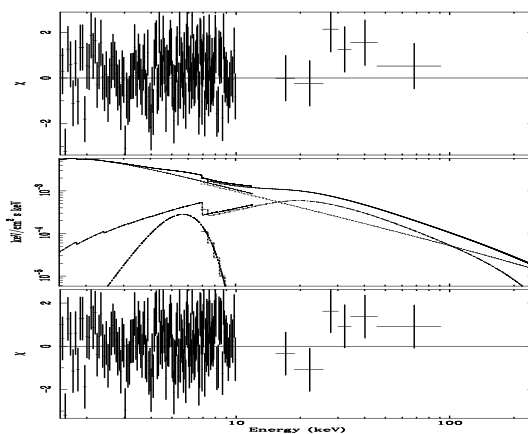
MCG 8-11-11



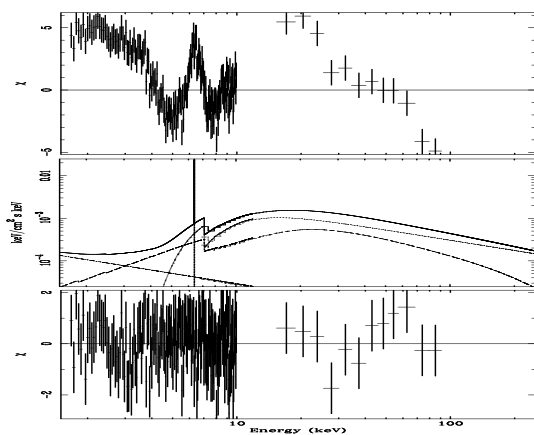
H0557-385 -a



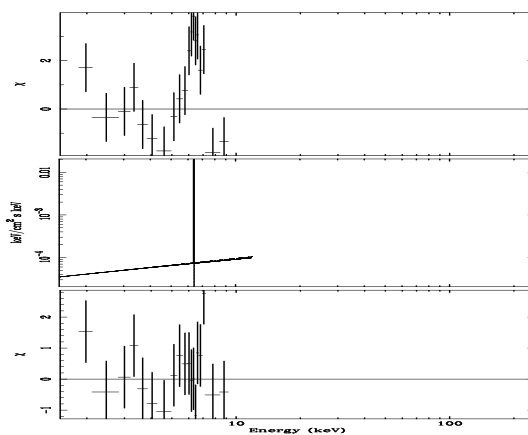
H0557-385 -b



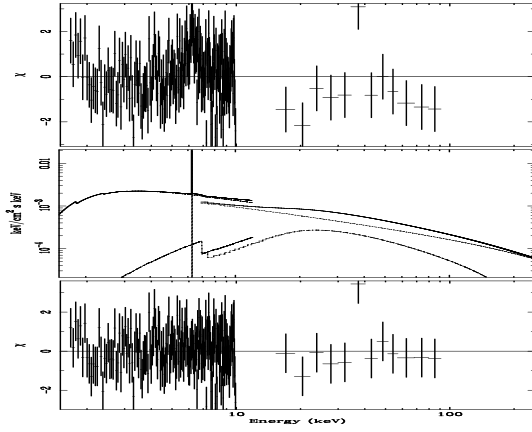
MKN 3



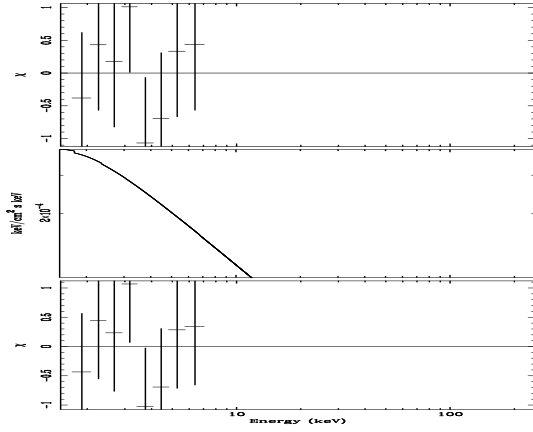
NGC 2273



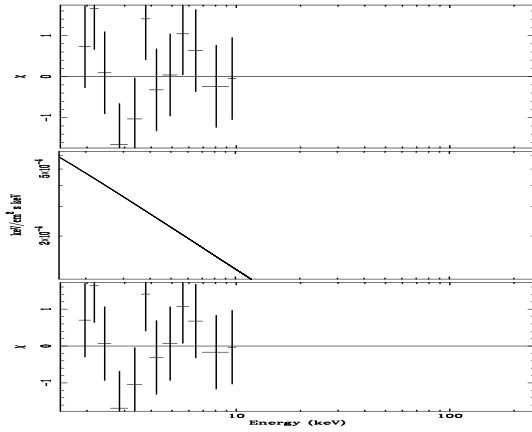
MKN 6



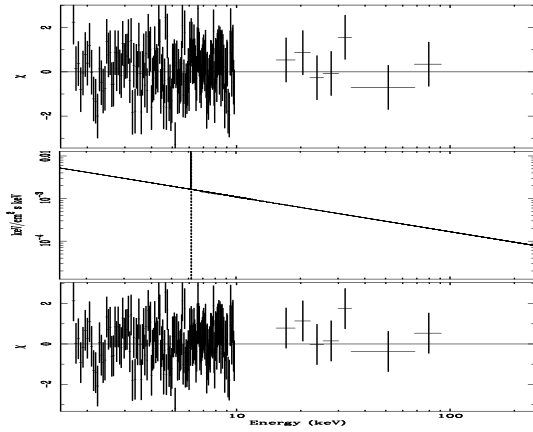
MCG-1-24-12 -a



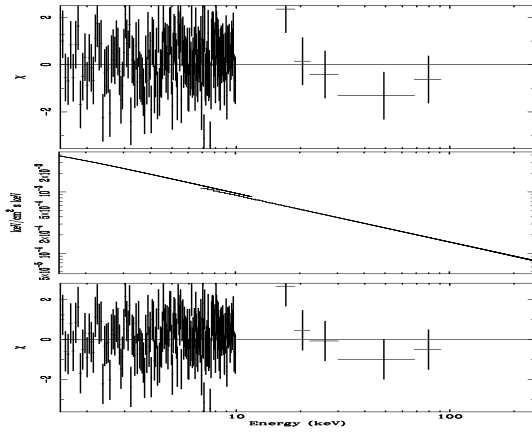
MCG-1-24-12 -b



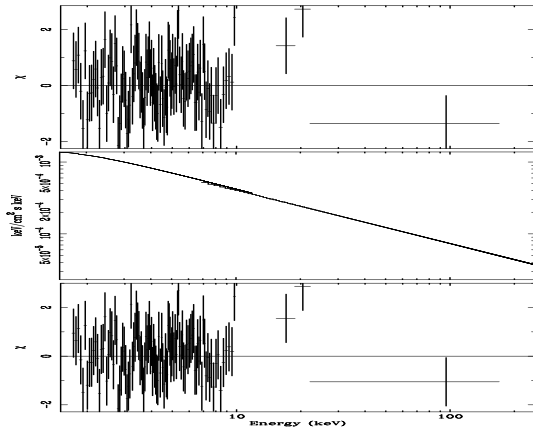
MKN 110 -a



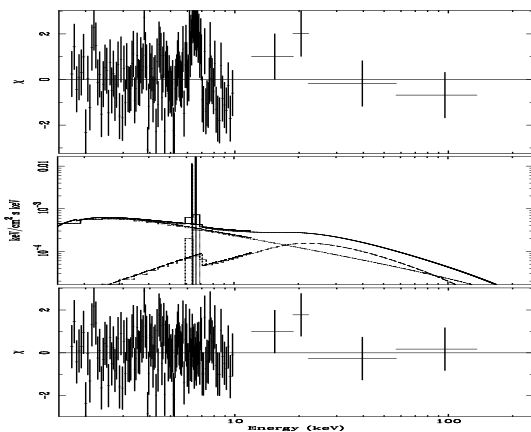
MKN 110 -b



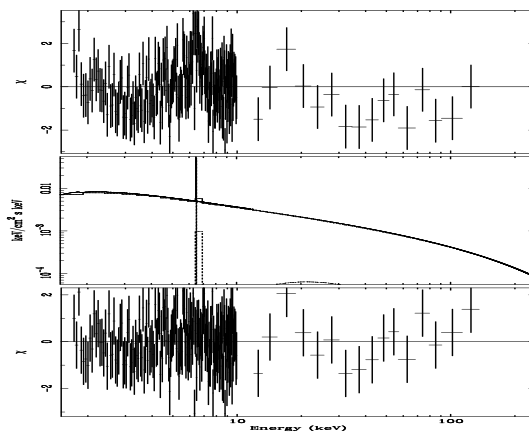
MKN 110 -c



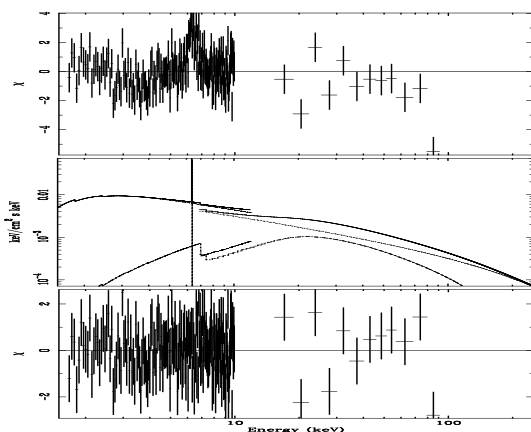
NGC 2992 -a



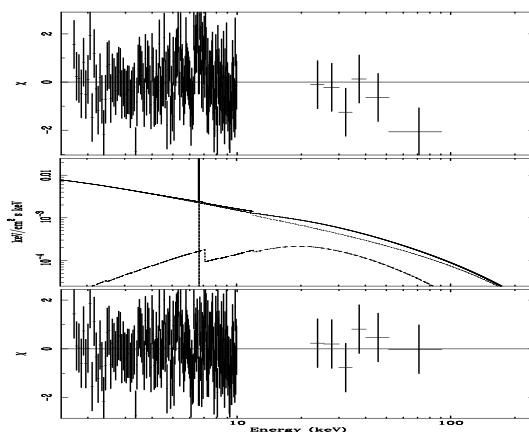
NGC 2992 -b



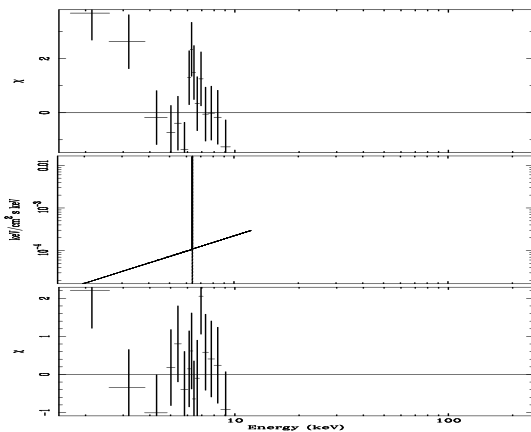
MCG-5-23-16



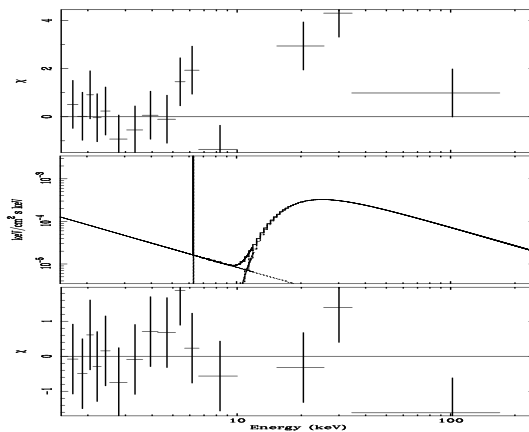
M 81



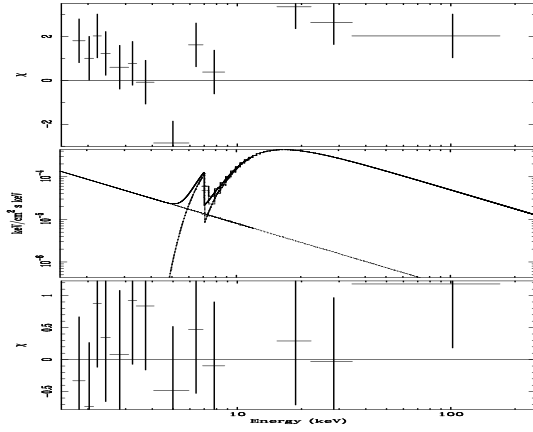
NGC 3081



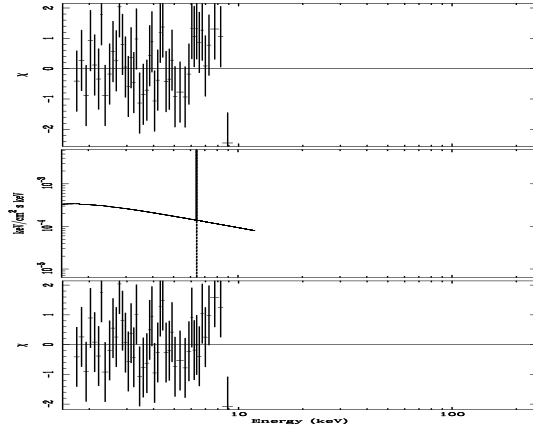
NGC 3079 -a



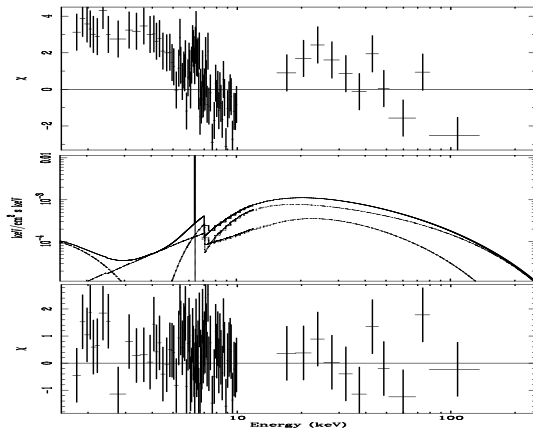
NGC 3079 -b



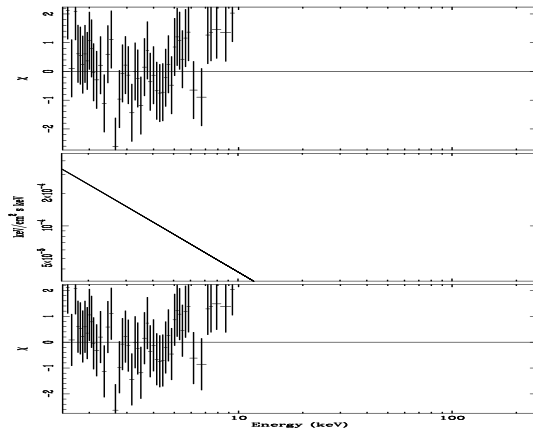
NGC 3147



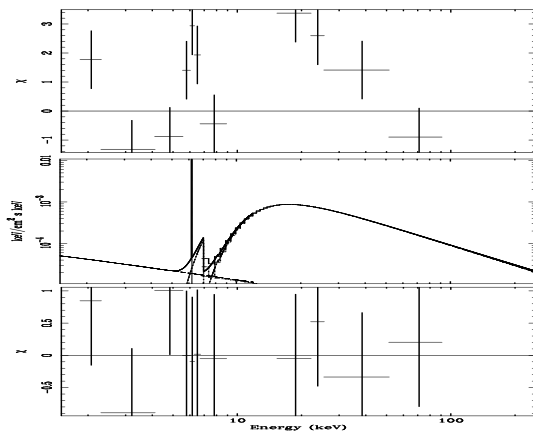
NGC 3281



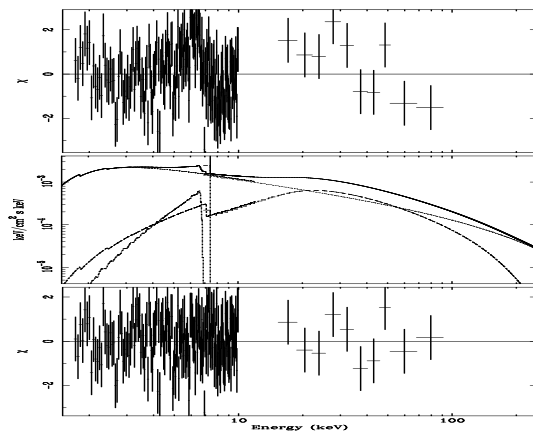
REJ1034+396



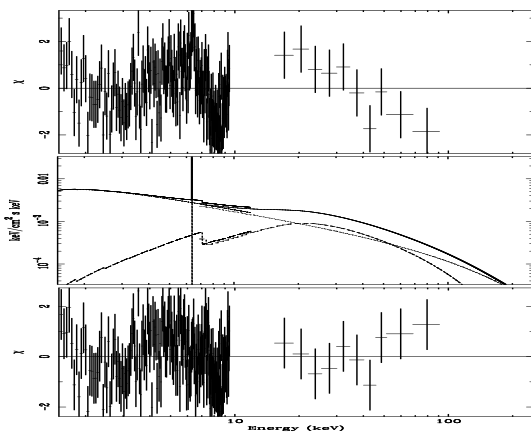
NGC 3393



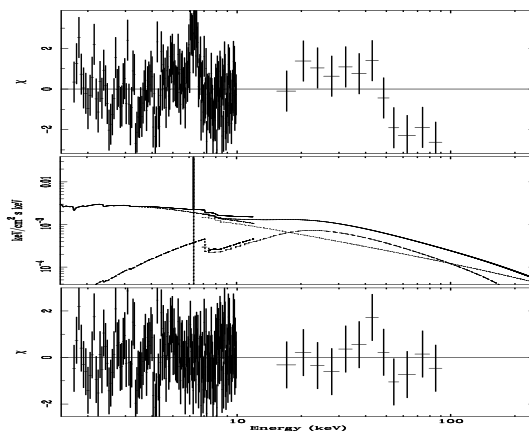
NGC 3516 -a



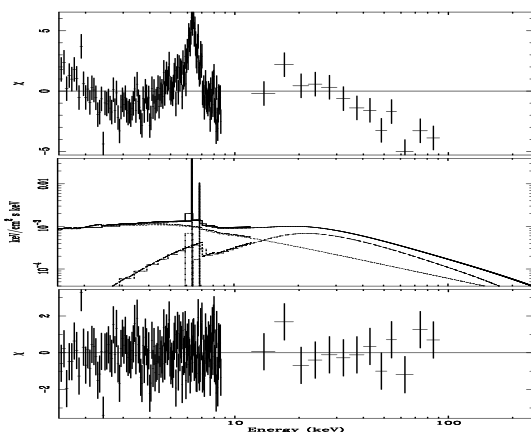
NGC 3516 -b



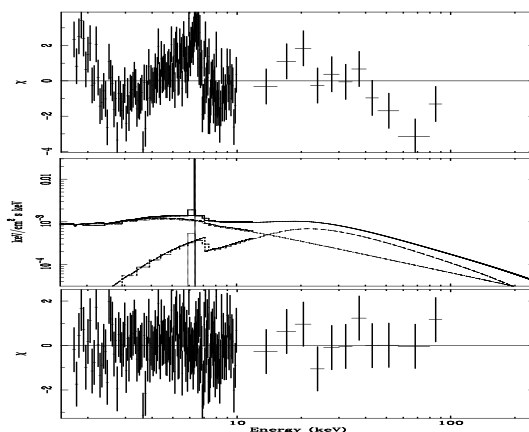
NGC 3516 -c



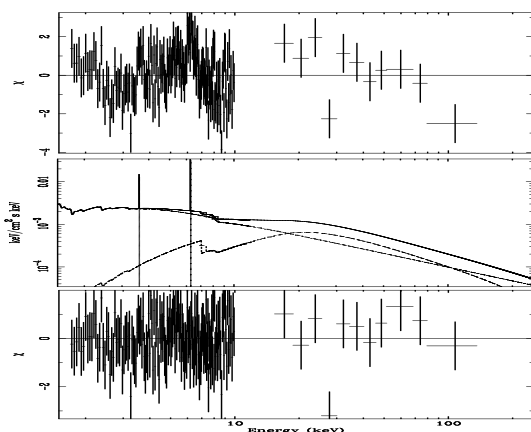
NGC 3516 -d



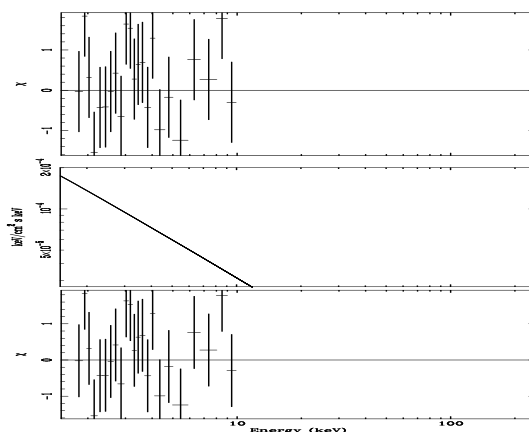
NGC 3516 -e



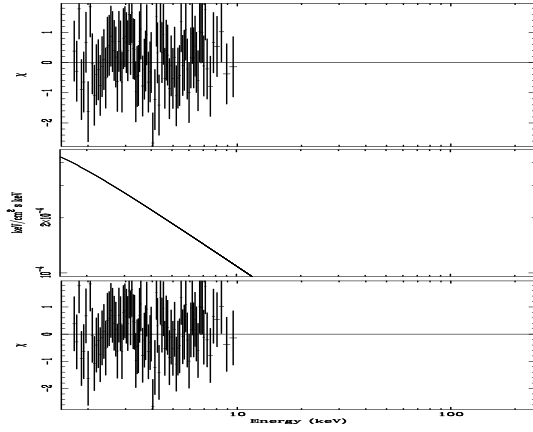
NGC 3516 -f



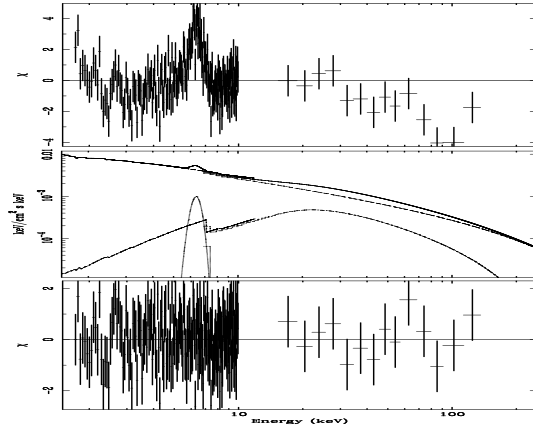
NGC 3627



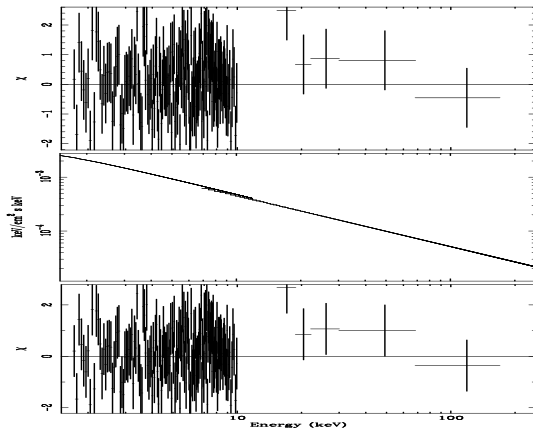
NGC 3660



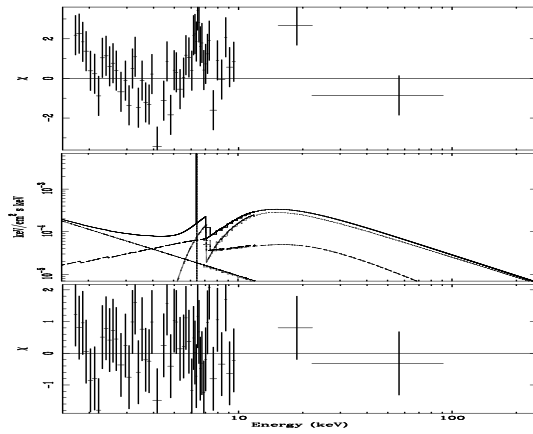
NGC 3783



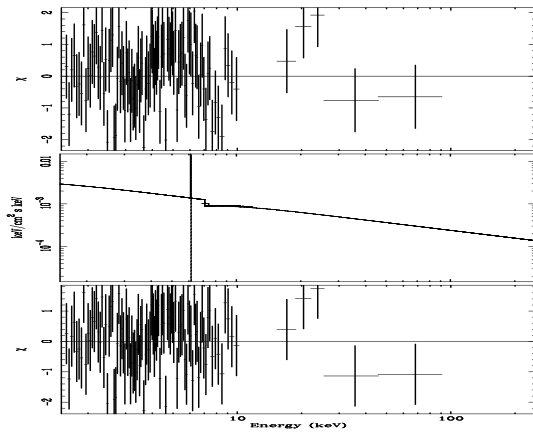
NGC 3998



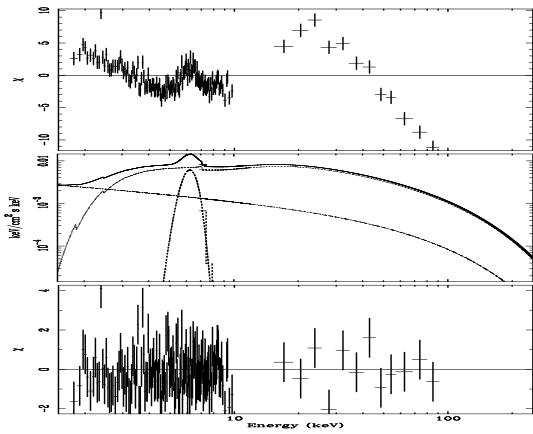
NGC 4051 -a



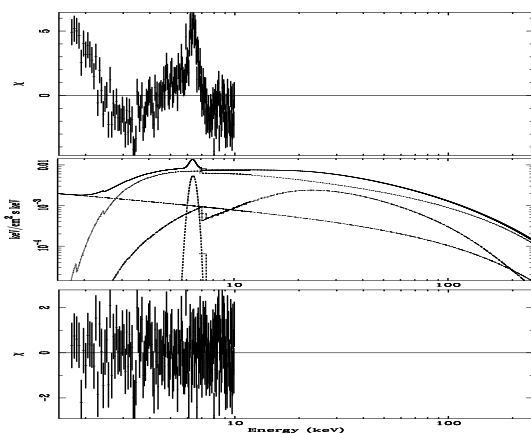
NGC 4051 -b



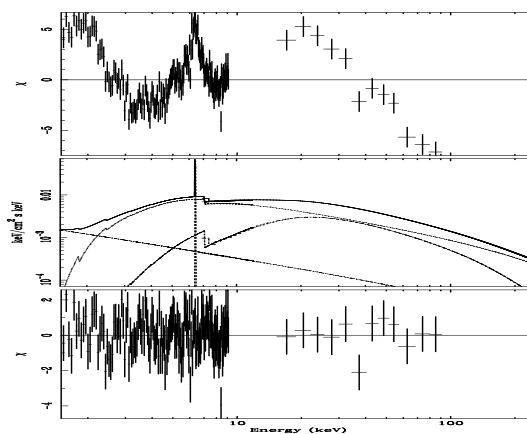
NGC 4151 -a



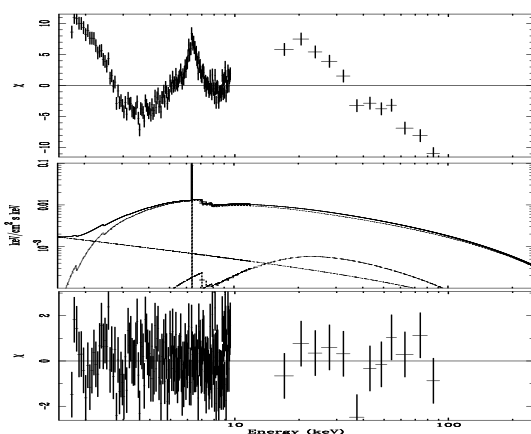
NGC 4151 -b



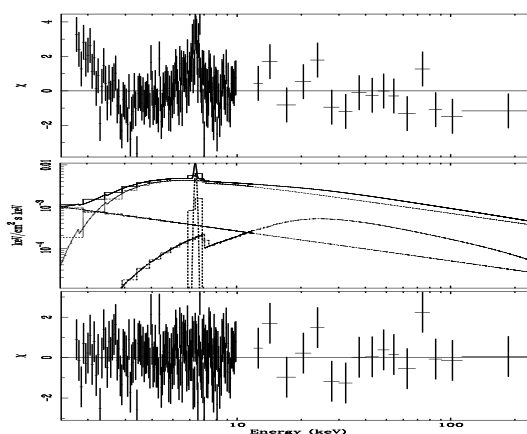
NGC 4151 -c



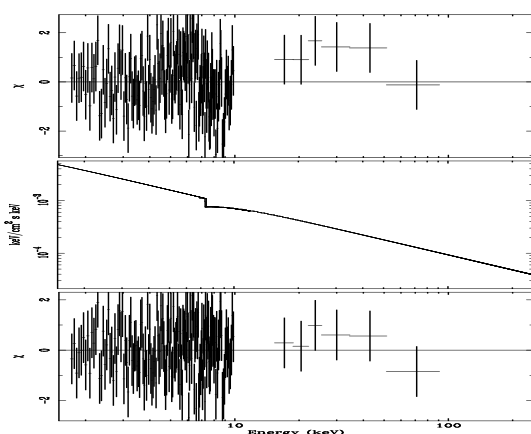
NGC 4151 -d



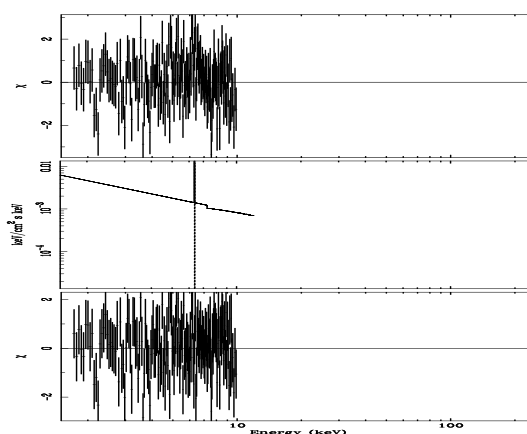
NGC 4151 -e



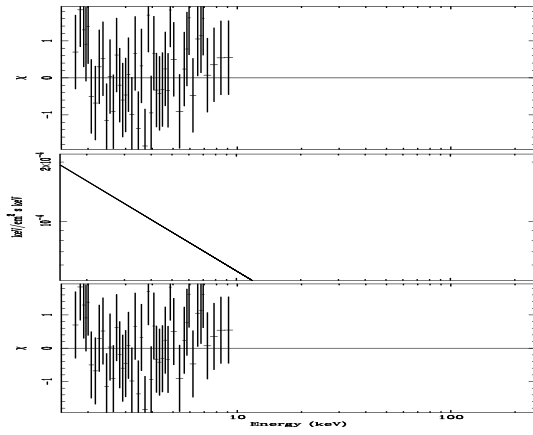
MKN 766 -a



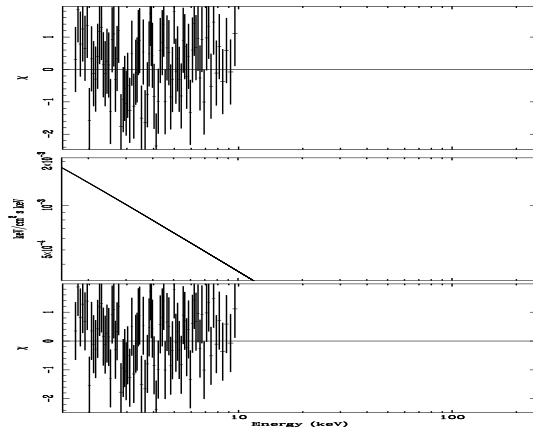
MKN 766 -b



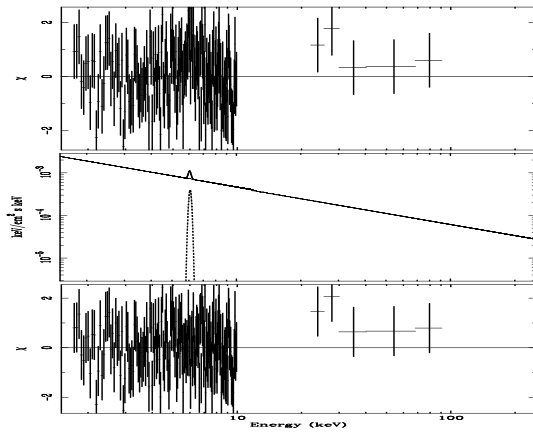
NGC 4261



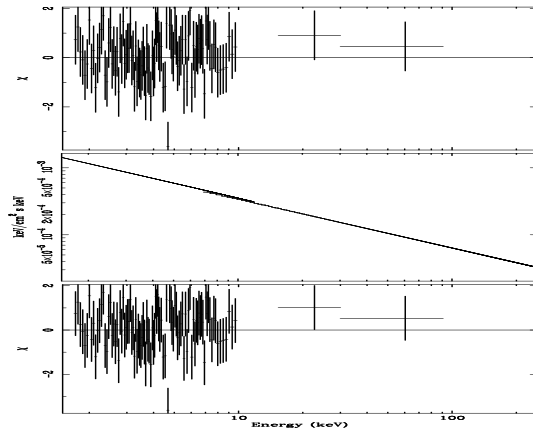
MKN 205 -a



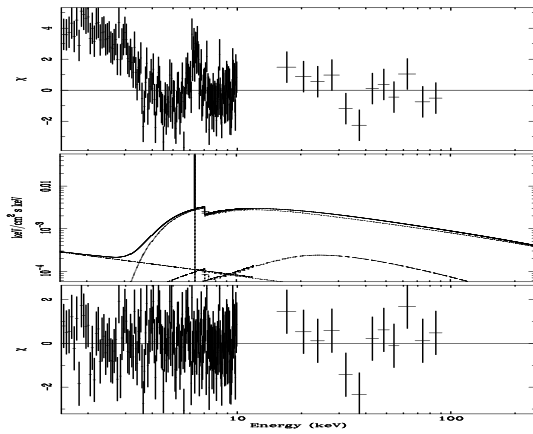
MKN 205 -b



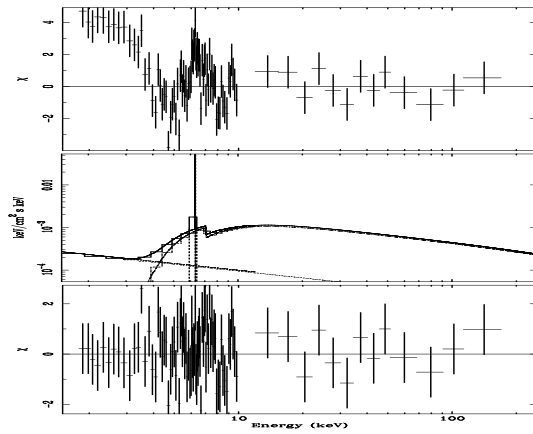
MKN 205 -c



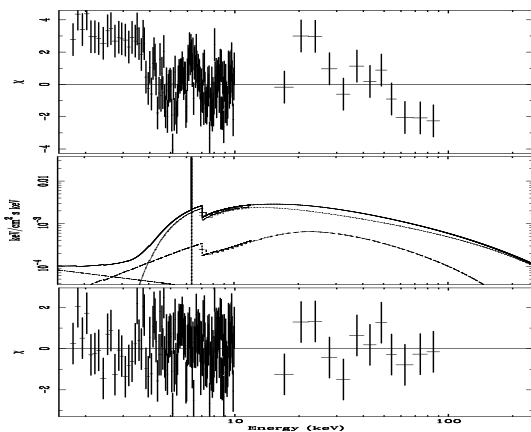
NGC 4388 -a



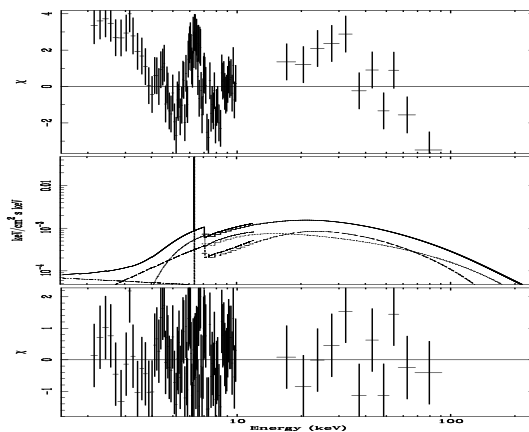
NGC 4388 -b



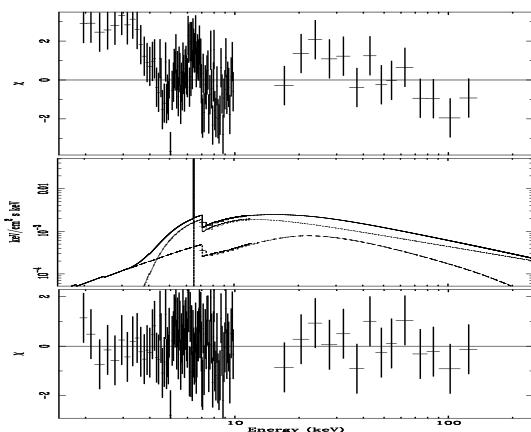
NGC 4507 -a



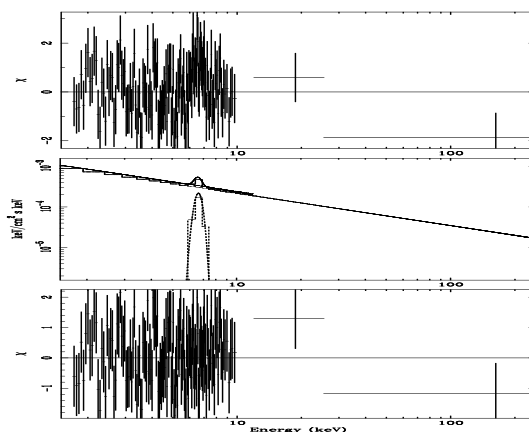
NGC 4507 -b



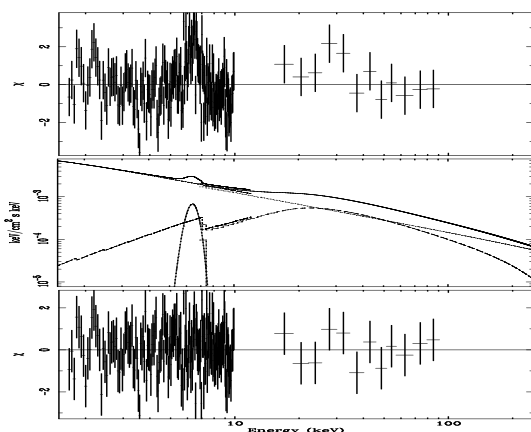
NGC 4507 -c



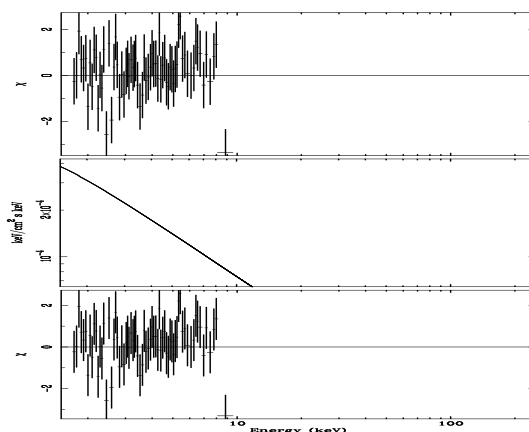
NGC 4579



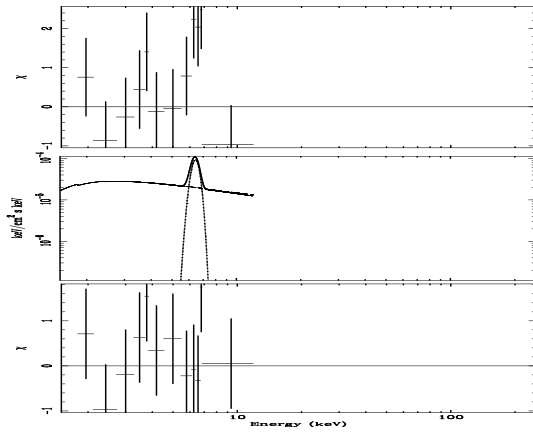
NGC 4593



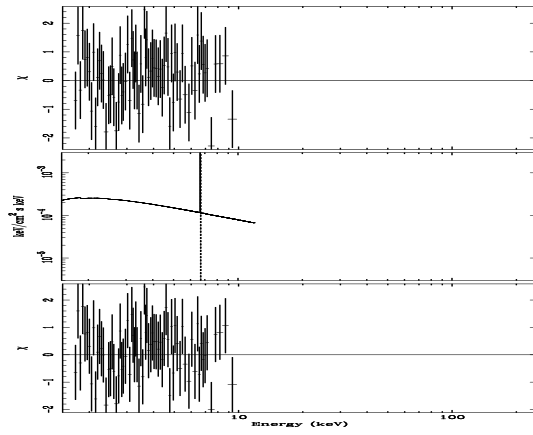
M 104



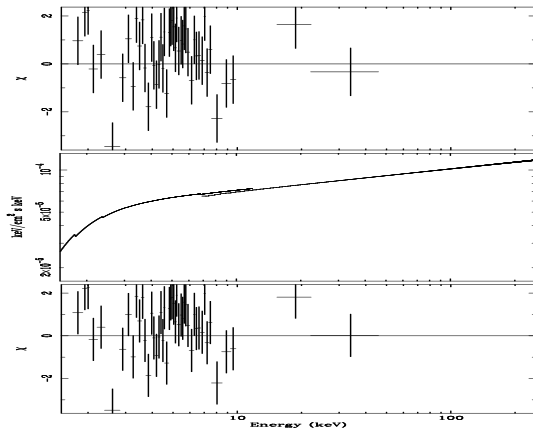
IC 3639



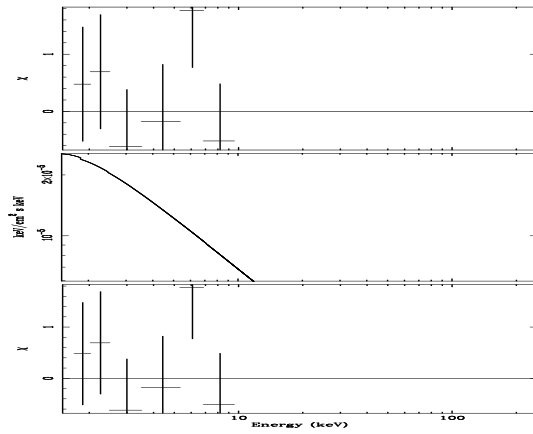
M 94



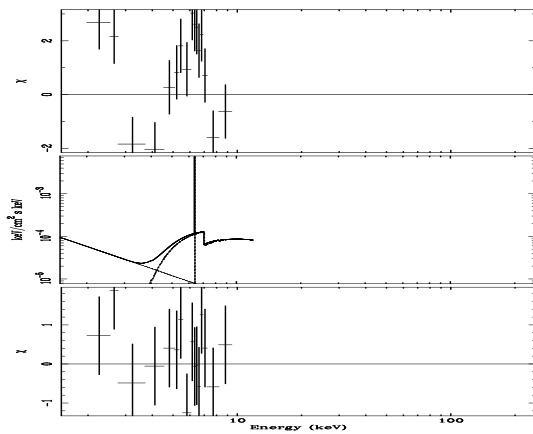
MARK 231



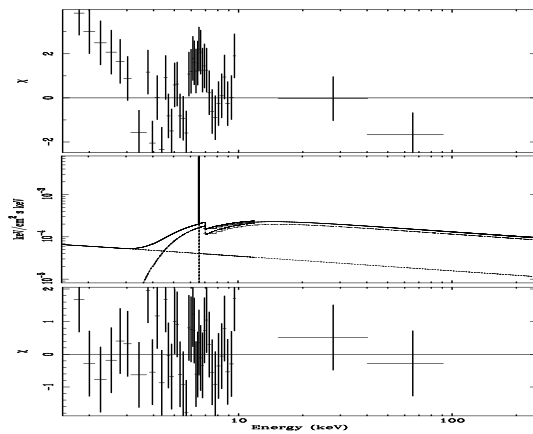
NGC 4826



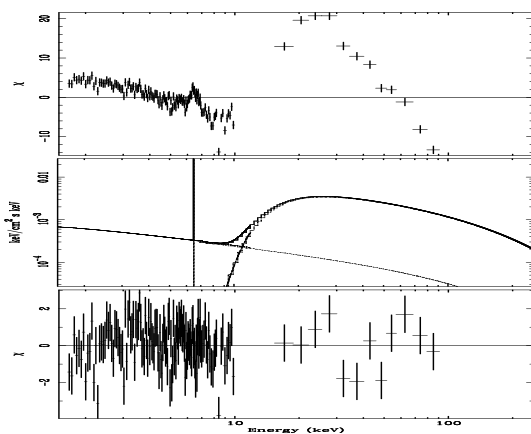
NGC 4941



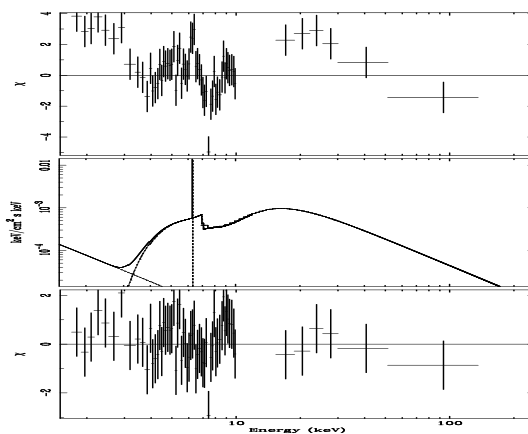
NGC 4939



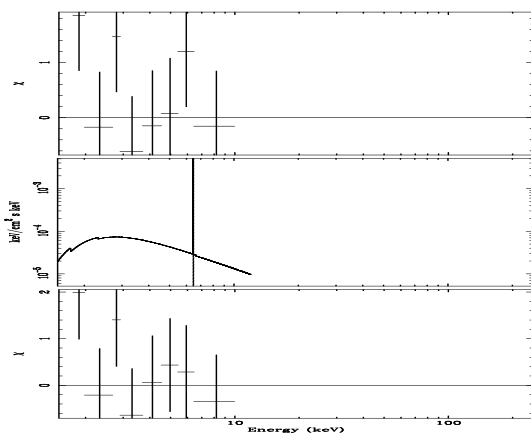
NGC 4945



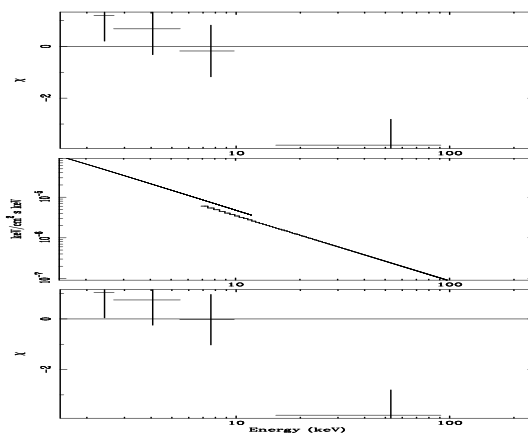
IRAS13197-1627



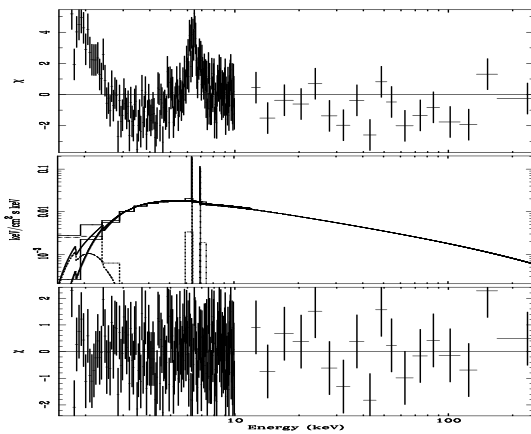
IRAS13224-3809-a



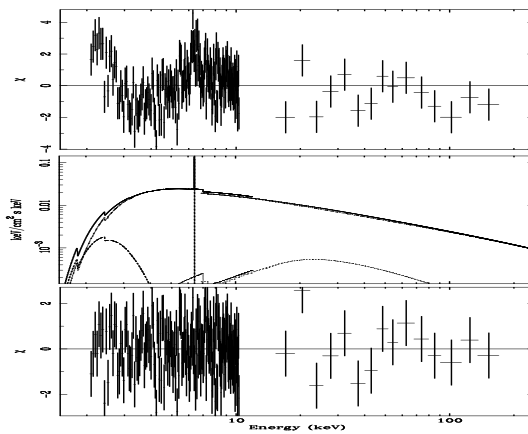
IRAS13224-3809-b



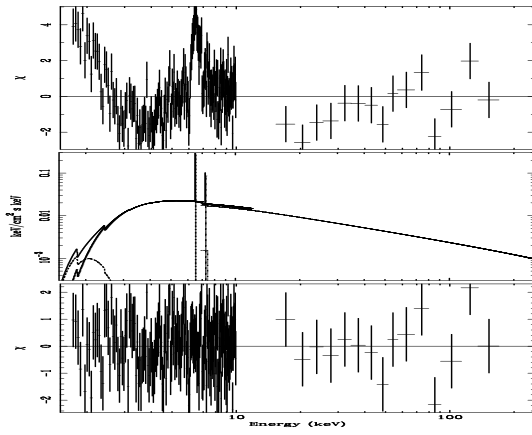
Centaurus A -a



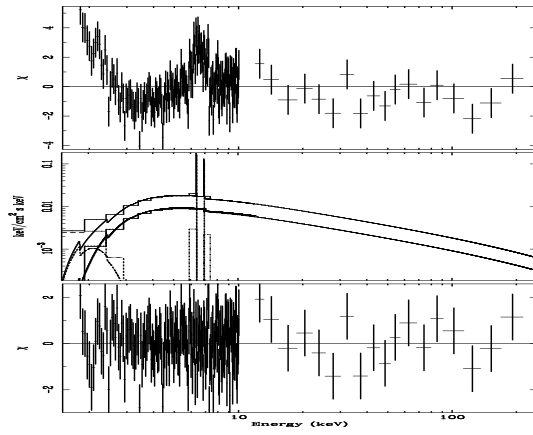
Centaurus A -b



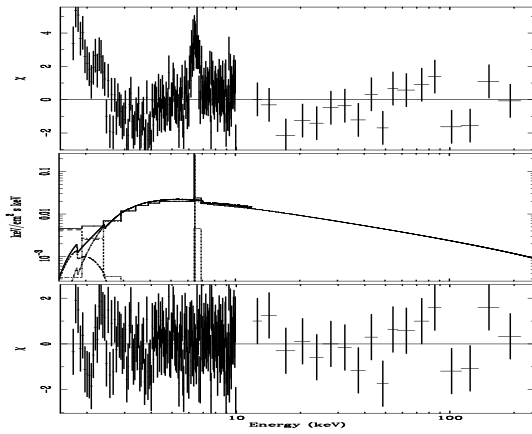
Centaurus A -c



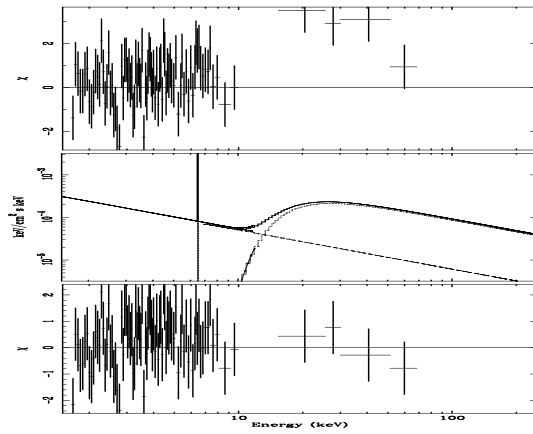
Centaurus A -d



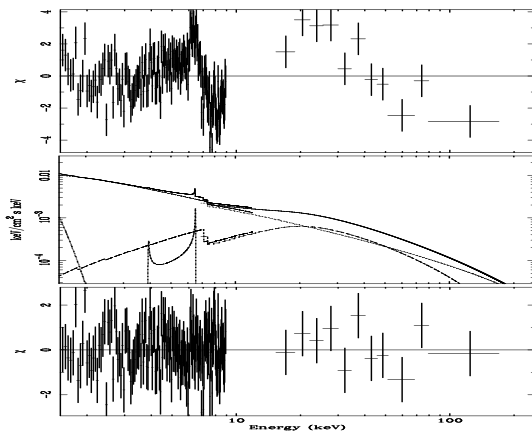
Centaurus A -e



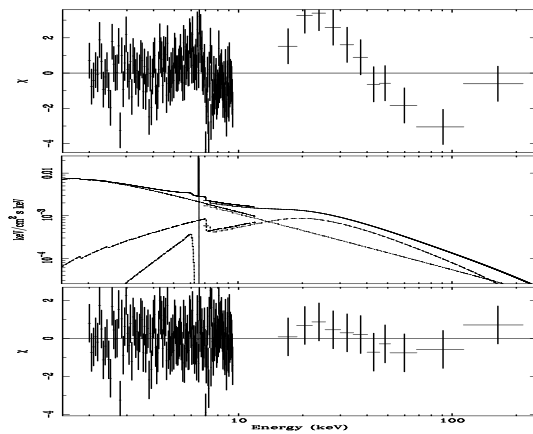
M 51



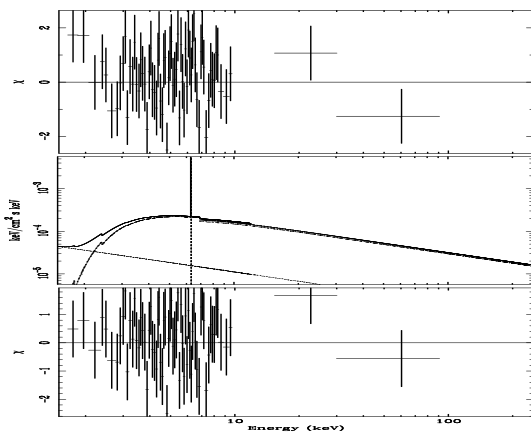
MCG-6-30-15 -a



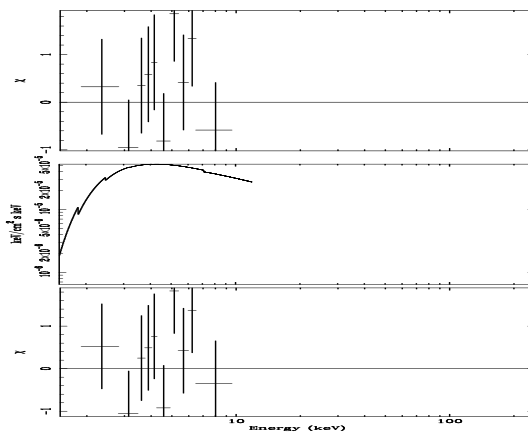
MCG-6-30-15 -b



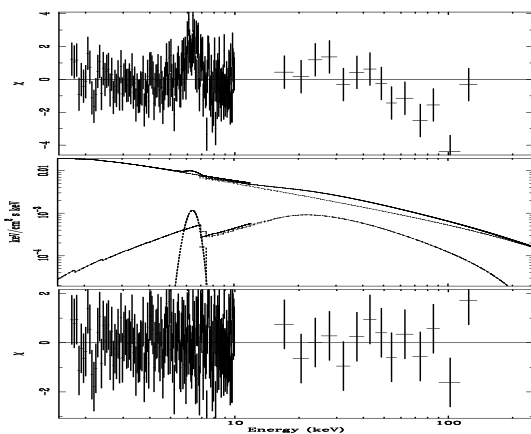
NGC 5252



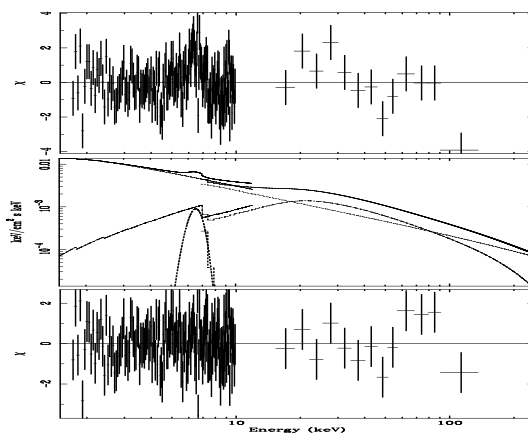
MARK 266



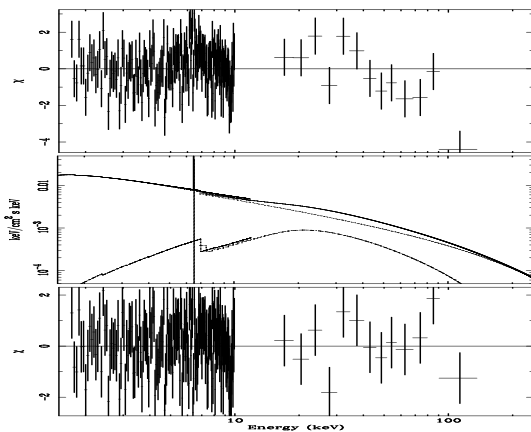
IC 4329a -a



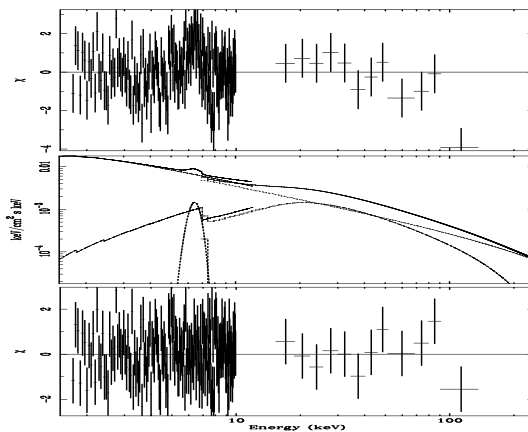
IC 4329a -b



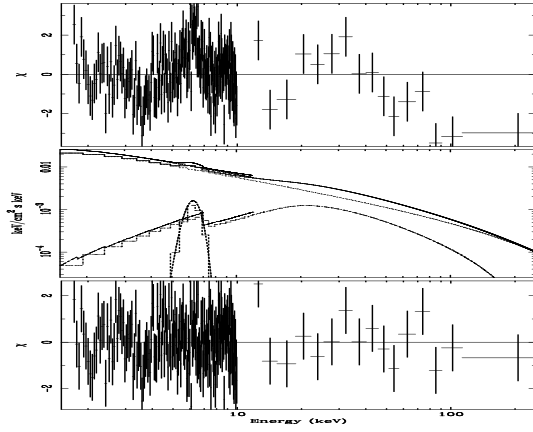
IC 4329a -c



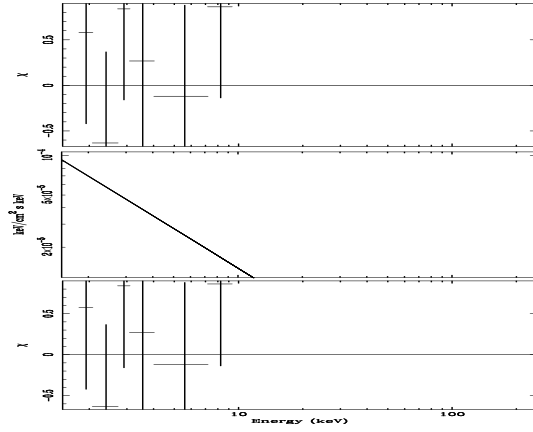
IC 4329a -d



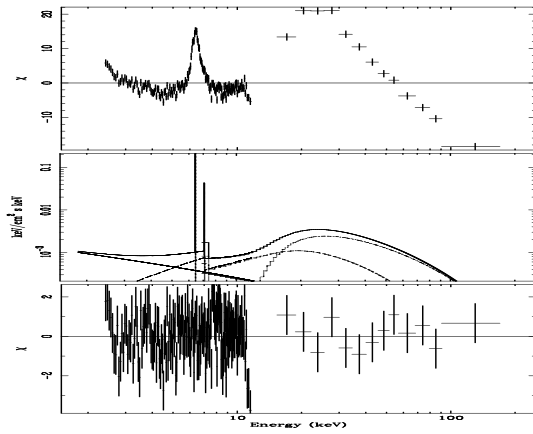
iC 4329a -e



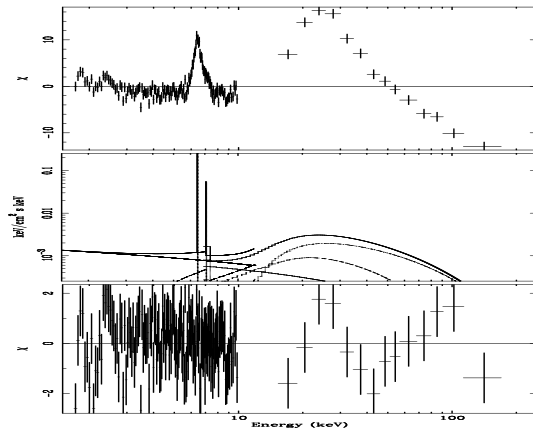
MKN 463



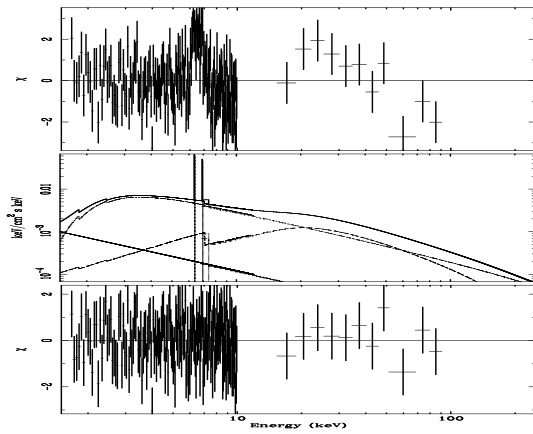
Circinus Galaxy -a



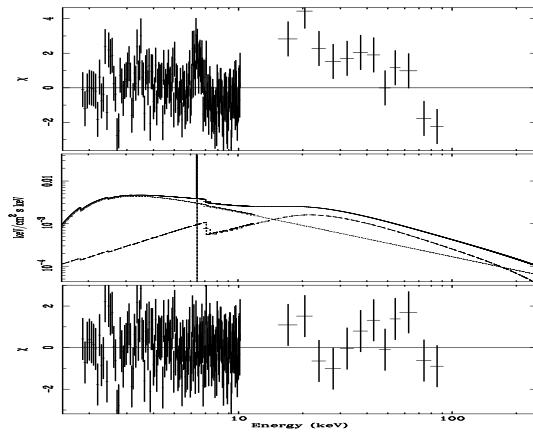
Circinus Galaxy -b



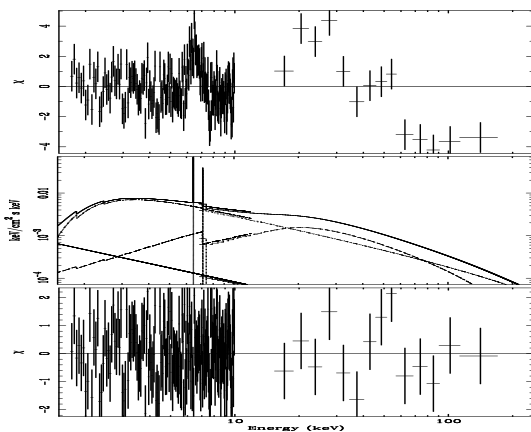
NGC 5506 -a



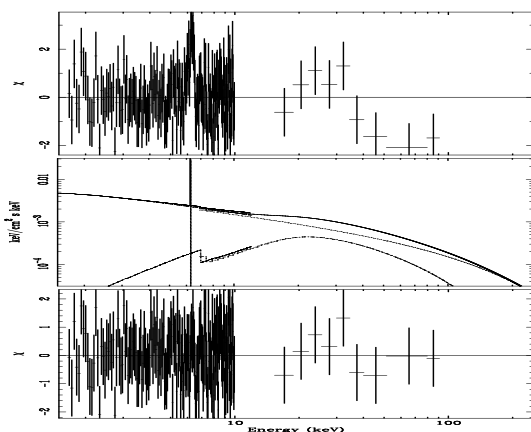
NGC 5506 -b



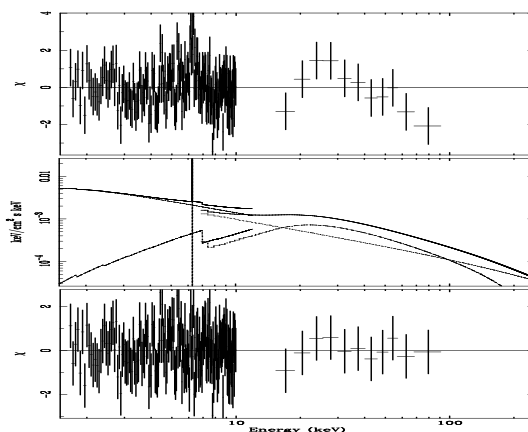
NGC 5506 -c



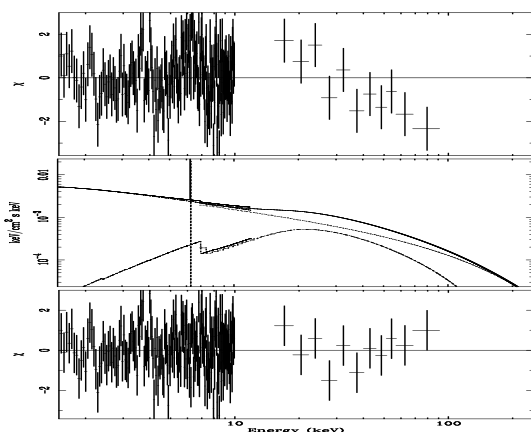
NGC 5548 -a



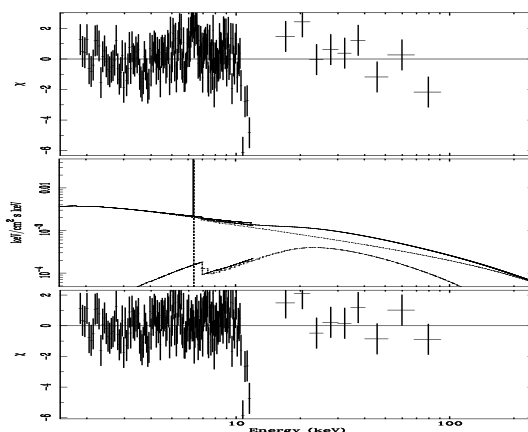
NGC 5548 -b



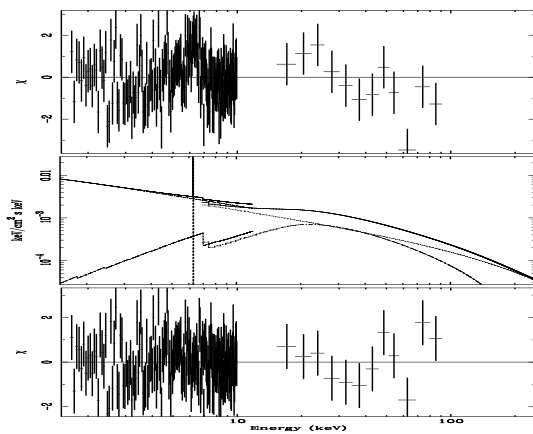
NGC 5548 -c



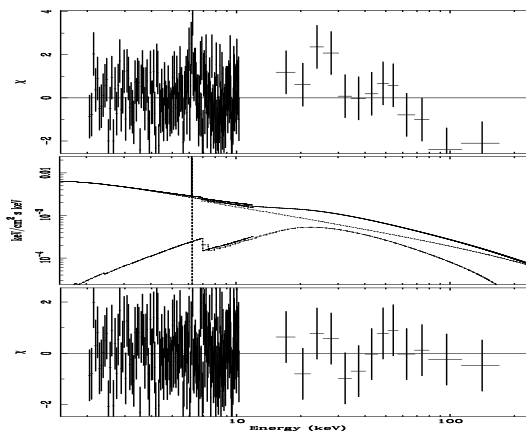
NGC 5548 -d



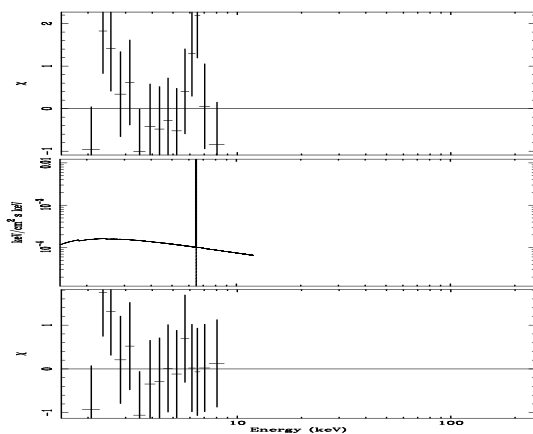
NGC 5548 -e



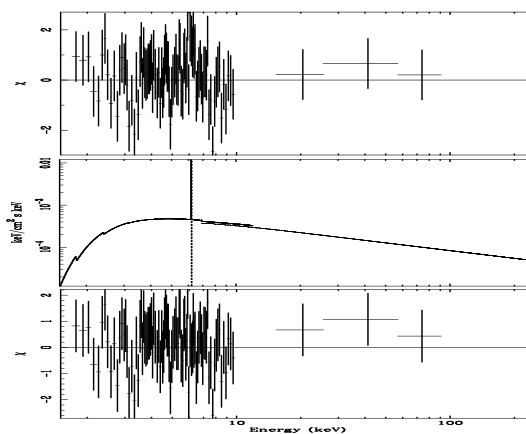
NGC 5548 -f



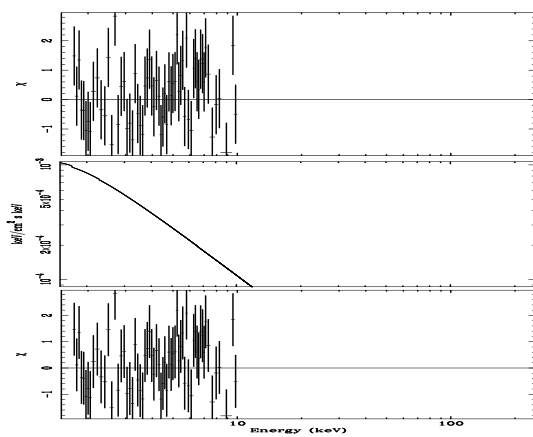
NGC 5643



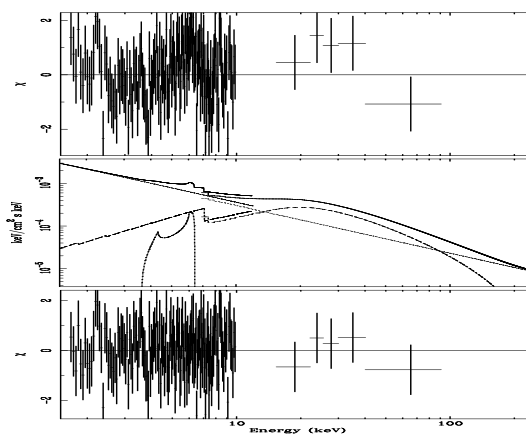
NGC 5674



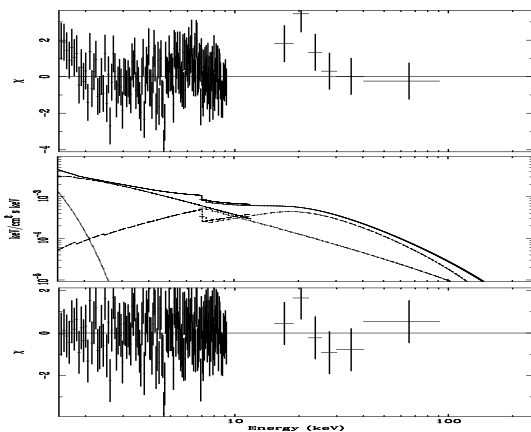
MKN 478



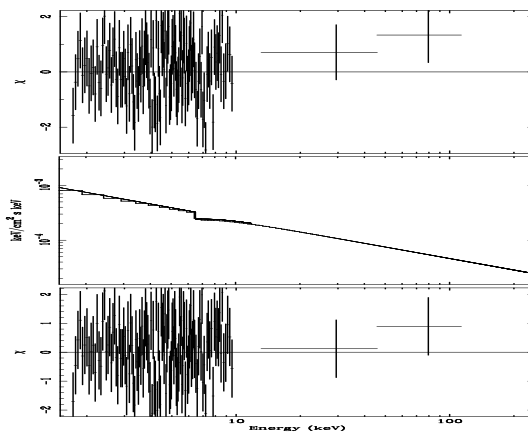
MKN 841 -a



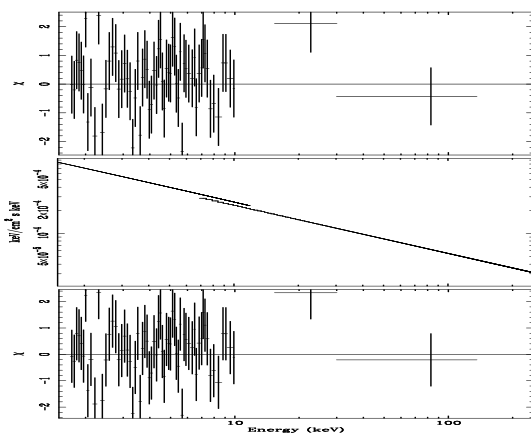
MKN 841 -b



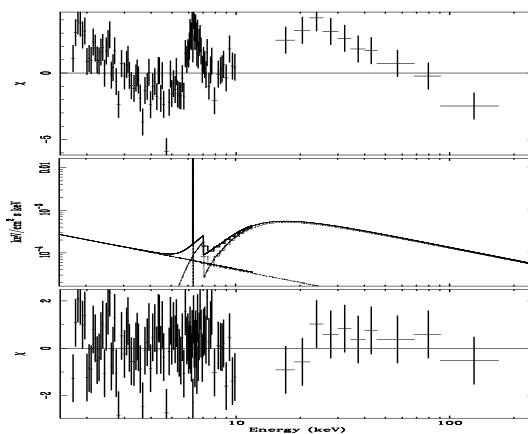
NGC 6251



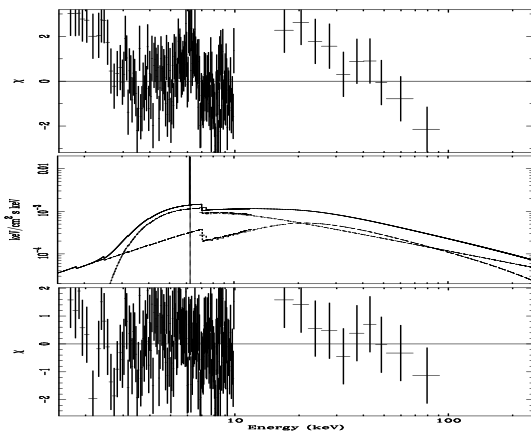
NGC 6212



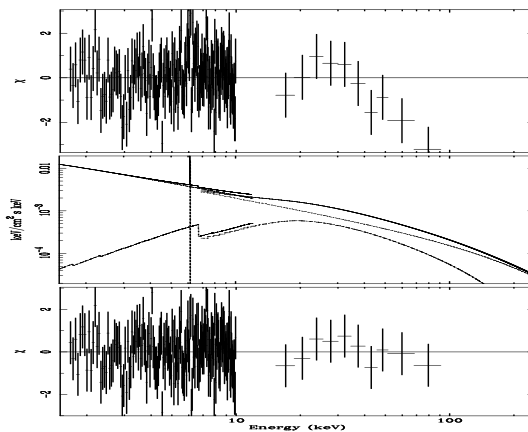
NGC 6240



NGC 6300



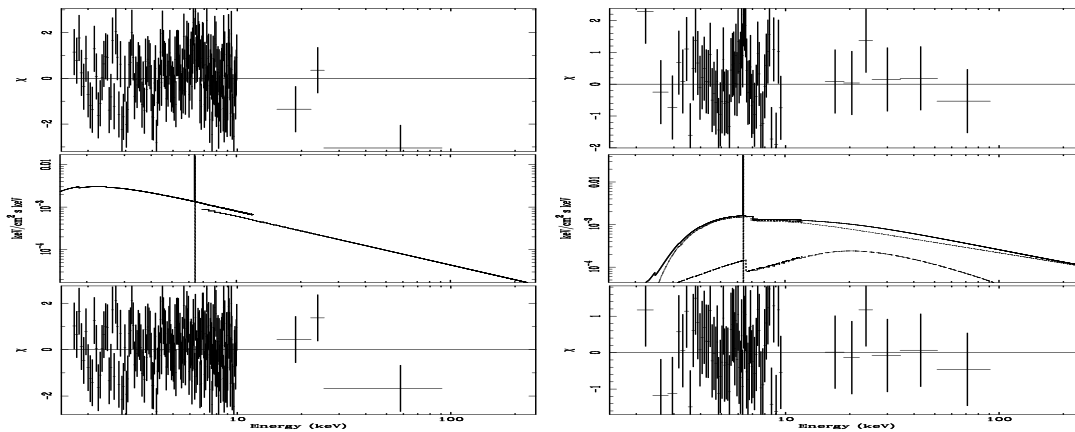
3C 382



Fairall

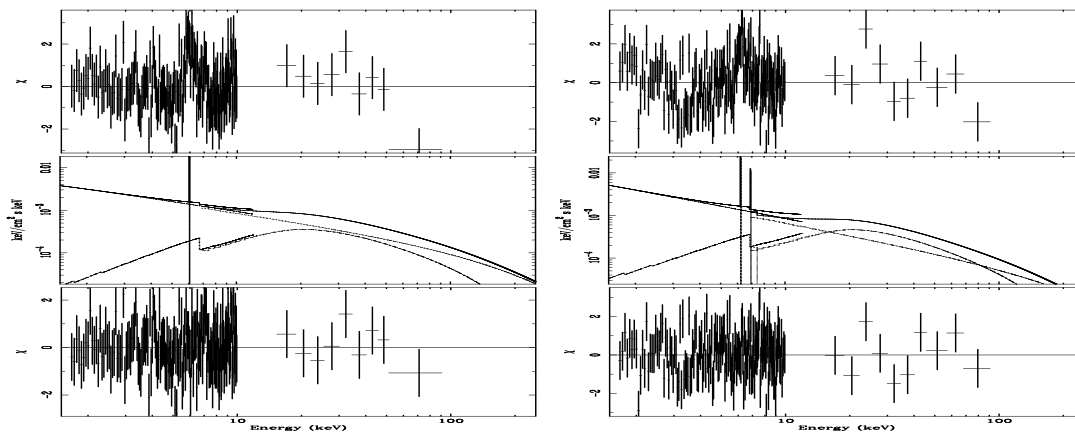
49

ESO103-G35



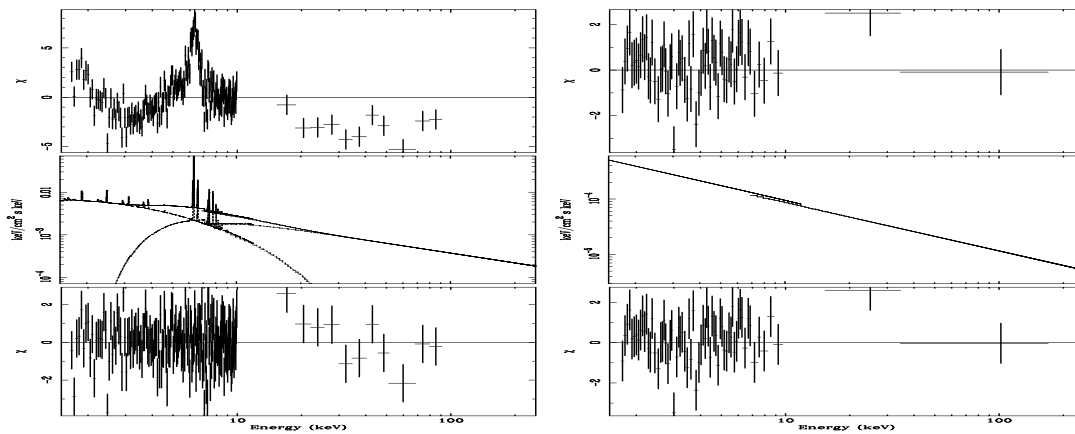
3C 390.3

ESO141-G55

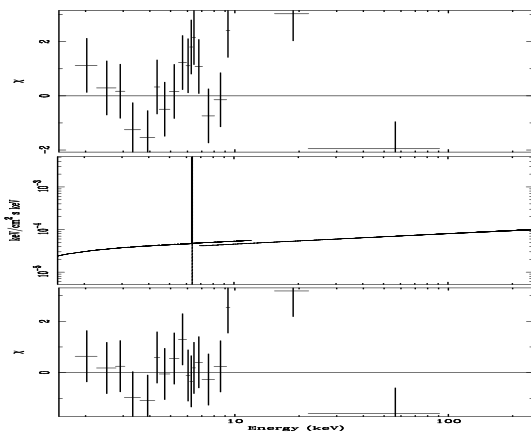


Cygnus A

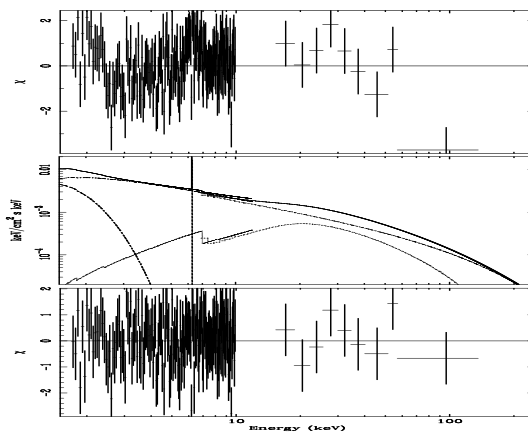
IRAS20051-1117



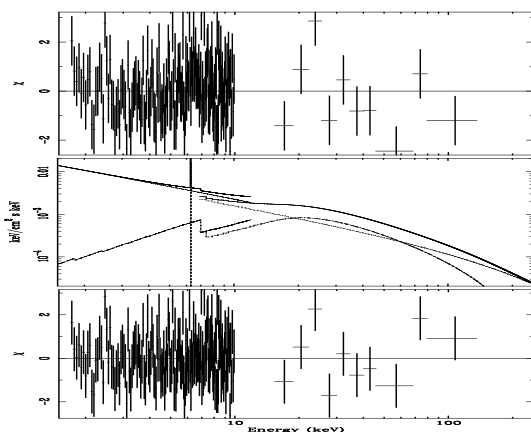
IRAS20210+1121



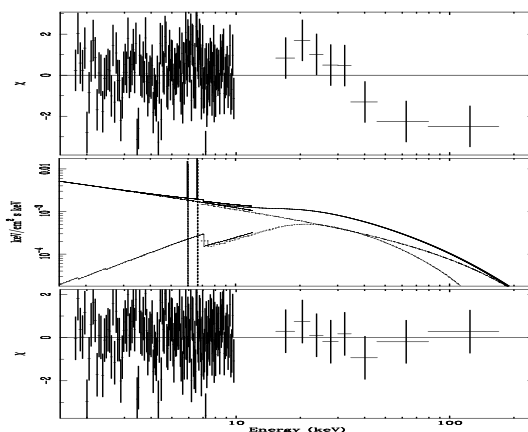
MKN 509 -a



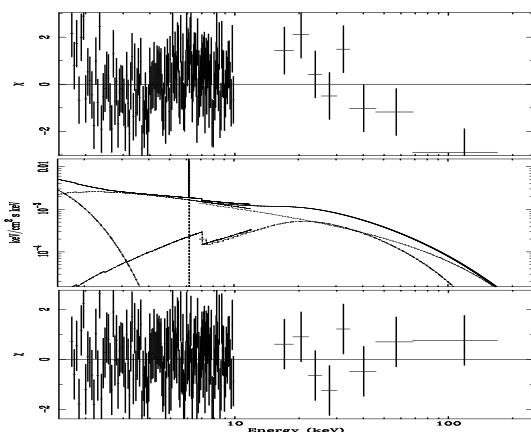
MKN 509 -b



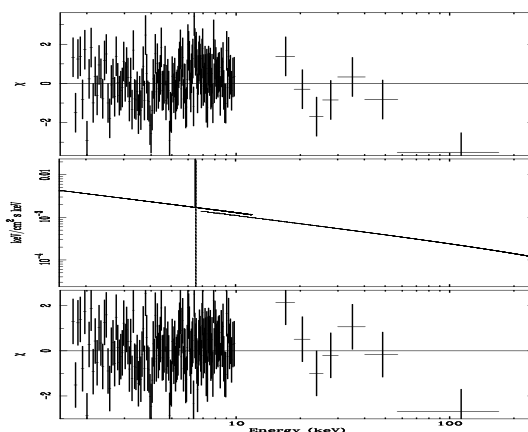
MKN 509 -c



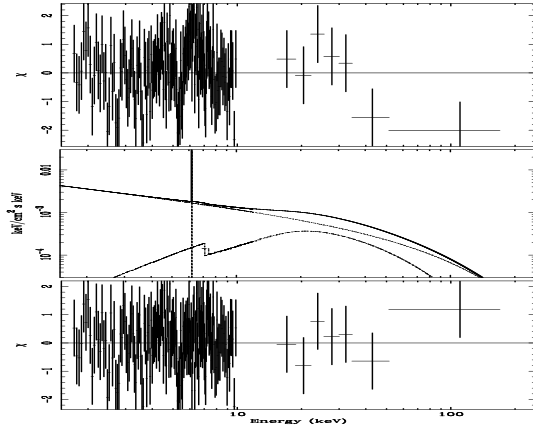
MKN 509 -d



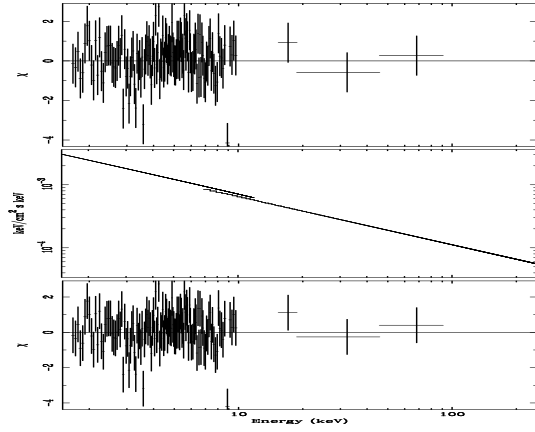
MKN 509 -e



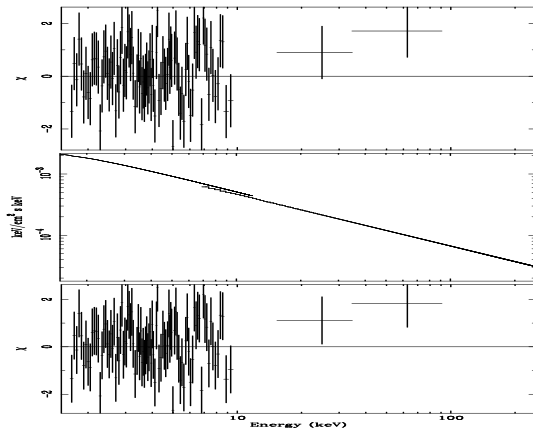
MKN 509 -f



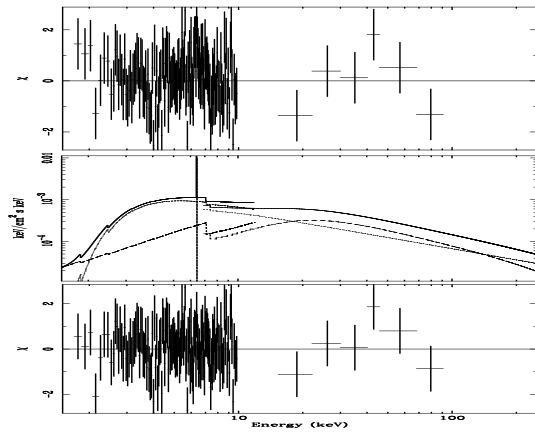
S52116+81 -a



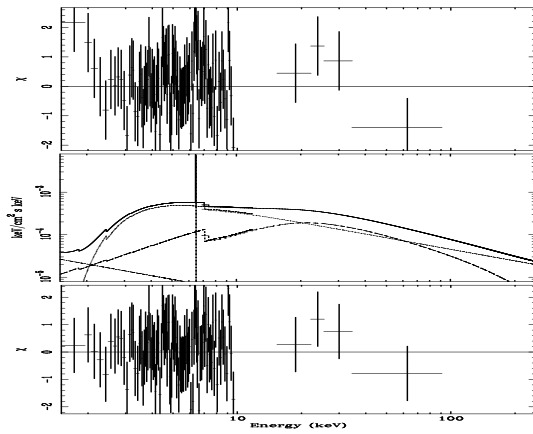
S52116+81 -b



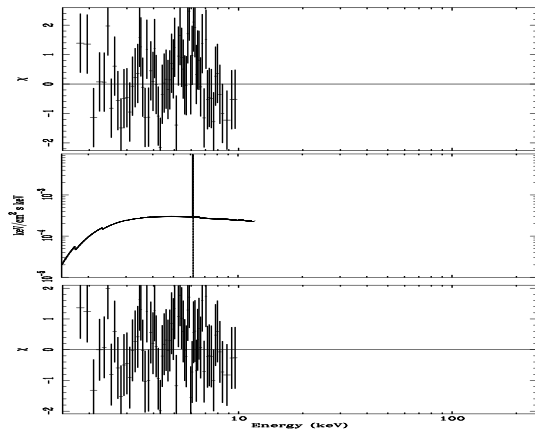
NGC 7172 -a



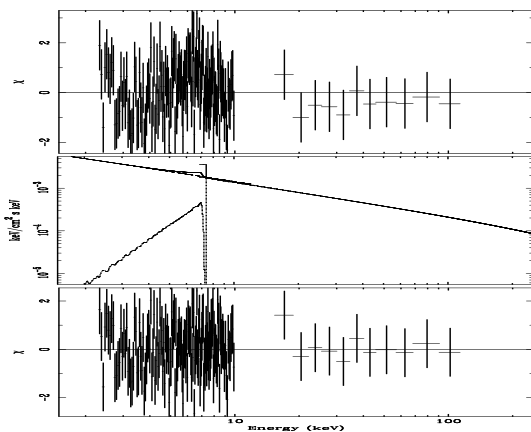
NGC 7172 -b



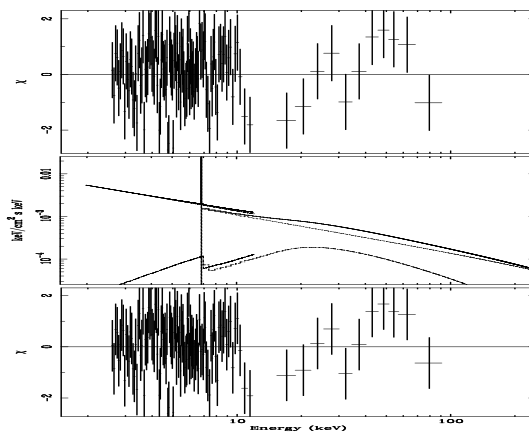
IRAS22017+01319



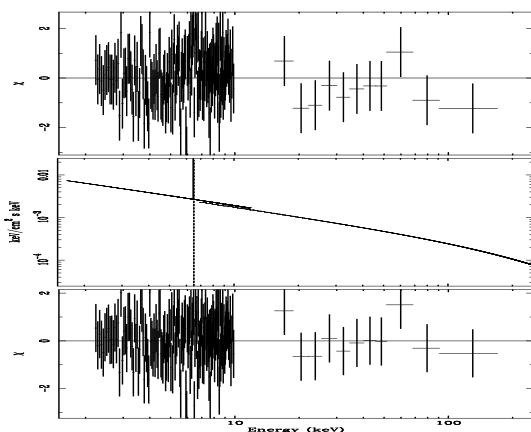
NGC 7213 -a



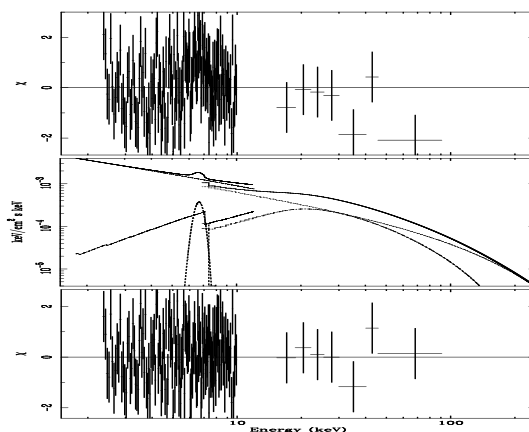
NGC 7213 -b



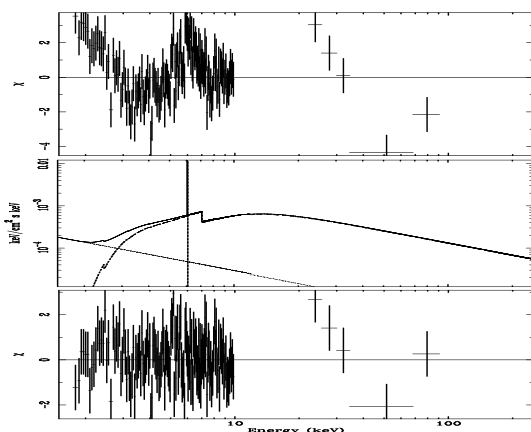
NGC 7213 -c



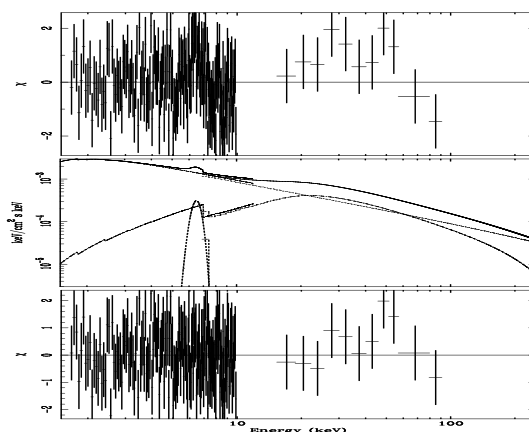
NGC 7213 -d



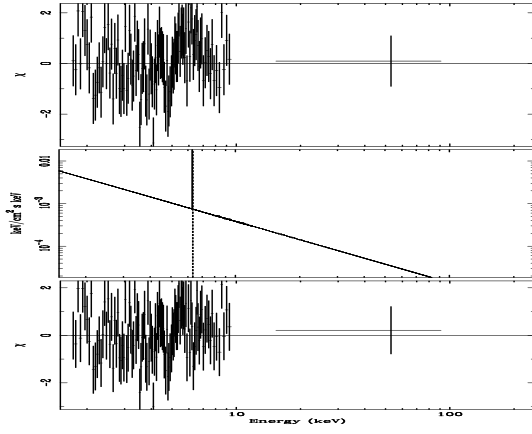
3C 445



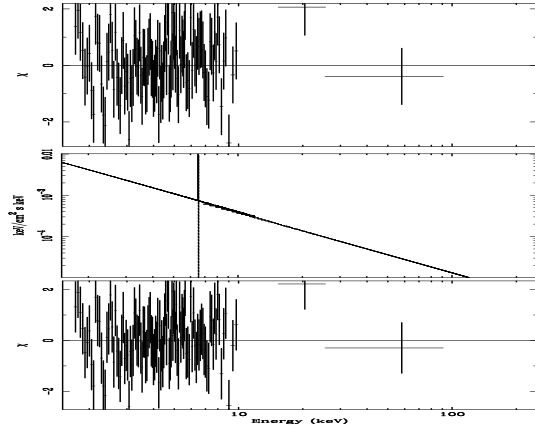
NGC 7314



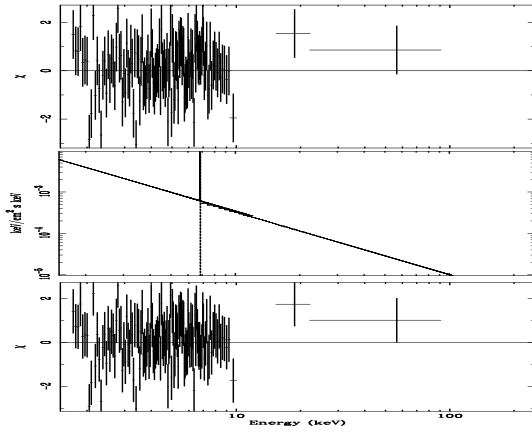
AKN 564 -a



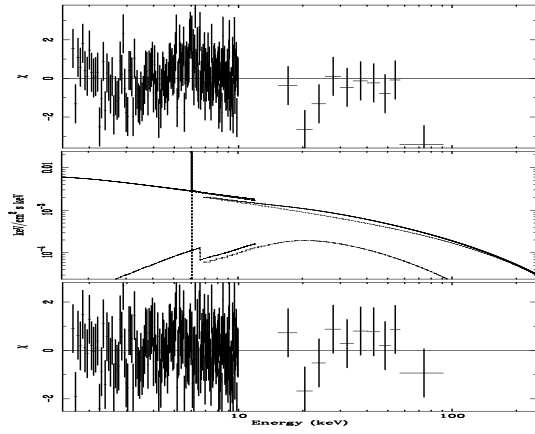
AKN 564 -b



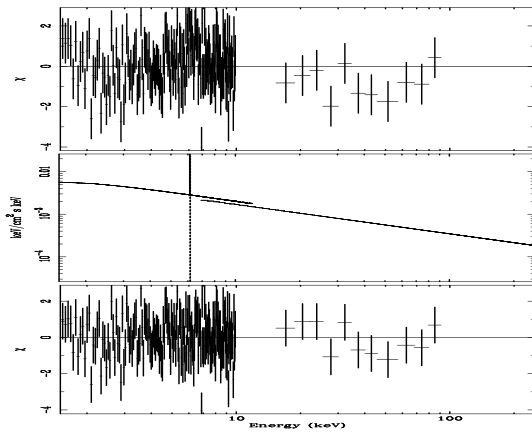
AKN 564 -c



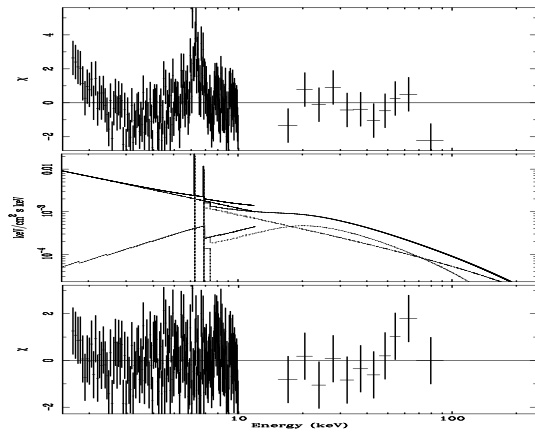
MR 2251-17.8 -a

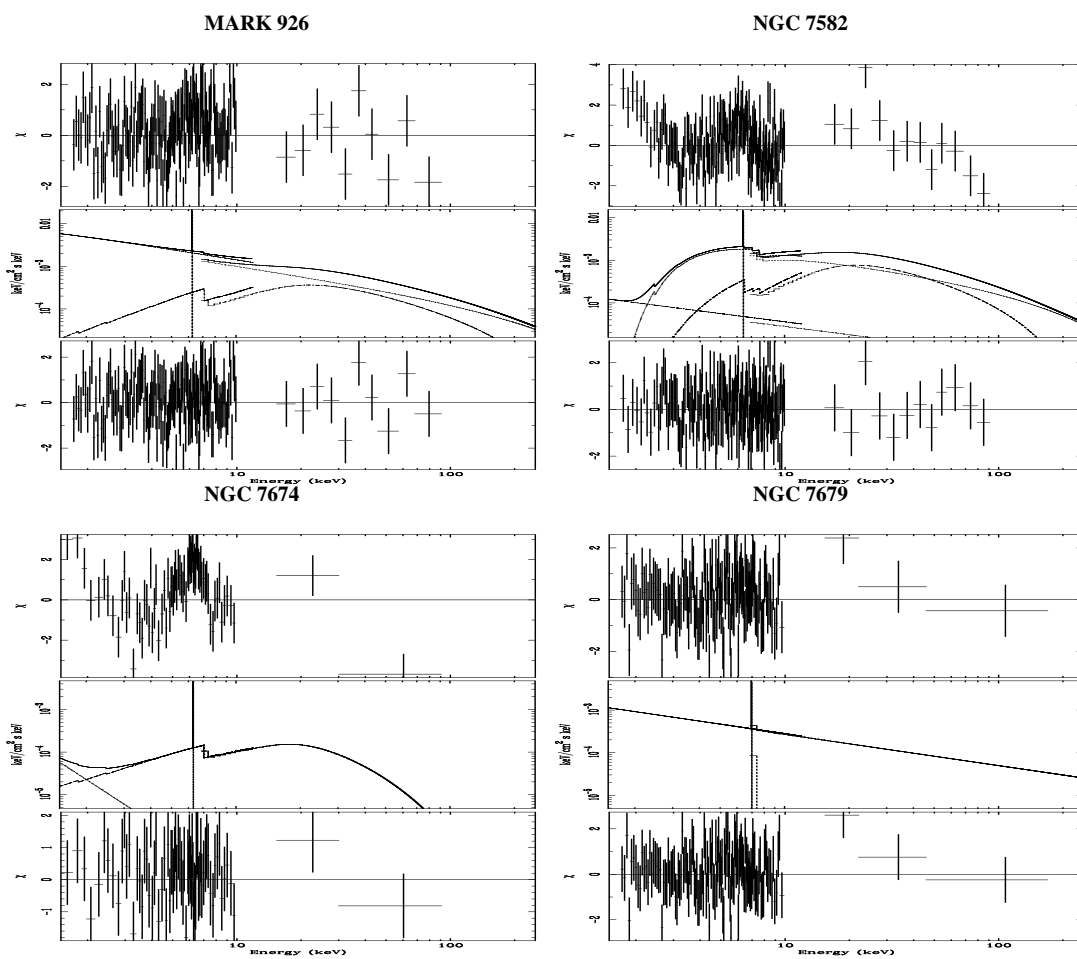


MR 2251-17.8 -b



NGC 7469





Appendix B

The $X-CfA$ sample data

Table B.1: **The $X-CfA$ galaxy sample** Col. (1): Galaxy name; Col. (2): optical classification, '*' = objects with a changed classification with respect to the original given by HFS97. The quality rating is given by ":" and "::" for uncertain and highly uncertain classification, respectively, as reported in HFS97.; Col. (3): Hubble type; Col. (4) total apparent B magnitude of the galaxy; Col. (5): galaxy distances; Col. (6): Col. (7)-(8) optical position in epoch J2000.

Name	Seyfert	Hubble	B	Distance	Ref.	R.A.	Dec.
	Type	Type	(mag)	(Mpc)		(2000)	(2000)
(1)	(2)	(3)	(4)	(5)	(6)	(7)	(8)
NGC185	S2	dE3pec	10.10	0.64	a	00 38 57.4	+48 20 14.4
NGC676	S2:	S0/a:spin	10.50	19.5	b	01 48 57.4	+05 54 25.7
NGC777	S2/L2	E1	12.49	66.5	b	02 00 15.0	+31 25 45.5
NGC1058	S2	Sc	11.82	9.1	b	02 43 30.2	+37 20 27.2
NGC1068	S1.9	Sb	9.61	14.4	b	02 42 40.7	-00 00 47.6
NGC1167	S2	S0-	13.38	65.3	b	03 01 42.4	+35 12 20.7
NGC1275	S1.5	Pec	12.64	70.1	b	03 19 48.2	+41 30 42.4
NGC1358	S2	SAB0/a	13.04	53.6	b	03 33 39.7	-05 05 21.8
NGC1667	S2	SABc	12.77	61.2	b	04 48 37.1	-06 19 11.9
NGC2273	S2	SBa	12.55	28.4	b	06 50 08.7	+60 50 45.0
NGC2336	L2/S2	SABbc	10.61	33.9	b	07 27 03.8	+80 10 39.6
NGC2639	S1.9	Sa?	12.46	42.6	b	08 43 38.0	+50 12 20.3

continued on next page

continued from previous page

Name	Seyfert	Hubble	B	Distance	Ref.	R.A.	Dec.
	Type	Type	(mag)	(Mpc)		(2000)	(2000)
(1)	(2)	(3)	(4)	(5)	(6)	(7)	(8)
NGC2655	S2	SAB0/a	10.96	24.4	b	08 55 38.8	+78 13 25.2
NGC2683	L2/S2	SAB	9.62	7.7	a	08 52 41.7	+33 25 10.4
NGC2685	S2/T2:	SB0+ pec	12.12	16.2	b	08 55 34.8	+58 44 01.6
NGC3031	S1.5	Sab	7.89	3.5	c	09 55 33.2	+69 03 55.0
NGC3079	S2	SBC spin	11.54	17.3	d	10 01 58.5	+55 40 50.1
NGC3147	S2	Sbc	11.43	40.9	b	10 16 53.3	+73 24 02.4
NGC3185	S2:	SB0/a	12.99	21.3	b	10 17 38.7	+21 41 17.2
NGC3227	S1.5	SABa pec	11.10	20.6	b	10 23 30.6	+19 51 53.9
NGC3254	S2	Sbc	12.41	23.6	b	10 29 19.9	+29 29 29.6
NGC3486	S2	SABc	11.05	7.4	b	11 00 24.1	+28 58 31.6
NGC3489	T2/S2	SAB+	11.15	6.4	b	11 00 18.6	+13 54 04.0
NGC3516	S1.2	SB0	12.50	35.7	b	11 06 47.5	+72 34 06.9
NGC3608	L2/S2	E2	11.69	23.4	b	11 16 59.1	+18 08 54.6
NGC3627	T2/S2	SABb	9.13	6.6	b	11 20 15.1	+12 59 21.6
NGC3655	H/S2	SAC	12.08	26.5	b	11 22 54.7	+16 35 22.0
NGC3735	S2	Sc: spin	12.50	41.0	b	11 35 57.5	+70 32 07.7
NGC3941	S2:	SB0	11.25	12.2	a	11 52 55.4	+36 59 10.5
NGC3976	S2	SABb	12.30	37.7	b	11 55 57.3	+06 44 57.0
NGC3982	S1.9	SABb:	11.78	20.5	e	11 56 28.1	+55 07 30.6
NGC4051	S1.2	SABbc	10.83	17.0	b	12 03 09.6	+44 31 52.8
NGC4138	S1.9	S0+	12.16	13.8	a	12 09 29.9	+43 41 06.0
NGC4151	S1.5	SABab:	11.50	20.3	b	12 10 32.6	+39 24 20.6
NGC4168	S1.9:	E2	12.11	31.7	f	12 12 17.3	+13 12 17.9
NGC4169	S2	S0	13.15	50.4	b	12 12 18.9	+29 10 44.0
NGC4235	S1.2	Sa spin	12.62	35.1	b	12 17 09.9	+07 11 29.1
NGC4258	S1.9	SABbc	9.10	7.2	a	12 18 57.5	+47 18 14.3
NGC4378	S2	Sa	12.63	35.1	b	12 25 18.1	+04 55 31.6
NGC4388	S1.9	Sb: spin	11.76	16.7	b	12 25 46.7	+12 39 40.9
NGC4395	S1*	Sm:	10.64	2.6	b	12 25 48.9	+33 32 47.8
NGC4472	S2::	E2	9.37	16.7	b	12 29 46.8	+07 59 59.9
NGC4477	S2	SB0?	11.38	16.8	b	12 30 02.2	+13 38 11.3
NGC4501	S1.9	Sb	10.36	16.8	b	12 31 59.3	+14 25 13.4

continued on next page

continued from previous page

Name	Seyfert	Hubble	B	Distance	Ref.	R.A.	Dec.
	Type	Type	(mag)	(Mpc)		(2000)	(2000)
(1)	(2)	(3)	(4)	(5)	(6)	(7)	(8)
NGC4565	S1.9	Sb? spin	10.42	9.7	a	12 36 21.1	+25 59 13.5
NGC4579	S1*	SABb	10.48	16.8	b	12 37 43.5	+11 49 04.9
NGC4639	S1.0	SABbc	12.24	22.9	b	12 42 52.5	+13 15 24.1
NGC4698	S2	Sab	11.46	16.8	b	12 48 22.9	+08 29 14.8
NGC4725	S2:	SABab pec	10.11	13.2	a	12 50 26.7	+25 30 02.3
NGC5033	S1.5	Sc	10.75	18.7	b	13 13 27.5	+36 35 37.8
NGC5194	S2	Sbc pec	8.96	8.4	bx	13 29 52.4	+47 11 40.8
NGC5273	S1.5	S0	12.44	16.5	a	13 42 08.3	+35 39 15.2
NGC5395	S2/L2	Sb pec	12.10	46.7	b	13 58 38.0	+37 25 28.3
NGC5548	S1.5	S0/a	13.30	70.2	b	14 17 59.5	+25 08 12.4
NGC5631	S2/L2	S0	12.41	27.8	a	14 26 33.3	+56 34 58.3
NGC6482	T2/S2	E	11.84	52.3	b	17 51 48.9	+23 04 19.1
NGC6503	T2/S2	SACd	10.11	5.2	g	17 49 26.6	+70 08 40.1
NGC6951	S2	SABbc	11.64	24.1	b	20 37 14.4	+66 06 19.7
NGC7479	S1.9	SBc	11.60	32.4	b	23 04 56.7	+12 19 23.2
NGC7743	S2	SB0+	12.38	24.4	b	23 44 21.4	+09 56 03.6

Notes: References on distances: (a) Tonry et al. (2001); (b) Tully (1988); (c) Paturel et al. (2002); (d) Cecil et al. 2002; (e) Stetson et al. (2001); (f) Merritt & Ferrarese (2001); (g) Karachentsev & Sharina (1997).

Table B.2: **Multi-wavelength luminosities and M_{BH} of the total X-ray sample:** Col. (1): galaxy name; Col. (2): optical classification; Col. (3): Satellite used: 'C'=Chandra, 'X'=XMM-Newton, 'A'=ASCA; Col. (4): logarithm of the 2-10 keV flux in units of $\text{erg cm}^{-2} \text{s}^{-1}$, not corrected for Compton thick candidates. Col. (5): logarithm of the 2-10 keV luminosity, corrected for Compton thick candidates. Col. (6): X-RAY REFERENCES: (1) Cappi et al. 2006; (2) This work; (3) Pappa et al. 2001; (4) Guainazzi et al. 2005b; (5) Terashima et al. 2002; (6) Eracleous et al. (2002); Col. (7): Final classification: ' \checkmark '=Compton thick candidates, ' \times '=Compton thin candidate and '?'=doubtful objects.; Col. (8): logarithm of the $[\text{OIII}]_{\lambda 5007}$ luminosity corrected for Galactic absorption and NLR extinction; Col. (9): logarithm of the $H\alpha$ (broad+narrow component) luminosity corrected for Galactic absorption and NLR extinction; Col. (10): logarithm of the M_{BH} value in units of M_{\odot} ; Col. (11): M_{BH} measurement methods; M: maser kinematics; G: gas kinematics; S: stellar kinematics; R: reverberation mapping; I_{σ} : inferred from the mass-velocity dispersion correlation; Col. (12): M_{BH} REFERENCES.

Name	Class	Sat	Log $F_{2-10\text{keV}}$	Log $L_{2-10\text{keV}}$	Ref.	CThick	Log $L_{[\text{OIII}]}$	Log $L_{H\alpha}$	Log M_{BH}	Method	Ref.
(1)	(2)	(3)	(4)	(5)	(6)	(7)	(8)	(9)	(10)	(11)	(12)
NGC676	S2:	X	-13.62	40.79	1	\checkmark	39.04	38.62	-	-	-
NGC1058	S2	C	< -14.42	< 37.55	2	?	37.90	38.16	4.88	I_{σ}	8
NGC1068	S1.9	X	-11.31	42.84	1	\checkmark	41.91	41.53	7.20	M	1
NGC1167	S2	A	-13.39	42.07	3	\checkmark	40.76	40.81	-	-	-
NGC1275	S1.5	X	-10.91	42.83	2	\times	41.91	42.07	8.51	I_{σ}	2
NGC1667	S2	A	-13.1	42.31	3	\checkmark	40.42	40.17	7.88	I_{σ}	2
NGC2273	S2	A	-12.16	42.58	4	\checkmark	40.94	40.92	7.30	I_{σ}	2
NGC2639	S1.9	A	-12.49	40.82	5	?	40.40	40.56	8.02	I_{σ}	9

continued on next page

Name	Class	Sat	Log F _{2-10keV}	Log L _{2-10keV}	Ref.	CThick	Log L _[OIII]	Log L _{Hα}	Log M _{BH}	Method	Ref.
(1)	(2)	(3)	(4)	(5)	(6)	(7)	(8)	(9)	(10)	(11)	(12)
NGC2655	S2	A	-10.98	41.85	5	×	39.92	40.03	7.77	I σ	9
NGC2683	L2/S2	C	-13.62	38.21	2	?	38.58	37.69	7.51	I σ	9
NGC2685	S2/T2:	X	-12.53	39.94	1	×	38.96	39.21	7.15	I σ	9
NGC3031	S1.5	X	-10.89	40.25	1	×	38.56	38.94	7.80	S	1
NGC3079	S2	C	-11.69	42.62	2	√	40.07	40.89	7.65	I σ	3
NGC3147	S2	C	-11.39	41.89	2	×	40.07	40.01	8.79	I σ	3
NGC3185	S2:	X	-13.7	40.79	1	√	39.90	40.07	6.06	I σ	2
NGC3227	S1.5	X	-10.94	41.74	1	×	40.51	40.20	7.59	R	4
NGC3486	S2	X	-12.93	38.86	1	?	37.99	37.85	6.14	I σ	8
NGC3489	T2/S2	C	< -13.57	< 39.88	2	√	38.86	38.48	7.48	I σ	5
NGC3516	S1.2	C	-10.87	42.29	2	×	40.50	39.91	7.36	R	1
NGC3608	L2/S2	C	-13.69	39.10	2	×	38.22	38.23	8.04	S	1
NGC3627	T2/S2	C	< -13.81	< 37.88	2	?	38.79	39.35	7.99	I σ	5
NGC3941	S2:	X	-13.35	38.88	1	×	38.63	38.78	8.15	I σ	7
NGC3982	S1.9	A	-13.28	41.18	2	√	40.50	39.87	6.09	I σ	2
NGC4051	S1.2	C	-11.2	41.31	2	×	39.81	39.68	6.11	R	4
NGC4138	S1.9	X	-11.04	41.29	1	×	38.74	38.69	7.75	I σ	9
NGC4151	S1.5	X	-10.2	42.47	1	×	41.47	40.94	7.18	R	4
NGC4168	S1.9:	X	-13.19	39.87	1	×	38.46	38.93	7.95	I σ	6

continued on next page

Name	Class	Sat	Log $F_{2-10keV}$	Log $L_{2-10keV}$	Ref.	CThick	Log $L_{[OIII]}$	Log $L_{H\alpha}$	Log M_{BH}	Method	Ref.
(1)	(2)	(3)	(4)	(5)	(6)	(7)	(8)	(9)	(10)	(11)	(12)
NGC4235	S1.2	A	-10.92	42.22	2	×	40.41	40.97	-	-	-
NGC4258	S1.9	C	-10.91	40.86	2	×	39.07	38.65	7.61	M	1
NGC4388	S1.9	C	-10.78	41.72	2	×	40.54	40.26	6.80	I_{σ}	3
NGC4395	S1	X	-11.07	39.81	1	×	38.28	38.53	5.04	S	1
NGC4472	S2::	C	< -13.18	< 39.32	2	×	< 37.81	< 37.59	8.80	I_{σ}	6
NGC4477	S2	X	-12.85	39.65	1	×	39.04	39.06	7.92	I_{σ}	9
NGC4501	S1.9	X	-12.91	39.59	1	×	39.23	39.06	7.90	I_{σ}	3
NGC4565	S1.9	X	-12.6	39.43	1	×	38.69	38.72	7.70	I_{σ}	3
NGC4579	S1	C	-11.47	41.03	6	×	39.42	39.72	7.78	I_{σ}	3
NGC4639	S1.0	X	-12.55	40.22	1	×	38.71	39.90	6.85	I_{σ}	8
NGC4698	S2	X	-13.34	39.16	1	×	38.86	38.74	7.84	I_{σ}	9
NGC4725	S2:	X	-13.4	38.89	1	×	38.58	38.24	7.49	I_{σ}	3
NGC5033	S1.5	X	-11.52	41.08	1	×	39.72	40.42	7.30	I_{σ}	3
NGC5194	S2	C	-12.77	40.91	2	√	39.90	39.87	6.95	I_{σ}	2
NGC5273	S1.5	X	-11.13	41.36	1	×	39.03	38.48	6.51	I_{σ}	2
NGC5548	S1.5	X	-10.5	43.25	2	×	41.16	40.26	8.03	I_{σ}	4
NGC6482	T2/S2	C	-13.33	40.16	2	×	-	39.26	8.75	I_{σ}	9
NGC6503	T2/S2	C	-14.39	37.10	2	?	-	37.41	5.56	I_{σ}	8
NGC7479	S1.9	X	-11.95	41.12	2	?	40.25	40.67	7.07	I_{σ}	9

continued on next page

Name	Class	Sat	Log $F_{2-10keV}$	Log $L_{2-10keV}$	Ref.	CThick	Log $L_{[OIII]}$	Log $L_{H\alpha}$	Log M_{BH}	Method	Ref.
(1)	(2)	(3)	(4)	(5)	(6)	(7)	(8)	(9)	(10)	(11)	(12)
NGC7743	S2	A	-13.14	41.47	5	√	40.21	40.24	6.59	I_{σ}	2

REFERENCES (1) Ho (2002); (2) Woo & Urry (2002); (3) Merloni et al. (2003); (4) Kaspi et al. (2000); (5) Pellegrini (2005); (6) Merritt & Ferrarese (2001); (7) di Nella et al. (1995); (8) Barth et al. (2002); (9) McElroy (1995).

Appendix C

The *XMM–Newton* sample data

Table C.1: **The *XMM–Newton* sample:** Col. (1): galaxy name. Col. (2): other name. Col. (3): optical classification as given by HFS97: “S” represents Seyfert, “L” represents LINER, and “T” represents objects with LINER plus H II-region spectra. “2” implies that no broad H α is detected; “1.9” implies that broad H α is present, but not broad H β ; “1.5” implies that both broad H α and broad H β are detected, with substantial contributions from both the BLR and NLR (Osterbrock 1981). Objects with a changed classification with respect to the original given by HFS97 (see also Ho et al. 1997b and HU01) are denoted by “*” after their name. Col. (4): Hubble type as listed in HFS97. Col. (5): distance from Tully (1988), except when marked with (a) Paturel et al. (2002), (b) Cecil et al. (2002), (c) Tonry et al. (2001), and (d) Thim et al. (2004). Col. (6): total apparent B_T magnitude of the galaxy. Col. (7)–(8): nuclear optical position in epoch J2000 as given by HU01.

Galaxy Name (1)	Other Name (2)	Seyfert Type (3)	Hubble Type (4)	Distance (Mpc) (5)	B_T (mag) (6)	R.A. (J2000) (7)	Decl. (J2000) (8)
NGC 676		S2:	S0/a: spin	19.5	10.50	01 48 57.4	+05 54 25.7
NGC 1058		S2	Sc	9.1	11.82	02 43 30.2	+37 20 27.2
NGC 1068		S1.9	Sb	14.4	9.61	02 42 40.7	-00 00 47.6
NGC 2685	Arp336	S2/T2:	SB0+ pec	16.2	12.12	08 55 34.8	+58 44 01.6
NGC 3031	M81	S1.5/L1.5	Sab	3.5 ^a	7.89	09 55 33.2	+69 03 55.0

continued on next page

Galaxy Name	Other Name	Seyfert Type	Hubble Type	Distance (Mpc)	B_T (mag)	R.A. (J2000)	Decl. (J2000)
(1)	(2)	(3)	(4)	(5)	(6)	(7)	(8)
NGC 3079		S2	SBc spin	17.3 ^b	11.54	10 01 58.5	+55 40 50.1
NGC 3185		S2:	SB0/a	21.3	12.99	10 17 38.7	+21 41 17.2
NGC 3227	Arp94	S1.5	SABa pec	20.6	11.10	10 23 30.6	+19 51 53.9
NGC 3486		S2	SABc	7.4	11.05	11 00 24.1	+28 58 31.6
NGC 3941		S2:	SB0	12.2 ^c	11.25	11 52 55.4	+36 59 10.5
NGC 4051		S1.5*	SABbc	17.0	10.83	12 03 09.6	+44 31 52.8
NGC 4138		S1.9	S0+	13.8 ^c	12.16	12 09 29.9	+43 41 06.0
NGC 4151		S1.5	SABab:	20.3	11.50	12 10 32.6	+39 24 20.6
NGC 4258	M106	S1.9	SABbc	7.2 ^c	9.10	12 18 57.5	+47 18 14.3
NGC 4388		S1.9	Sb: spin	16.7	11.76	12 25 46.7	+12 39 40.9
NGC 4395		S1.5*	Sm:	4.1 ^d	10.64	12 25 48.9	+33 32 47.8
NGC 4472	M49	S2::	E2	16.7	9.37	12 29 46.8	+07 59 59.9
NGC 4477		S2	SB0?	16.8	11.38	12 30 02.2	+13 38 11.3
NGC 4501	M88	S2	Sb	16.8	10.36	12 31 59.3	+14 25 13.4
NGC 4565		S1.9	Sb? spin	9.7 ^c	10.42	12 36 21.1	+25 59 13.5
NGC 4579	M58	S1.5/L1.5*	SABb	16.8	10.48	12 37 43.4	+11 49 04.9
NGC 4639		S1.5*	SABbc	16.8	12.24	12 42 52.5	+13 15 24.1
NGC 4698		S2	Sab	16.8	11.46	12 48 22.9	+08 29 14.8
NGC 4725		S2:	SABab pec	13.0 ^c	10.11	12 50 26.7	+25 30 02.3
NGC 5033		S1.5	Sc	18.7	10.75	13 13 27.5	+36 35 37.8
NGC 5194	M51	S2	Sbc pec	8.4	8.96	13 29 52.4	+47 11 40.8
NGC 5273		S1.5	S0	16.5 ^c	12.44	13 42 08.3	+35 39 15.2

Notes: Two sources (NGC 3031 and NGC 4579) have classifications which fall near the somewhat arbitrary boundary between a Seyfert and a LINER, depending on the adopted criteria. Because they are on the Seyfert side in HFS97, they are included here and classified as “S/L”. In objects like NGC 676, NGC 2685, NGC 3185, NGC 4472, and NGC 4725, the starlight subtraction process has been particularly difficult, leading to uncertain classifications. Following HFS97, we marked these sources with a quality rating “:” (uncertain) or “::” (highly uncertain).

XMM–Newton observation log: Col. (1): galaxy name. Col. (2): observation start date. Col. (3): observation orbital period. Col. (4): cleaned exposure of MOS1/MOS2/pn. Col. (5): filters used for MOS1/MOS2/pn.

Galaxy	Start	Obs.	Exposure (s)	Filter
Name	Date (UT)	orbit	M1/M2/pn	M1/M2/pn
(1)	(2)	(3)	(4)	(5)
NGC 676	2002-07-14	475	17296/17578/15757	thin/thin/thick
NGC 1058	2002-02-01	393	11749/11798/6574	thin/thin/med
NGC 1068	2000-07-29	117	38351/34735/33521	med/med/med
NGC 2685	2001-10-15	339	6397/6687/4841	thin/thin/thin
NGC 3031	2001-04-22	251	-/84400*	-/med*
NGC 3079	2001-04-13	246	21434/21776/10922	med/med/thin
NGC 3185	2001-05-07	258	11791/12117/8041	thin/thin/thick
NGC 3227	2000-11-28	178	36514/36517/32579	med/med/med
NGC 3486	2001-05-09	259	4600/4663/5061	thin/thin/med
NGC 3941	2001-05-09	259	6233/6286/5302	thin/thin/med
NGC 4051	2002-11-22	541	47814/48311/41889	med/med/med
NGC 4138	2001-11-26	360	13575/13567/8856	thin/thin/med
NGC 4151	2000-12-21	190	29233/29253/21241	med/med/med
NGC 4168	2001-12-04	364	21886/21916/16009	thin/thin/med
NGC 4258	2000-12-08	183	20224/20246/13535	med/med/med
NGC 4388	2002-07-07	472	8768/8798/3866	med/med/thin
NGC 4395	2002-05-31	562	37096/30453/10873	thin/thin/thin
NGC 4472	2002-06-05	456	15181/15300/11043	thin/thin/thin
NGC 4477	2002-06-08	457	13329/13393/8457	thin/thin/med
NGC 4501	2001-12-04	364	12645/12637/2565	thin/thin/med
NGC 4565	2001-07-01	286	14100/14113/8912	thin/thin/med
NGC 4579	2003-06-12	642	19568/20015/15396	thin/thin/thin
NGC 4639	2001-12-16	370	13672/13683/8863	thin/thin/med
NGC 4698	2001-12-16	370	14321/14427/8961	thin/thin/med
NGC 4725	2002-06-14	460	17062/17076/11941	thin/thin/med
NGC 5033	2001-07-02	286	7372/7232/869	thin/thin/med
NGC 5194	2003-01-15	568	20429/20465/17218	thin/thin/thin
NGC 5273	2002-06-14	460	15414/15474/9263	thin/thin/med

Notes: “*” means that MOS1 was not considered because it was operated in fast uncompressed mode, and MOS2 was not considered because it was operated in full-frame mode, so the data could thus be affected by pile-up.

Table C.2: Col. (1): galaxy name. Col (2): Galactic absorption along the line of sight, in units of 10^{20} cm^{-2} . Col. (3): measured absorption column density, in units of 10^{22} cm^{-2} . Col. (4): power-law photon index. Col. (5): photon index of the soft power-law component. Col. (6): temperature of the thermal component (kT) in units of keV. Col. (7): equivalent width of the Fe K line, in units of keV. Col. (8): reduced chi-squared and number of degrees of freedom. Col. (9)–(10): observed fluxes in the soft (0.5–2 keV) and hard (2–10 keV) X-ray bands, in units of $10^{-13} \text{ erg cm}^{-2} \text{ s}^{-1}$. Col. (11)–(12): Log of the absorption-corrected luminosities in the soft (0.5–2 keV) and hard (2–10 keV) X-ray bands (computed using distances from Table C.1)

Galaxy name	N_{HGal}	N_H	Γ_{HX}	Γ_{SX}	kT	EW(Fe K)	χ^2_{red}/ν	F_{SX}	F_{HX}	$\log L_{SX}^{int.}$	$\log L_{HX}^{int.}$
(1)	(2)	(3)	(4)	(5)	(6)	(7)	(8)	(9)	(10)	(11)	(12)
NGC 676	4.4	≤ 0.1	1.9 ± 0.3	-	-	-	1.2/12	0.1	0.2	38.9	39.0
NGC 1058 [‡]	6.7	≤ 0.6	1.3 ± 0.9	-	-	-	0.2/2	< 0.1	< 0.4	< 38.1	< 38.6
NGC 1068 ^{†*}	3.5	≤ 0.1	1.0 ± 0.1	3.5 ± 0.5	0.7 ± 0.2	1200 ± 500	4.3/1399	111.3	46.2	41.4	41.1
NGC 2685	4.1	≤ 0.3	0.5 ± 0.2	-	-	-	1.5/8	0.2	2.7	38.8	39.9
NGC 3031*	4.1	≤ 0.1	1.9 ± 0.1	-	0.6 ± 0.1	40 ± 20	1.2/1651	87.0	120.0	40.2	40.3
NGC 3079 [†]	0.8	0.05 ± 0.03	1.7 ± 0.1	-	0.7 ± 0.1	1480 ± 500	1.1/264	< 2.5	3.3	< 40.0	40.1
NGC 3185	2.1	≤ 0.2	2.1 ± 0.1	-	-	-	0.6/5	0.2	0.2	39.0	39.0
NGC 3227	2.2	6.8 ± 0.3	1.5 ± 0.1	$\equiv \Gamma_{HX}$	-	190 ± 40	1.1/1863	4.0	81.4	41.2	41.7
NGC 3486	1.9	≤ 0.3	0.9 ± 0.2	-	-	-	1.1/6	0.2	1.1	38.0	38.9
NGC 3941	1.9	≤ 0.1	2.1 ± 0.3	-	-	-	1.8/8	0.4	0.4	38.8	38.9
NGC 4051*	1.3	≤ 0.3	1.2 ± 0.1	3 ± 0.5	0.2 ± 0.1	240 ± 40	2.2/2006	47.3	62.7	41.2	41.3

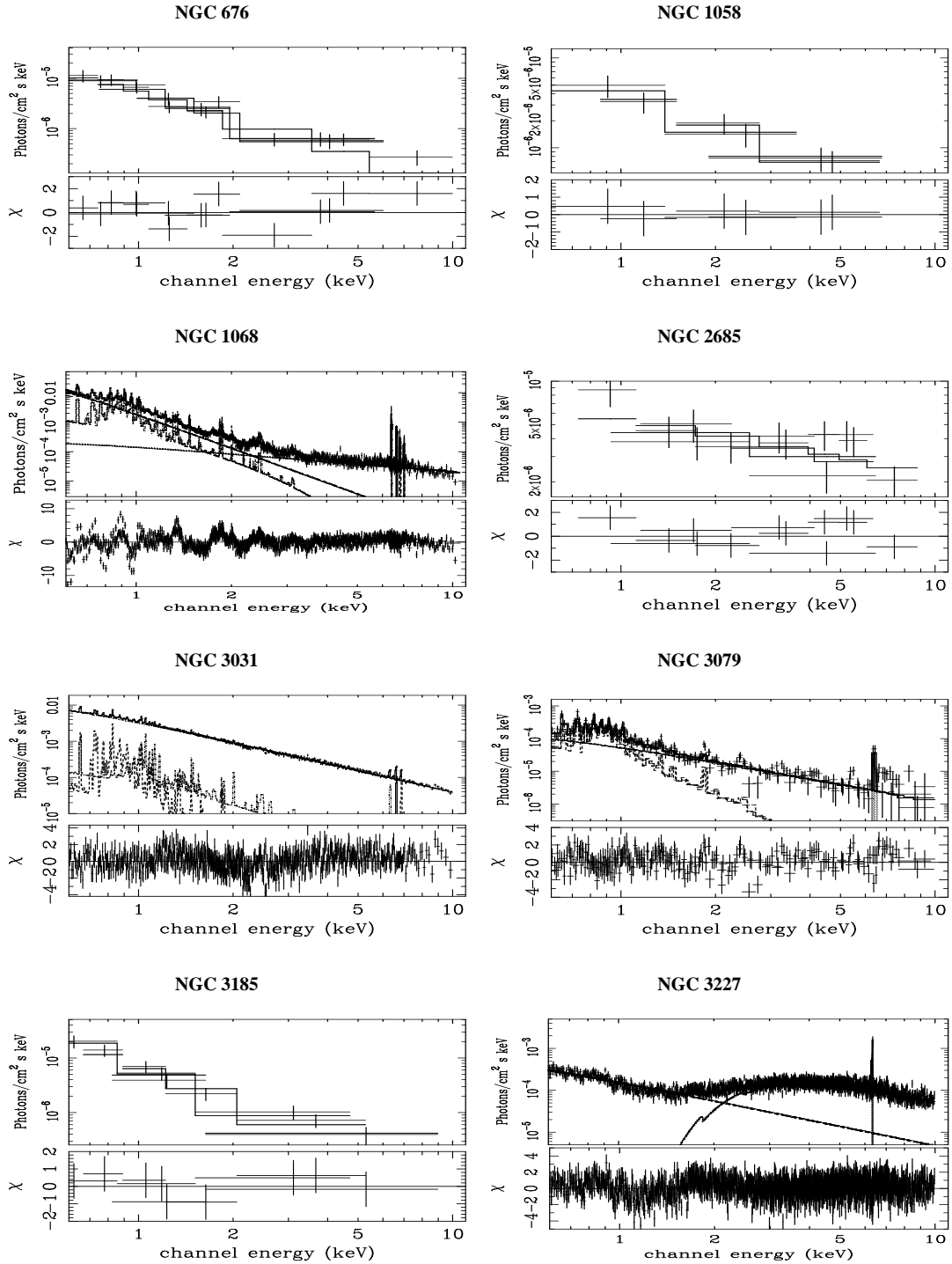
continued on next page

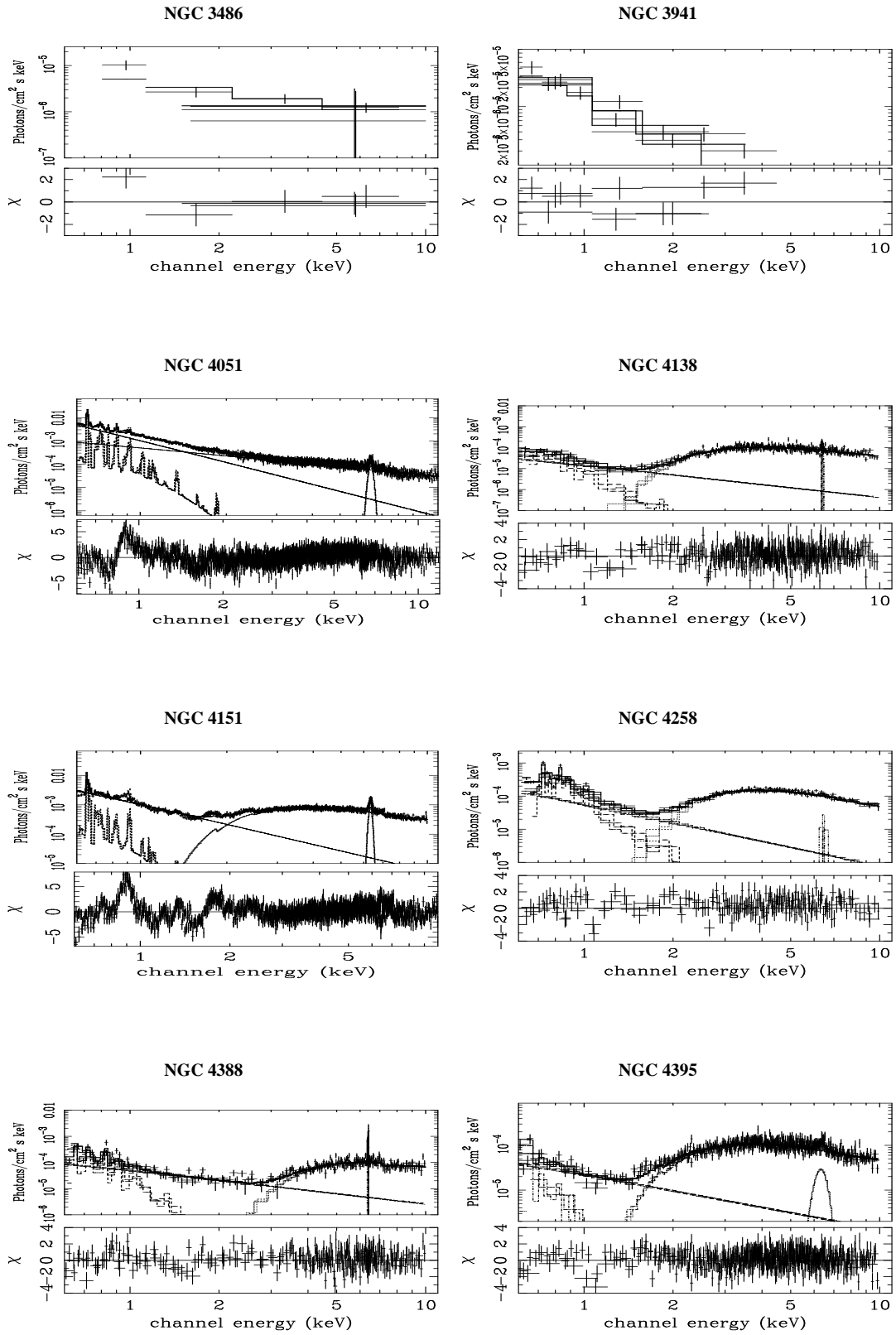
Galaxy name	N_{HGal}	N_H	Γ_{HX}	Γ_{SX}	kT	EW(Fe K)	χ^2_{red}/ν	F_{SX}	F_{HX}	$\log L_{SX}^{int.}$	$\log L_{HX}^{int.}$
(1)	(2)	(3)	(4)	(5)	(6)	(7)	(8)	(9)	(10)	(11)	(12)
NGC 4138	1.4	8.0±1	1.5±0.1	≡ Γ_{HX}	0.3±0.1	83±30	1.0/408	0.6	55.0	40.9	41.3
NGC 4151*	2.0	7.5±1	1.6±0.2	1.8±0.5	-	300±30	1.9/2785	29.7	451.0	42.0	42.5
NGC 4258†	1.2	8.7±0.3	1.7±0.1	1.9±0.1	0.5±0.1	27±20	1.0/899	< 3.4	83.7	<40.7	40.9
NGC 4388	2.6	27±2	1.3±0.2	≡ Γ_{HX}	0.3±0.1	450±70	1.0/283	2.2	76.2	41.2	41.8
NGC 4395	1.3	5.3±0.3	1.2±0.1	≡ Γ_{HX}	0.2±0.1	100±25	0.97/535	1.0	61.6	39.2	39.8
NGC 4472‡	1.7	0.3±0.1	2.7±0.3	-	0.8±0.2	-	1.8/483	< 19.8	< 3.8	<40.8	<40.1
NGC 4477	2.6	≤ 2	1.9±0.3	-	0.4±0.1	-	1.0/106	< 2.0	1.2	<40.0	39.6
NGC 4501	2.5	≤ 0.2	1.5±0.3	-	0.4±0.1	-	1.1/28	0.9	1.1	39.5	39.6
NGC 4565	1.3	0.12±0.04	1.8±0.2	-	-	-	1.2/70	1.1	2.4	39.2	39.4
NGC 4579	2.4	≤ 0.02	1.7±0.1	-	0.6±0.1	170±50	1.1/1043	25.3	38.5	41.0	41.1
NGC 4639	2.4	≤ 0.01	1.8±0.1	-	-	-	1.0/176	3.0	4.9	40.0	40.2
NGC 4698	1.9	≤ 0.4	2.0±0.2	-	-	-	1.2/17	0.3	0.4	39.1	39.2
NGC 4725	0.1	≤ 5	1.9±0.5	-	0.3±0.1	-	0.84/44	0.7	0.4	39.2	38.9
NGC 5033	0.1	≤ 0.03	1.7±0.1	-	-	466±215	0.97/335	15.0	28.7	40.8	41.1
NGC 5194	1.6	≤ 0.03	0.6±0.1	-	0.5±0.1	986±210	1.65/361	7.3	4.8	39.8	39.6
NGC 5273	0.1	0.9±0.1	1.4±0.1	≡ Γ_{HX}	0.2±0.1	226±75	1.1/1009	13.2	67.1	41.0	41.4

Notes: SX = 0.5–2 keV, HX = 2–10 keV. Galaxies marked with † and ‡ indicate that the nuclear regions are contaminated (by more than 10%) by off-nuclear point-sources and/or diffuse emission in only the soft band (†) or in both the soft and hard bands (‡). Galaxies marked with "*" indicate sources with very complex spectra for which only a rough parametrization is given here.

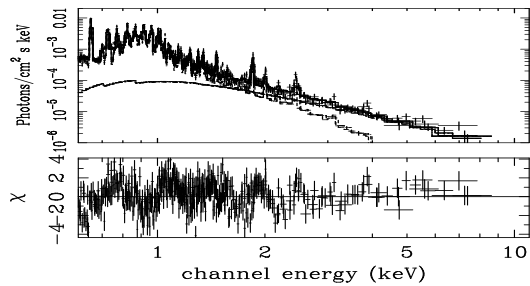
C.1 Atlas of X-ray spectra

Spectra in order of increasing NGC number are shown. For each object, the upper panel shows the unfolded spectrum and the baseline parameterization, together with the contributions to the model of the various additive components. Residuals are shown in the lower panel in units of σ .

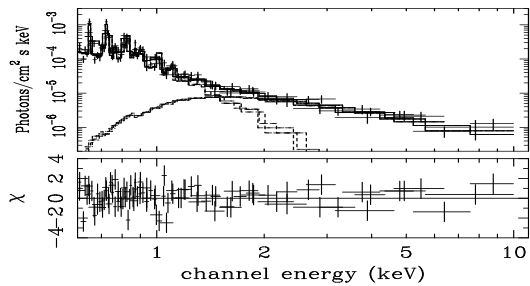




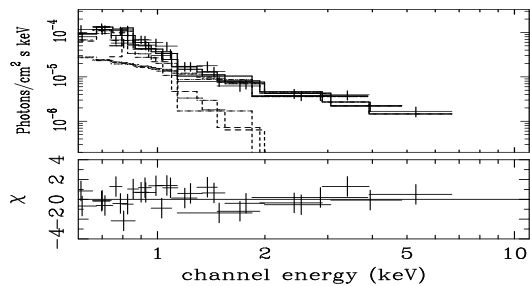
NGC 4472



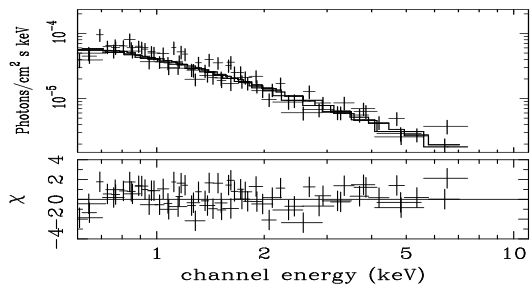
NGC 4477



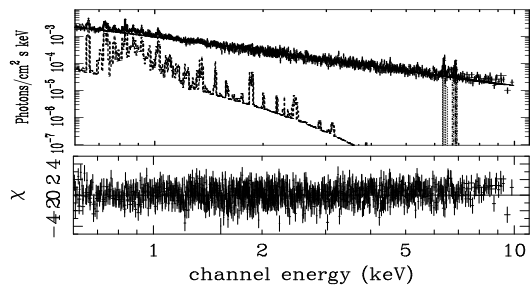
NGC 4501



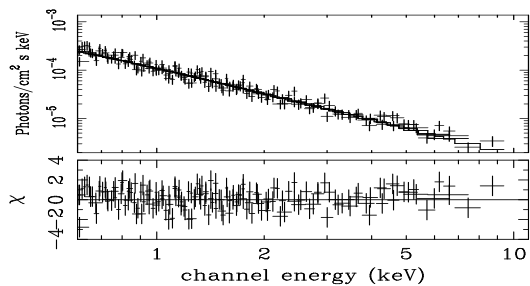
NGC 4565



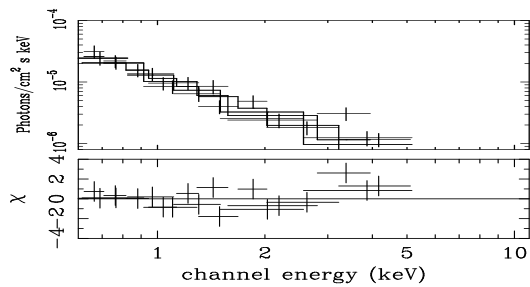
NGC 4579



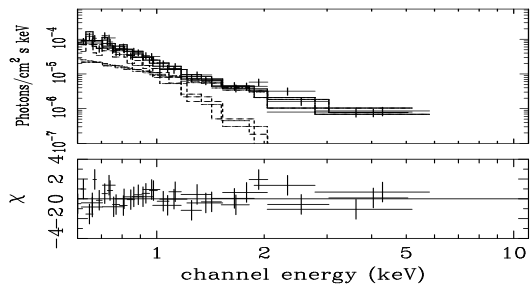
NGC 4639



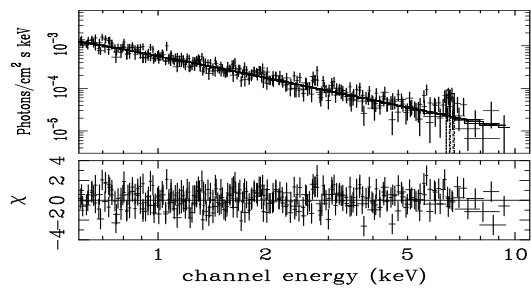
NGC 4698



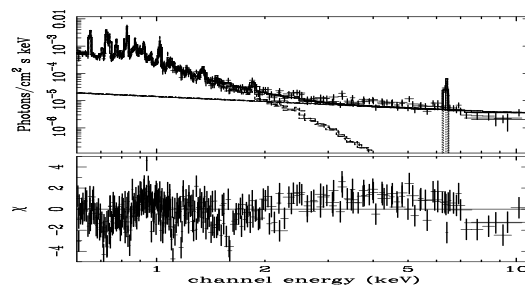
NGC 4725



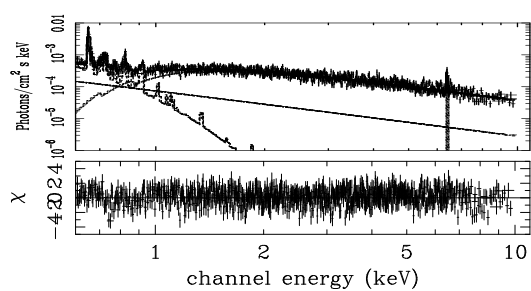
NGC 5033



NGC 5194



NGC 5273



Bibliography

- [] Abramowicz, M. A. 1997, LNP Vol. 487: Accretion Disks - New Aspects, 487, 320
- [] Agüero E.L., Calderon J.H., Paolantonio S., Suarez-Boedo E., 1994, PASP, 106, 978
- [] Alonso-Herrero, A., Rieke, M. J., Rieke, G. H., & Shields, J. C. 2000, ApJ, 530, 688
- [] Alonso-Herrero, A., Ward, M. J., & Kotilainen, J. K. 1997, MNRAS, 288, 977
- [] Antonucci, R. R. J. 1993, ARAA, 31, 473
- [] Antonucci, R.J., & Miller, J.S., 1985, ApJ 297, 621
- [] Avni, Y. 1976, ApJ, 210, 642
- [] Baan, W. A., & Klöckner, H.-R. 2006, A&A, 449, 559
- [] Barcons, X., Carrera, F. J., & Ceballos, M. T. 2003, MNRAS, 339, 757
- [] Barth, A. J., Ho, L. C., Filippenko, A. V., Rix, H.-W., & Sargent, W. L. W. 2001, ApJ, 546, 205
- [] Barth, A. J., Ho, L. C., & Sargent, W. L. W. 2002, AJ, 124, 2607
- [] Barth, A. J., Reichert, G. A., Filippenko, A. V., Ho, L. C., Shields, J. C., Mushotzky, R. F., & Puchnarewicz, E. M. 1996, AJ, 112, 1829
- [] Barvainis, R., Lehár, J., Birkinshaw, M., Falcke, H., & Blundell, K. M. 2005, ApJ, 618, 108
- [] Basko, M. M. 1978, ApJ, 223, 268
- [] Bassani, L., Dadina, M., Maiolino, R., et al. 1999, ApJS, 121, 473
- [] Beloborodov, A. M. 1999, ApJ, 510, L123
- [] Bianchi, S., Corral, A., Panessa, F., Barcons, X., Matt, G., Bassani, L., Carrera, F. J., & Jiménez-Bailón, E. 2008a, MNRAS, 385, 195
- [] Bianchi, S., Guainazzi, M., Matt, G., & Fonseca Bonilla, N. 2007, A&A, 467, L19
- [] Bianchi, S., La Franca, F., Matt, G., Guainazzi, M., Jimenez Bailón, E., Longinotti, A. L., Nicastro, F., & Pentericci, L. 2008, MNRAS, 389, L52
- [] Bianchi, S., & Matt, G. 2002, A&A, 387, 76
- [] Bianchi, S., Matt, G., Balestra, I., Guainazzi, M., & Perola, G. C. 2004, A&A, 422, 65
- [] Bianchi S., Matt G., Nicastro F., Porquet D., Dubau J., 2005b, MNRAS, 357, 599

- [] Bianchi S., Miniutti G., Fabian A.C., Iwasawa K., 2005a, MNRAS, 360, 380
- R. D., & Begelman, M. C. 1999, MNRAS, 303, L1
- [] Boella, G., Butler, R. C., Perola, G. C., Piro, L., Scarsi, L., & Bleeker, J. A. M. 1997, A&As, 122, 299
- [] Braito, V., et al. 2004, A&A, 420, 79
- S., & Elvis, M. 1997, MNRAS, 285, L25
- [] Brennenman, L. W., & Reynolds, C. S. 2006, ApJ, 652, 1028
- [] Brightman, M., & Nandra, K. 2008, MNRAS, 390, 1241
- [] Brindle, C., Hough, J. H., Bailey, J. A., Axon, D. J., Ward, M. J., Sparks, W. B., & McLean, I. S. 1990, MNRAS, 244, 577
- [] Burm, H. 1986, A&A, 165, 120
- [] Caccianiga, A., et al. 2004, A&A, 416, 901
- [] Caldwell, N., Rose, J. A., & Concannon, K. D. 2003, AJ, 125, 2891
- [] Cappi, M., 2006, stronomische Nachrichten, 327, 1012
- [] Cappi, M., et al. 2006, A&A, 446, 459
- [] Cecil, G., Bland-Hawthorn, J., & Veilleux, S. 2002, ApJ, 576, 745
- [] Chiaberge, M., Macchetto, F. D., Sparks, W. B., Capetti, A., Allen, M. G., & Martel, A. R. 2002, ApJ, 571, 247
- [] Cid Fernandes R., Gu Q., Melnick J., Terlevich E., Terlevich R., Kunth D., Rodrigues Lacerda R., Joguet B., 2004, MNRAS, 355, 273
- [] Colbert, E. J. M., Baum, S. A., Gallimore, J. F., O'Dea, C. P., & Christensen, J. A. 1996, ApJ, 467, 551
- [] Collin-Souffrin, S., Czerny, B., Dumont, A.-M., & Zycki, P. T. 1996, A&A, 314, 393
- [] Comastri, A., Setti, G., Zamorani, G., & Hasinger, G. 1995, A&A, 296, 1
- [] Condon, J. J., & Broderick, J. J. 1991, AJ, 102, 1663
- [] Condon, J. J., Cotton, W. D., & Broderick, J. J. 2002, AJ, 124, 675
- [] Condon J.J., Helou G., Sanders D.B., Soifer B.T., 1996, ApJS, 103, 81
- [] Contini, M. 2004, MNRAS, 354, 675
- [] Corral, A., Barcons, X., Carrera, F. J., Ceballos, M. T., & Mateos, S. 2005, A&A, 431, 97
- [] Costantini, E., et al. 2007, A&A, 461, 121
- [] Crenshaw, D. M., & Kraemer, S. B. 2007, ApJ, 659, 250
- [] Crummy, J., Fabian, A. C., Gallo, L., & Ross, R. R. 2006, MNRAS, 365, 1067
- [] Czerny, B., Doroshenko, V. T., Nikolajuk, M., Schwarzenberg-Czerny, A., Loska, Z., & Madejski, G. 2003a, MNRAS, 342, 1222
- [] Czerny, B., Nikolajuk, M., Róžańska, A., Dumont, A.-M., Loska, Z., & Zycki, P. T. 2003b, A&A, 412, 317
- [] Dadina M., Cappi M., 2004, A&A, 413, 921
- [] Dadina, M., Cappi, M., Malaguti, G., Ponti, G., & de Rosa, A. 2005, A&A, 442, 461

- [] Davidson, K., & Netzer, H. 1979, *Reviews of Modern Physics*, 51, 715
- [] De Marco, B., Cappi, M., Dadina, M., & Palumbo, G.G.C., 2006, *Astron. Nach.*, astro-ph/0610882
- [] Jder de Robertis M.M., Hutchings J.B., Pitts R.E., 1988, *AJ*, 95, 1371
- [] De Rosa, A., Fabian, A. C., & Piro, L. 2002a, *MNRAS*, 334, L21
- [] De Rosa, A., Piro, L., Fiore, F., Grandi, P., Maraschi, L., Matt, G., Nicastro, F., & Petrucci P.O. 2002b, *A&A*, 387, 838
- [] De Rosa, A., Piro, L., Matt, G., & Perola, G. C. 2004, *A&A*, 413, 895
- [] de Rosa, A., Piro, L., Perola, G. C., Capalbi, M., Cappi, M., Grandi, P., Maraschi, L., & Petrucci, P. O. 2007, , 463, 903
- [] Dickey & Lockman, 1990, *Ann. Rev. Ast. Astr.* 28, 215.
- [] di Nella, H., Garcia, A. M., Garnier, R., & Paturel, G. 1995, *A&As*, 113, 151
- [] Dovčiak, M., Bianchi, S., Guainazzi, M., Karas, V., & Matt, G. 2004, *MNRAS*, 350, 745
- [] Eckart, A., & Genzel, R. 1996, *Nature*, 383, 415
- [] Elitzur, M., & Shlosman, I. 2006, , 648, L101
- [] Elvis, M. et al. 1994, *ApJs*, 95, 1
- [] Elvis M., 2000, *ApJ*, 545, 63
- [] Elvis, M., Risaliti, G., Nicastro, F., Miller, J. M., Fiore, F., & Puccetti, S. 2004, *ApJl*, 615, L25
- [] Elvis, M., Soltan, A., & Keel, W. C. 1984, *ApJ*, 283, 479
- [] Eracleous, M., Shields, J. C., Chartas, G., & Moran, E. C. 2002, *ApJ*, 565, 108
- [] Fabian, A. C., Iwasawa, K., Reynolds, C. S., & Young, A. J. 2000, *PASP*, 112, 1145
- [] Fabian A.C., Miniutti G., 2006, to appear in “Kerr Spacetime: Rotating Black Holes in General Relativity” eds. D.L. Wilshire, M. Visser and S.M. Scott Cambridge Univ. Press (preprint astro-ph/0507409)
- [] Fabian A.C., Miniutti G., Gallo L., Boller Th., Tanaka Y., Vaughan S., Ross R.R., 2005, *MNRAS*, 353, 1071
- [] Fabian A.C., Vaughan S., 2003, *MNRAS*, 340, L28
- [] Falcke, H., K rding, E., & Markoff, S. 2004, *A&A*, 414, 895
- [] Farrah, D., Afonso, J., Efstathiou, A., Rowan-Robinson, M., Fox, M., & Clements, D. 2003, *MNRAS*, 343, 585
- [] Feigelson, E. D., & Nelson, P. I. 1985, *ApJ*, 293, 192
- [] Ferrarese, L. 2002, *ApJ*, 578, 90
- [] Filippenko, A. V., Ho, L. C., & Sargent, W. L. W. 1993, *ApJl*, 410, L75
- [] Filippenko, A. V. & Sargent, W. L. W. 1985, *ApJs*, 57, 503
- [] Filippenko, A. V. & Sargent, W. L. W. 1989, *ApJl*, 342, L11
- [] Fiore, F., et al. 2001a, *MNRAS*, 327, 771
- [] Fiore, F., et al. 2001b, *ApJ*, 556, 150

- [] Fiore, F., Guainazzi, M. & Grandi, P., 1999, "Handbook for NFI spectral analysis", <http://www.asdc.asi.it/bepposax/software/cookbook/>
- [] Franceschini, A., et al. 2003, MNRAS, 343, 1181
- [] Frontera, F., Costa, E., dal Fiume, D., Feroci, M., Nicastro, L., Orlandini, M., Palazzi, E., & Zavattini, G. 1997, , 3114, 206
- [] Fukazawa, Y., Iyomoto, N., Kubota, A., Matsumoto, Y., & Makishima, K. 2001, A&A, 374, 73
- [] Georgantopoulos, I., & Zezas, A. 2003, ApJ, 594, 704
- [] Ghisellini, G., Haardt, F., & Matt, G. 1994, MNRAS, 267, 743
- [] Gierliński, M., & Done, C. 2006, MNRAS, 371, L16
- [] Gilfanov, M., Churazov, E., & Revnivtsev, M. 1999, A&A, 352, 182
- [] Gilli, R., Comastri, A., & Hasinger, G. 2007, A&A, 463, 79
- [] Gilli, R., Salvati, M., & Hasinger, G. 2001, A&A, 366, 407
- [] Giuricin, G., Mardirossian, F., Mezzetti, M., & Bertotti, G. 1990, ApJs, 72, 551
- [] Goad, M., & Koratkar, A. 1998, ApJ, 495, 718
- [] Grandi, P., Malaguti, G., & Fiocchi, M. 2006, ApJ, 642, 113
- [] Grandi, P., et al. 2003, ApJ, 593, 160
- [] Guainazzi, M., et al. 1998, MNRAS, 301, L1
- [] Guainazzi, M., Bianchi, S., & Dovčiak, M. 2006, Astronomische Nachrichten, 327, 1032
- [] Guainazzi, M., Fabian, A. C., Iwasawa, K., Matt, G., & Fiore, F. 2005, MNRAS, 356, 295
- [] Guainazzi, M., Marshall, W., & Parmar, A. N. 2001, MNRAS, 323, 75
- [] Guainazzi, M., Matt, G., Brandt, W. N., Antonelli, L. A., Barr, P., & Bassani, L. 2000, A&A, 356, 463
- [] Guainazzi M., Matt G., Perola G.C., 2005, A&A, 444, 119
- [] Haardt, F. 1993, ApJ, 413, 680
- [] Haardt, F., & Maraschi, L. 1991, ApJ, 380, L51
- [] Haardt, F., & Maraschi, L. 1993, ApJ, 413, 507
- [] Harris, D. E., & Krawczynski, H. 2002, ApJ, 565, 244
- [] Haardt, F., Maraschi, L., & Ghisellini, G. 1997, ApJ, 476, 620
- [] Heckman, T. M., Ptak, A., Hornschemeier, A., & Kauffmann, G. 2005, ApJ, 634, 161
- [] Ho, L. C. 1999, ApJ, 516, 672
- [] Ho, L. C. et al. 2001, ApJ, 549, L51
- [] Ho, L. C. 2002, ApJ, 564, 120
- [] Ho, L. C. 2003, ASP Conf. Ser. 290: Active Galactic Nuclei: From Central Engine to Host Galaxy, 290, 379
- [] Ho, L. C., Filippenko, A. V., & Sargent, W. L. 1995, ApJs, 98, 477

- [] Ho, L. C., Filippenko, A. V., & Sargent, W. L. W. 1997a, *ApJs*, 112, 315 (HFS97)
- [] Ho, L. C., Filippenko, A. V., Sargent, W. L. W., & Peng, C. Y. 1997b, *ApJs*, 112, 391
- [] Ho, L. C. & Peng, C. Y. 2001, *ApJ*, 555, 650
- [] Ho, L. C., & Ulvestad, J. S. 2001, *ApJs*, 133, 77 (HU01)
- [] Isobe, T., Feigelson, E. D., & Nelson, P. I. 1986, *ApJ*, 306, 490
- [] Iwasawa, K., et al. 1996, *MNRAS*, 282, 1038
- [] Iwasawa, K., Fabian, A. C., Almaini, O., Lira, P., Lawrence, A., Hayashida, K., & Inoue, H. 2000, *MNRAS*, 318, 879
- [] Iwasawa, K., Fabian, A. C., & Matt, G. 1997, *MNRAS*, 289, 443
- [] Iwasawa, K., Miniutti, G., & Fabian, A. C. 2004, *MNRAS*, 355, 1073
- [] Iwasawa, K., & Taniguchi, Y. 1993, *ApJl*, 413, L15
- [] Iyomoto, N., Fukazawa, Y., Nakai, N., & Ishihara, Y. 2001, *ApJl*, 561, L69
- [] Jiang, P., Wang, J. X., & Wang, T. G. 2006, *ApJ*, 644, 725
- [] Kaastra, J. S., Steenbrugge, K. C., Raassen, A. J. J., van der Meer, R. L. J., Brinkman, A. C., Liedahl, D. A., Behar, E., & de Rosa, A. 2002, *A&A*, 386, 427
- [] Kaspi, S., Smith, P. S., Netzer, H., Maoz, D., Jannuzi, B. T., & Giveon, U. 2000, *ApJ*, 533, 631
- [] Kaspi, S., et al. 2001, *ApJ*, 554, 216
- [] Kato, S. 2001, *PASJ*, 53, L37
- [] Keel, W. C., & Miller, J. S. 1983, *ApJl*, 266, L89
- [] Kollmeier, J.A., et al., 2005, submitted to *ApJ*, (astro-ph/0508657)
- [] Koratkar, A. P., & Gaskell, C. M. 1991, *ApJl*, 370, L61
- [] Kormendy, J. & Richstone, D. 1995, *ARA&A*, 33, 581
- [] Kriss, G. A., et al. 2000, *ApJl*, 538, L17
- [] Krolik J.H., 2001, *ApJ*, 551, 72
- [] La Franca, F., et al. 2005, *ApJ*, 635, 864
- [] Lamastra A., Perola G.C., Matt G., 2006, *A&A*, 449, 551
- [] Lamer, G., Uttley, P., & McHardy, I. M. 2003a, *MNRAS*, 342, L41
- [] Lamer, G., McHardy, I. M., Uttley, P., & Jahoda, K. 2003b, *MNRAS*, 338, 323
- [] Leahy, D. A., & Creighton, J. 1993, *MNRAS*, 263, 314
- [] Lee W.H., Abramowicz M.A., & Kluzniak W., 2004, *ApJ*, 603, L93
- [] Lee, J. C., Fabian, A. C., Reynolds, C. S., Brandt, W. N., & Iwasawa, K. 2000, *MNRAS*, 318, 857
- [] Longinotti, A. L., Bianchi, S., Santos-Lleo, M., Rodríguez-Pascual, P., Guainazzi, M., Cardaci, M., & Pollock, A. M. T. 2007, *A&A*, 470, 73

- [] Longinotti, A. L., de La Calle, I., Bianchi, S., Guainazzi, M., & Dovčiak, M. 2008, *Memorie della Societa Astronomica Italiana*, 79, 259
- [] Lyubarskii, Y. E. 1997, *MNRAS*, 292, 679
- [] Maccacaro, T., Perola, G. C., & Elvis, M. 1982, *ApJ*, 257, 47
- [] Machida, M., & Matsumoto, R. 2003, *ApJ*, 585, 429
- [] Magdziarz, P., & Zdziarski, A. A. 1995, *MNRAS*, 273, 837
- [] Magorrian, J., et al. 1998, *AJ*, 115, 2285
- [] Maiolino, R., Salvati, M., Bassani, L., Dadina, M., della Ceca, R., Matt, G., Risaliti, G., & Zamorani, G. 1998, *A&A*, 338, 781
- [] Maiolino, R., et al. 2003, *MNRAS*, 344, L59
- [] Maiolino, R., Marconi, A., & Olivia, E. 2001b, *A&A* 365, 37
- [] Maiolino, R., Marconi, A., Salvati, M., et al. 2001a, *A&A* 365, 28
- [] Maiolino, R., Rieke, G.H., 1995, *ApJ* 454, 95
- [] Makishima, K. 1986, *LNP Vol. 266: The Physics of Accretion onto Compact Objects*, 266, 249
- [] Malizia, A., Bassani, L., Capalbi, M., Fabian, A. C., Fiore, F., & Nicastro, F. 2003, *A&A*, 406, 105
- [] Malizia, A., Bassani, L., Stephen, J. B., Malaguti, G., & Palumbo, G. G. C. 1997, *ApJs*, 113, 311
- [] Malkan M.A., Gorijn V, Tam R., 1998, *ApJS*, 117, 25
- [] Maraschi, L., & Haardt, F. 1997, *IAU Colloq. 163: Accretion Phenomena and Related Outflows*, 121, 101
- [] Marconi, A., & Hunt, L. K. 2003, *ApJl*, 589, L21
- [] Marconi, A., Risaliti, G., Gilli, R., Hunt, L. K., Maiolino, R., & Salvati, M. 2004, *MNRAS*, 351, 169
- [] Markovic D. & Lamb F.K., 1998, *ApJ*, 507, 316
- [] Markowitz, A. 2005, *ApJ*, 635, 180
- [] Martins, L. P., Viegas, S. M., & Gruenwald, R. 2003, *ApJ*, 587, 562
- [] Marx, M., Kruegel, E., Klein, U., & Wielebinski, R. 1994, *A&A*, 281, 718
- [] Marziani, P., Sulentic, J. W., Zamanov, R., Calvani, M., Dultzin-Hacyan, D., Bachev, R., & Zwitter, T. 2003, *ApJs*, 145, 199
- [] Mateos, S., Barcons, X., Carrera, F. J., Ceballos, M. T., Hasinger, G., Lehmann, I., Fabian, A. C., & Streblyanska, A. 2005, *A&A*, 444, 79
- [] Matt, G., et al. 1997, *A&A*, 325, L13
- [] Matt, G., et al. 1999, *A&A*, 341, L39
- [] Matt G., 2002, *MNRAS*, 337, 147
- [] Matt, G., Fabian, A. C., Guainazzi, M., Iwasawa, K., Bassani, L., & Malaguti, G. 2000a, *MNRAS*, 318, 173
- [] Matt, G., Fabian, A. C., & Ross, R. R. 1996, *MNRAS*, 278, 1111
- [] Mattson, B. J., & Weaver, K. A. 2004, *ApJ*, 601, 771

- [] McElroy, D. B., 1995, *ApJs*, 100, 105
- [] McHardy, I. M., Papadakis, I. E., & Uttley, P. 1998, *The Active X-ray Sky: Results from BeppoSAX and RXTE*, 509
- [] McKernan B., Yaqoob T., Reynolds C.S., 2004, *ApJ*, 617, 232
- [] McKernan B., Yaqoob T., Reynolds C.S., 2005, *MNRAS*, 361, 1337
- [] Merloni, A., Heinz, S., & di Matteo, T. 2003, *MNRAS*, 345, 1057
- [] Merloni A., Malzac J., Fabian A.C., Ross R.R., 2006, *MNRAS*, 370, 1699
- [] Merritt, D., & Ferrarese, L. 2001a, *ApJ*, 547, 140
- [] Merritt, D., & Ferrarese, L. 2001b, *MNRAS*, 320, L30
- [] Miller J.M. & Homan J., 2005, *ApJ*, 618, L107
- [] Miller, L., Turner, T. J., Reeves, J. N. et al. 2006, *A&A*, 453, L13
- [] Miller, L., Turner, T. J., Reeves, J. N., George, I. M., Kraemer, S. B., & Wingert, B. 2007, *A&A*, 463, 131
- [] Miniutti, G., et al. 2007, *PASJ*, 59, 315
- [] Miniutti, G., & Fabian, A. C. 2004, *MNRAS*, 349, 1435
- [] Miniutti G., Fabian A.C., 2006, *MNRAS*, 366, 115
- [] Miniutti G., Fabian A.C., Goyder R., Lasenby A.N., 2003, *MNRAS*, 344, L22
- [] Molendi, S., Bianchi, S., & Matt, G. 2003, *MNRAS*, 343, L1
- [] Morganti, R., Tsvetanov, Z. I., Gallimore, J., & Allen, M. G. 1999, *A&As*, 137, 457
- [] Mulchaey, J. S., Koratkar, A., Ward, M. J., Wilson, A. S., Whittle, M., Antonucci, R. R. J., Kinney, A. L., & Hurt, T. 1994, *ApJ*, 436, 586
- [] Nagar, N. M., Wilson, A. S., Mulchaey, J. S., & Gallimore, J. F. 1999, *ApJs*, 120, 209
- [] Nandra, K. 2006, *MNRAS*, 368, L62
- [] Nandra, K., George, I. M., Mushotzky, R. F., Turner, T. J., & Yaqoob, T. 1997, *ApJ*, 477, 602
- [] Nandra, K., O'Neill, P. M., George, I. M., & Reeves, J. N. 2007, *MNRAS*, 382, 194
- [] Nandra, K., & Pounds, K. A. 1994, *MNRAS*, 268, 405
- [] Narayan, R., & Yi, I. 1994, *ApJl*, 428, L13
- [] Netzer, H., Chelouche, D., George, I. M., Turner, T. J., Crenshaw, D. M., Kraemer, S. B., & Nandra, K. 2002, *ApJ*, 571, 256
- [] Nicastro, F., 2000, *ApJl*, 530, L65
- [] O'Neill, P. & Nandra, K., 2006, in preparation
- [] Osterbrock, D. E. 1981, *ApJ*, 249, 462
- [] Osterbrock D.E., de Robertis M.M., 1985, *PASP*, 97, 1129
- [] Page, M. J., Davis, S. W., & Salvi, N. J. 2003, *MNRAS*, 343, 1241
- [] Page, K. L., O'Brien, P. T., Reeves, J. N., & Turner, M. J. L. 2004, *MNRAS*, 347, 316

- [] Palmeri, P., Mendoza, C., Kallman, T. R., & Bautista, M. A. 2003, *A&A*, 403, 1175
- [] Panessa, F. & Bassani, L. 2002, *A&A*, 394, 435
- [] Panessa, F. 2004, PhD Thesis, University of Bologna, (<http://venus.ifca.unican.es/panessa/>)
- [] Papadakis, I. E., Kazanas, D., & Akylas, A. 2005, *ApJ*, 631, 727
- [] Parmar, A. N., et al. 1997, *A&As*, 122, 309
- [] Pappa, A., Georgantopoulos, I., Stewart, G. C., & Zezas, A. L. 2001, *MNRAS*, 326, 995
- [] Park, M.-G., & Ostriker, J. P. 2001, *ApJ*, 549, 100
- [] Paturel, G., Teerikorpi, P., Theureau, G., Fouqué, P., Musella, I., & Terry, J. N. 2002, *A&A*, 389, 19
- [] Pellegrini, S. 2005, *ApJ*, 624, 155
- [] Pérez García, A. M. & Rodríguez Espinosa, J. M. 2001, *ApJ*, 557, 39
- [] Perez-Olea, D. E., & Colina, L. 1996, *ApJ*, 468, 191
- [] Perley, R. A., Dreher, J. W., & Cowan, J. J. 1984, *ApJ*, 285, L35
- [] Perola, G. C., Matt, G., Cappi, M., Fiore, F., Guainazzi, M., Maraschi, L., Petrucci, P. O., & Piro, L. 2002, *A&A*, 389, 802
- [] Peterson, B. M., et al. 2004, *ApJ*, 613, 682
- [] Petre, R., Mushotzky, R. F., Holt, S. S., & Krolik, J. H. 1984, *ApJ*, 280, 499
- [] Petrucci, P. O., et al. 2007, *A&A*, 470, 889
- [] Ponti, G., Cappi, M., Dadina, M., & Malaguti, G. 2004, *A&A*, 417, 451
- [] Ponti G., Miniutti G., Cappi M., Maraschi L., Fabian A.C., Iwasawa K., 2006, *MNRAS*, 368, 903
- [] Pounds, K. A., Nandra, K., Stewart, G. C., George, I. M., & Fabian, A. C. 1990, *Nature*, 344, 132
- [] Pounds, K. A., Reeves, J. N., King, A. R., & Page, K. L. 2004, *MNRAS*, 350, 10
- [] Pounds, K., Reeves, J., O'Brien, P., Page, K., Turner, M., & Nayakshin, S. 2001, *ApJ*, 559, 181
- [] Pounds, K. A., Reeves, J. N., Page, K. L., Edelson, R., Matt, G., & Perola, G. C. 2003, *MNRAS*, 341, 953
- [] Poutanen, J., & Fabian, A. C. 1999, *MNRAS*, 306, L31
- [] Poutanen, J., & Svensson, R. 1996, *ApJ*, 470, 249
- [] Psaltis D., 2001, *Adv Space Res.*, 28, 481
- [] Ptak, A., Heckman, T., Levenson, N. A., Weaver, K., & Strickland, D. 2003, *ApJ*, 592, 782
- [] Ptak, A., Terashima, Y., Ho, L. C., & Quataert, E. 2004, *ApJ*, 606, 173
- [] Puccetti, S., Risaliti, G., Fiore, F., Elvis, M., Nicastro, F., Perola, G. C., Capalbi M. 2003, To appear in *Proc. of the BeppoSAX Symposium: "The Restless High-Energy Universe,"* ed. E. P. J. van den Heuvel, J. J. M. in't Zand, & R. A. M. J. Wijers (astro-ph/0311446)
- [] Reeves, J., Done, C., Pounds, K., Terashima, Y., Hayashida, K., Anabuki, N., Uchino, M., & Turner, M. 2008, *MNRAS*, 385, L108
- [] Reeves, J. N., et al. 2006, *Astronomische Nachrichten*, 327, 1079

- [] Reeves, J. N., Nandra, K., George, I. M. et al. 2004, *ApJ*, 602, 648
- [] Reeves J.N., O'Brien P.T., Ward M.J., 2003, *ApJ*, 593, L65
- [] Revnivtsev, M., Borozdin, K., & Emelyanov, A. 1999, *A&A*, 344, L25
- [] Revnivtsev, M., Sazonov, S., Jahoda, K., & Gilfanov, M. 2004, *A&A*, 418, 927
- [] Reynolds, C. S. 1997, *MNRAS*, 286, 513
- [] Reynolds, C. S., Brenneman, L. W., Wilms, J., & Kaiser, M. E. 2004, *MNRAS*, 352, 205
- [] Reynolds, C. S., & Nowak, M. A. 2003, *Phys. Rep*, 377, 389
- [] Rezzolla L., Yoshida S., Maccarone T.J., Zanotti O., 2003, *MNRAS*, 344, L37
- [] Risaliti, G. 2002, *A&A*, 386, 379
- [] Risaliti, G., Bianchi, S., Matt, G., Baldi, A., Elvis, M., Fabbiano, G., & Zezas, A. 2005, *ApJ*, 630, L129
- [] Risaliti, G., & Elvis, M. 2004, *ASSL Vol. 308: Supermassive Black Holes in the Distant Universe*, 187
- [] Risaliti, G., Elvis, M., Fabbiano, G., Baldi, A., & Zezas, A. 2005, *ApJL*, 623, L93
- [] Risaliti G., Elvis M., Nicastro F., 2002, *ApJ*, 571, 234
- [] Risaliti, G., Maiolino, R., & Salvati, M. 1999, *ApJ*, 522, 157
- [] Ross, R. R., & Fabian, A. C. 1993, *MNRAS*, 261, 74
- [] Ross R.R., Fabian A.C., 2005, *MNRAS*, 358, 211
- [] Roy, A. L., Norris, R. P., Kesteven, M. J., Troup, E. R., & Reynolds, J. E. 1994, *ApJ*, 432, 496
- [] Roy, A. L., Norris, R. P., Kesteven, M. J., Troup, E. R., & Reynolds, J. E. 1998, *MNRAS*, 301, 1019
- [] Rush, B., Malkan, M. A., & Edelson, R. A. 1996, *ApJ*, 473, 130
- [] Sandage, A., & Bedke, J. 1994, *The Carnegie Atlas of galaxies. Volume I*, Carnegie Institution of Washington
- [] Sandage, A., Tammann, G. A., & Yahil, A. 1979, *ApJ*, 232, 352
- [] Sanders D.B., Mazzarella J.M., Kim D.-C., Surace J.A., Soifer B.T., 2003, *ApJ*, 126, 1607
- [] Sazonov, S., Revnivtsev, M., Krivonos, R., Churazov, E., & Sunyaev, R. 2007, *A&A*, 462, 57
- [] Schmitt H.R., Antonucci R.R.J., Ulvestad J.S., Kinney A.L., Clarke C.J., Pringle J.E., 2001a, *ApJ*, 555, 663
- [] Schmitt H.R., Ulvestad J.S., Antonucci R.R.J., Kinney A.L., 2001b, *ApJS*, 132, 199
- [] Schnittman J.D., Homan J., Miller J.M., 2006, *ApJ*, 642, 420
- [] Shakura, N. I. & Sunyaev, R. A. 1973, *A&A*, 24, 337
- [] Shih, D. C., Iwasawa, K., & Fabian, A. C. 2002, *MNRAS*, 333, 687
- [] Shih, D. C., Iwasawa, K., & Fabian, A. C. 2003, *MNRAS*, 341, 973
- [] Smith, R. A. N., Page, M. J., & Branduardi-Raymont, G. 2007, , 461, 135
- [] Smith, P. S., Schmidt, G. D., Allen, R. G., & Angel, J. R. P. 1995, *ApJ*, 444, 146
- [] Stetson, P. B. & Gibson, B. K. 2001, *MNRAS*, 328, L1

- [] Tanaka, Y., et al. 1995, *Nature*, 375, 659
- [] Taylor, G. B., Vermeulen, R. C., Readhead, A. C. S., Pearson, T. J., Henstock, D. R., & Wilkinson, P. N. 1996, *ApJs*, 107, 37
- [] Terashima Y., Ho L. C., Ptak A. F. 2000, *ApJ*, 533, 729
- [] Terashima, Y., Iyomoto, N., Ho, L. C., & Ptak, A. F. 2002, *ApJs*, 139, 1
- [] Terashima, Y., Kunieda, H., & Misaki, K. 1999, *PASJ*, 51, 277
- [] Terashima, Y., & Wilson, A. S. 2001, *ApJ*, 560, 139
- [] Terashima, Y., & Wilson, A. S. 2003, *ApJ*, 583, 145
- [] Thean, A., Pedlar, A., Kukula, M. J., Baum, S. A., & O'Dea, C. P. 2000, *MNRAS*, 314, 573
- [] Thim, F., Hoessel, J. G., Saha, A., Claver, J., Dolphin, A., & Tammann, G. A. 2004, *AJ*, 127, 2322
- [] Tombesi, F., de Marco, B., Iwasawa, K., Cappi, M., Dadina, M., Ponti, G., Miniutti, G., & Palumbo, G. G. C. 2007, *A&A*, 467, 1057
- [] Tonry, J. L., Dressler, A., Blakeslee, J. P., Ajhar, E. A., Fletcher, A. B., Luppino, G. A., Metzger, M. R., & Moore, C. B. 2001, *ApJ*, 546, 681
- [] Tremaine, S., et al. 2002, *ApJ*, 574, 740
- [] Trussoni, E., Vagnetti, F., Massaglia, S., Feretti, L., Parma, P., Morganti, R., Fanti, R., & Padovani, P. 1999, *A&A*, 348, 437
- [] Tully, R. B. 1988, *Nearby Galaxies Catalog* (Cambridge: Cambridge University Press)
- [] Turner, T. J. et al. 2002, *ApJl*, 574, L123
- [] Turner, T. J., George, I. M., Nandra, K., & Mushotzky, R. F., 1997, *ApJS*, 113, 23
- [] Turner, T. J., George, I. M., Nandra, K., & Mushotzky, R. F. 1998, *ApJ*, 493, 91
- [] Turner, T. J., George, I. M., Nandra, K., & Turcan, D. 1999, *ApJ*, 524, 667
- [] Turner, T. J., Kraemer, S. B., George, I. M., Reeves, J. N., & Bottorff, M. C. 2005, *ApJ*, 618, 155
- [] Turner, T. J., Miller, L., George, I. M., & Reeves, J. N. 2006, *A&A*, 445, 59
- [] Turner, T. J., Perola, G. C., Fiore, F., Matt, G., George, I. M., Piro, L., & Bassani, L. 2000, *ApJ*, 531, 245
- [] Turner, T. J., & Pounds, K. A. 1989, *MNRAS*, 240, 833
- [] Ueda, Y., Ishisaki, Y., Takahashi, T., Makishima, K., & Ohashi, T. 2001, *ApJs*, 133, 1
- [] Ueno S. PhD Thesis 1995
- [] Ueno, S., Koyama, K., Nishida, M., Yamauchi, S., & Ward, M. J. 1994, *ApJl*, 431, L1
- [] Ulrich, M.-H., Maraschi, L., & Urry, C. M. 1997, *ARA&A*, 35, 445
- [] Ulvestad, J. S., & Ho, L. C. 2001, *ApJl*, 562, L133
- [] Urry, C. M., & Padovani, P. 1995, *PASP*, 107, 803
- [1] 2003ApJ...595..656U Uttley, P., Fruscione, A., McHardy, I., & Lamer, G. 2003, *ApJ*, 595, 656
- [] Vaughan, S., & Edelson, R. 2001, *ApJ*, 548, 694

- [] Vaughan, S., Iwasawa, K., Fabian, A. C., & Hayashida, K. 2005, MNRAS, 356, 524
- [] Vaughan, S., Reeves, J., Warwick, R., & Edelson, R. 1999, MNRAS, 309, 113
- [] Véron-Cetty, M.-P., & Véron, P. 2001, A&A, 374, 92
- [] Véron-Cetty, M.-P., & Véron, P. 2006, A&A, 455, 773
- [] Wang, J.-M., Watarai, K.-Y., & Mineshige, S. 2004, ApJl, 607, L107
- [] Ward, M. J., Done, C., Fabian, A. C., Tennant, A. F., & Shafer, R. A. 1988, ApJ, 324, 767
- [] Weaver K.A., 2001, in "The central kpc of starburst and AGN: the La Palma connection", eds. J.H. Knapen, J.E. Beckman, I. Shlosman, T.J. Mahoney, ASP Conf. Ser., 249, 389
- [] Weingartner, J. C., & Murray, N. 2002, ApJ, 580, 88
- [] Woo, J.-H., & Urry, C. M. 2002, ApJ, 579, 530
- [] Xu, C., Livio, M., & Baum, S. 1999, AJ, 118, 1169
- [] Yaqoob, T., McKernan, B., Kraemer, S. B., Crenshaw, D. M., Gabel, J. R., George, I. M., & Turner, T. J. 2003, ApJ, 582, 105
- [] Yaqoob, T., & Padmanabhan, U. 2004, ApJ, 604, 63
- [] Yee, H. K. C., & Oke, J. B. 1978, ApJ, 226, 753
- [] Young S., Hough J.H., Efstathiou A., Wills B.J., Bailey J.A., Ward M.J., Axon D.J., 1996, MNRAS, 281, 1206
- [] Young, A. J., Lee, J. C., Fabian, A. C., Reynolds, C. S., Gibson, R. R., & Canizares, C. R. 2005, ApJ, 631, 733
- [] Yuan, W., Brinkmann, W., Siebert, J., & Voges, W. 1998, A&A, 330, 108
- [] Yun, M. S., Reddy, N. A., & Condon, J. J. 2001, ApJ, 554, 803
- [] Zdziarski, A. A., Lubiński, P., Gilfanov, M., & Revnivtsev, M. 2003, MNRAS, 342, 355
- [] Zdziarski, A. A., Lubinski, P., & Smith, D. A. 1999, MNRAS, 303, L11
- [] Zhou, X.-L., & Wang, J.-M. 2005, ApJl, 618, L83
- [] Zycki P.T. & Sobolewska M.A., 2005, MNRAS, 364, 891

Aknowledgements

First of all, I would like to thank my supervisor, Prof. Giorgio Palumbo, that, *again*, decided to support and drive me in such an adventure....

I deeply thank Massimo. He knows why.

I deeply thank the members of the sometimes 'frayed team' to which I belong: Paola, Pino, Luigi, Guido, Valentina, Gabriele, Barbara, Valentina, Francesco, Lorenzo, and Eleonora.

I thank all the wonderful friends of the FLC/CGIL

I thank all the wonderful friends of PRECAREA

I thank all the wonderful friends of LRC

I thank Ornella, Federico and Francesca.

I thank Gigio and Stefano and their wonderful families.

I thank the ones that left me (and my kids) too early.